Towards the Understanding of the Molecular and Physiological Role of Hexose-6-Phosphate Dehydrogenase

Inauguraldissertation

zur

Erlangung der Würde eines Doktors der Philosophie

vorgelegt der

Philosophisch-Naturwissenschaftlichen Fakultät

der Universität Basel

von

Michael Weingartner

Basel, 2021

Genehmigt von der Philosophisch-Naturwissenschaftlichen Fakultät

auf Antrag von

Prof. Dr. Alex Odermatt, Prof. Dr. Jörg Huwyler und Prof. Dr. David Hoogewijs

Basel, 30.03.2021

Dekan

Prof. Dr. Marcel Mayor

Table of Contents

Abbreviations

AGR2	Anterior gradient 2 protein homolog
AE	Alveolar echinococcosis
ABZ	Albendazole
BA	Bile acids
BioID	Proximity-dependent **bio**tin **id**entification
CBX	Carbenoxolone
CNX	Calnexin
CRT	Calreticulin
Co-IP	Co-immunoprecipitation
CORT	Corticosterone
E. Mulitilocularis	*Echinococcus multilocularis*
ER	Endoplasmic reticulum
ERAD	Endoplasmic-reticulum-associated protein degradation
ERS	Endoplasmic reticulum stress
Glu	Glucose
Gly	Glycine
G6P	Glucose-6-phosphate
G6PD	Glucose-6-phosphate dehydrogenase
G6S	Glucose-6-sulfate
G6PT	Glucose-6-phosphate translocase / Glucose-6-phosphate transporter
GSH	Glutathione (reduced)
GSSG	Glutathione (oxidized)
H6PD	Hexose-6-phosphate dehydrogenase
HSD	Hydroxysteroid dehydrogenase
IP	Immunoprecipitation
NADPH	Dihydronicotinamide-adenine dinucleotide phosphate (reduced)
$NADP^+$	Dihydronicotinamide-adenine dinucleotide phosphate (oxidized)
MS / LC-MS	Mass spectrometry / Liquid chromatography–mass spectrometry
PDI	Protein disulfide isomerase
PPI	Protein-protein interaction
PPP	Pentose phosphate pathway
RMF	Rossmann fold
SDR	Short-chain dehydrogenase/reductase
Tau	Taurine
UPR	Unfolded protein response
6PGL	6-phosphogluconolactone
11β-HSD1	11β-hydroxysteroid dehydrogenase type 1
11β-HSD2	11β-hydroxysteroid dehydrogenase type 2
11-DHC	11-dehydrocorticosterone

1 Summary

The endoplasmic reticulum (ER) is a multifunctional organelle, responsible for a variety of cellular functions such as protein synthesis and folding, calcium storage, lipid and steroid synthesis and carbohydrate metabolism. In addition, the ER is dynamic in nature and its morphologically fluidity is influenced by various factors such as the cell cycle and cell type. The complexity of all tasks carried out by the ER requires a plethora of proteins and conditions which differ from other cellular compartments.

In the last decades, efforts were made to understand the mechanisms underlying luminal processes. New findings indicate that the ER consists of different structural (sub-) domains and several proteins associated with these subdivided compartments were identified. However, many questions remain unanswered with respect to luminal functions and compartmental interrelations and therefore the ER is still considered as a poorly studied cellular organelle.

The aim of this thesis was to improve the comprehension of luminal processes in mammalian cells. The main focus was the examination of the physiological and molecular role of the only known source of NADPH in the ER, hexose-6-phosphate dehydrogenase (H6PD). NADPH, generated by luminal H6PD, is needed as cofactor for reduction reactions such as the interconversion of inactive glucocorticoid cortisone to active cortisol by luminal 11β-hydroxysteroid dehydrogenase type 1 (11β-HSD1). However, besides its interaction with 11β-HSD1 and its role as a NADPH generating enzyme, little is known about H6PD.

Therefore, the first project of this thesis was aimed at the elucidation of the interactome of luminal H6PD. In order to tackle this task, we applied the BioID approach, a recently introduced method to screen for protein-protein interactions (PPI) by proximity biotinylation. We were not only able to demonstrate the functionality of this new tool for luminal applications but also to reveal potential novel interactors of H6PD. One of the identified hits, anterior gradient 2 protein homolog (AGR2), a member of the protein disulfide isomerase (PDI) family, seemed to directly interact with H6PD in MCF7 cells. Our results further indicated that AGR2 has an impact on H6PD activity and H6PD protein expression, which directly affects the luminal pool of reduced phosphorylated pyridine nucleotides.

The second project was dedicated to develop a better understanding of ER stress (ERS) in the context of parasitic infections. Since the ER represents the major site of synthesis and folding of proteins in eukaryotic cells, it is essential that the luminal folding machinery and protein transport systems, which facilitate crossing the ER membrane, function efficiently. Disturbances regarding folding of polypeptides can lead to an accumulation of misfolded proteins in the ER lumen and therefore induce ERS and, as consequence, the activation of the unfolded protein response (UPR). Various diseases have been shown to be associated with ERS, and therefore the potential to identify druggable targets of UPR-related process would be of interest to the pharmaceutical industry. In the second project, we examined whether an infection by the fox tapeworm *Echinococcus multilocularis* causes ERS in mice. We could demonstrate that the expression levels of several proteins of the activating transcription factor 6 alpha (ATF6) branch of the UPR were significantly upregulated upon *E. multilocularis* infection in mice compared to non-infected animals. Protein expression levels of inositol-requiring protein 1 alpha (IRE1α), a major sensor of ERS and regulator of the UPR, and activating transcription

factor-4 (ATF4) were found to be significantly decreased in mice upon infection compared to the non-infected group. In contrast, increased protein expression levels of H6PD and ER resident chaperone calreticulin (CRT) were detected after *E. multilocularis* infection. Furthermore, we demonstrate that treatment of infected animals using the anthelmintic drug albendazole (ABZ) (partially) restored protein expression levels back to the baseline of non-infected animals.

Following up this finding, we focused on alterations of bile acid (BA) profiles upon *E. multilocularis* infection in mice. Since selected BA and their corresponding ratios are considered as potential biomarkers for several diseases, we were interested whether parasitic infection, caused by *E. multilocularis*, alters the BA concentrations in infected animals. In the third project of the presented thesis, we showed that infected animals exhibited significantly lower unconjugated primary and secondary BA levels in serum compared to non-infected animals. Moreover, taurocholic acid (TCA) and tauro-β-muricholic acid (TβMCA), two taurine-conjugated BA were found at significantly higher serum concentrations when compared to the non-infected group. Regarding the expression of hepatic BA transporters, we found decreased mRNA and protein expression levels for the bile salt export pump (BSEP) and Na^+-taurocholate co-transporting polypeptide (NTCP) upon *E. multilocularis* infection, which could be a result of inflammation due to the parasite proliferation in the liver. Finally, restored BA and protein expression levels were observed following ABZ treatment of infected animals, showing the effectiveness of this drug.

The fourth project aimed to identify novel biomarker(s) to assess 11β-HSD1 activity. By the examination of different BA (-ratios) we found that the ratio of ursodeoxycholyltaurine (UDC-Tau) to 7-oxolithocholyltaurine (7oxo-Tau) represents a suitable biomarker to detect decreased 11β-HSD1 activity. The applicability of the presented biomarker was confirmed in four independent mouse models and the application of pharmacological 11β-HSD1 inhibitor carbenoxolone (CBX).

In summary, the four projects in this thesis improve our understanding of ER-related processes. The PDI family member AGR2 was found to interact with H6PD in MCF7 cells. Furthermore, modulation of H6PD activity by AGR2 was shown. In the context of a better understanding of ERS, we were able to demonstrate that *E. multilocularis* infection alters BA profiles and induces ERS. The latter aspect provides evidence that ERS- and UPR-modulating therapies may be used to treat *E. multilocularis* infection. Finally, to address the problem of detecting 11β-HSD1 activity *in vivo*, we analyzed BA (ratios) in multiple mouse models. In doing so, we identified a novel, robust biomarker to assess the enzymatic activity of this pivotal player in steroid metabolism.

2 Preface

This thesis is divided into three main parts, dealing with the physiological and molecular role of H6PD and ER related processes. The four manuscripts in this work outline different projects I contributed to, which are not directly interlinked.

The first part focuses on the elucidation of the interactome of H6PD by the application of BioID, a recently introduced application for proximity labeling.

The second part is devoted to a better understanding of the UPR upon ERS induced by parasitic infection. Linked to this approach I was involved in a project where we analyzed alterations in BA profiles upon *Echinococcus multilocularis* infection in mice, to evaluate whether BA (ratios) may be used as biomarkers to detect the specific parasitic infection.

The third and final part focuses on defining the applicability of measuring BA (ratios) as biomarkers to assess enzymatic activity of 11β-HSD1, an enzyme known to interact with H6PD. The findings of this project were recently published in the British Journal of Pharmacology (BJP).

3 Introduction

3.1 Endoplasmic reticulum dependent physiological processes

The endoplasmic reticulum (ER) is the largest and most multifunctional organelle in eukaryotic cells (Phillips and Voeltz, 2016). Consisting of a widespread dynamic network of membranous tubules and sacs, the ER is found in different shapes and forms, depending on cell cycle state and cell type (Puhka *et al.*, 2007). The ER is generally divided into different subdomains such as the smooth ER (SER) and the rough ER (RER), and the fractions which are either linked to the nuclear envelope or in contact with organelles such as the Golgi complex (Voeltz *et al.*, 2002; Schwarz and Blower, 2016) and the mitochondria (Marchi *et al.*, 2014; Lee and Min, 2018).

The RER, dotted with ribosomes, represents the site where a notable fraction of newly synthesized proteins enter into the ER (Hebert and Molinari, 2007). Translocation of signal sequence containing nascent polypeptides is followed by their folding and quality control. Once freshly synthesized proteins enter the ER, a wide variety of luminal chaperones such as calreticulin (CRT), calnexin (CNX) or glucose-regulated protein 78 (GRP78) and members of the protein disulfide isomerase (PDI) family, for instance protein disulfide-isomerase A3 (ERP57) and protein disulfide-isomerase A4 (ERP72), facilitate their correct arrangement (Halperin *et al.*, 2014; Okumura *et al.*, 2015). Simultaneously, glycosylation of Asn, Ser or Thr residues of nascent polypeptides is performed (Xu and Ng, 2015). Before exiting the ER, incorrectly folded or modified proteins undergo a sophisticated quality control system to ensure proper arrangement of the polypeptide chain and therefore protein function. However, proteins that fail quality control are transported to the cytosol and targeted proteasomal degradation following lysine ubiquitination (Setz *et al.*, 2013). Finally, correctly folded and modified proteins exit the ER and are transported to their subcellular destination (Benham, 2012). In contrast to proteins produced by free ribosomes in the cytosol, proteins synthesized in the ER lumen are mainly destined to either be secreted or directed towards endosomes, lysosomes or the plasma membrane (Andrews and Tata, 1971; Sandoval and Bakke, 1994; King *et al.*, 2020).

In contrary to the RER, the SER lacks ribosomes and is generally considered to play an important role in the regulation of calcium homeostasis, metabolism of carbohydrates, and the synthesis of fatty acids, lipids and steroids (Schonthal, 2012; Sanvictores and Davis, 2020).

Cell type dependent estimates for luminal calcium concentrations range from 10 µM to 1 mM, whereas the concentration of calcium ions in the cytosol is considered to be somewhere between 10 nM and 300 nM. Furthermore, it is assumed that the Ca^{2+} concentration in the extracellular

milieu is about 10^4 fold higher than in the cytosol (Mattson *et al.*, 2000; Samtleben *et al.*, 2013; Segal and Korkotian, 2014; Raffaello *et al.*, 2016; Bagur and Hajnoczky, 2017). Low Ca^{2+} levels in the cytoplasm are maintained by the activity of the plasma membrane Ca^{2+} transport ATPase (PMCA) and the sodium calcium exchanger (NCX). In contrast, the sarco/endoplasmic reticulum Ca^{2+} - ATPase (SERCA) is responsible for the active transport of Ca^{2+} from the cytosol to the ER lumen and therefore the comparatively high luminal Ca^{2+} concentrations (Brini and Carafoli, 2011). Ca^{2+}, released from the ER acts as a second messenger and modulates various Ca^{2+}-dependent cytosolic proteins, such as phosphatases, ion channels and kinases and thereby several cellular processes such as proliferation and development of organs (Hribkova *et al.*, 2018; Paudel *et al.*, 2018).

Besides its role in Ca^{2+} homeostasis, the SER is known to be involved in the synthesis of (very) long-chain fatty acids ((V)LCFAs). Several ER proteins are involved in the synthesis of LCFAs, such as 17β-hydroxysteroid dehydrogenase type 12 (17β-HSD12), elongase (1-7) of LCFA (ELOVL1-7), 3-hydroxyacy-CoA dehydratases (1-4) (HACD1-4) and trans-2,3-trans-enoyl-CoA reductase (TER) (Tsachaki *et al.*, 2020). Numerous indications point to an important function of LCFAs in cancer. The ER as site of synthesis of LCFAs is thus assigned an essential role in this context (Marin de Mas et al., 2018; Rossi Sebastiano and Konstantinidou, 2019).

Moreover, the ER is a workhorse in the biosynthesis of steroids. Cholesterol is the precursor of the five main steroid hormone classes: the mineralcorticoids, glucocorticoids, estrogens, androgens and progestanes. A multitude of enzymes involved in cholesterol homeostasis and steroid metabolism are harbored in the ER, which highlights the importance of the ER in steroid homeostasis and endocrine regulation (Field *et al.*, 1998; Black *et al.*, 2002).

Last but not least, the ER contains a large number of cytochrome P450 (CYP) enzymes involved in the metabolism and detoxification of endogenous compounds, as well as xenobiotics, including drugs and carcinogens (Manikandan and Nagini, 2018). These biotransformation reactions are usually classified as phase I and phase II reactions. Phase I reactions are roughly summarized into three intramolecular modifications: hydrolysis, oxidation and reduction; whereas phase II reactions consist of conjugation reactions such as acetylation, glucuronidation and sulfatation (Iyanagi, 2007; Wu *et al.*, 2011)

This non-exhaustive list of ER functions summarize the importance of this organelle. However, many roles of the ER remain unclear and further investigations of this poorly understood cellular compartment are urgently needed.

3.1.1 Hexose-6-phosphate dehydrogenase

Besides the features already mentioned in the previous chapter, the ER has an autonomous luminal pyridine nucleotide pool, which is independent from other compartments such as the cytosol (Piccirella *et al.*, 2006; Legeza *et al.*, 2013). Pyridine nucleotides such as NAD(P)(H) are well known for their role as cofactors in various reactions. However, new evidence suggests that pyridine nucleotides and their ratio of the corresponding oxidized and reduced species affect numerous cellular functions including ion channel regulation, cell signaling and redox status (Nakamura *et al.*, 2012; Wang *et al.*, 2019). The nonexistence of directed pyridine nucleotide transport into the ER lumen and the inability of these cofactors to cross the ER membrane (in either oxidized or reduced state) by simple diffusion, indicates that an internal pyridine nucleotide production system in the ER lumen is indispensable (Piccirella *et al.*, 2006).

Luminal H6PD represents the only characterized enzyme capable of *de novo* generation of the reduced form of the phosphorylated pyridine nucleotide NADPH. H6PD reduces $NADP^+$ in the course of the conversion of glucose-6-phosphate (G6P) to 6-phosphogluconate (6PG) (Fig. 1). Luminal NADPH is utilized by the bidirectional enzyme 11β-HSD1, to convert physiologically inactive cortisone or 11-dehydrocorticosterone ((11-DHC) in rodents) to the potent glucocorticoid cortisol or corticosterone ((CORT) in rodents) (Atanasov *et al.*, 2004; Banhegyi *et al.*, 2004; Lavery *et al.*, 2006). H6PD differs from its cytosolic counterpart glucose-6-phosphate dehydrogenase (G6PD). While cytosolic G6PD only catalyzes the first step of the pentose-phosphate pathway (PPP), namely the conversion of G6P to 6-phosphogluconolactone (6PGL), luminal H6PD is capable to catalyze the first and the second step of the PPP. The ability to perform the second step of the PPP is owed to the 6-phosphogluconolactonase activity of H6PD. Moreover, compared to its cytosolic equivalent G6PD, H6PD has been shown to have a much broader substrate specificity, characterized by its capability to not only convert G6P but also to utilize galactose-6-phosphate, glucosamine-6-phosphate, 2-deoxyglucose-6-phosphate, or glucose-6-sulfate to generate NADPH (Clarke and Mason, 2003; White *et al.*, 2007). Besides, depending on the substrate, H6PD has been found to reduce NAD^+ instead of $NADP^+$, demonstrating its capability to accept different cofactors (Hino and Minakami, 1982b).

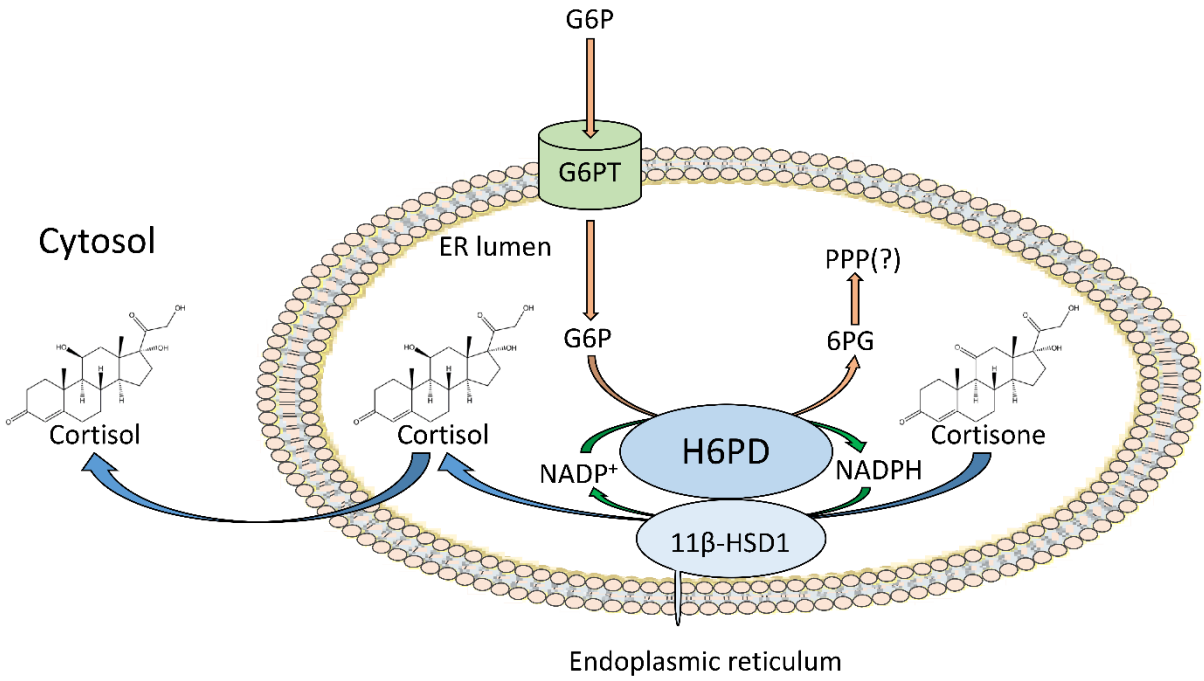

Figure 1. Luminal generation of NADPH by H6PD and conversion of inactive glucocorticoid by 11β-HSD1 under physiological conditions. Glucose-6-phosphate (G6P) is transported across the ER membrane by glucose-6-translocase/glucose-6-phosphate transporter (G6PT). H6PD converts G6P to 6-phosphogluconate (6PG) to reduce $NADP^+$ and therefore generate NADPH (adapted from (Senesi *et al.*, 2010)).

In addition, compared to its 58 kDa cytosolic counterpart, the 89 kDa H6PD has a higher molecular weight and, due to this fact, most likely a different quaternary structure (Senesi *et al.*, 2010). Analyzing the crystal structure of human G6PD revealed that the protein exists in a dimer-tetramer (composed by two dimers) equilibrium, which is depending on the surrounding $NADP^+$ concentration (Au *et al.*, 2000). The missing crystal structure of H6PD makes it difficult to draw conclusions regarding the quaternary structure of this enzyme. However, studies addressed to explore luminal glucocorticoid activation demonstrated the direct interaction between H6PD and 11β-HSD1 (Atanasov *et al.*, 2008). This insight is crucial and underpins the (in)direct role of H6PD in glucocorticoid activation and metabolism (White, 2018).

Several studies have explored the physiological role of H6PD. By measuring 11-DHC to CORT conversion in microsomal preparations of H6PD-knockout mice, an enormous shift of 11β-HSD1 bidirectional oxidoreductase from reductase to dehydrogenase activity was observed, providing an explanation for the reduced CORT production and increased CORT to 11-DHC conversion (Lavery *et al.*, 2006); however, this has not been tested *in vivo*. Furthermore, H6PD null mice were shown to exhibit signs of glucocorticoid resistance, increased insulin sensitivity and increased glucose uptake in type II (fast-twitch) muscle fibers. In addition, animals lacking

H6PD developed skeletal myopathy marked by a switch from type II to type I (slow-twitch) muscle fibers (Lavery *et al.*, 2008a; Lavery *et al.*, 2008b; Talbot and Maves, 2016).

However, several questions regarding the physiological role of H6PD remain unanswered. Although H6PD is considered to be the major source of NADPH in the ER, H6PD-knockout mice did not show a complete elimination of NADPH levels when analyzing pyridine nucleotide content in microsomal preparations isolated from muscle and liver (Rogoff *et al.*, 2010; Weingartner *et al.*, 2021). It was further demonstrated that 11β-HSD1 reductase activity in bone marrow-derived macrophages isolated from H6PD knockout mice was only decreased by approximately 40-50% (Marbet *et al.*, 2018). These independent findings indicate that the ER comprises at least one alternative source of NADPH. Accordingly, further investigations to address luminal NADP(H)-homeostasis and the physiological role of H6PD are required.

3.1.2 11β-Hydroxysteroid dehydrogenase type 1

11β-HSD1 is a representative of the hydroxysteroid dehydrogenases (HSDs), belonging to the NAD(P)(H)-dependent oxidoreductases, and known to catalyze the conversion of a variety of substrates including steroids and BA (Chatuphonprasert *et al.*, 2018). HSDs are generally attributed to the superfamilies of aldo-keto reductases (AKR) and short-chain dehydrogenases/reductases (SDR). While AKR superfamily members are soluble cytoplasmic proteins, HSDs of the SDR-type are also found to be located in different cellular compartments such as the ER, peroxisomes or mitochondria (Filling *et al.*, 2001). Moreover, members of the two families show different characteristics regarding their structural features. Proteins of the AKR superfamily display a highly conserved motive, called the triose-phosphate isomerase (TIM; $(\alpha/\beta)_8$)-barrel structure. SDRs on the other hand are found to have an α/β-folding pattern called the Rossmann fold (RMF), which represents the NAD(P)(H)-binding site (Mindnich and Penning, 2009; Medvedev *et al.*, 2019). 11β-HSDs appear in at least two isoforms, 11β-HSD1 and 11β-HSD2, which belong to the SDR superfamily. They are involved in the interconversion of the inactive glucocorticoid cortisone and its active form cortisol, respectively. 11β-HSD2, mainly expressed in kidney, colon, placenta and salivary glands, utilizes NAD^+ to oxidize cortisol to its inactive form cortisone (and mainly CORT to 11-DHC in mice and rats). 11β-HSD2 has a higher substrate affinity (K_m in nM range) compared to its isoform 11β-HSD1 (K_m in µM range) and a higher molecular weight ($MW_{11\beta\text{-HSD2}}$: 45 kDa; $MW_{11\beta\text{-HSD1}}$: 34 kDa) (Glorioso *et al.*, 2005; Ferrari, 2010; Chapman *et al.*, 2013). The roles of 11β-HSD1 and 11β-HSD2 in the steroidogenesis are illustrated in Fig. 2.

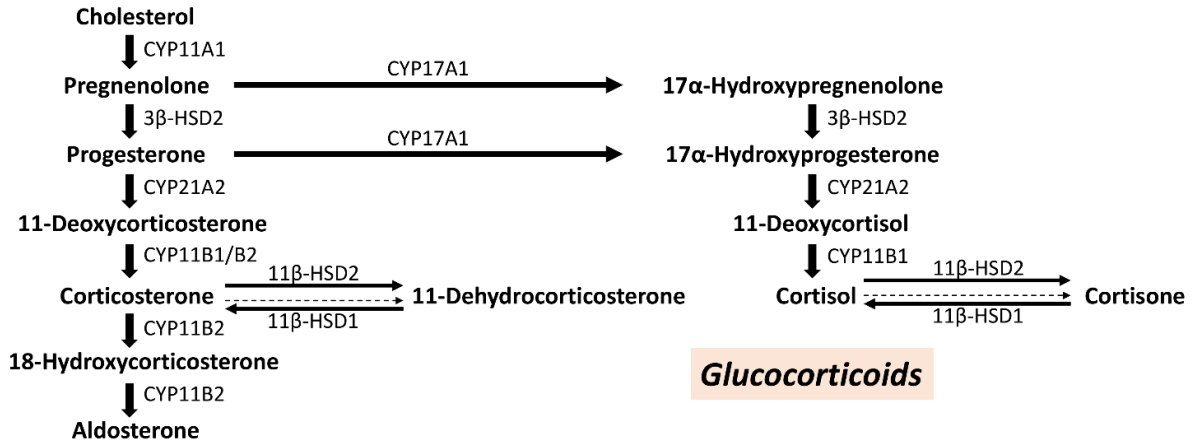

Figure 2. Schematic overview of the synthesis of mineralocorticoids and glucocorticoids and the corresponding roles of 11β-HSD1 and 11β-HSD2. Cholesterol side-chain cleavage enzyme (CYP11A1); 3β-hydroxysteroid dehydrogenase type 2 (3β-HSD2); Steroid 21-hydroxylase (CYP21A2); Steroid 11β-hydroxylase isoform 1 (CYP11B1); Steroid 11β-hydroxylase isoform 2 (CYP11B2); Steroid 17α-hydroxylase (CYP17A1) (adapted from (Cuevas-Ramos and Fleseriu, 2014)).

11β-HSD1, as mentioned previously (chapter 3.1.1), plays an important role in tissue-specific glucocorticoid activation. It is expressed in various organs and tissues such the liver, brain, muscle, vasculature and adipose tissue where it is often found to be co-expressed with H6PD (Odermatt and Kratschmar, 2012; Peng *et al.*, 2016).

Peripheral regulation of glucocorticoids is considered as an important mechanism in several diseases (Tomlinson and Stewart, 2001; Gathercole *et al.*, 2013). Increased expression levels of 11β-HSD1 and glucocorticoid receptor (GR) have been linked to elevated circulating glucose, insulin and corticosterone levels in db/db (diabetic) mice, which in turn was associated with aggravation of the phenotype of type 2 diabetes (Liu *et al.*, 2005). Further, irrespective of gender, increased 11β-HSD1 mRNA levels were found in both, visceral and subcutaneous adipose tissue of obese patients compared to lean subjects. Therefore, regarding its molecular function, 11β-HSD1 expression in adipose tissue was suggested to contribute to the metabolic syndrome in obese patients (Paulsen *et al.*, 2007). Besides, elevated ratios of cortisol/cortisone have been associated with various pathologies and, hypertension, hyperglycemia, dyslipidemia, insulin resistance as well as (iatrogenic) Cushing's syndrome are well known consequences of (prolonged) elevated cortisol levels (Whitworth *et al.*, 2005).

Therefore, it is not surprising that in the past decades 11β-HSD1 has been increasingly brought into focus as a new potential drug target. Roughly 250 patents from more than 25

pharmaceutical companies have been published regarding novel approaches to inhibit 11β-HSD1 (Scott *et al.*, 2012). However, to date no compounds were successfully introduced to the market. The reasons for the failure of potential 11β-HSD1 inhibitors are manifold: insufficient therapeutic benefit compared to existing treatment such as metformin, non-selective inhibition of 11β-HSD1 and 11β-HSD2 or poor bioavailability are worth mentioning in this regard (Gregory *et al.*, 2020). Moreover, measurement of 11β-HSD1 activity *in vivo* represents a major challenge. Currently, 11β-HSD1 activity has been assessed by measuring the metabolites of cortisol and cortisone, namely tetrahydrocortisol, 5α-tetrahydrocortisol and tetrahydrocortisone (and the corresponding CORT- and 11-DHC analogues in rodents). The ratio of (tetrahydrocortisol+5α-tetrahydrocortisol)/ tetrahydrocortisone can be used to determine 11β-HSD1 activity, however 24 h urine sample collection is needed for this approach, which represents a challenge in (animal) experimentation. Furthermore, the ratio does not specifically represent 11β-HSD1 but also 11β-HSD2 enzymatic activity, thus limiting the utility of this biomarker (Wang, 2005; Lavery *et al.*, 2008a).

Besides its function in steroidogenesis, 11β-HSD1 catalyzes the conversion of other endogenous compounds such as 7-ketocholesterol (Schweizer *et al.*, 2004), 7-keto,27-hydroxycholesterol (Beck *et al.*, 2019a), 7-keto,25-hydroxycholesterol (Beck *et al.*, 2019b), and the BA 7-oxolithocholic acid and its taurine- and glycine-conjugated species (Fig 3.) (Odermatt *et al.*, 2011; Penno *et al.*, 2013; Penno *et al.*, 2014). However, while the physiological role and relevance of 11β-HSD1 in glucocorticoid metabolism is generally accepted, it remains largely unknown how its function in BA homeostasis affects physiological processes.

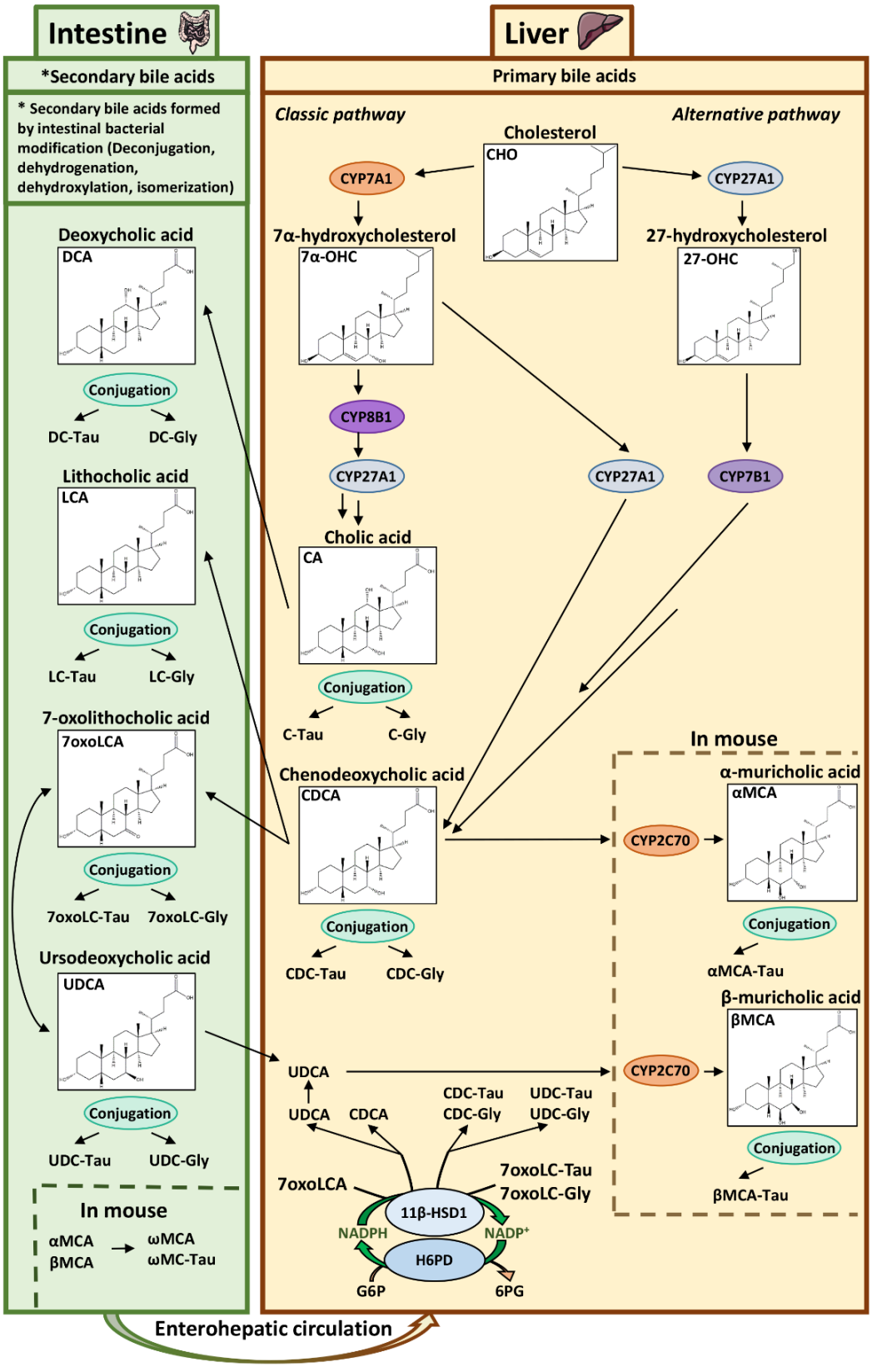

Figure 3. The roles of H6PD and 11β-HSD1 in the BA homeostasis. H6PD provides NADPH for 11β-HSD1 mediated conversion of 7oxoLCA (-Tau/-Gly) to UDCA (-Tau/-Gly) and CDCA (-Tau/-Gly). Enzymes involved in the BA synthesis as indicated. Cholesterol 7α-hydroxylase (CYP7A1); Sterol 27-hydroxylase (CYP27A1); Sterol 12α-hydroxylase (CYP8B1); Oxysterol 7α-hydroxylase (CYP7B1); Cytochrome P450 2C70 (murine, CYP2C70); Glycine conjugated (-Gly); Taurine conjugated (-Tau) (adapted from (Weingartner *et al.*, 2021)).

3.2 Endoplasmic reticulum stress and the unfolded protein response

A major function of the ER is the synthesis of proteins and the control of their proper folding. A smooth running translation- and folding-machinery is indispensable for protein quality control and therefore for cellular survival, and disturbances of protein homeostasis can lead to fatal outcome (Chaudhuri and Paul, 2006). Perturbation of luminal protein homeostasis marked by the accumulation of misfolded proteins leads to ERS and the activation of the UPR (Haeri and Knox, 2012; Corazzari *et al.*, 2017). Upon activation, the UPR is programmed to perform three distinct processes: degradation of improperly folded proteins, upregulation of the production of (ER) chaperones and deceleration of (luminal) protein synthesis (Brodsky and Scott, 2007). The UPR is orchestrated by three main ERS sensors: ATF6, IRE1 and Protein kinase R (PKR) like ER kinase (PERK). During homeostasis GRP78, the major regulator of the UPR, is bound to the three ERS sensors and thereby inhibits their molecular activities (Bertolotti *et al.*, 2000). Accumulation of unfolded proteins in the ER lumen results in GRP78 binding to the misfolded polypeptides and thus freeing the ERS sensors (Fig. 4). Unbound ATF6, translocates from the ER to the Golgi where it is processed to its cleaved, active form. Cleaved ATF6 then further translocates to the nucleus, where it activates the transcription of its UPR related target genes such as CCAAT/enhancer binding protein homologous protein (CHOP). The ER transmembrane protein IRE1 is bound to GRP78 upon the sensing of misfolded proteins. Autophosphorylation and dimerization leads to the activation of IRE1, resulting in the splicing of X-box binding protein 1 (XBP1) mRNA, which in turn leads to translation of the transcription factor. Spliced form of XBP1 (XBP1-s) initiates the upregulation of UPR-associated genes involved in protein folding and ER-associated degradation (ERAD). PERK is activated upon autophosphorylation and dimerization. The kinase domain of PERK leads to the phosphorylation of eukaryotic initiation factor 2α (eIF2α), which in turn causes global translation inhibition and the promotion of the translation of activating transcription factor-4 (ATF4). The latter transcription factor upregulates genes associated to be involved in the resolution of the ERS (Yoo *et al.*, 2017; Lin and Stone, 2020).

While the fundamental underlying mechanisms of the UPR upon ERS are widely explored and accepted, little is known about role of H6PD regarding this particular aspect of the cellular stress response. Depletion of luminal NADPH and a decreased NADPH/$NADP^+$ ratio were shown to trigger ERS (Kapuy and Banhegyi, 2013). The role of the NADPH-generating H6PD in the UPR was further supported by the analysis of natural gene variations in *Drosophila melanogaster* in the context of ERS and UPR (Chow *et al.*, 2013). Moreover, a recently published article by Tsachaki *et al.* further supports the hypothesis of the impact of H6PD on

the UPR during ERS. Knockdown of H6PD in the triple negative breast cancer cell line SUM159 resulted in decreased protein levels of UPR related target genes such as CHOP, ATF4, ATF6, XBP1-s and GRP78. In contrast, protein levels of luminal PDI family member endoplasmic reticulum ERP72 and lectin chaperone CRT were increased, indicating an effect of knockdown of H6PD on the luminal protein folding machinery (Tsachaki *et al.*, 2018).

Either way, further investigation is needed to affirm the role of H6PD in the UPR and UPR-related processes and to elucidate the exact mechanism how H6PD influences these pathways. This proposal may be important considering the recent efforts made in the identification and development of potential UPR modulating drugs (Maly and Papa, 2014).

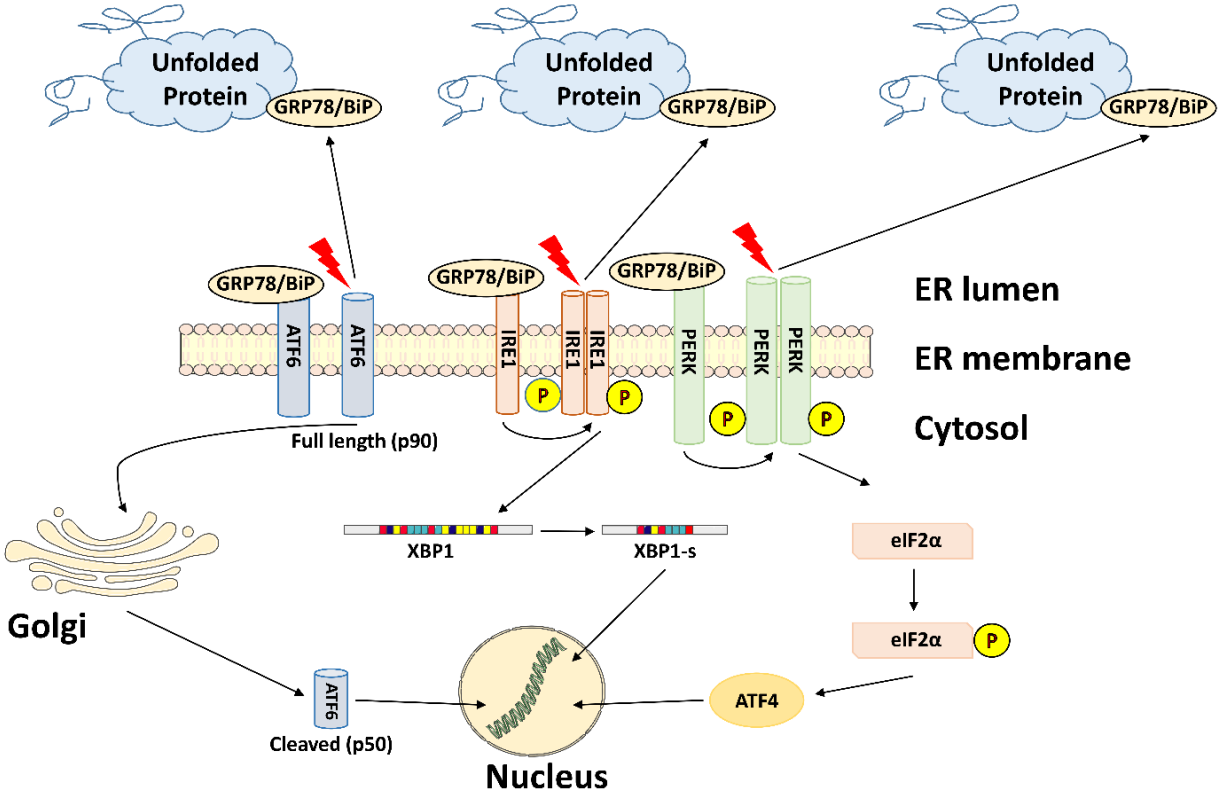

Figure 4. Schematic overview of the unfolded protein response (UPR) in mammalian cells. The major ERS sensors ATF6, IRE1 and PERK are and key players in each pathway are indicated. Phosphorylated proteins are signalized (P).

3.2.1 Endoplasmic reticulum stress in disease

Emerging evidence points to a link between a panoply of human diseases and (chronic) ERS or defects in the UPR signaling (Park *et al.*, 2019). Noteworthy are different forms of metabolic disorders, for example hereditary diabetes mellitus (DM) in the form of Wolcott-Rallison

syndrome (WRS). WRS is assumed to be caused by mutations in the *Perk* gene, leading to the inactivation of this ERS sensor and therefore an insufficient UPR (Julier and Nicolino, 2010). Further, a high-fat diet and therefore chronic exposure to high free fatty acid (FFA) levels in patients suffering from type 2 DM, were reported to activate the ERS response in β-cells (Eizirik *et al.,* 2008). FFA, in particular palmitate, leads to the phosphorylation of PERK and, as a consequence, the phosphorylation of eIF2α, which in turn induces ATF4 and CHOP. Finally, CHOP induction was associated with apoptosis of insulin-secreting β-cells. The other ERS sensors of the UPR, IRE1 and ATF6 were shown to be activated by palmitate too, but to a lesser extent compared to the PERK-mediated stress response (Karaskov *et al.,* 2006; Cnop *et al.,* 2007; Laybutt *et al.,* 2007).

Involvement of ERS was further demonstrated in the pathogenesis of different neurodegenerative diseases. Mutations in the presenilin-1 (PS1) gene of patients suffering of Alzheimer's disease were reported to cause an increase in pro-apoptotic CHOP protein levels, and therefore contribute to the course of this dreadful malady (Milhavet *et al.,* 2002; Prasanthi *et al.,* 2011).

A mention should also be made of Parkinson's disease (PD), the second most common neurodegenerative disorder after Alzheimer's disease, affecting approximately 1% of the elderly population in Europe (von Campenhausen *et al.,* 2005). The pathogenesis of PD was previously linked to ERS and activation of the UPR as a result of an accumulation of misfolded proteins such as α-synuclein (Bernal-Conde *et al.,* 2019) and parkin or parkin-associated endothelin receptor-like protein (PAEL) (Rao and Bredesen, 2004). Moreover, upregulation of human ubiquitin ligase (HRD1), a protein involved in the degradation of misfolded proteins in PD was shown to suppress ERS associated cell death and therefore improve PD symptoms (Omura *et al.,* 2013).

Finally, the pathogenesis of a considerable number of infectious diseases was linked to ERS and the activation of the UPR. Bacterial virulence factor subtilase (SubA), a ctytotoxin produced by Shiga-toxigenic *Escherichia coli* acts as a protease by cleaving GRP78, resulting in ERS and inhibition of cell growth and, at a later stage, CHOP induced apoptosis (Morinaga *et al.,* 2008). Another bacterium to mention in this regard is *Listeria monocytogenes*, a facultative intracellular pathogen found in food products capable of causing life threatening listeriosis (O'Byrne and Utratna, 2010). All sensors of ERS were activated upon *Listeria monocytogenes* infection. While activation UPR was linked to reduced intracellular bacterial

number, prolonged infection with *Listeria monocytogenes* resulted in ERS induced apoptosis of infected cells (Pillich *et al.*, 2012).

Besides bacterial infections, a plethora of publications described ERS and activation of the UPR in the context of viral-infections and, -diseases. Manipulation of host UPR by activation of the PERK-pathway was reported during *SARS-CoV* infection, resulting in enhanced protein folding and promotion of viral protein production. In particular, the viral spike protein (S) of *SARS-CoV* was linked to the induction of luminal chaperones and GRP78 and, as a consequence, facilitated replication of virions (Chan *et al.*, 2006; Versteeg *et al.*, 2007). Other viruses suppress certain players of the host's UPR to prevent degradation of viral protein within the ER lumen. Suppression of the IRE1-XBP1 branch is suggested be an important feature in the replication and expression strategy of *Hepatitis C virus* (Tardif *et al.*, 2004).

Involvement of ERS and modulation of the UPR were also reported in parasitic infections and diseases. *Plasmodium falciparum*, to take a specific example, was recently reported to increase UPR associated protein levels in the liver (Kaushansky and Kappe, 2015). Although, the molecular aspects of inducing ERS in this case remain unclear due to a lack of data. Overall, the understanding of the role of ERS and the UPR during parasitic infections remains poorly explored compared to various maladies associated with bacterial or viral infection.

4 Aims of the thesis

One major aim of this thesis was to gain further mechanistic knowledge of the physiological role of H6PD in the ER. A tide of evidence points towards a role of H6PD in malignancies. However, little is known about this luminal enzyme, besides its function as provider of NADPH and its interaction with lumen-facing ER membrane protein 11β-HSD1. Under physiological conditions, the bidirectional enzyme 11β-HSD1 utilizes NADPH provided by H6PD to convert inactive cortisone to active cortisol, which has many functions in the human body, such as regulating metabolism, immune response, stress response and inflammatory response.

The first part of the thesis was devoted to developing a deeper understanding of the interactome of H6PD. The discovery of enzymes utilizing luminal NADP(H) or of proteins regulating NADPH production by modulating H6PD activity, as well as the identification of alternative sources of (reduced) pyridine nucleotides were addressed in the first project of this thesis.

Linked to the first task, the second aim was to gather novel insights into the roles of the ER and H6PD in pathophysiological processes. It has previously been shown that disturbances of ER function(s) are linked to different disease etiologies. Accumulation of misfolded or unfolded proteins leads to ERS and the activation of the unfolded protein response (UPR). To contribute to a better understanding of mechanisms related to ERS, we examined mice infected with *Echinococcus multilocularis* to evaluate the importance of ERS during parasitic disease development.

Finally, the third goal of this thesis was to identify and address the applicability of novel biomarkers to estimate 11β-HSD1 activity *in vivo*. As mentioned above, conversion of cortisone to cortisol is crucial for a variety of physiological processes and therefore methods to estimate the activity of 11β-HSD1 *in vivo* are of great interest. To tackle this challenge, we made use of the recent discovery of alternative substrates of 11β-HSD1 to test a BA ratio as biomarker of the enzyme activity.

5 Elucidating the H6PD interactome

5.1 Investigation of potential interactors of luminal H6PD by proximity biotinylation

5.1.1 Manuscript in preparation:

Mapping the neighborhood: A BioID-based approach to elucidate the interactome of luminal hexose-6-phosphate dehydrogenase reveals anterior gradient protein 2 homolog as an interacting partner

Michael Weingartner[1], Maria Tsachaki[1], Thomas Bock[2], Julia Birk[1], Alex Odermatt[1]

[1] Division of Molecular and Systems Toxicology, Department of Pharmaceutical Sciences, University of Basel, Klingelbergstrasse 50, 4056 Basel, Switzerland.

[2] Proteomics Core Facility, Biozentrum, University of Basel, Klingelbergstrasse 70, 4056 Basel, Switzerland.

Contribution to the project:

- Conceptualization
- Experimental work
- Analysis and interpretation of the data
- Writing the first manuscript draft (including figures and tables)

Mapping the neighborhood: A BioID-based approach to elucidate the interactome of luminal hexose-6-phosphate dehydrogenase reveals anterior gradient protein 2 homolog as an interacting partner

Michael Weingartner[1], Maria Tsachaki[1], Thomas Bock[2], Julia Birk[1], Alex Odermatt[1*]

[1] Division of Molecular and Systems Toxicology, Department of Pharmaceutical Sciences, University of Basel, Klingelbergstrasse 50, 4056 Basel, Switzerland.

[2] Proteomics Core Facility, Biozentrum, University of Basel, Klingelbergstrasse 50, 4056 Basel, Switzerland.

* To whom correspondence should be addressed:
Dr. Alex Odermatt, Division of Molecular and Systems Toxicology, Department of Pharmaceutical Sciences, University of Basel, Klingelbergstrasse 50, 4056 Basel, Switzerland
Email: alex.odermatt@unibas.ch

Disclosures: The authors declare no commercial or financial conflict of interest

Keywords: AGR2, co-immunoprecipitation, endoplasmic reticulum, H6PD, NADPH, proximity biotinylation, protein-protein interaction

Abstract

Background

Hexose-6-phosphate dehydrogenase (H6PD) represents the only characterized enzyme capable of generating NADPH in the endoplasmic reticulum (ER) lumen. Based on the inability of NADP(H) to penetrate the ER membrane and the lack of an ER directed NADP(H)-transporter, H6PD has a crucial role in maintaining an adequate luminal NADPH concentration to provide cofactor for enzymatic reduction reactions. 11β-hydroxysteroid dehydrogenase 1 (11β-HSD1), catalyzing the conversion of inactive cortisone to active cortisol using NADPH as cofactor, is currently the sole known interacting partner of H6PD. In an attempt to better understand the roles of H6PD in the ER, this study explored the interactome of H6PD.

Methods

The BioID technique was applied for the screening of H6PD-interacting proteins in the triple negative breast cancer cell line MDA-MB 231. Enriched biotinylated proteins were analyzed by mass spectrometry (MS) and potential candidates further investigated by co-immunoprecipitation (Co-IP). Knock-down experiments using small interfering RNA (siRNA) and H6PD enzyme activity measurements were employed to determine the direct effect of candidate proteins on H6PD expression and activity, and therefore for luminal NADPH generation.

Results

The resulting proteome, generated by our ER directed BioID approach, revealed a potential hit cluster consisting of members of the protein disulfide isomerase (PDI) family, different ER resident chaperones and luminal calcium binding proteins. PDI Anterior gradient protein 2 homolog (AGR2) was then thoroughly examined as a H6PD interacting partner. Gene silencing of ARG2 by siRNA caused increased H6PD protein levels in both the MDA-MB 231 cells and the estrogen and progesterone receptor positive breast cancer cell line MCF7. Co-IP experiments in MCF7 revealed a physical interaction between AGR2 and H6PD

Conclusion

The BioID approach revealed AGR2 as novel interacting partner of H6PD, enhancing its activity. As both AGR2 and H6PD were found to promote the proliferation of breast cancer cells, further investigations should address a link between these two proteins in cancer.

Furthermore, physical and functional interactions between H6PD and AGR2 and also with other PDI members identified in the BioID approach need to be investigated in follow-on experiments.

Introduction

Localized in the lumen of the endoplasmic reticulum (ER), hexose-6-phosphate dehydrogenase (H6PD) catalyzes the first two steps of the pentose phosphate pathway (PPP), *i.e.* the conversion of glucose-6-phosphate (G6P) to 6-phosphogluconate (6PG) and thereby the reduction of $NADP^+$ to NADPH [1, 2]. Whilst the first step is analogous to the cytosolic reaction performed by glucose-6-phosphate dehydrogenase (G6PD), the second step, marked by the lactonase activity, represents an exclusive feature of luminal H6PD. Contrary, cytosolic 6-phosphogluconolactonase is required for the conversion of 6-phosphogluconolactone (6PGL) to 6PG in the cytoplasm [3]. In contrast to its luminal homolog H6PD, which is known to have a broader substrate pool including G6P, glucose-6-sulfate (G6S) and galactose-6-phosphate (Gal6P), G6PD shows selective substrate affinity, exclusively converting G6P [4, 5].

NADPH does not permeate freely and is not transported across the ER membrane, therefore luminal NADPH is independent from the cytosolic pyridine-nucleotide pool [6, 7]. Whilst a cytosolic NADPH/$NADP^+$ ratio of 50-100:1 was reported, the luminal proportion of reduced to oxidized phosphorylated pyridine nucleotides, representing the activity of H6PD, was estimated to display a NADPH/$NADP^+$ ratio of at least 10:1, maintaining predominant reductase activity of 11β-hydroxysteroid dehydrogenase type 1 (11β-HSD1) [8-10].

The conversion of physiologically inactive cortisone to active cortisol (or 11-dehydrocorticosterone to corticosterone in mice and rats), performed by lumen-facing transmembrane protein 11β-HSD1, represents the most extensively described NADPH-dependent process within the ER [11-15]. Besides its role in the activation of glucocorticoids, H6PD was shown to impact the regulation of ERS, calcium homeostasis and luminal redox balance in breast cancer cell lines [16, 17]. However, beside the reported interaction between H6PD and 11β-HSD1, no other interacting partners have been described for H6PD so far [18, 19].

Besides factors including the concentration of metal ions, the availability of specific cofactors and post-translational modifications, the activity of a protein is widely regulated by its interacting partners [20-25]. Therefore, the understanding of protein-protein interactions (PPIs) became indispensable for the understanding of protein functions [26]. Furthermore, increasing efforts regarding the understanding of PPIs revealed the interactome of proteins as a new class of potential drug targets [27, 28]. Owed to the fact of the unique role of H6PD in the

glucocorticoid activation, we wanted to investigate potential PPIs to contribute to a better understanding of the luminal NADPH homeostasis and regulation of H6PD activity.

In the present study we employed BioID, a method for proximity dependent **bio**tin **id**entification, to screen for neighboring proteins of H6PD. The underlying principle of BioID, which was recently described by Roux *et al.*, is to make use of a mutated (R118G), promiscuous biotin ligase (BirA*), fused to a bait protein (here, H6PD) [29-31]. Biotinylation of proteins in proximity is achieved by the successful expression of the fusion-protein along with additional supplementation of biotin in the cell culture medium. Biotinylated proteinogenic lysine residues, representing neighboring proteins can further be analyzed by immunochemical or mass spectrometric (MS) methods. In addition, Co-IP experiments were performed to confirm interacting partners of H6PD. Finally, gene silencing experiments using siRNA targeting a selected interactor was performed to test potential H6PD-regulatory mechanisms.

Materials and methods

Chemicals

All chemicals used were purchased from Merck (former Sigma-Aldrich, Darmstadt, Germany) unless otherwise stated.

Cell lines

The cell lines MDA-MB 231, MCF7, HEK-293 and SUM 159 were purchased from American Type Culture Collection (ATCC, Manassas, VA, USA), tested regularly to exclude mycoplasma contamination, and cultured under standard conditions (37°C, 5% CO_2). MDA-MB 231 cells were cultured in RPMI-1640 medium supplemented with 10% fetal bovine serum (FBS), MCF7 cells in DMEM containing 2 mM-L-glutamine, 4.5 g L^{-1} glucose, 10% FBS and non-essential amino acid mixture, SUM 159 cells in Ham's F-12 Nutrient Mix (Thermo Fisher Scientific, Waltham, MA, USA) supplemented with 5% FBS and 5µg ml^{-1} bovine pancreas insulin (Cat# I6634), and HEK-293 cells in DMEM containing 2 mM-L-glutamine, 4.5 g L^{-1} glucose, non-essential amino acid mixture and 10% FBS. All cell culture media were supplemented with 10 mM hydroxyethylpiperazinethanesulfonic acid (HEPES) buffer pH 7.4, 100 U mL^{-1} penicillin and 0.1 mg mL^{-1} streptomycin.

Transfections

DNA transfections were conducted using Lipofectamine 2000 reagent (Cat#11668030, Thermo Fisher Scientific). BioID-fusion protein construct (H6PD-BirA*-HA) (Suppl. Table 1) was produced by PCR amplification, using full-length H6PD coding sequence from a donor vector as template and inserting the product in a pcDNA3.1 MCS-BirA(R118G)-HA plasmid bearing a resistance gene for G418 (Cat#36047, Addgene, Watertown, MA, USA). C-terminally FLAG-tagged 11β-HSD1 (11β-HSD1-FLAG, (Odermatt *et al.*, 1999)) was recloned into a pcDNA3.1 plasmid bearing a puromycin resistance gene (Cat#13884, Cayman Chemical, Ann Arbor, MI, USA).

For transfection (construct: H6PD-BirA*-HA) of MDA-MB 231 cells, 3.75 µg of plasmid DNA and 7.5 µl reagent were used per 300'000 cells. For transfection (construct: 11β-HSD1-FLAG) of MDA-MB 231 cells or the BioID-clone, 2.5 µg of plasmid DNA and 5 µl reagent were used per 250'000 cells. Transfections were conducted according to the manufacturer's protocol. The supernatant was replaced with fresh culture medium 5 h after transfection.

Transient transfection of HEK-293 cells was conducted by the calcium-phosphate precipitation method described earlier [32]. Briefly, per 10 cm dish of HEK-293 cells (80% confluent), 12 µg plasmid DNA encoding H6PD-MYC in pcDNA3.1 and 12 µg empty vector or 12 µg of plasmid encoding H6PD-MYC and 12 µg AGR2-FLAG (Cat#OHu09079;NM_ 006408, in pcDNA3.1; Genscript, Piscataway, NJ, USA) were used per transfection. Empty vector pcDNA3 served as control. Cells were collected 24 h post-transfection for microsome preparation.

Gene silencing experiments were performed using Lipofectamine RNAiMax (Thermo Fisher Scientific) according to the manufacturer's protocol. Target siRNA (Microsynth, Balgach, St. Gallen, Switzerland) sequences were as follows: H6PD 5′- GGG CUA CGC UCG GAU CUU G -3′; AGR2: 5'-GAA GCU CUA UAU AAA UCC A- 3'; Mock 5′-UGG UUU ACA UGU UUU CUG A-3′.

For siRNA transfection experiments MDA-MB 231 and MCF7 cells were seeded at 350'000 cells per well in 6-well plates, and treated with 29 nM siRNA and 2.9 µL Lipofectamine RNAiMAX reagent. Mock siRNA served as control.

Establishment of H6PD-BirA*-HA expressing cell lines

MDA-MB 231 cells were exposed 72 h after transfection to medium containing 1000 µg mL^{-1} geneticin (G418, Cat#36047, Addgene) to start the selection process. Resistant cells were serially diluted to generate single cell clones. Clones were screened for correct localization and expression of H6PD-BirA*-HA by western blotting and immunohistochemical analysis.

Establishment of 11β-HSD1-FLAG expressing cell lines

Cell culture medium was replaced 72 h after transfection and MDA-MB 231 or stably expressing H6PD-BirA*-HA cells were exposed to selection medium supplemented with 0.5 µg mL^{-1} puromycin. Puromycin resistant cells were serially diluted to generate single cell colonies and selected clones analyzed for expression of 11β-HSD1-FLAG by western blotting.

Generation of biotinylated proteins

Cells stably expressing H6PD-BirA*-HA were cultured under standard conditions. The cell culture medium was supplemented 72 h prior to cell lysis with 50 µM biotin (Cat#B4639, Sigma Aldrich) to stimulate biotinylation.

Sample preparation for MS

Biotinylated proteins for MS analysis were prepared as follow: MDA-MB 231 or stably expressing H6PD-BirA*-HA cells were cultured with (+) or without (-) supplemented biotin (50 µM final concentration) for 72 h. Cells were lysed using radio immunoprecipitation assay (RIPA) buffer (Cat#89900, Thermo Fisher Scientific) containing protease inhibitor cocktail (Cat#CO-RO) and incubated on a thermo-shaker for 10 min at 4°C at 1000 rpm. Lysate was further centrifuged for 10 min at 16'100 x g. Supernatant was collected and the protein concentration determined by the bicinchoninic acid assay (Cat#23225, Thermo Fisher Scientific). Supernatants were stored at -20°C until further analysis by liquid chromatography–mass spectrometry (LC-MS) or western blot.

To enrich biotinylated proteins, 60 µL streptavidin magnetic beads (Cat#88817, Thermo Fisher Scientific) were mixed thoroughly and washed 3 times with 1 ml washing buffer (20 mM potassium-dihydrogenphosphate, 0.15 M NaCl). After washing, the beads were incubated for 2 h at 4°C under continuous rotation with standardized amount of total protein (1-1.5 mg). The beads were then vortexed and washed 4 times using 1 mL RIPA buffer per washing step. Finally, the beads were washed 5 times using HNN buffer (50 mM HEPES pH 7.5, 150 mM NaCl, 5 mM EDTA, 50 mM NaF).

Sample preparation for MS - on bead digestion

After the last washing step, 142.5 µl 100 mM ammonium bicarbonate (ABC) buffer was added to the beads, which were vortexed and sonicated. Subsequently, 7.5 µl of 200 mM tris(2-carboxyethyl)phosphine (TCEP) was added to the samples and vortexed. Next, 3.2 µl of 750 mM chloracetamide (CAA) was added to the samples and vortexed. Thereafter, the beads were incubated in the dark for 1 h at 37°C on a thermo-shaker at 600 rpm. 1 µg trypsin (Cat# V5111, Progema, Fitchburg, WI, USA) was administered and beads were gently mixed and incubated overnight (o/n) at 37°C with continuous shaking at 800 rpm. Beads were then separated by magnetic separation and supernatant was collected and stored at 4°C. The beads were then incubated for 2 h in 150 µl ABC buffer supplied with 1 µg trypsin. Following, the beads were separated, the aqueous phase was collected, pooled with the first aspirated fraction and stored at 4°C. Next, the beads were mixed with 200 µl 0.1% trifluoroacetic acid. After shaking for 5 min at 1000 rpm, followed by bead separation, the acidic phase was pooled with previous fractions. Protein purification and desalting of the pooled fractions were achieved through the application of C-18 MiniSpin® columns (The Cat #SEM SS18V, The Nest Group, Southborough, MA, USA) according to manufacturer's instructions. After purification and desalting, the peptides were dried by centrifugal evaporation for 2 h using a CentriVap concentrator (Kansas City, MO, USA). Dried peptides were stored at -20°C until analysis.

MS data acquisition

Dried peptides were dissolved in 0.1% aqueous formic acid solution at a concentration of 0.25 mg ml^{-1} prior to injection into the MS. For each sample, a total of 0.25 µg peptides (in 0.1% aqueous formic acid) was subjected to LC-MS analysis using a dual pressure LTQ-Orbitrap Elite mass spectrometer connected to an electrospray ion source (both Thermo Fisher Scientific) and a custom-made column heater set to 60°C. Peptide separation was carried out using an EASY nLC-1000 system (Thermo Fisher Scientific) equipped with a RP-HPLC column (75 µm × 30 cm) packed in-house with C18 resin (ReproSil-Pur C18–AQ, 1.9 µm resin; Dr. Maisch GmbH, Germany). Peptides were separated using a step wise linear gradient from 95% solvent A (0.1% formic acid, in water) and 5% solvent B (80% acetonitrile, 0.1% formic acid, in water) to 35% solvent B over 50 min, to 50% solvent B over 10 min, to 95% solvent B over 2 min, and to 95% solvent B over 18 min at a flow rate of 0.2 μL^{-1}. The data acquisition mode was set to obtain one high resolution MS scan at a resolution of 240'000 full width at half maximum (at 400 m/z, MS1) followed by MS/MS (MS2) scans in the linear ion trap of the 20 most intense MS signals. The charged state screening modus was enabled to exclude unassigned and singly

charged ions and the dynamic exclusion duration was set to 30 s. The collision energy was set to 35%, and one microscan was acquired for each spectrum.

Protein identification and label-free quantification

The acquired raw-files were imported into the Progenesis QI software (v2.0, Nonlinear Dynamics Limited, Newcastle upon Tyne, United Kingdom), which was used to extract peptide precursor ion intensities across all samples applying the default parameters. The generated mgf-files were searched using MASCOT (Matrix Science, Boston, MA, USA) against a decoy database containing normal and reverse sequences of the concatenated *Homo sapiens* (UniProt, 26th April 2016) proteome including commonly observed contaminants (in total 141'240 sequences) generated using the SequenceReverser tool from the MaxQuant software (Version 1.0.13.13, Max Planck Institute of Biochemistry, Martinsried, Germany). The following search criteria were used: full tryptic specificity was required (cleavage after lysine or arginine residues, unless followed by proline); 3 missed cleavages were allowed; carbamidomethylation (C) was set as fixed modification; oxidation (M) and protein N-terminal acetylation were applied as variable modifications; mass tolerance of 10 ppm (precursor) and 0.6 Da (fragments) was set. The database search results were filtered using the ion score to set the false discovery rate (FDR) to 1% on the peptide and protein level, respectively, based on the number of reverse protein sequence hits in the datasets. Quantitative analysis results from label-free quantification were normalized and statistically analyzed using the SafeQuant R package v.2.3.4 (https://github.com/eahrne/SafeQuant/; PMID: 27345528) to obtain protein relative abundances. This analysis included summation of peak areas per protein and LC-MS/MS run followed by calculation of protein abundance ratios. Only isoform specific peptide ion signals were considered for quantification. The summarized protein expression values were used for statistical testing of differentially abundant proteins between conditions. Here, empirical Bayes moderated t-tests were applied, as implemented in the R/Bioconductor limma package (http://bioconductor.org/packages/release/bioc/html/limma.html). The resulting p-values were adjusted for multiple testing using the Benjamini-Hochberg method.

All LC-MS/MS analysis runs were acquired from samples of three independent experiments. To meet additional assumptions (normality and homoscedasticity) underlying the use of linear regression models and Student's t-test MS-intensity signals were transformed from the linear to the log-scale. Unless stated otherwise linear regression was performed using the ordinary least square (OLS) method as implemented in base package of R v.3.1.2 (http://www.R-project.org/).

The sample size of three biological replicates was chosen assuming a within-group MS-signal coefficient of variation of 10%. When applying a two-sample, two-sided Student's t-test this was found to give adequate power (80%) to detect protein abundance fold changes higher than 1.65, per statistical test. The statistical package used to assess protein abundance changes, SafeQuant, employs a moderated t-test, which has been shown to provide higher power than the Student's t-test. No simulations were conducted to assess power, upon correction for multiple testing (Benjamini-Hochberg correction), as a function of different effect sizes and assumed proportions of differentially abundant proteins.

Protein expression – western blot

Procedures for cell lysis, protein extraction, sodium dodecyl sulfate polyacrylamide gel electrophoresis (SDS-PAGE), western blotting and detection of proteins examined in this study, except biotinylated proteins, were previously described [33]. Percentage of SDS-gels were adjusted to the protein size of interest, ranging from 8%-14%. Proteins were transferred on Polyvinylidene fluoride (PVDF) membranes with a pore size of 0.45 µm (Cat#IPVH00010, Merck) or 0.2 µm (Cat#42515.01, Serva, Heidelberg, Germany). Depending on the manufacturer's recommendation, skimmed milk (milk, 5%) or bovine serum albumin (BSA, 5%) in Tris-buffered saline with Tween 20 (TBST) served as blocking agents and to dilute the specific antibody.

For the detection of biotinylated proteins, PVDF membranes were blocked in 5% BSA-TBST for 1 h and incubated o/n at 4°C, in 5% BSA-TBST containing streptavidin-horseradish peroxidase (HRP) at a dilution 1:10,000. The next day, membranes were washed 3 times for 15 min in TBS-T, followed by incubation in adult bovine serum blocking buffer (ABS; 10% adult bovine serum, 1% Triton X-100 in phosphate buffered saline; PBS) for 5 min. Afterwards, membranes were washed 3 times for 1 min in PBS and analyzed using enhanced chemiluminescence substrate (Cat#WBKLS0500, Merck).

Antibodies for the detection of following proteins were applied according to the manufacturer's protocol: Polyclonal rabbit anti-H6PD antibody (Cat#HPA004824, Sigma-Aldrich, RRID: AB_1079037), monoclonal mouse anti-H6PD antibody (Cat#sc-377180, Santa Cruz Biotechnology, Dallas, TX, USA, RRID: N/A), monoclonal mouse anti-AGR2 antibody (Cat#sc-101211, Santa Cruz, RRID: N/A), Streptavidin-HRP (Cat#21130, Thermo Fisher Scientific, RRID: N/A), monoclonal mouse anti-β-Actin antibody (Cat#sc-47778, Santa Cruz Biotechnology, RRID: N/A), monoclonal rabbit anti-Lamin B1 antibody (Cat# ab133741, Abcam, Cambridge, United Kingdom, RRID: AB_2616597), rabbit IgG Isotype control

(Cat#10500C, Thermo Fisher Scientific, RRID: AB_2532981), monoclonal mouse anti-MOGS (Cat#sc-374006, Santa Cruz Biotechnoloy, RRID: N/A), polyclonal rabbit anti-Calnexin antibody (Cat#SAB4503258, Sigma Aldrich, RRID: AB_10746486), polyclonal rabbit anti-Calreticulin antibody (Cat#2891, Cell Signaling Technology, Danvers, MA, USA, RRID: AB_2275208), monoclonal mouse anti-FLAG antibody (Cat#F1804, Sigma Aldrich, RRID: AB_262044), monoclonal rat anti-HA antibody (Cat#11867423001, Roche, Basel, Switzerland, RRID: AB_390918). All primary antibodies were used at dilutions 1:500-1:2'000. The following secondary antibodies were used: HRP-conjugated goat anti-mouse antibody (Cat# A0168, Sigma Aldrich, RRID: AB_257867), HRP-conjugated goat anti-rabbit antibody (Cat#A0545, Sigma Aldrich, RRID: AB_257896) and HRP-conjugated goat anti-rat antibody (Cat#7077S, Cell signaling, RRID: AB_10694715). Secondary antibodies were diluted 1:2'000-1:4'000. For experiments shown in this study, 10-35 µg protein were subjected to SDS-PAGE. Densitometry analysis, where appropriate, was carried out using ImageJ software (version 1.53n, RRID:SCR_003070).

Reversible crosslinking and Co-IP

The presented technique for crosslinking followed by Co-IP was adapted from previously presented studies [34, 35]. Briefly, MCF7 or MDA-MB 231 cells cultured in 10 cm dishes were washed twice with PBS. Intracellular crosslinking was performed by incubating the cells with PBS containing the crosslinking agents dithiobis(succinimidylpropionate) (DSP; Cat#c1106, ProteoChem, Hurricane, UT, USA) at a final concentration of 2 mM and dithiobismaleimidoethane (DTME; Cat# c1138, ProteoChem) at a concentration of 0.5 mM. After incubating for 45 min at room temperature, cells were washed twice with PBS, followed by quenching of the crosslinking-reaction using PBS containing 20 mM Tris-HCl pH 7.5 and 5 mM L-cysteine for 15 min. Finally, cells were washed twice with PBS and immediately lysed with Co-IP lysis buffer (50 mM Tris pH 7.5, 1% Triton, 150 mM NaCl, 10% glycerol, 5 mM $MgCl_2$ and protease inhibitor cocktail). The lysate was incubated for 10 min at 4°C at 1000 rpm, and centrifuged at 16'100 x g for 10 min, at 4°C. The supernatant was further processed. After protein concentration was determined by bicinchoninic acid assay, 1 mg of protein was added to 2 µg of either polyclonal rabbit anti-H6PD antibody (IP) or rabbit IgG Isotype control (IGG). The protein-antibody mixture was then incubated o/n at 4°C under permanent rotation. The next day, protein A magnetic beads (Cat#88846, Thermo Fisher Scientific) were activated according to the manufacturer's instructions. Briefly, 25 µL of activated protein A magnetic beads were mixed with the protein-antibody mixture and incubated for 1 h at room temperature

under continuous rotation. After incubation, the beads were washed by gentle vortex 5 times with 1 mL washing buffer (20 mM Tris, 0.5 M NaCl, 0.05% Tween-20) and once with 0.5 mL ultrapure water. 120 µL of SDS-PAGE sample buffer consisting of 70% v/v Co-IP lysis buffer, 5% v/v Tris(2-carboxyethyl)phosphine (TCEP) 0.5 M and 25 % v/v SDS-PAGE loading sample buffer 4X (240 mM Tris-HCl pH 6.8, 40% glycerol, 277 mM SDS, 0.04% bromophenol blue) was added to the beads, which were boiled for 10 min. Finally, the beads were separated and samples stored at -20°C until further use. 30 µL of sample were later loaded on the SDS-gel for the detection of interacting proteins.

Indirect immunofluorescence microscopy

Experiments of indirect immunofluorescence were performed to a great extent as previously described [36]. For the visualization of H6PD-BirA*-HA, the anti-HA antibody listed in the method description for "protein expression – western blot" was used at a dilution 1:150, followed by secondary goat anti-rat antibody alexa-555 (Cat#A-21434, Thermo Fisher Scientific, RRID: AB_141733) diluted 1:200. Biotinylated proteins were made optically visible using the streptavidin-alexa-488 (Cat# S11223, Thermo Fisher Scientific, RRID: N/A) antibody at 1:2000 dilution. Staining of the nuclei was performed using Hoechst 33342 (Cat#62249, Thermo Fisher Scientific) diluted 1:2000. All images were acquired with the ×40 objective of the microscope (Leica DMI4000 B, Leica, Wetzlar, Germany).

Effect of H6PD on 11β-HSD1 activity

For the indirect determination of H6PD activity, the 11β-HSD1-dependent conversion of cortisone to cortisol was determined. 350'000 cells stably expressing 11β-HSD1-FLAG were either mock-transfected or transfected with siRNA against AGR2 or H6PD. Cells were re-seeded at 15'750 cells per well in 96-well plates in a total volume of 90 µL per well. The medium was changed 72 h after transfection to serum-free culture medium (SFM) and cells were incubated for another 1 h 45 min. Finally, the medium was aspirated and replaced with 40 µL SFM and 10 µL SFM supplemented with 200 nM cortisone, of which 2.5% was radiolabeled [1,2-^{3}H]-cortisone (American Radiolabeled Chemicals, St. Louis, MO, USA). The NADPH-/H6PD-dependent reduction of cortisone by 11β-HSD1 was stopped after 1 h or 4 h, respectively, by the addition of unlabeled cortisol and cortisone (2 mM, in methanol). The mixture was then separated on a thin-layer chromatography (TLC) glass-plate using a mixture of methanol-chloroform (1:9). Bands for cortisone and cortisol were visualized by UV light,

and isolated bands analyzed on a liquid scintillation analyzer (TRI-CARB 2900 TR, PerkinElmer, Waltham, MA, USA).

Microsomal preparation and direct H6PD activity

Microsomes from HEK-293 cells were isolated as follows: Confluent 10 cm dishes of HEK-293 cells were washed with 3 mL pre-warmed PBS. 1 mL ice cold PBS was added and cells were collected and centrifuged for 4 min 150 x g at 4°C. The washing process was repeated and supernatant aspirated. Remaining pelleted cells were resuspended in 950 µL homogenization buffer (20 mM Tris pH 7.5, 50 mM KCl, 2 mM $MgCl_2$, 0.25 M sucrose and protease inhibitor cocktail). Cells were transferred to a dounce homogenizer (2 mL, stored on ice) and processed by 20 strokes with periods of repeated cooling on ice every 5 strokes for 10 seconds. Supernatant was centrifuged for 20 min at 4°C at 12'000 x g. The supernatant was transferred to fresh tubes and centrifuged for 1 h at 4°C at 104'900 x g. Supernatant was aspirated and the pellet, corresponding to the microsomal fraction resuspended in 35-50 µL resuspension buffer (20 mM 3-(N-morpholino)propanesulfonic acid (MOPS) pH 7.2, 100 mM KCl, 20 mM NaCl, 1 mM $MgCl_2$ and protease inhibitor cocktail). Protein concentration was determined by BCA-assay method and microsomal fractions were stored on ice before further use. 33 µg of microsomal protein fraction in resuspension buffer (total volume: 100 µL) was permeabilized by Triton X-100 (0.5% v/v). After 5 min, microsomes were incubated with 0.4 mM $NADP^+$ and 10 mM H6PD-specific substrate G6S (Glycoteam GmbH, Hamburg, Germany) [1]. H6PD activity was estimated by the measurement of absorbance at 340 nm, representing the formation of NADPH, 0, 1, 5, 10, 15, 20 and 30 min after substrate and cofactor administration [37].

Statistical analysis

GraphPad Prism software 8.0 (GraphPad, La Jolla, CA, USA, RRID:SCR_002798) and Microsoft Excel (Microsoft, Redmond, WA, USA) were used for analysis of data. In the context of data presentation, the respective statistical test is indicated. A p-value below 0.05 was considered statistically significant.

Results

Stable expression of H6PD-BirA*-HA in MDA-MB 231 cells leads to sufficient biotinylation of vicinal proteins upon biotin supplementation

To identify novel interacting partners of luminal H6PD we adapted the recently developed BioID approach and fused the promiscuous biotin ligase BirA*, marked with a HA-tag to H6PD. We transfected the triple negative breast cancer cell line MDA-MB 231, endogenously expressing H6PD, with the constructed fusion protein and generated stably expressing clones. Stimulation of biotinylation was achieved by the adding biotin to the cell culture medium (final concentration: 50 µM) and incubation for 72 h. Cells expressing H6PD-BirA*-HA showed increased levels of biotinylated proteins compared to MDA-MB 231 cells (Fig 1). Moreover, cells exposed to additional biotin showed increased levels of biotinylated proteins compared to cells cultured without biotin supplementation (Fig 2A). We further generated MDA-MB 231 cell clones stably expressing H6PD-BirA*-HA and 11β-HSD1-FLAG, which showed similar biotinylation patterns than clones exclusively expressing H6PD-BirA*-HA (Fig 2B).

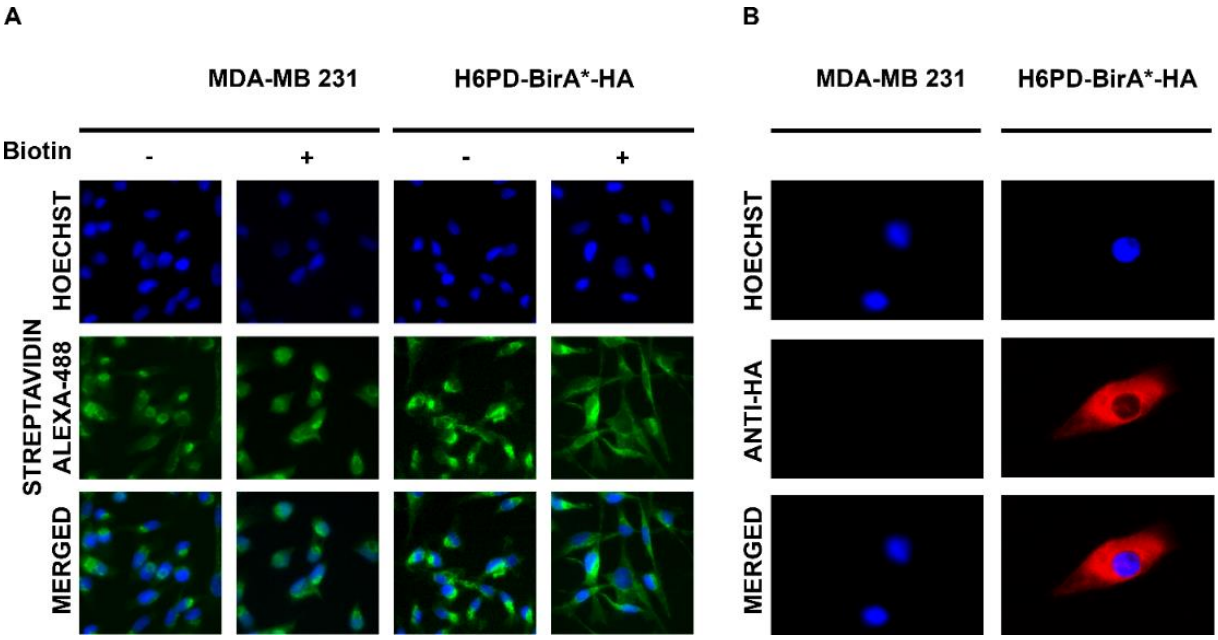

Figure 1. Site specific biotinylation in MDA-MB 231 cells expressing H6PD-BirA*-HA compared to control (MDA-MB 231). Representative images. A) Biotinylation is shown by the application of Streptavidin Alexa-488 antibody. B) Luminal expression pattern of H6PD-BirA*-HA demonstrated by Anti-HA antibody (followed by goat anti-rat antibody alexa-555).

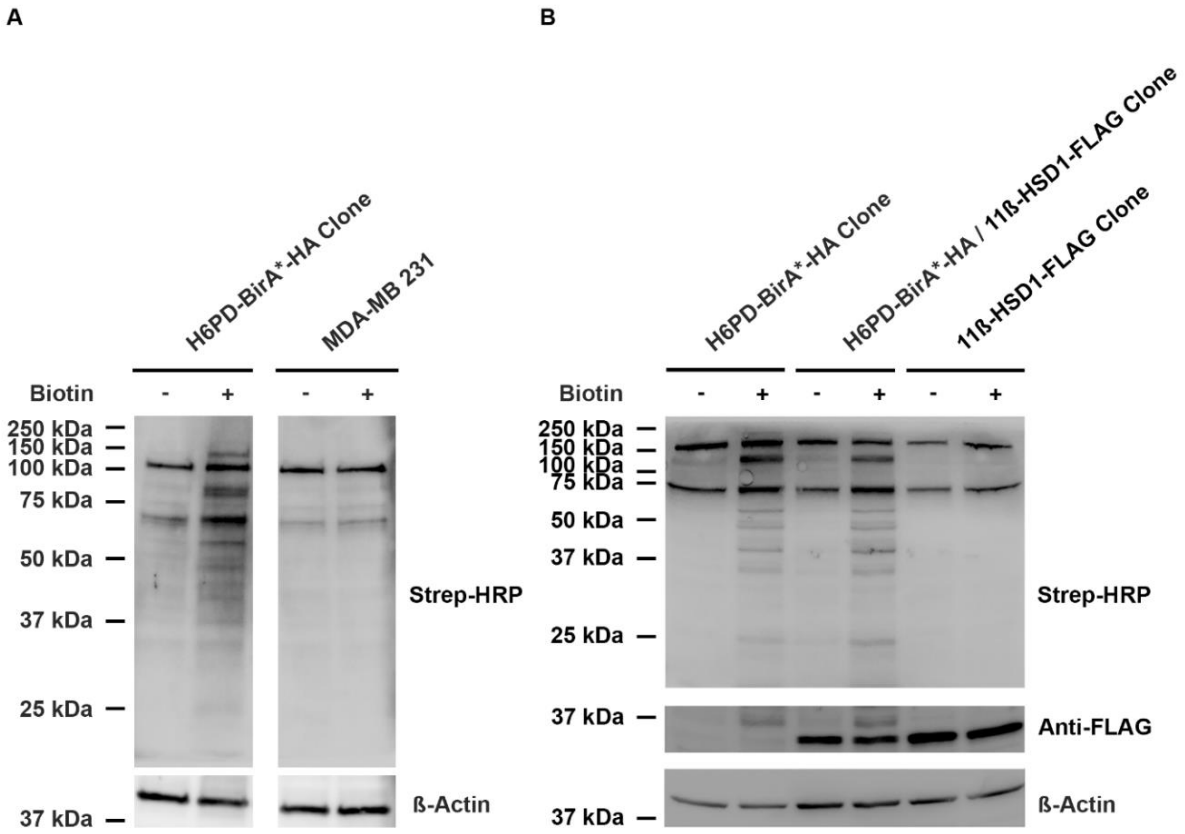

Figure 2. Representative western blot analysis demonstrates the generation of biotinylated proteins in the ER of MDA-MB 231 cells stably expressing H6PD-BirA*-HA. A) Western blot analysis of lysates from H6PD-BirA*-HA expressing clones and MDA-MB 231 cells. Operators indicate presence of 50 µM biotin during the 72h incubation period. Membranes were probed with HRP labeled streptavidin (Strep-HRP) to detect biotinylated proteins. β-Actin served as loading control. B) Western blot analysis of lysates from different clones expressing H6PD-BirA*-HA, H6PD-BirA*-HA / 11β-HSD1-FLAG or 11β-HSD1-FLAG. Membranes were probed with HRP labeled streptavidin to detect biotinylated proteins. β-Actin served as loading control.

The latter clones generated were used to demonstrate the reported interaction between H6PD and 11β-HSD1 [18, 19] (Suppl. Fig 1). While 11β-HSD1 was not enriched in cells solely expressing 11β-HSD1-FLAG, there was a statistically significant enrichment of peptides originating from the 11β-HSD1-FLAG construct in cells stably expressing both 11β-HSD1-FLAG and H6PD-BirA*-HA.

Proteomic analysis of potential H6PD interacting partners reveals clusters consisting of PDI family members, luminal chaperones, calcium binding proteins and proteins involved in quality control and processing of glycoproteins.

Next, we performed large scale experiments to identify biotinylated proteins by mass spectrometry. Briefly, cells stably expressing H6PD-BirA*-HA and native MDA-MB 231 cells were cultured in presence of biotin (50 µM) for 72 h and subsequently lysed and subjected to affinity purification using streptavidin-conjugated magnetic beads. Biotinylated proteins were afterwards analyzed by label-free quantitative MS by comparing samples of H6PD-BirA*-HA with those of parental MDA-MB 231 control. Overall, 1098 proteins could be assigned, including the bait protein H6PD. 1049 of the proteins were identified by at least 2 peptides and 904 of them by at least 3. 82 proteins showed a $\log_2$-fold change ≥ 1 (qValue ≤ 0.01) and 50 proteins were enriched in the samples from H6PD-BirA*-HA expressing cells by a factor of at least 10, corresponding by a $\log_2$-fold change ≥ 3.33 and a qValue ≤ 0.01, respectively (Table 1). Regarding the subcellular location, 46 out of the 50 most enriched proteins were clearly allocated to the ER. Based on presented circumscribed data set (Table 1) we focused on proteins with similar gene function in order to obtain clusters for potential interacting partners. Among the 50 proteins listed (Table 1), 9 members of the protein disulfide isomerase (PDI) family were identified: Cysteine-rich with EGF-like domain protein 2 (CRELD2), Anterior gradient protein 2 homolog (AGR2), Protein disulfide-isomerase A4 (PDIA4), Thioredoxin domain-containing protein 5 (TXNDC5), Prolyl 4-hydroxylase subunit beta (P4HB), Protein disulfide-isomerase A3 (PDIA3), Endoplasmic reticulum resident protein 29 (ERP29), Thioredoxin-related transmembrane protein 1 (TMX1) and Protein disulfide-isomerase A6 (PDIA6) [38-40]. A second cluster of 10 proteins was detected, representing luminal (co-) chaperones, affiliated to different heat shock protein families and ER resident lecithin chaperones: Hypoxia up-regulated protein 1 (HYOU1), DnaJ homolog subfamily B member 12 (DNAJB12), DnaJ homolog subfamily B member 11 (DNAJB11), DnaJ homolog subfamily C member 3 (DNAJC3), Endoplasmic reticulum chaperone BiP (HSPA5), LRP chaperone MESD (MESDC2), Endoplasmin (HSP90B1), co-chaperone Protein canopy homolog 3 (CNPY3) as well as the two lectins Calreticulin (CALR) and Calnexin (CNX) [41-45]. Further, 6 proteins with calcium binding features were registered, namely Reticulocalbin-1 (RCN1), Calumenin (CALU), 45 kDa calcium-binding protein (SDF4), Inactive C-alpha-formylglycine-generating enzyme 2 (SUMF2), VIP36-like protein (LMAN2L) and Reticulocalbin-2 (RCN2) [46].

Gene	Peptides	Log2 ratio	Gene function	Subcellular localization
MOGS	3	9.68	Mannosyl-oligosaccharide glucosidase	ER membrane
CRELD2	1	8.51	Protein disulfide isomerase	ER
TMTC3	2	8.12	Mannosyltransferase	ER
TMED2	2	7.64	Vesicular protein trafficking	ER membrane / Golgi
IKBIP	3	7.40	Target of p53 with pro-apoptopic function	ER membrane
AGR2	5	6.16	Protein disulfide isomerase	ER
SELENOF	7	5.47	Quality control of protein folding	ER
HYOU1	52	5.39	Chaperone	ER
RCN1	12	5.37	Calcium binding protein	ER
PDIA4	46	5.20	Protein disulfide isomerase	ER
MCFD2	2	5.17	Part of a cargo receptor for ER-to Golgi transport	ER/ Golgi
DNAJB12	2	5.16	Chaperone	ER/ Nucleus
H6PD	**84**	**5.10**	**BAIT / Luminal NADPH generation**	**ER**
MYDGF	3	5.08	Promotes cardiac myocyte survival and angiogenesis	ER/ Golgi / Extracellular secreted
TMED9	4	5.04	Involved in vesicular protein trafficking	ER membrane / Golgi apparatus
LMAN1	16	4.88	Part of a cargo receptor for ER-to Golgi transport	ER/ Golgi
PRKCSH	16	4.86	Glucosidase (subunit)	ER
TXNDC5	16	4.85	Protein disulfide isomerase	ER
CALU	17	4.83	Calcium binding protein	ER membrane / Golgi
SDF4	2	4.80	Calcium binding protein	Plasma membrane / Cytoplasm
P4HB	36	4.76	Protein disulfide isomerase	ER
PDIA3	49	4.75	Protein disulfide isomerase	ER
DNAJB11	12	4.58	Chaperone	ER
DNAJC3	16	4.55	Chaperone	ER
HSPA5	61	4.49	Chaperone	ER
ITGB1	9	4.48	Integrin	Endosome / Plasma membrane
PCYOX1	4	4.48	Oxidoreductase	Lysosome
NUP210	7	4.44	Nucleoporin	ER/ Nucleus
UGGT1	59	4.31	Glycosyltransferase	ER
ERO1A	13	4.18	Oxidoreductase	ER
CNPY3	8	4.17	(co-) Chaperone	ER
SUMF2	7	4.14	Calcium binding protein	ER
LMAN2L	2	4.12	Calcium binding protein	ER/ Golgi
PLOD3	3	4.11	Hydroxylase / Glycosyltransferase	ER/ Extracellular secreted
ERP29	9	4.07	Protein disulfide isomerase	ER
TMX1	3	4.02	Protein disulfide isomerase	ER
MANF	12	3.95	Growth factor	ER/ Extracellular secreted
FKBP2	8	3.87	Isomerase	ER
NENF	4	3.83	Growth factor	Extracellular secreted
CALR	16	3.83	Chaperone	ER
P3H1	3	3.81	Oxidoreductase	ER/ Extracellular secreted
MLEC	7	3.73	Carbohydrate binding protein	ER
PDIA6	15	3.62	Protein disulfide isomerase	ER
MESDC2	8	3.61	Chaperone	ER
CNX	24	3.60	Chaperone	ER
PRDX4	15	3.55	Thioredoxin peroxidase	ER/ Cytoplasm
TMEM43	3	3.49	Nuclear membrane protein	ER/ Nucleus
HSP90B1	43	3.45	Chaperone	ER
CHID1	4	3.37	Oligosaccharide binding protein	Lysosome / Extracellular secreted
RCN2	4	3.33	Calcium binding protein	ER

Table 1. Top 50 biotinylated proteins identified by mass spectrometry after immunoprecipitation using streptavidin-labeled magnetic beads (log_2-fold change ≥ 3.33 and a qValue ≤ 0.01). PDI family members are highlighted in green, proteins with calcium binding features are marked in blue, ER resident (co-) chaperones in yellow. Bait protein H6PD (bold) is marked in orange. The presented log_2-fold change represents enrichment of identified peptides in H6PD-BirA*-HA clone samples compared to MDA-MB 231 control samples. The numbers of peptides used for quantification of each protein is listed in the "Peptides" column. Suspected gene function and subcellular localization were adapted from UniProt (24th December 2020) and sources cited in this work. The presented data were determined on the basis of results from three independent experiments.

Finally, Mannosyl-oligosaccharide glucosidase (MOGS), Protein O-mannosyl-transferase TMTC3 (TMTC3), Selenoprotein F (SELENOF), Glucosidase 2 subunit beta (PRKCSH), UDP-glucose glycoprotein glucosyltransferase 1 (UGGT1), Multifunctional procollagen lysine hydroxylase and glycosyltransferase LH3 (PLOD3), Chitinase domain-containing protein 1

(CHID1) were associated with different, not directly interrelated, tasks of luminal glycoprotein quality control and processing [47-52]. Regarding further investigations, we decided to enclose potential interactors descending from presented clusters by restricting selection parameters (*i.e* log_2-fold change and numbers of peptides used for protein quantification). AGR2, a PDI family member was found to show the highest log_2-fold change (6.16) regarding potential interacting candidates which were quantified by more than 2 peptides. We therefore decided to further investigate this particular potential interacting partner of H6PD.

PDI family member AGR2 interacts directly with H6PD in MCF7 cells endogenously expressing H6PD and AGR2

To confirm the interaction between AGR2 and H6PD *in vivo*, we performed Co-IP experiments as described, using reversible crosslinking agents. Previous to these examinations, we tested different breast cancer cell lines for AGR2 and H6PD protein expression levels (Suppl. Figure 2) to identify suitable cell lines for Co-IP experiments. The estrogen receptor and progesterone receptor positive cell line MCF7 showed the most abundant protein expression of AGR2 compared to triple negative breast cancer cell lines SUM 159 and MDA-MB 231 (H6PD-BirA*-HA clone) and was therefore subjected to Co-IP along with MDA-MB 231 [53] (Suppl Fig 2). After using an anti-H6PD antibody for Co-IP, bands for AGR2 were detected following 10 s and 35 s of exposure in immunoprecipitation (IP) samples (Fig 3). AGR2 protein bands were absent in samples incubated with IGG control.

Additionally, MOGS, CRT and CNX were probed with the corresponding antibodies to test potential interacting partners of H6PD, descending from other hit clusters. Whereas probing MOGS and CNX showed weak band signals in IP samples, supporting a direct interaction, bands for CRT were not detected. β-Actin was probed to exclude non-specific binding of the anti-H6PD antibody used. Previous to Co-IP experiments we tested the anti-H6PD antibody for its suitability regarding IP applications to ensure sufficient antigen binding (Suppl. Fig 3).

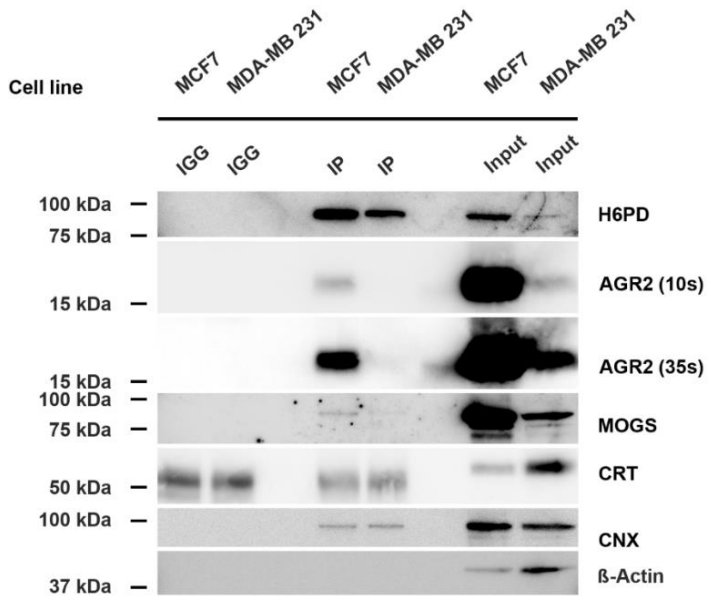

Figure 3. AGR2 interacts with H6PD in MCF7 cells. Co-IP assay of MCF7 and MDA-MB 231 cells. Reversible crosslinking using DSP and DTME as crosslinking agents was carried out as described. AGR2, MOGS, CRT and CNX were probed using the corresponding antibodies. β-Actin was used as negative control to exclude non-specific binding.

AGR2 silencing using siRNA increases H6PD protein levels in MCF7 cells and MDA-MB 231 cells

In order to investigate a potential direct effect of AGR2 on H6PD protein expression, we transfected MCF7 and MDA-MB 231 cells with siRNA against AGR2 and compared H6PD protein expression levels in relation to mock-transfected cells. Transfection using siRNA against H6PD served for verification of the anti-H6PD antibody. H6PD protein expression was significantly increased in MCF7 cells transfected with siRNA against AGR2 72 h after transfection (Fig 4A-B). MDA-MB 231 cells showed significantly increased H6PD protein levels 48 h after transfection using siRNA against AGR2 (Fig 4C-D).

However, AGR2 silencing did neither affect H6PD protein levels in MCF7 cells 48 h after transfection, nor in MDA-MB 231 cells 72 h after transfection. Furthermore, H6PD silencing did not affect AGR2 expression in any of the two cell lines (data not shown).

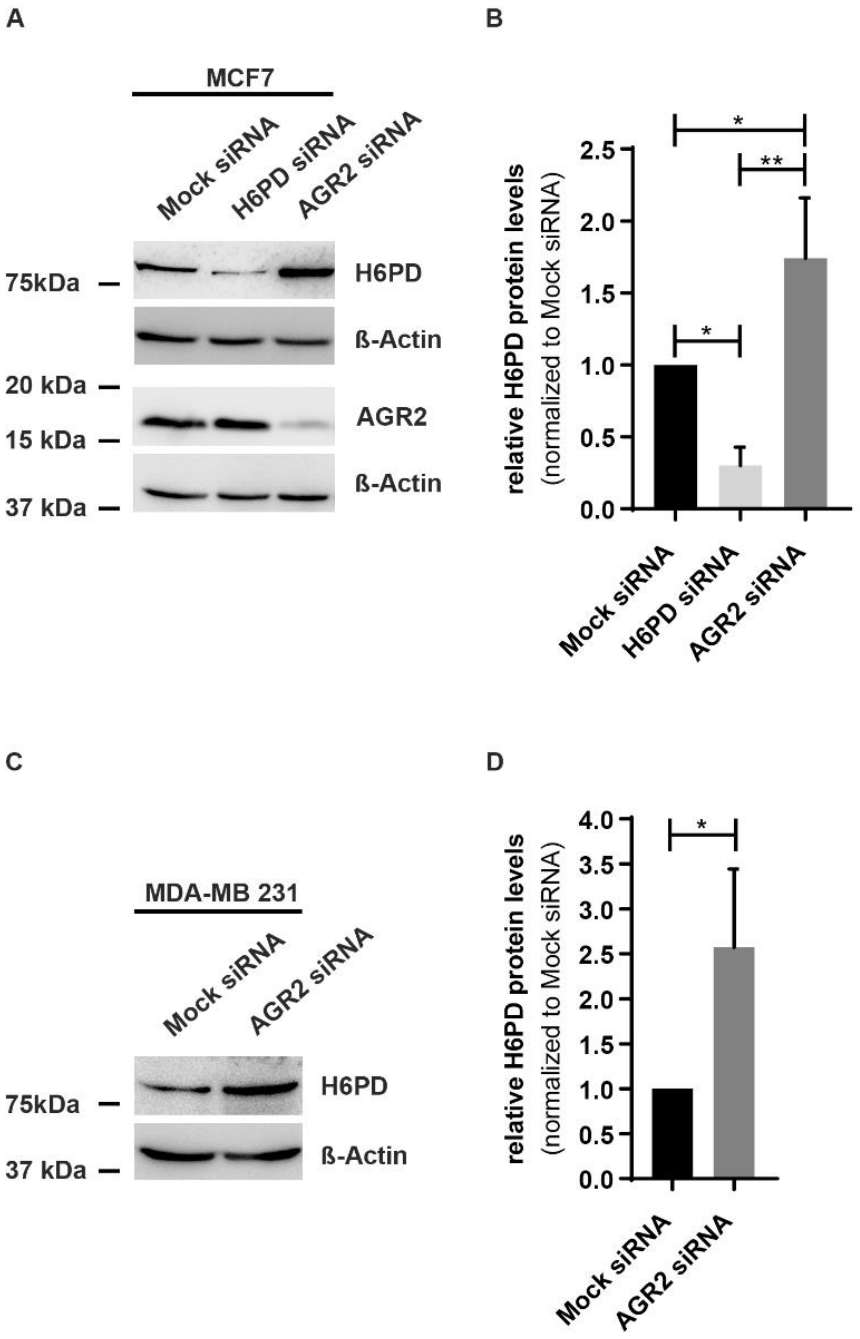

Figure 4. AGR2 knockdown leads to increased H6PD protein expression levels in MCF7 and MDA-MB 231 cells. A) H6PD and AGR2 protein expression levels in MCF7 cells upon transfection with mock siRNA, H6PD siRNA or AGR2 siRNA. Protein levels were detected 72 h post-transfection as shown in a representative western blot analysis. β-Actin served as loading control B) Relative H6PD protein levels determined by densitometry analysis (normalized to mock siRNA treated cells). Data represent mean ± SD from three independent experiments. One-way ANOVA with Tukey's post hoc test, p values: *<0.05, **<0.01, ***<0.001. C) H6PD protein expression levels in MDA-MB 231 cells upon transfection with mock siRNA or H6PD siRNA. Protein levels were detected 48 h post transfection as shown in a representative western blot image. β-Actin served as loading control. D) Relative H6PD protein levels determined by densitometry analysis (normalized to mock siRNA treated cells). Data represent mean ± SD from three independent experiments Two-tailed Student's t-test, p values: *<0.05, **<0.01, ***<0.001.

H6PD activity is increased in HEK-293 cells co-transfected with H6PD-MYC / AGR2-FLAG compared to H6PD-MYC transfected control

In order to assess the direct impact of AGR2 on H6PD activity, we transfected HEK-293 cells with plasmids encoding H6PD-MYC combined with or without plasmids encoding AGR2-FLAG. Microsomal fractions were isolated and H6PD activity was measured. To estimate H6PD activity over a period of 30 min, we measured absorbance at 340 nm, monitoring the formation of NADPH. H6PD activity was compared between the two groups by examining the slopes of the linear regression lines to the data points obtained (Fig 5). The presented linear regressions obtained from cells transfected with both H6PD-MYC and AGR2-FLAG showed a significantly steeper slope compared to cells expressing H6PD-MYC only ($p = 0.0008$), indicating a direct impact of AGR2 on H6PD activity. We further analyzed the H6PD protein expression levels in the two different groups to clarify whether the increased microsomal H6PD activity of co-transfected cells was due to higher H6PD expression. However, there was no significant difference in H6PD protein expression between the two groups, suggesting that AGR2 co-expression did not increase total expression but enhanced the fraction of active H6PD enzyme.

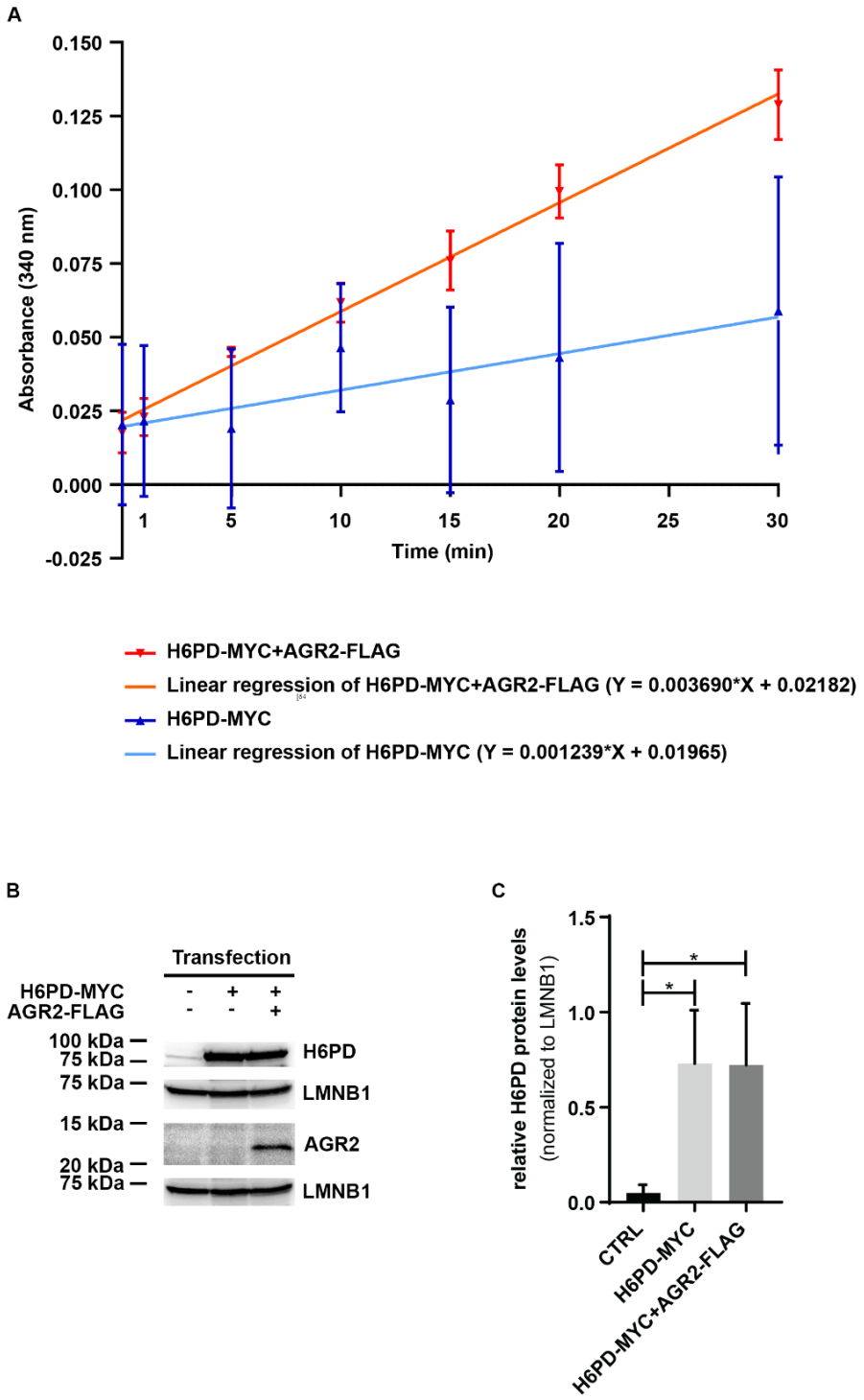

Figure 5. H6PD-MYC / AGR2-FLAG co-transfection accelerates NADPH generation in HEK-293 cells compared to cells transfected with H6PD-MYC. A) H6PD activity assay in microsomal preparations from HEK-293 cells transfected with H6PD-MYC or co-transfected with H6PD-MYC and AGR2-FLAG. NADPH specific absorbance at 340 nm was measured 0, 1, 5, 10, 15, 20 and 30 min after administration the H6PD-specific substrate glucose-6-sulfate and cofactor $NADP^+$, respectively. Linear regressions were applied and compared, resulting in significantly different slopes (*p = 0.0008*). B) Representative western blot of transfected HEK-293 cells. C) H6PD protein levels determined by densitometry analysis (relative to Lamin B1 protein levels). Lamin B1 served as loading control. Data represent mean ± SD from three independent experiments. One-way ANOVA with Tukey's post hoc test, p values: *<0.05, **<0.01, ***<0.001.

Increased H6PD protein levels upon AGR2 silencing do not alter 11β-HSD1 activity in MDA-MB 231 cells

Next, we tested whether the observed increase of H6PD protein levels upon AGR2 knockdown would result in altered 11β-HSD1-mediated conversion of cortisone to cortisol, which in turn represents an indirect indicator of H6PD activity. MDA-MB 231 cells stably expressing 11β-HSD1-FLAG were subjected to transfection using siRNA against H6PD or AGR2. Mock-transfected cells served as control. Cortisone to cortisol conversion was determined after 1 h and 4 h respectively as described before. There was no observable difference in cortisol formation between the examined groups 1 h after the experiment start (Fig 6A). Significant differences in cortisone to cortisol conversion within the differently treated cells were observed after 4 h, illustrated in significantly decreased 11β-HSD1 activity in cells subjected to H6PD silencing (Fig 6B). However, no difference in cortisol formation was observed between cells subjected to mock-transfection or AGR2 silencing. This is in contrast to H6PD protein levels, which were significantly increased upon AGR2 knockdown compared to mock-transfection (Fig 6C), suggesting accumulation of inactive protein.

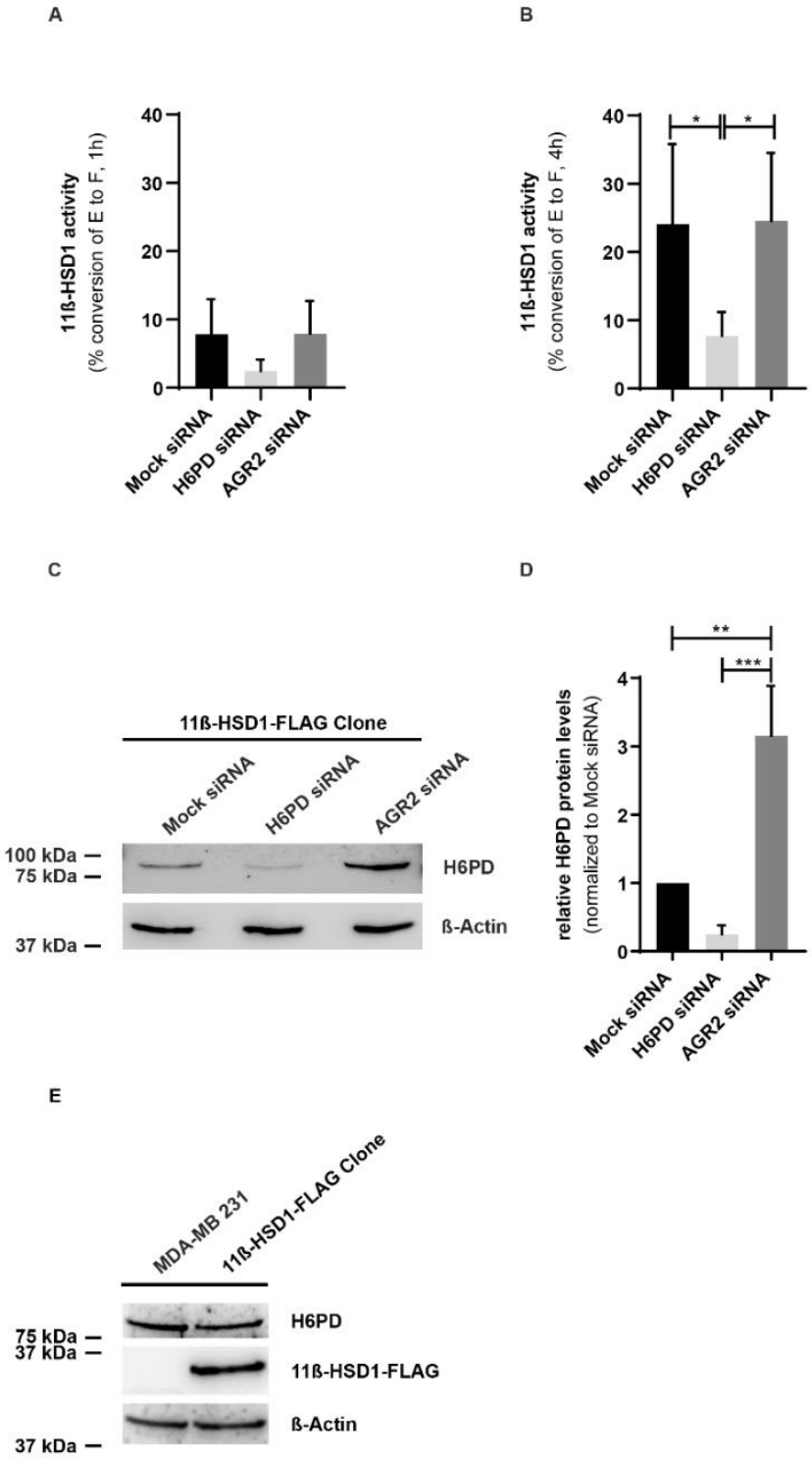

Figure 6. AGR2 knockdown does not alter cortisone to cortisol conversion in MDA-MB 231 cells stably expressing 11β-HSD1-FLAG (11β-HSD1-FLAG clone) despite significantly increased H6PD protein expression levels. A) Conversion (%) of cortisone to cortisol 1 h and B) 4 h after administration of (radioactive labeled) cortisone, in 11β-HSD1-FLAG clone, previously transfected with mock siRNA, H6PD siRNA or AGR2 siRNA. C) Representative western blot of H6PD protein and D) Relative H6PD protein levels determined by densitometry (normalized to mock siRNA treated cells). E) Characterization of 11β-HSD1-FLAG clone by western blot analysis. Data represent mean ± SD from three independent experiments. One-way ANOVA with Tukey's post hoc test, p values: *<0.05, **<0.01, ***<0.001.

Discussion

Almost a decade ago, Roux and colleagues developed BioID, a tool for proximity labeling of proteins in living mammalian cells [54]. Ever since, numerous publications affirmed the applicability of BioID in the elucidation of protein interactomes. BioID was successfully deployed not only in the focus of studying mammalian cells but also during examinations of plants, viruses, bacteria, protozoa and even living animals [55-59]. In the presented study, we used the approach of BioID to identify novel interacting partners of the ER resident protein H6PD, the only known source of luminal NADPH.

The triple negative breast cancer cell line MDA-MB 231 served as a model system for the generation of cells stably expressing H6PD-BirA*-HA. Thorough validation of luminal biotinylation was followed by MS analysis of biotinylated proteins. The specificity of our approach was underpinned by the fact that 45 of the 50 most enriched proteins were found to be spatially associated with the ER.

AGR2 was selected from the pool of potential interactors and further examined for its role regarding protein expression and functionality of H6PD. The expression of AGR2 was previously shown to be positively correlated with the expression of the estrogen receptor in estrogen receptor positive breast cancers cell lines. Furthermore, breast cancer patients suffering from AGR2-postive carcinomas were associated with a significantly shorter survival time compared to patients with AGR2-negative tumors [60, 61]. The results of the present study suggest that AGR2 enhances the fraction of functionally expressed and active H6PD protein. H6PD was recently found to promote breast cancer cell proliferation and migratory capacity and knockdown suppressed these effects [17]. Interestingly, studies exploring the interactome of AGR2 revealed a partially overlapping list of interacting partners with that obtained in the present study on H6PD. HSPA5, ERP29, PRXV, ERO1A, PDIA3, PDIA6 and CNX were found in a screening for AGR2 interactors using Co-IP as well as in our presented data set [62]. Thus, the functional interactions of H6PD and the above mentioned proteins remains to be explored.

Moreover, Maurel *et al.* showed that TMED2, ranked as fourth most enriched protein in the present work, was found to directly regulate AGR2 dimerization. Additionally, among the 71 presented candidates involved in AGR2 regulation, 7 of them were also found in the screening for H6PD interactors. HYOU1, ERO1A and HSP90B1 represented the fraction of candidate AGR2 homodimer inhibitors, which were also found in our screening. TMED2, LMAN1, UGGT1 and H6PD were assumed to be AGR2 homodimer enhancers [63]. Focusing on the

physiological point of view, AGR2 has been shown to play an important role in the folding of cysteine rich proteins by forming mixed disulfides with protein substrates and, subsequently re-arranging disulfide bonds [64, 65]. The amino acid sequence of H6PD (Sequence: NM_001282587.2) displays 10 cysteine residues, which could be involved in the interaction with AGR2.

In the present study we demonstrated a direct interaction between AGR2 and H6PD, in MCF7 cells with endogenous expressing, by reversible crosslinking followed by Co-IP. AGR2 silencing using siRNA had a direct impact on H6PD protein expression levels in MCF7 and MDA-MB 231 cells. Further, an enhanced activity of H6PD in the presence of AGR2 was shown in HEK-293 cells co-transfected with both enzymes, compared to cells expressing H6PD only. Despite the significantly higher H6PD protein levels upon AGR2 silencing in 11β-HSD1 expressing MDA-MB 231 cells, an increase in cortisone to cortisol conversion could not be observed. This leads to the assumption that the observation of higher H6PD protein levels was due to the accumulation of immature and/or misfolded, inactive H6PD enzyme. This assumption is in line with a role for AGR2 as a PDI family member, involved in controlling protein folding. However, this needs further investigation.

Finally, it should be noted that none of the listed potential interactors of H6PD could be assigned to the short-chain dehydrogenases/reductases (SDR) family. SDRs represent one of the largest protein families with more than 70 genes in human and roles in the metabolism of xenobiotics, lipids, prostaglandins, retinoids and steroid hormones [66]. We anticipated that besides the SDR 11β-HSD1, where a direct interaction was shown [18], other SDR members would exist that require NADPH in the ER. The absence of such NADPH-interacting SDR partners supports the prevailing hypothesis of the existence of an alternative source capable of generating luminal NADPH [69, 70].

In conclusion, BioID is a useful tool for the screening of protein interactions, also in the ER lumen, and therefore a valuable technique to expand our understanding of this still insufficiently understood cellular compartment. However, incubation periods for sufficient biotinylation might be extended when applying BioID as discovery tool for luminal protein-portein-interactions compared to applications in the cytoplasm. Moreover, validation of potential interactors is crucial and false positive hits were found to be a concern when using BioID to screen for interactions [71, 72]. Potential interactors identified by BioID based approaches need to be further examined by a second method, which ideally includes an endogenous cell system (e.g. Co-IP or fluorescence image co-localization analysis). Finally, it has to be addressed that

endogenously biotinylated proteins, such as biotin-dependent carboxylases, may limit the applicability of BioID [73].

Conflict of interest

The authors declare no conflicts of interest.

Acknowledgments

This work was supported by Swiss National Science Foundation Grants 31003A-179400.

Author contribution

Michael Weingartner: Conceptualization, Data curation, Formal analysis, Investigation, Methodology, Project administration, Validation, Visualization, Writing – original draft, editing

Maria Tsachaki: Investigation, Supervision, Writing – review & editing

Thomas Bock: Investigation, Data curation, Formal analysis, Software, Visualization,

Julia Birk: Investigation, Writing – review & editing

Alex Odermatt: Conceptualization, Funding acquisition, Project administration, Resources, Supervision, Validation, Writing – review & editing

References

1. Lavery GG, Walker EA, Draper N, Jeyasuria P, Marcos J, Shackleton CHL, et al. Hexose-6-phosphate Dehydrogenase Knock-out Mice Lack 11β-Hydroxysteroid Dehydrogenase Type 1-mediated Glucocorticoid Generation. J Biol Chem. 2006;281(10):6546-51. doi: 10.1074/jbc.M512635200.
2. Rogoff D, Black K, McMillan DR, White PC. Contribution of hexose-6-phosphate dehydrogenase to NADPH content and redox environment in the endoplasmic reticulum. Redox Rep. 2010;15(2):64-70. doi: 10.1179/174329210X12650506623249.
3. Ge T, Yang J, Zhou S, Wang Y, Li Y, Tong X. The Role of the Pentose Phosphate Pathway in Diabetes and Cancer. Front Endocrinol. 2020;11. doi: 10.3389/fendo.2020.00365.
4. Senesi S, Legeza B, Balázs Z, Csala M, Marcolongo P, Kereszturi É, et al. Contribution of Fructose-6-Phosphate to Glucocorticoid Activation in the Endoplasmic Reticulum: Possible Implication in the Metabolic Syndrome. Endocrinology. 2010;151(10):4830-9. doi: 10.1210/en.2010-0614.
5. White PC, Rogoff D, McMillan DR, Lavery GG. HEXOSE 6-PHOSPHATE DEHYDROGENASE (H6PD) AND CORTICOSTEROID METABOLISM. Mol Cell Endocrinol. 2007;265-266:89-92. doi: 10.1016/j.mce.2006.12.022.
6. Lewis CA, Parker SJ, Fiske BP, McCloskey D, Gui DY, Green CR, et al. Tracing compartmentalized NADPH metabolism in the cytosol and mitochondria of mammalian cells. Mol Cell. 2014;55(2):253-63. doi: 10.1016/j.molcel.2014.05.008.
7. Pollak N, Niere M, Ziegler M. NAD Kinase Levels Control the NADPH Concentration in Human Cells. J Biol Chem. 2007;282(46):33562-71. doi: 10.1074/jbc.M704442200.
8. Dzyakanchuk AA, Balázs Z, Nashev LG, Amrein KE, Odermatt A. 11beta-Hydroxysteroid dehydrogenase 1 reductase activity is dependent on a high ratio of NADPH/NADP(+) and is stimulated by extracellular glucose. Mol Cell Endocrinol. 2009;301(1-2):137-41. doi: 10.1016/j.mce.2008.08.009.
9. Sallin O, Reymond L, Gondrand C, Raith F, Koch B, Johnsson K. Semisynthetic biosensors for mapping cellular concentrations of nicotinamide adenine dinucleotides. eLife. 2018;7:e32638. doi: 10.7554/eLife.32638.
10. Veech RL, Eggleston LV, Krebs HA. The redox state of free nicotinamide–adenine dinucleotide phosphate in the cytoplasm of rat liver. Biochem J. 1969;115(4):609-19.

11. Boudon S, Heidl M, Vuorinen A, Wandeler E, Campiche R, Odermatt A, et al. Design, synthesis, and biological evaluation of novel selective peptide inhibitors of 11β-hydroxysteroid dehydrogenase 1. Bioorganic & Medicinal Chemistry. 2018;26(18):5128-39. doi: 10.1016/j.bmc.2018.09.009.
12. DiNicolantonio JJ, Mehta V, Onkaramurthy N, O'Keefe JH. Fructose-induced inflammation and increased cortisol: A new mechanism for how sugar induces visceral adiposity. Progress in Cardiovascular Diseases. 2018;61(1):3-9. doi: 10.1016/j.pcad.2017.12.001.
13. Kardon T, Senesi S, Marcolongo P, Legeza B, Bánhegyi G, Mandl J, et al. Maintenance of luminal NADPH in the endoplasmic reticulum promotes the survival of human neutrophil granulocytes. FEBS Letters. 2008;582(13):1809-15. doi: 10.1016/j.febslet.2008.04.045.
14. Meyer A, Vuorinen A, Zielinska AE, Strajhar P, Lavery GG, Schuster D, et al. Formation of Threohydrobupropion from Bupropion Is Dependent on 11β-Hydroxysteroid Dehydrogenase 1. Drug Metab Dispos. 2013;41(9):1671-8. doi: 10.1124/dmd.113.052936.
15. Nashev LG, Chandsawangbhuwana C, Balazs Z, Atanasov AG, Dick B, Frey FJ, et al. Hexose-6-phosphate Dehydrogenase Modulates 11β-Hydroxysteroid Dehydrogenase Type 1-Dependent Metabolism of 7-keto- and 7β-hydroxy-neurosteroids. PLOS ONE. 2007;2(6):e561. doi: 10.1371/journal.pone.0000561.
16. Lavery GG, Walker EA, Turan N, Rogoff D, Ryder JW, Shelton JM, et al. Deletion of Hexose-6-phosphate Dehydrogenase Activates the Unfolded Protein Response Pathway and Induces Skeletal Myopathy. J Biol Chem. 2008;283(13):8453-61. doi: 10.1074/jbc.M710067200.
17. Tsachaki M, Mladenovic N, Štambergová H, Birk J, Odermatt A. Hexose-6-phosphate dehydrogenase controls cancer cell proliferation and migration through pleiotropic effects on the unfolded-protein response, calcium homeostasis, and redox balance. FASEB J. 2018;32(5):2690-705. doi: 10.1096/fj.201700870RR.
18. Atanasov AG, Nashev LG, Gelman L, Legeza B, Sack R, Portmann R, et al. Direct protein–protein interaction of 11β-hydroxysteroid dehydrogenase type 1 and hexose-6-phosphate dehydrogenase in the endoplasmic reticulum lumen. Biochimica et Biophysica Acta (BBA) - Molecular Cell Research. 2008;1783(8):1536-43. doi: 10.1016/j.bbamcr.2008.03.001.
19. Legeza B, Balázs Z, Nashev LG, Odermatt A. The Microsomal Enzyme 17β-Hydroxysteroid Dehydrogenase 3 Faces the Cytoplasm and Uses NADPH Generated by Glucose-6-Phosphate Dehydrogenase. Endocrinology. 2013;154(1):205-13. doi: 10.1210/en.2012-1778.

20. Brandes RP, Weissmann N, Schröder K. Nox family NADPH oxidases: Molecular mechanisms of activation. Free Radical Biology and Medicine. 2014;76:208-26. doi: 10.1016/j.freeradbiomed.2014.07.046.

21. Lai J-Q, Li Z, Lü Y-H, Yang Z. Specific ion effects of ionic liquids on enzyme activity and stability. Green Chem. 2011;13(7):1860-8. doi: 10.1039/C1GC15140A.

22. McMillan DGG, Marritt SJ, Firer-Sherwood MA, Shi L, Richardson DJ, Evans SD, et al. Protein–Protein Interaction Regulates the Direction of Catalysis and Electron Transfer in a Redox Enzyme Complex. J Am Chem Soc. 2013;135(28):10550-6. doi: 10.1021/ja405072z.

23. Nooren IMA, Thornton JM. Diversity of protein–protein interactions. The EMBO Journal. 2003;22(14):3486-92. doi: 10.1093/emboj/cdg359.

24. Page MJ, Di Cera E. Role of Na+ and K+ in Enzyme Function. Physiological Reviews. 2006;86(4):1049-92. doi: 10.1152/physrev.00008.2006.

25. Schreiber G. Kinetic studies of protein–protein interactions. Current Opinion in Structural Biology. 2002;12(1):41-7. doi: 10.1016/S0959-440X(02)00287-7.

26. Deng M, Zhang K, Mehta S, Chen T, Sun F. Prediction of protein function using protein-protein interaction data. J Comput Biol. 2003;10(6):947-60. Epub 2004/02/26. doi: 10.1089/106652703322756168. PubMed PMID: 14980019.

27. Mabonga L, Kappo AP. Protein-protein interaction modulators: advances, successes and remaining challenges. Biophys Rev. 2019;11(4):559-81. doi: 10.1007/s12551-019-00570-x.

28. Scott DE, Bayly AR, Abell C, Skidmore J. Small molecules, big targets: drug discovery faces the protein–protein interaction challenge. Nat Rev Drug Discov. 2016;15(8):533-50. doi: 10.1038/nrd.2016.29.

29. Roux KJ, Kim DI, Burke B, May DG. BioID: A Screen for Protein-Protein Interactions. Current Protocols in Protein Science. 2018;91(1):19 23 1-19 23 15. Epub 2018/03/09. doi: 10.1002/cpps.51. PubMed PMID: 29516480.

30. DI, Jensen SC, Roux KJ. Identifying Protein-Protein Associations at the Nuclear Envelope with BioID. Methods Mol Biol. 2016;1411:133-46. doi: 10.1007/978-1-4939-3530-7_8.

31. Sears RM, May DG, Roux KJ. BioID as a Tool for Protein-Proximity Labeling in Living Cells. Methods Mol Biol. 2019;2012:299-313. Epub 2019/06/05. doi: 10.1007/978-1-4939-9546-2_15. PubMed PMID: 31161514; PubMed Central PMCID: PMCPMC6583792.

32. Beck KR, Sommer TJ, Schuster D, Odermatt A. Evaluation of tetrabromobisphenol A effects on human glucocorticoid and androgen receptors: A comparison of results from human- with yeast-based in vitro assays. Toxicology. 2016;370:70-7. Epub 2016/10/25. doi: 10.1016/j.tox.2016.09.014. PubMed PMID: 27693315; PubMed Central PMCID: PMCPMC6828555.

33. Engeli RT, Rhouma BB, Sager CP, Tsachaki M, Birk J, Fakhfakh F, et al. Biochemical analyses and molecular modeling explain the functional loss of 17β-hydroxysteroid dehydrogenase 3 mutant G133R in three Tunisian patients with 46, XY Disorders of Sex Development. The Journal of Steroid Biochemistry and Molecular Biology. 2016;155:147-54. doi: 10.1016/j.jsbmb.2015.10.023.

34. Mattson G, Conklin E, Desai S, Nielander G, Savage MD, Morgensen S. A practical approach to crosslinking. Mol Biol Rep. 1993;17(3):167-83. doi: 10.1007/BF00986726.

35. Smith AL, Friedman DB, Yu H, Carnahan RH, Reynolds AB. ReCLIP (Reversible Cross-Link Immuno-Precipitation): An Efficient Method for Interrogation of Labile Protein Complexes. PLOS ONE. 2011;6(1):e16206. doi: 10.1371/journal.pone.0016206.

36. Tsachaki M, Birk J, Egert A, Odermatt A. Determination of the topology of endoplasmic reticulum membrane proteins using redox-sensitive green-fluorescence protein fusions. Biochimica et Biophysica Acta (BBA) - Molecular Cell Research. 2015;1853(7):1672-82. doi: 10.1016/j.bbamcr.2015.04.002.

37. Wu JT, Wu LH, Knight JA. Stability of NADPH: effect of various factors on the kinetics of degradation. Clin Chem. 1986;32(2):314-9. Epub 1986/02/01. PubMed PMID: 3943190.

38. Dennis EP, Edwards SM, Jackson RM, Hartley CL, Tsompani D, Capulli M, et al. CRELD2 Is a Novel LRP1 Chaperone That Regulates Noncanonical WNT Signaling in Skeletal Development. J Bone Miner Res. 2020;35(8):1452-69. Epub 2020/03/18. doi: 10.1002/jbmr.4010. PubMed PMID: 32181934.

39. Appenzeller-Herzog C, Ellgaard L. The human PDI family: versatility packed into a single fold. Biochim Biophys Acta. 2008;1783(4):535-48. Epub 2007/12/21. doi: 10.1016/j.bbamcr.2007.11.010. PubMed PMID: 18093543.

40. Galligan JJ, Petersen DR. The human protein disulfide isomerase gene family. Hum Genomics. 2012;6:6. Epub 2012/12/19. doi: 10.1186/1479-7364-6-6. PubMed PMID: 23245351; PubMed Central PMCID: PMCPMC3500226.

41. Kakiuchi C, Ishiwata M, Nanko S, Kunugi H, Minabe Y, Nakamura K, et al. Association analysis of HSP90B1 with bipolar disorder. J Hum Genet. 2007;52(10):794-803. Epub 2007/09/07. doi: 10.1007/s10038-007-0188-4. PubMed PMID: 17805476.

42. Song L, Zhang J, Li C, Yao J, Jiang C, Li Y, et al. Genome-wide identification of hsp40 genes in channel catfish and their regulated expression after bacterial infection. PLOS ONE. 2014;9(12):e115752. Epub 2014/12/30. doi: 10.1371/journal.pone.0115752. PubMed PMID: 25542027; PubMed Central PMCID: PMCPMC4277396.

43. Hsieh JC, Lee L, Zhang L, Wefer S, Brown K, DeRossi C, et al. Mesd encodes an LRP5/6 chaperone essential for specification of mouse embryonic polarity. Cell. 2003;112(3):355-67. Epub 2003/02/13. doi: 10.1016/s0092-8674(03)00045-x. PubMed PMID: 12581525.

44. Mutoh H, Kato M, Akita T, Shibata T, Wakamoto H, Ikeda H, et al. Biallelic Variants in CNPY3, Encoding an Endoplasmic Reticulum Chaperone, Cause Early-Onset Epileptic Encephalopathy. Am J Hum Genet. 2018;102(2):321-9. Epub 2018/02/06. doi: 10.1016/j.ajhg.2018.01.004. PubMed PMID: 29394991; PubMed Central PMCID: PMCPMC5985471.

45. Theocharides AP, Lundberg P, Lakkaraju AK, Lysenko V, Myburgh R, Aguzzi A, et al. Homozygous calreticulin mutations in patients with myelofibrosis lead to acquired myeloperoxidase deficiency. Blood. 2016;127(25):3253-9. Epub 2016/03/26. doi: 10.1182/blood-2016-02-696310. PubMed PMID: 27013444.

46. Honore B. The rapidly expanding CREC protein family: members, localization, function, and role in disease. Bioessays. 2009;31(3):262-77. Epub 2009/03/05. doi: 10.1002/bies.200800186. PubMed PMID: 19260022.

47. Graham JB, Sunryd JC, Mathavan K, Weir E, Larsen ISB, Halim A, et al. Endoplasmic reticulum transmembrane protein TMTC3 contributes to O-mannosylation of E-cadherin, cellular adherence, and embryonic gastrulation. Mol Biol Cell. 2020;31(3):167-83. Epub 2019/12/19. doi: 10.1091/mbc.E19-07-0408. PubMed PMID: 31851597; PubMed Central PMCID: PMCPMC7001481.

48. Volker C, De Praeter CM, Hardt B, Breuer W, Kalz-Fuller B, Van Coster RN, et al. Processing of N-linked carbohydrate chains in a patient with glucosidase I deficiency (CDG type IIb). Glycobiology. 2002;12(8):473-83. Epub 2002/07/30. doi: 10.1093/glycob/cwf050. PubMed PMID: 12145188.

49. Yim SH, Everley RA, Schildberg FA, Lee SG, Orsi A, Barbati ZR, et al. Role of Selenof as a Gatekeeper of Secreted Disulfide-Rich Glycoproteins. Cell Rep. 2018;23(5):1387-98. Epub 2018/05/03. doi: 10.1016/j.celrep.2018.04.009. PubMed PMID: 29719252.

50. Pan J, Hu Y, Sun S, Chen L, Schnaubelt M, Clark D, et al. Glycoproteomics-based signatures for tumor subtyping and clinical outcome prediction of high-grade serous ovarian cancer. Nat Commun. 2020;11(1):6139. Epub 2020/12/03. doi: 10.1038/s41467-020-19976-3. PubMed PMID: 33262351; PubMed Central PMCID: PMCPMC7708455.

51. Ewans LJ, Colley A, Gaston-Massuet C, Gualtieri A, Cowley MJ, McCabe MJ, et al. Pathogenic variants in PLOD3 result in a Stickler syndrome-like connective tissue disorder with vascular complications. J Med Genet. 2019;56(9):629-38. Epub 2019/05/28. doi: 10.1136/jmedgenet-2019-106019. PubMed PMID: 31129566.

52. Lee CG, Da Silva CA, Dela Cruz CS, Ahangari F, Ma B, Kang MJ, et al. Role of chitin and chitinase/chitinase-like proteins in inflammation, tissue remodeling, and injury. Annu Rev Physiol. 2011;73:479-501. Epub 2010/11/09. doi: 10.1146/annurev-physiol-012110-142250. PubMed PMID: 21054166; PubMed Central PMCID: PMCPMC3864643.

53. Comsa S, Cimpean AM, Raica M. The Story of MCF-7 Breast Cancer Cell Line: 40 years of Experience in Research. Anticancer Res. 2015;35(6):3147-54. Epub 2015/05/31. PubMed PMID: 26026074.

54. Roux KJ, Kim DI, Raida M, Burke B. A promiscuous biotin ligase fusion protein identifies proximal and interacting proteins in mammalian cells. J Cell Biol. 2012;196(6):801-10. Epub 2012/03/14. doi: 10.1083/jcb.201112098. PubMed PMID: 22412018; PubMed Central PMCID: PMCPMC3308701.

55. Das PP, Macharia MW, Lin Q, Wong SM. In planta proximity-dependent biotin identification (BioID) identifies a TMV replication co-chaperone NbSGT1 in the vicinity of 126kDa replicase. J Proteomics. 2019;204:103402. Epub 2019/06/04. doi: 10.1016/j.jprot.2019.103402. PubMed PMID: 31158515.

56. Cheerathodi MR, Meckes DG, Jr. BioID Combined with Mass Spectrometry to Study Herpesvirus Protein-Protein Interaction Networks. Methods Mol Biol. 2020;2060:327-41. Epub 2019/10/17. doi: 10.1007/978-1-4939-9814-2_19. PubMed PMID: 31617188.

57. Olson MG, Jorgenson LM, Widner RE, Rucks EA. Proximity Labeling of the Chlamydia trachomatis Inclusion Membrane. Methods Mol Biol. 2019;2042:245-78. Epub 2019/08/07. doi: 10.1007/978-1-4939-9694-0_17. PubMed PMID: 31385281.

58. Khosh-Naucke M, Becker J, Mesen-Ramirez P, Kiani P, Birnbaum J, Frohlke U, et al. Identification of novel parasitophorous vacuole proteins in P. falciparum parasites using BioID. Int J Med Microbiol. 2018;308(1):13-24. Epub 2017/08/09. doi: 10.1016/j.ijmm.2017.07.007. PubMed PMID: 28784333.

59. Rudolph F, Fink C, Huttemeister J, Kirchner M, Radke MH, Lopez Carballo J, et al. Deconstructing sarcomeric structure-function relations in titin-BioID knock-in mice. Nat Commun. 2020;11(1):3133. Epub 2020/06/21. doi: 10.1038/s41467-020-16929-8. PubMed PMID: 32561764; PubMed Central PMCID: PMCPMC7305127.

60. Barraclough DL, Platt-Higgins A, de Silva Rudland S, Barraclough R, Winstanley J, West CR, et al. The metastasis-associated anterior gradient 2 protein is correlated with poor survival of breast cancer patients. Am J Pathol. 2009;175(5):1848-57. Epub 2009/10/17. doi: 10.2353/ajpath.2009.090246. PubMed PMID: 19834055; PubMed Central PMCID: PMCPMC2774050.

61. Thompson DA, Weigel RJ. hAG-2, the human homologue of the Xenopus laevis cement gland gene XAG-2, is coexpressed with estrogen receptor in breast cancer cell lines. Biochem Biophys Res Commun. 1998;251(1):111-6. Epub 1998/10/29. doi: 10.1006/bbrc.1998.9440. PubMed PMID: 9790916.

62. Worfolk JC, Bell S, Simpson LD, Carne NA, Francis SL, Engelbertsen V, et al. Elucidation of the AGR2 Interactome in Esophageal Adenocarcinoma Cells Identifies a Redox-Sensitive Chaperone Hub for the Quality Control of MUC-5AC. Antioxid Redox Signal. 2019;31(15):1117-32. Epub 2019/08/23. doi: 10.1089/ars.2018.7647. PubMed PMID: 31436131.

63. Maurel M, Obacz J, Avril T, Ding YP, Papadodima O, Treton X, et al. Control of anterior GRadient 2 (AGR2) dimerization links endoplasmic reticulum proteostasis to inflammation. EMBO Mol Med. 2019;11(6). Epub 2019/05/02. doi: 10.15252/emmm.201810120. PubMed PMID: 31040128; PubMed Central PMCID: PMCPMC6554669.

64. Park SW, Zhen G, Verhaeghe C, Nakagami Y, Nguyenvu LT, Barczak AJ, et al. The protein disulfide isomerase AGR2 is essential for production of intestinal mucus. Proc Natl Acad Sci U S A. 2009;106(17):6950-5. Epub 2009/04/11. doi: 10.1073/pnas.0808722106. PubMed PMID: 19359471; PubMed Central PMCID: PMCPMC2678445.

65. Delom F, Mohtar MA, Hupp T, Fessart D. The anterior gradient-2 interactome. Am J Physiol Cell Physiol. 2020;318(1):C40-C7. Epub 2019/10/24. doi: 10.1152/ajpcell.00532.2018. PubMed PMID: 31644305.

66. Persson B, Kallberg Y, Bray JE, Bruford E, Dellaporta SL, Favia AD, et al. The SDR (short-chain dehydrogenase/reductase and related enzymes) nomenclature initiative. Chem Biol Interact. 2009;178(1-3):94-8. Epub 2008/11/26. doi: 10.1016/j.cbi.2008.10.040. PubMed PMID: 19027726; PubMed Central PMCID: PMCPMC2896744.

67. Rossmann MG, Moras D, Olsen KW. Chemical and biological evolution of nucleotide-binding protein. Nature. 1974;250(463):194-9. Epub 1974/07/19. doi: 10.1038/250194a0. PubMed PMID: 4368490.

68. Kallberg Y, Persson B. Prediction of coenzyme specificity in dehydrogenases/reductases. A hidden Markov model-based method and its application on complete genomes. FEBS J. 2006;273(6):1177-84. Epub 2006/03/08. doi: 10.1111/j.1742-4658.2006.05153.x. PubMed PMID: 16519683.

69. Marbet P, Klusonova P, Birk J, Kratschmar DV, Odermatt A. Absence of hexose-6-phosphate dehydrogenase results in reduced overall glucose consumption but does not prevent 11beta-hydroxysteroid dehydrogenase-1-dependent glucocorticoid activation. FEBS J. 2018;285(21):3993-4004. Epub 2018/08/29. doi: 10.1111/febs.14642. PubMed PMID: 30153376.

70. Dzyakanchuk AA, Balazs Z, Nashev LG, Amrein KE, Odermatt A. 11beta-Hydroxysteroid dehydrogenase 1 reductase activity is dependent on a high ratio of NADPH/NADP(+) and is stimulated by extracellular glucose. Mol Cell Endocrinol. 2009;301(1-2):137-41. Epub 2008/09/10. doi: 10.1016/j.mce.2008.08.009. PubMed PMID: 18778749.

71. Boucher MJ, Ghosh S, Zhang L, Lal A, Jang SW, Ju A, et al. Integrative proteomics and bioinformatic prediction enable a high-confidence apicoplast proteome in malaria parasites. PLoS Biol. 2018;16(9):e2005895. Epub 2018/09/14. doi: 10.1371/journal.pbio.2005895. PubMed PMID: 30212465; PubMed Central PMCID: PMCPMC6155542.

72. Chojnowski A, Sobota RM, Ong PF, Xie W, Wong X, Dreesen O, et al. 2C-BioID: An Advanced Two Component BioID System for Precision Mapping of Protein Interactomes. iScience. 2018;10:40-52. Epub 2018/12/01. doi: 10.1016/j.isci.2018.11.023. PubMed PMID: 30500481; PubMed Central PMCID: PMCPMC6263017.

73. Tytgat HL, Schoofs G, Driesen M, Proost P, Van Damme EJ, Vanderleyden J, et al. Endogenous biotin-binding proteins: an overlooked factor causing false positives in streptavidin-based protein detection. Microb Biotechnol. 2015;8(1):164-8. Epub 2014/09/12. doi: 10.1111/1751-7915.12150. PubMed PMID: 25211245; PubMed Central PMCID: PMCPMC4321382.

Supplementary data

MWNMLIVAMCLALLGCLQAQELQGHVSIILLGATGDLAKKYLWQGLFQLYLDEAGRGHSFSFHGAALTAPKQGQELMAKALESLSCPKD
MAPSHCAEHKDQFLQLSQYRQLKTAEDYQALNKDIEAQLQHAGLREAGRIFYFSVPPFAYEDIARNINSSCRPGPGAWLRVVLEKPFGHDH
FSAQQLATELGTFFQEEEMYRVDHYLGKQAVAQILPFRDQNRKALDGLWNRHHVERVEIIMKETVDAEGRTSFYEEYGVIRDVLQNHLTEV
LTLVAMELPHNVSSAEAVLRHKLQVFQALRGLQRGSAVVGQYQSYSEQVRRELQKPDSFHSLTPTFAAVLVHIDNLRWEGVPFILMSGKAL
DERVGYARILFKNQACCVQSEKHWAAAQSQCLPRQLVFHIGHGDLGSPAVLVSRNLFRPSLPSSWKEMEGPPGLRLFGSPLSDYYAYSPVR
ERDAHSVLLSHIFHGRKNFFITTENLLASWNFWTPLLESLAHKAPRLYPGGAENGRLLDFEFSSGRLFFSQQQPEQLVPGPGPAPMPSDFQV
LRAKYRESPLVSAWSEELISKLANDIEATAVRAVRRFGQFHLALSGGSSPVALFQQLATAHYGFPWAHTHLWLVDERCVPLSDPESNFQGL
QAHLLQHVRIPYYNIHPMPVHLQQRLCAEEDQGAQIYAREISALVANSSFDLVLLGMGADGHTASLFPQSPTGLDGEQLVVLTTSPSQPHR
RMSLSLPLINRAKKVAVLVMGRMKREITTLVSRVGHEPKKWPISGVLPHSGQLVWYMDYDAFLGGSKDNTVPLKLIALLANGEFHSGEQL
GETLGMSRAAINKHIQTLRDWGVDVFTVPGKGYSLPEPIQLLNAKQILGQLDGGSVAVLPVIDSTNQYLLDRIGELKSGDACIAEYQQAGRG
GRGRKWFSPFGANLYLSMFWRLEQGPAAAIGLSLVIGIVMAEVLRKLGADKVRVKWPNDLYLQDRKLAGILVELTGKTGDAAQIVIGAGIN
MAMRRVEESVVNQGWITLQEAGINLDRNTLAAMLIRELRAALELFEQEGLAPYLSRWEKLDNFINRPVKLIIGDKEIFGISRGIDKQGALLLE
QDGIIKPWMGGEISLRSAEKAYPYDVPDYA

Suppl. Table 1. Sequence of H6PD-BirA*-HA construct. Sequences of different motifs are shown as follows: Hexose-6-phosphate dehydrogenase (H6PD) – Linker - promiscuous biotin ligase (BirA*) - human influenza hemagglutinin (HA).

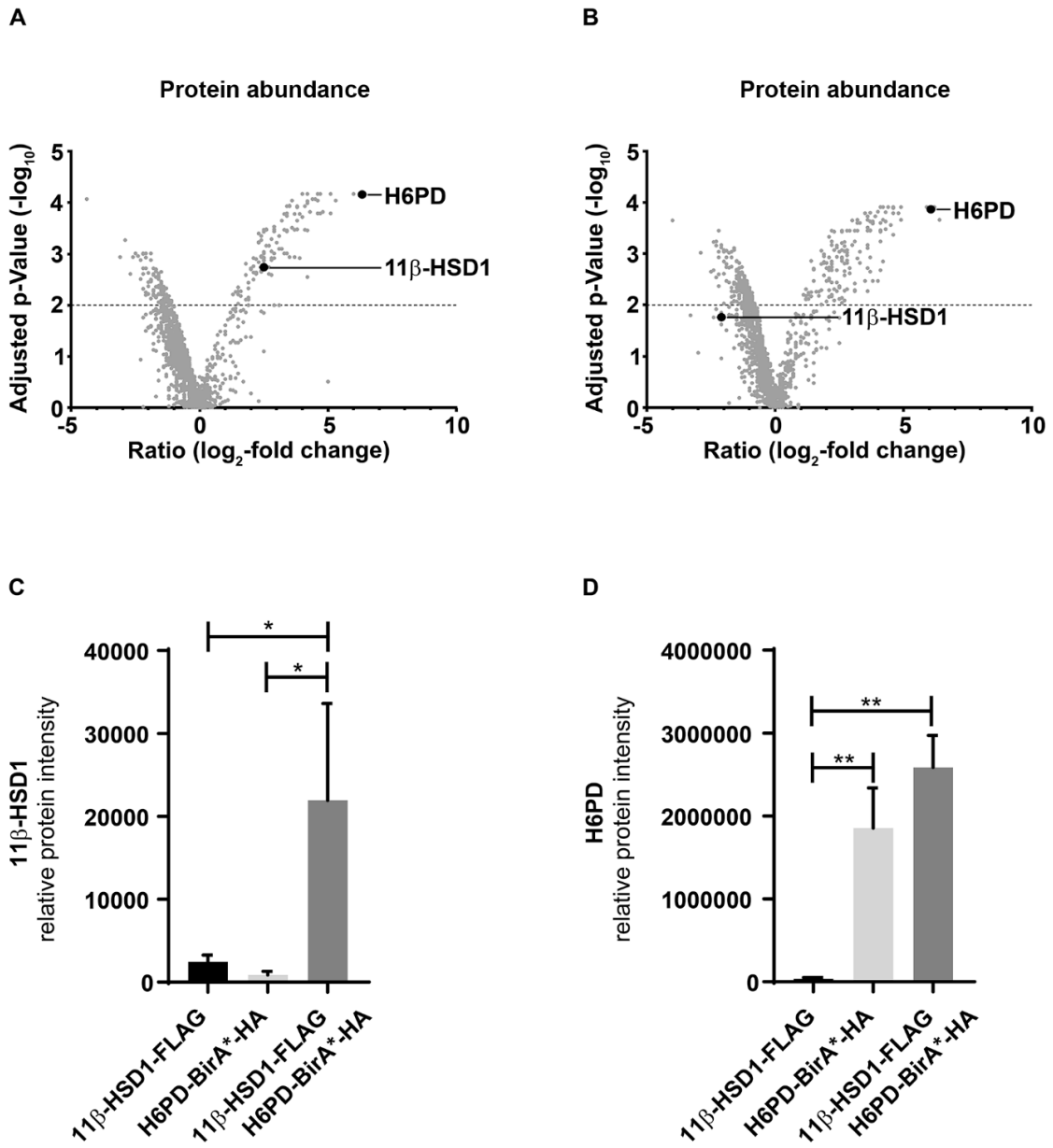

Suppl. Figure 1. Identification of biotinylated 11β-HSD1 by quantitative mass spectrometry in cells stable expressing H6PD-BirA*HA and 11β-HSD1-FLAG. The x axis of presented volcano plots show the ratio (log_2-fold-change) of median protein abundance in A) samples from cells stably co-expressing H6PD-BirA*-HA and 11β-HSD1-FLAG in comparison to cells stably expressing 11β-HSD1-FLAG and B) samples from cells stably expressing H6PD-BirA*-HA in comparison to cells stably expressing 11β-HSD1-FLAG. Dashed line in A) and B) represents a qValue of 0.01. Relative protein intensities of C) 11β-HSD1 and D) H6PD measured in the presented groups are indicated. Data represent mean ± SD from three independent experiments. One-way ANOVA with Tukey's post hoc test, p values: *<0.05, **<0.01, ***<0.001.

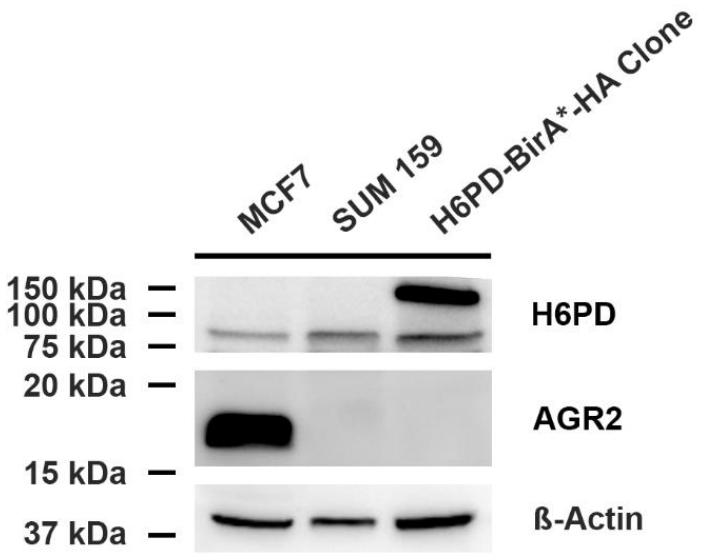

Suppl. Figure 2. Representative western blot analysis indicates relative H6PD and AGR2 protein expression levels in MCF7, SUM 159 and MDA-MB 231 cells (H6PD-BirA*-HA clone). Cell lysates were probed for H6PD and AGR2 protein expression levels, demonstrating high AGR2 protein expression levels in estrogen and progesterone receptor positive breast cancer cell line MCF7 compared to barely detectable AGR2 protein expression levels in triple negative breast cancer cell line SUM 159 cells and MDA-MB 231 (H6PD-BirA*-HA clone) cells. β-Actin served as loading control.

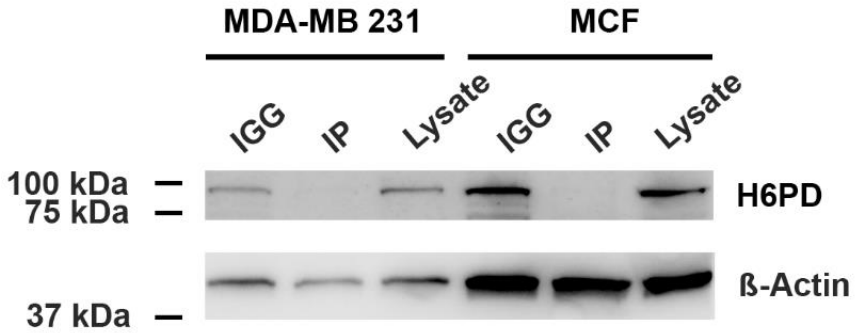

Suppl. Figure 3. Representative western blot analysis to indicate the suitability of polyclonal rabbit anti-H6PD antibody for Co-IP. Samples of MDA-MB 231 and MCF7 cell lysate (input) were incubated using IGG control or polyclonal rabbit anti-H6PD antibody (IP) over night and afterwards mixed with protein A magnetic beads, to form an anti-H6PD-antibody-protein A magnetic beads complex. Remaining lysates were probed for the detection of H6PD protein expression levels after separation of magnetic beads. Non-incubated lysate (input) serves as positive control. β-Actin served as loading control.

6 Endoplasmic reticulum stress caused by parasitic infection

6.1 *Echinococcus multilocularis* induced endoplasmic reticulum stress

6.1.1 Submitted manuscript

Albendazole reduces endoplasmic reticulum stress induced by *Echinococcus multilocularis* in mice

Michael Weingartner[1#], Fadi Jebbawi[1#], Junhua Wang[2,3], Simon Stücheli[1], Bruno Gottstein[2,3], Guido Beldi[4], Britta Lundström-Stadelmann[2], and Alex Odermatt[1*]

[1] Division of Molecular and Systems Toxicology, Department of Pharmaceutical Sciences, University of Basel, Klingelbergstrasse 50, 4056 Basel, Switzerland.
[2] Institute of Parasitology, Department of Infectious Diseases and Pathobiology, Vetsuisse Faculty, University of Bern, Längassstrasse 122, 3012, Berne, Switzerland.
[3] Institute for Infectious Diseases, Faculty of Medicine, University of Berne, Friedbühlstrasse 51, 3010, Berne, Switzerland.
[4] Department of Visceral Surgery and Medicine, University Hospital of Berne, Freiburgstrasse, 3010 Berne, Switzerland

[#] These authors contributed equally to the presented study

Target journal: PLOS Neglected Tropical Diseases
Available preprint: https://doi.org/10.1101/2021.02.03.429530

Contribution to the project:

- Experimental work
- Analysis and interpretation of the data
- Writing the paper manuscript (including figures and tables)
- Revising the manuscript

Albendazole reduces endoplasmic reticulum stress induced by *Echinococcus multilocularis* in mice

Running title: ER-stress induced by *E. multilocularis*

Michael Weingartner[1#], Fadi Jebbawi[1#], Junhua Wang[2,3], Simon Stücheli[1], Bruno Gottstein[2,3], Guido Beldi[4], Britta Lundström-Stadelmann[2], and Alex Odermatt[1*]

[1] Division of Molecular and Systems Toxicology, Department of Pharmaceutical Sciences, University of Basel, Klingelbergstrasse 50, 4056 Basel, Switzerland.
[2] Institute of Parasitology, Department of Infectious Diseases and Pathobiology, Vetsuisse Faculty, University of Bern, Längassstrasse 122, 3012, Berne, Switzerland.
[3] Institute for Infectious Diseases, Faculty of Medicine, University of Berne, Friedbühlstrasse 51, 3010, Berne, Switzerland.
[4] Department of Visceral Surgery and Medicine, University Hospital of Berne, Freiburgstrasse, 3010 Berne, Switzerland

* To whom correspondence should be addressed:
Dr. Alex Odermatt, Division of Molecular and Systems Toxicology, Department of Pharmaceutical Sciences, University of Basel, Klingelbergstrasse 50, 4056 Basel, Switzerland
Email: alex.odermatt@unibas.ch

[#]These authors contributed equally to the presented study

Disclosures: The authors declare no commercial or financial conflict of interest

Keywords: Alveolar echinococcosis; benzimidazole; endoplasmic reticulum; unfolded protein response; parasite; inflammation; infection; microRNA

Abstract

Background

Echinococcus multilocularis causes alveolar echinococcosis (AE), a rising zoonotic disease in the northern hemisphere. Treatment of this fatal disease is limited to chemotherapy using benzimidazoles and surgical intervention, with relatively frequent disease recurrence in cases without radical surgery. Elucidating the molecular mechanisms underlying *E. multilocularis* infections and host-parasite interactions aids developing novel therapeutic options. This study explored an involvement of unfolded protein response (UPR) and endoplasmic reticulum-stress (ERS) during *E. multilocularis* infection in mice.

Methods

E. multilocularis- and mock-infected C57BL/6 mice were subdivided six weeks after infection into vehicle and albendazole (ABZ) treated groups. Eight weeks later, liver tissue was collected to examine mRNA, microRNA (miR) and protein expression of UPR- and ERS-related genes.

Results

E. multilocularis infection upregulated UPR- and ERS-related proteins, including ATF6, CHOP, GRP78, ERP72, H6PD and calreticulin, whilst PERK and its target eIF2α were not affected, and IRE1α and ATF4 were downregulated. ABZ treatment in *E. multilocularis* infected mice reversed the increased ATF6 and calreticulin protein expression, tended to reverse increased CHOP, GRP78, ERP72 and H6PD expression, and decreased ATF4 and IRE1α expression to levels seen in mock-infected mice. The expression of miR-146a-5p (downregulated by IRE1α) and miR-1839-5p (exhibiting a unique target site in the IRE1α 3'UTR) were significantly increased in *E. multilocularis* infected mice, an effect reversed by ABZ treatment. Other miRs analyzed were not altered in *E. multilocularis* infected mice.

Conclusions and Significance

AE causes UPR activation and ERS in mice. The *E. multilocularis*-induced ERS was ameliorated by ABZ treatment, indicating its effectiveness to inhibit parasite proliferation and downregulate its activity status. ABZ itself did not affect UPR in control mice. Identified miR-146a-5p and miR-1839-5p might represent biomarkers of *E. multilocularis* infection. Modulation of UPR and ERS, in addition to ABZ administration, could be exploited to treat *E. multilocularis* infection.

Author summary

Alveolar echinococcosis is a zoonotic disease caused by the fox tapeworm *Echinococcus multilocularis*. Treatment of this fatal disease is limited to surgical intervention, preferably radical curative surgery if possible, and the use of parasitostatic benzimidazoles. It is not yet fully understood how the parasite can remain in the host's tissue for prolonged periods, complicating the development of therapeutic applications. This work investigated an involvement of the unfolded protein response (UPR) and endoplasmic reticulum-stress (ERS) during *E. multilocularis* infection and upon treatment with albendazole (ABZ) in mice. The results revealed increased expression levels of the ERS sensor ATF6 and of downstream target genes in liver tissue of *E. multilocularis*- compared to mock-infected mice. Additionally, H6PD, generating NADPH within the endoplasmic reticulum, and the lectin-chaperone calreticulin were increased in *E. multilocularis* infected liver tissue while the expression of the ERS associated genes ATF4 and IRE1α were decreased. The miR-1839-5p and miR-146-p, linked to IRE1α, were elevated upon *E. multilocularis* infection, offering potential as novel biomarkers of alveolar echinococcosis. The observed gene expression changes were at least partially reversed by ABZ treatment. Whether modulation of UPR and ERS targets can improve the therapy of alveolar echinococcosis remains to be investigated.

Abbreviations

ABZ, albendazole; AE, alveolar echinococcosis; ATF4, activating transcription factor 4; ATF6, activating transcription factor 6; CHOP, CCAAT/enhancer-binding protein homologous protein; CNX, calnexin; CRT, calreticulin; CTRL, control; eIF2α, eukaryotic initiation factor 2α; *E. multilocularis*, *Echinococcus multilocularis*; ER, endoplasmic reticulum; ERAD, ER-associated degradation; ERP72, endoplasmic reticulum resident protein 72; ERS, endoplasmic reticulum stress; GRP78, glucose-regulated protein 78; H6PD, hexose-6-phosphate dehydrogenase; HRP, horse-radish peroxidase; IRE1α, inositol-requiring enzyme 1α; microRNA(s), miR(s); PERK, protein kinase R (PKR) like ER kinase; PVDF, polyvinylidene difluoride; RIPA, radioimmunoprecipitation assay; RT-qPCR, real-time quantitative polymerase chain reaction; UPR, unfolded protein response; XBP1(-s), X-box binding protein 1 (-spliced);

Introduction

Alveolar echinococcosis (AE) is a severe helminthic disease caused by accidental ingestion of eggs from the fox tapeworm *Echinococcus multilocularis (E. multilocularis)* [1, 2]. After an incubation period of 5 up to 15 years without perceivable symptoms, AE has a fatal outcome in up to 90% of cases when left untreated [3-5]. AE is characterized by a slow but progressive tumor-like growth of metacestodes (larval stage) mainly in the liver, with a tendency to spread to various organs like spleen, brain, heart and other tissues such as bile ducts and blood vessels [6-8]. Treatment by radical surgical resection is limited by the diffuse infiltrations of AE lesions in liver and other tissues in advanced cases [9, 10]. If lesions cannot be completely removed by surgery, a lifelong medication is required, usually using benzimidazoles, which can cause adverse side effects. For example, several cases with hepatotoxic effects due to treatment with the benzimidazole albendazole (ABZ) were reported with various outcomes [11-14]. An inadequate adherence to chemotherapy, due to adverse side effects, can explain the relapsing spread of AE and a worsening general condition of patients with severe *E. multilocularis* infiltrations [15, 16]. Considering these circumstances, the rising numbers of reported cases of AE especially in Europe and the lack of a curative drug treatment, emphasizes the necessity to further investigate the mechanisms underlying this threat and search for improved therapeutic options [17-22].

Several bacteria and viruses have been described to modulate endoplasmic reticulum (ER) stress (ERS) and unfolded protein response (UPR), either by bacterial virulence factors such as toxins (e.g. cholera toxin, pore-forming toxins) or by the increased demand of newly synthesized proteins for the production of virions [23-28]. Activation of the UPR via an induction of glucose-regulated protein 78 (GRP78) has previously been shown in cells infected with *Human immunodeficiency virus* (HIV) [27, 29], *Dengue virus* (DENV) [30], *West Nile virus* (WNV) [31] or *Human cytomegalovirus* (HCMV) [32]. Moreover, facilitated replication of viruses and immune evasion represent key features following UPR activation by *Mouse hepatitis virus* (MHV) [33] and *Herpes simplex virus 1* (HSV-1) [34]. On the other hand, an ERS-induced upregulation of UPR-related genes was linked to an enhanced production of pro-inflammatory cytokines in B-cells and stellate cells [35, 36]. A modulation of the UPR pathway was reported not only during viral but also bacterial infections. *Legionella pneumophila* infection led to an inhibition of X-box binding protein 1 (XBP1) splicing in mammalian host cells, thereby suppressing the host UPR pathway [37]. *Mycobacterium tuberculosis* was found to induce ERS, indicated by increased CCAAT/enhancer-binding protein homologous protein (CHOP) and GRP78 protein levels in infected macrophages, leading to host cell apoptosis.

Decreased levels of phosphorylated eukaryotic initiation factor 2α (eIF2α) in infected cells were associated with enhanced bacterial survival [38].

However, to date the knowledge of pathogen-induced ERS and UPR activation is incomplete and mainly limited to bacterial and viral infections. In this regard, a modulation of the host's UPR with an upregulation of CHOP was observed in *Toxoplasma gondii* infected cells, leading to apoptosis of host cells [39]. Another study in a mouse model provided evidence that *Plasmodium berghei* exploits the host's UPR machinery for its survival [40]. However, little is known about the involvement of ERS and UPR activation in *E. multilocularis* infection.

The present study addressed a possible role of the modulation of UPR- and ERS-related proteins in host cells in response to AE and investigated the effect of these pathways using *E. multilocularis* infected mice as a model. A better understanding of a contribution of proteins of the UPR and ERS pathways in the context of infectious diseases is of interest regarding the development of improved therapeutic strategies to cope with parasitic infections [41-43].

Additionally, this work investigated whether microRNAs (miRs), small non-coding single stranded RNAs (17-24 nucleotides) that regulate the post-transcriptional levels of mRNAs by inhibiting their translation to proteins, may be altered upon *E. multilocularis* infection. Several studies revealed a functional interaction between UPR/ERS signaling and the expression of miRs [44-46]. Silencing of miRs was found to be involved in ERS signaling and miRs act as effectors and modulators of the UPR and ERS pathways [47]. The miRs, isolated from human specimen, including urine, saliva, serum and tissues, are considered as biomarkers of several immune pathologies such as cancer, autoimmune diseases and viral or bacterial infections [48-54]. In this regard, recent investigations provided evidence for a role of some miRs in the regulation of UPR signaling, with miR-181a-5p and miR-199a-5p shown to suppress the UPR master regulator GRP78 [47, 55, 56]. On the other side, UPR pathways also can affect the expression of some miRs, as shown by inositol-requiring enzyme 1α (IRE1α) that cleaves the precursors of anti-apoptotic miR-17-5p, miR-34a-5p, miR-96-5p and mir-125b-5p, which in turn negatively regulate the expression of caspase 2 and thioredoxin-interacting protein [57, 58]. In addition, the activation of protein kinase R (PKR)-like ER kinase (PERK) induces the expression of miR-30c-2-3p, which downregulates XBP1, representing a possible negative crosstalk between PERK and IRE1α [58].

Boubaker *et al.* recently described a murine miR signature in response to early stage *E. multilocularis* egg infection where the expression of seven miRs (miR-148a-3p, miR-143-3p, miR-101b-3p, miR-340-5p, miR-22-3p, miR-152-3p and miR-30a-5p) was decreased in AE-infected compared to mock-infected mice. In contrast, *E. multilocularis* infected mice exhibited

significantly higher levels of miR-21a-5p, miR-28a-5p, miR-122-5p and miR-1839-5p compared to the mock-infected controls [59]. The miRs mentioned above were therefore also analyzed in the present study.

Materials and Methods

Chemicals and reagents

Polyvinylidene difluoride (PVDF) membranes (Cat# IPVH00010, pore size: 0.45 µm), Immobilon Western Chemiluminescence horseradish-peroxidase (HRP) substrate kit, radioimmunoprecipitation assay (RIPA) buffer, β-mercaptoethanol, HRP-conjugated goat anti-mouse secondary antibody (Cat# A0168, RRID:AB_257867), rabbit polyclonal anti-hexose-6-phosphate dehydrogenase (H6PD) antibody (Cat# HPA004824, RRID:AB_1079037), protease inhibitor cocktail, dNTPs, KAPA SYBR® FAST kit and qPCR kit were purchased from Merck (Darmstadt, Germany). RNeasy Mini kit and QIAcube were obtained from Qiagen (Venlo, Netherlands), GoScript reverse transcriptase (Cat# A5003) from Promega (Fitchburg, WI, USA), rabbit monoclonal anti-lamin B1 antibody (Cat# ab133741, RRID:AB_2616597) from Abcam (Cambridge, UK) and mouse monoclonal anti-GRP78 antibody (Cat# 610978, RRID:AB_398291) from BD Bioscience (Franklin Lakes, NJ, USA). HRP-conjugated goat anti-rabbit secondary antibody (Cat# 7074, RRID:AB_2099233), mouse monoclonal anti-CHOP antibody (Cat# 2895, RRID:AB_2089254), rabbit polyclonal anti-calreticulin (CRT) antibody (Cat# 2891, RRID:AB_2275208), rabbit polyclonal anti-eIF2α antibody (Cat# 9722, RRID:AB_2230924), rabbit monoclonal anti-ATF4 antibody (Cat# 11815, RRID:AB_2616025) and rabbit monoclonal anti-ATF6 antibody (Cat# 65880, RRID:AB_2799696) were purchased from Cell Signaling (Cambridge, UK). Mouse monoclonal anti-PERK antibody (Cat# sc-377400, RRID:AB_2762850), anti-IRE1α antibody (Cat# sc-390960, RRID: N/A) and anti-ERp72 antibody (Cat# sc-390530, RRID: N/A) were obtained from Santa Cruz Biotechnology (Dallas, TX, USA). Pierce® bicinchoninic acid protein assay kit, Nanodrop™ One C (Cat# 13-400-519) and Trizol® total RNA isolation reagent were purchased from Thermo Fisher Scientific (Waltham, MA, USA). Precellys-24 tissue homogenizer was purchased from Bertin Instruments (Montigny-le-Bretonneux, France). Primers for real-time quantitative polymerase chain reaction (RT-qPCR) were obtained from Microsynth (Balgach, Switzerland). TaqMan microRNA Assays, snoRNA234, TaqMan microRNA reverse transcription kit (Cat# 4366596), TaqMan fast advanced master mix (Cat# 4444556), TaqMan probes (Cat# 4427975, Assay IDs 000468, 000389, 000398, 000470, 121135_mat, 000416, and 001234) and ViiA 7 real-time PCR system (Cat# 4453545) were

purchased from Applied Biosystems (Foster City, CA, USA). Rabbit polyclonal anti-calnexin (CNX) antibody (Cat# SAB4503258, RRID:AB_10746486) and all other reagents were purchased from Sigma-Aldrich (St. Louis, MO, USA).

Ethics Statement

The animal studies were performed in compliance with the recommendations of the Swiss Guidelines for the Care and Use of Laboratory Animals. The protocol used for this work was approved by the governmental Commission for Animal Experimentation of the Canton of Bern (approval no. BE112/17).

Animal experimentation and sampling

Animal experimentation, liver tissue extraction and corresponding liver tissue samples were previously described by Wang *et al.* [60]. Briefly, female 8-week-old wild type C57BL/6 mice were randomly distributed into 4 groups with 6 animals per group: 1) mock-infected (corn oil treated) control mice (referred to as "CTRL"); 2) *E. multilocularis* infected, vehicle treated mice (referred to as "AE"); 3) *E. multilocularis* infected, ABZ-treated mice (referred to as "AE-ABZ"); and 4) mock-infected, ABZ-treated mice (referred to as "ABZ") (S1 Fig). All animals were housed under standard conditions in a conventional daylight/night cycle room with access to feed and water *ad libitum* and in accordance with the Federation of European Laboratory Animal Science Association (FELASA) guidelines. During the experimental period animals were examined weekly for subjective presence of health status and changes in weight. At the end of the experiment the mice were euthanized by CO_2 and liver tissue was resected followed by immediate freezing in liquid nitrogen and storage at -80°C until use.

Parasite preparation and secondary infection of mice by intraperitoneal administration

Infection with *E. multilocularis* by intraperitoneal injection was conducted as previously described [61]. Briefly, *E. multilocularis* (isolate H95) was extracted and maintained by serial passages in C57BL/6-mice. Aseptic removal of infectious material from the abdominal cavity of infected animals was used for continuation of AE in mice. Collected tissue was grinded through a sterile 50 μm sieve, roughly 100 vesicular cysts were suspended in 100 μL sterile PBS and administrated *via* intraperitoneal injection to group 2 ("AE") and 3 ("AE-ABZ"). Mice of the mock-infected groups 1 ("CTRL") and 4 ("ABZ") received 100 μL of sterile PBS.

Treatment

Treatment started 6 weeks after initial infection (S1 Fig). 100 µL corn oil were orally administrated to groups 1 ("CTRL") and 2 ("AE") five times per week. Group 3 ("AE-ABZ") and 4 ("ABZ") received 100 µL corn oil containing ABZ (200 mg/kg body weight) orally five times per week. The treatment was terminated after 8 weeks and mice were euthanized.

Analysis of protein expression by western blot

The procedures for liver sample preparation and western blot analysis have been previously described [62]. Briefly, liver samples (approximately 7 mg) were homogenized (30s, 6500 rpm, at 4°C, using a Precellys-24 tissue homogenizer) in 450 µL RIPA buffer (50 mM Tris-HCl, pH 8.0, with 150 mM NaCl, 1.0% NP-40, 0.5% sodium deoxycholate and 0.1% sodium dodecyl sulfate) containing protease inhibitor cocktail and centrifuged (4 min, 16,000 × g, 4°C). Protein concentration was measured by a standard bicinchoninic acid assay (Pierce® BCA Protein Assay Kit). Samples were boiled (5 min at 95°C) in Laemmli solubilization buffer (60 mM Tris-HCl, 10% glycerol, 0.01% bromophenol blue, 2% sodium dodecyl sulfate, pH 6.8, 5% β-mercaptoethanol). The protein extract (20 µg) was separated by 10-14% SDS-PAGE and blotted on PVDF membranes. The membranes were blocked (1 h, room temperature) in TBST-BSA, (20 mM Tris buffered saline with 0.1% Tween-20, 1% bovine serum albumin). All primary and secondary antibody dilutions and incubations were performed in TBST-BSA. For the detection of primary antibodies raised in rabbit, secondary HRP-conjugated goat anti-rabbit antibody was used. Primary antibodies raised in mouse were detected by HRP-conjugated goat anti-mouse antibody. Primary antibodies were incubated at 4°C over-night. Secondary antibodies were applied at room temperature for 1 h. Protein content was visualized by Immobilon Western Chemiluminescence HRP substrate. Protein bands were quantified by densitometry normalized to Lamin B1 protein levels using ImageJ software (version 1.53n). The applications of primary and secondary antibodies can be found in S1 Table.

Quantification of mRNA by RT-qPCR

Methods for preparation of liver samples, RNA isolation and RT-qPCR analysis were performed as described [60]. Briefly, total RNA was isolated from liver tissue (approximately 8 mg) by homogenization (30 s, 6500 rpm, 4°C; Precellys-24 tissue homogenizer) in 350 µL RLT buffer (RNeasy Mini Kit) supplied with 40 mM dithiothreitol, followed by centrifugation (3 min, 16,000 × g). The supernatant was further processed according to the manufacturer's protocol for RNA isolation from animal tissues and cells using QIAcube. RNA quality and

concentration was analyzed using Nanodrop™ One C. 1000 ng of RNA was transcribed into cDNA using GoScript Reverse Transcriptase. KAPA SYBR® FAST Kit was used for RT-qPCR (4 ng of cDNA per reaction in triplicates, 40 cycles) analysis, and reactions were performed using a Rotor Gene Real-Time Cycler (Corbett Research, Sydney, New South Wales, Australia). Data was normalized to the expression levels of the endogenous control gene β-actin. Comparison of gene expression was performed using the 2-ΔCT-method using β-actin as housekeeping gene [63]. Primers used for RT-qPCR are listed in S2 Table.

Extraction and quantification of miRNA by qPCR

Total RNA was extracted from liver tissues using Trizol® total RNA isolation reagent and RNA concentration quantified using Nanodrop™ One C. TaqMan microRNA assays were used to quantify mature miR expression. SnoRNA234 was used as endogenous control of miR expression. Thus, miR-specific reverse transcription was performed for each miR using 10 ng of purified total RNA, 100 mM dNTPs, 50 U multiple reverse transcriptase, 20 U RNase inhibitor, and 50 nM of miR-specific reverse transcription primer samples using the TaqMan MicroRNA Reverse Transcription kit. Reactions with a volume of 15 µL were incubated for 30 min at 16°C, 30 min at 42°C, and 5 min at 85°C to inactivate the reverse transcriptase. RT-qPCR (5 µL of reverse transcription product, 10 µL TaqMan Fast Advanced Master Mix and 1 µL TaqMan microRNA Assay Mix containing PCR primers and TaqMan probes) were run in triplicates at 95°C for 10 min followed by 40 cycles at 95°C for 15 s and 60°C for 1 min. Quantitative miR expression data were acquired and analyzed using the ViiA 7 real-time PCR system (Applied Biosystems, Cat# 4453545).

Statistical analyses

Data are presented as mean ± SD. The significance of the differences between the examined animals were determined by Kruskal-Wallis test or one-way ANOVA, whereby the specific test is indicated in the Figure legend. No outliers were excluded. *P≤0.05; **P≤0.01; ***P≤0.001 significantly different as indicated. GaphPad Prism software (version 8.0.2, GraphPad, La Jolla, CA, USA) was used for statistical analysis.

Results

Effects of AE on the expression of proteins related to UPR and ERS pathways

As the present knowledge on the modulation of UPR and ERS pathways during parasitic infections is limited, this study examined the expression of key proteins related to these

pathways in liver tissues of mice infected with *E. multilocularis*. In the applied model of secondary *E. multilocularis* infection, differential effects on the expression of proteins of the different UPR and ERS branches were observed. Among the PERK pathway, ATF4 protein levels were significantly decreased in liver tissue of AE mice compared to mock-infected controls (Table 1, Fig 1). The expression of PERK and its target protein eIF2α were not affected by *E. multilocularis* infection. However, the most pronounced effects were observed for ERS related proteins of the ATF6 branch of the UPR (Table 1, Fig 2). The levels of all four proteins analyzed were elevated, whereby the luminal chaperone and protein disulfide isomerase ERP72 and the ERS marker CHOP were 2.0-fold and 4.5-fold increased and ATF6 and GRP78 tended to be elevated with 2.2-fold and 2.7-fold higher levels, respectively. IRE1α protein expression was decreased by about 3-fold in *E. multilocularis* infected compared to control mouse liver tissues (Table 1, Fig 3), whilst its target the spliced form of XBP1 showed a trend to lower levels in liver tissues of infected mice (S2 Fig). However, XBP1 protein expression could not be assessed as no specific antibody could be identified.

		Group			
Classification Pathway	**Relative protein expression** (normalized to CTRL)	**CTRL** (n=6)	**AE** (n=6)	**AE-ABZ** (n=6)	**ABZ** (n=6)
PERK branch	PERK	1.0	1.1 (±0.8)	1.1 (±0.5)	2.8 (±2.6)
	eIF2α	1.0	1.5 (±0.5)	1.6 (±0.4)	1.1 (±0.4)
	ATF4	1.0	0.3 (±0.1)*,§	0.8 (±0.2)	1.0 (±0.4)
ATF6 branch	ATF6	1.0	2.2 (±1.0)$^{\#}$	0.6 (±0.2)	1.2 (±0.5)
	CHOP	1.0	4.5 (±2.0)*,§	3.0 (±1.4)§	1.0 (±0.3)
	GRP78	1.0	2.7 (±1.5)§	1.3 (±1.1)	1.0 (±0.3)
	ERP72	1.0	2.0 (±0.6)*,§	1.3 (±0.6)	0.9 (±0.4)
IRE1 branch	IRE1α	1.0	0.3 (±0.2)*,§	0.8 (±0.4)	1.3 (±0.7)
ER chaperones	Calnexin (CNX)	1.0	0.9 (±0.2)	1.2 (±0.6)	1.2 (±0.5)
	Calreticulin (CRT)	1.0	1.6 (±0.5)$^{\#,\S}$	0.9 (±0.3)	0.8 (±0.3)
NADPH generation	H6PD	1.0	2.6 (±1.8)*	1.4 (±0.6)	1.4 (±0.6)

Table 1. Expression of proteins involved in UPR and ERS pathways. Protein levels in liver tissue samples were analyzed by western blot and densitometry (animals per group n=6). Numbers represent protein expression levels normalized to those of the control (CTRL) group (mean ± SD). Significantly decreased protein levels are highlighted in red and increased protein levels in blue. Symbols indicate significant differences ($p \leq 0.05$) between groups: *, compared to CTRL; §, compared to ABZ; #, compared to AE-ABZ. No outliers were excluded. Non-parametric, Kruskal-Wallis test.

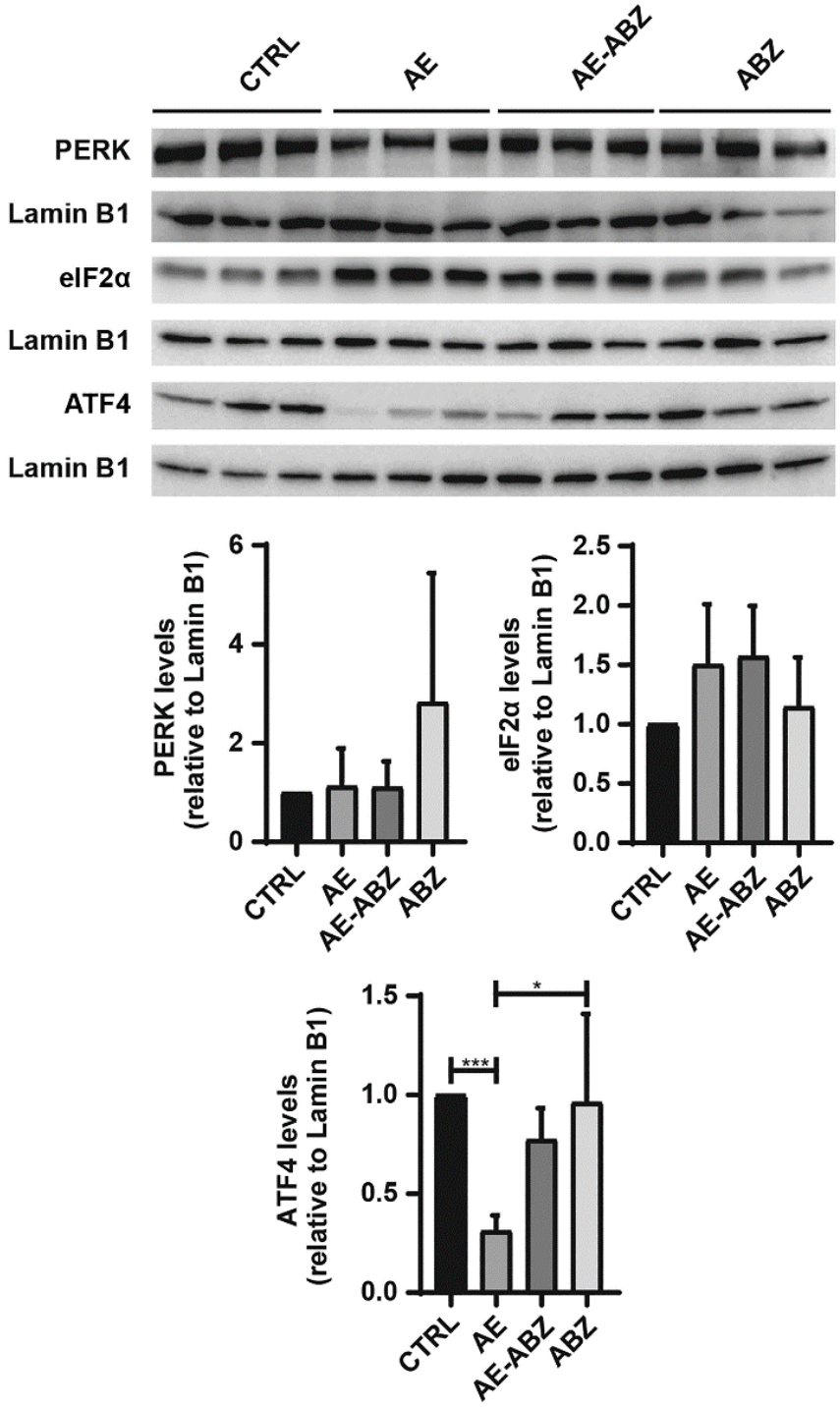

Fig 1. *E. multilocularis* infection decreases ATF4 protein levels. Western blot and semi-quantitative analysis by densitometry of protein levels of PERK, eIF2α and ATF4 in mock-infected control mice (CTRL), *E. multilocularis* infected mice (AE), infected mice treated with ABZ (AE-ABZ) or uninfected mice treated with ABZ (ABZ). One representative blot (of two) containing samples from three different mice is shown in the top panel. Densitometry results represent data from the two blots on samples from six mice (mean ± SD), normalized to lamin B1 control and with CTRL set as 1. No outliers were excluded. The non-parametric Kruskal-Wallis test was used to assess significance. *P≤0.05; ***p≤ 0.001.

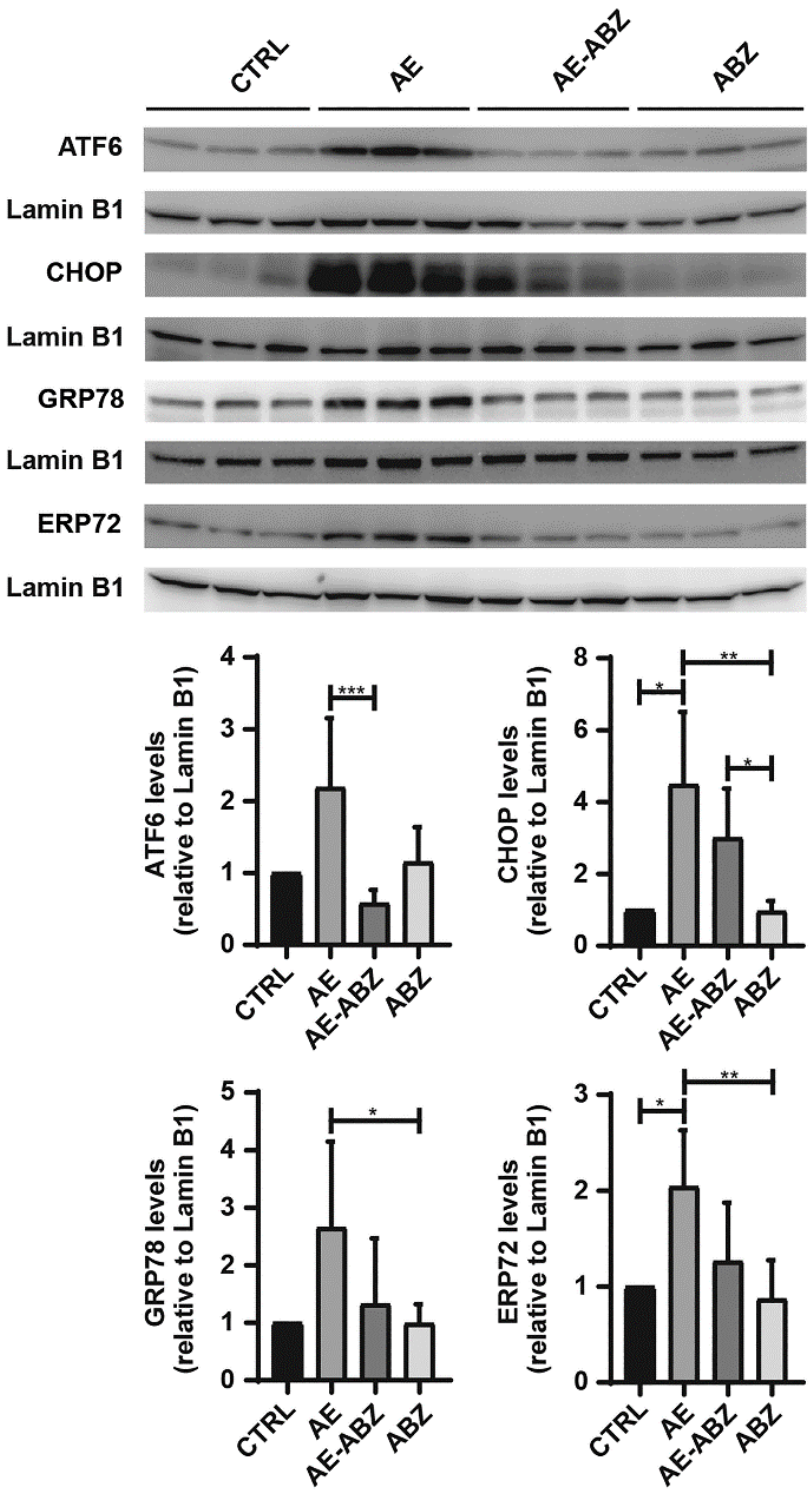

Fig 2. Induction of the ATF6 branch of the UPR by *E. multilocularis* infection. Western blot and semi-quantitative analysis by densitometry of the protein levels of ATF6, CHOP, GRP78 and ERP72 in mock-infected control mice (CTRL), *E. multilocularis* infected mice (AE), infected mice treated with ABZ (AE-ABZ) or uninfected mice treated with ABZ (ABZ). One representative blot (of two) containing samples from three different mice is shown in the top panel. Densitometry results represent data from the two blots on samples from six mice (mean ± SD), normalized to lamin B1 control and with CTRL set as 1. No outliers were excluded. The non-parametric Kruskal-Wallis test was used to assess significance. *P≤0.05; **p≤0.01; ***p≤ 0.001.

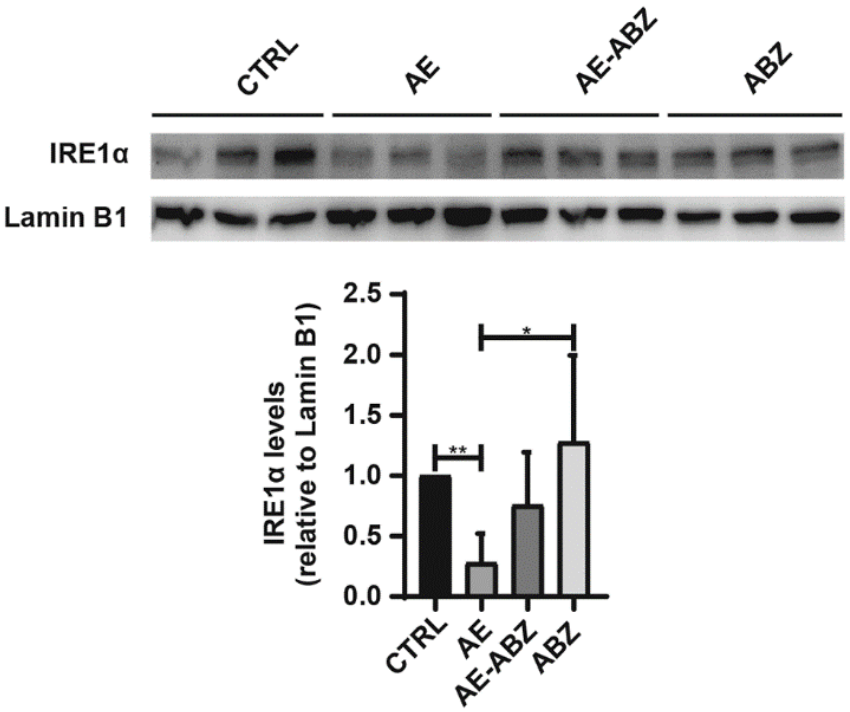

Fig 3. Decreased IRE1α protein expression upon *E. multilocularis* infection. Western blot and semi-quantitative analysis by densitometry of IRE1α protein levels in mock-infected control mice (CTRL), *E. multilocularis* infected mice (AE), infected mice treated with ABZ (AE-ABZ) or uninfected mice treated with ABZ (ABZ). One representative blot (of two) containing samples from three different mice is shown in the top panel. Densitometry results represent data from the two blots on samples from six mice (mean ± SD), normalized to lamin B1 control and with CTRL set as 1. No outliers were excluded. The non-parametric Kruskal-Wallis test was used to assess significance. *P≤0.05; **p≤0.01.

Additional proteins with a role in ER-redox regulation and ERS include the ER resident lectin chaperones CNX and CRT. Whilst CNX protein levels were unaffected by *E. multilocularis* infection, CRT protein expression was significantly increased in AE mice compared to controls (Table 1, Fig 4). Additionally, the expression levels of the luminal NADPH-generating enzyme H6PD were determined, revealing a 2.6-fold higher expression in AE compared to control mice (Table 1, Fig 5).

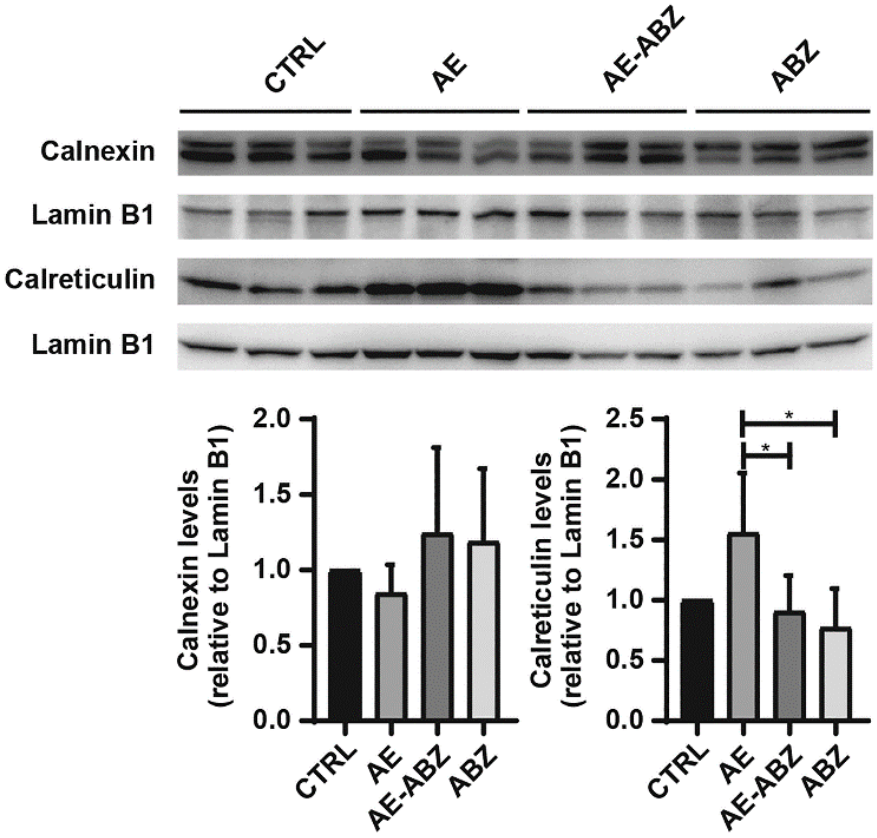

Fig 4. The expression of the luminal chaperone CRT is increased upon *E. multilocularis* infection and reversed by ABZ treatment. Western blot and semi-quantitative analysis by densitometry of CNX and CRT protein levels in mock-infected control mice (CTRL), *E. multilocularis* infected mice (AE), infected mice treated with ABZ (AE-ABZ) or uninfected mice treated with ABZ (ABZ). One representative blot (of two) containing samples from three different mice is shown in the top panel. Densitometry results represent data from the two blots on samples from six mice (mean ± SD), normalized to lamin B1 control and with CTRL set as 1. No outliers were excluded. The non-parametric Kruskal-Wallis test was used to assess significance. *P≤0.05.

Treatment with ABZ reverses the effects of AE on proteins involved in UPR and ERS

Treatment of AE mice with ABZ (AE-ABZ group) resulted in a reversal of the *E. multilocularis* induced alterations of UPR and ERS related protein expression (Table 1). Also the effects on the ER chaperones CNX and the NADPH-generating H6PD were reversed by ABZ treatment. An exception was CHOP that was still upregulated in ABZ treated infected mice. Importantly, ABZ did not cause any significant alterations in the expression of the proteins analyzed in uninfected control mice (Table 1, Figs 1-5). Protein levels of PERK show a trend to be increased in ABZ treated, uninfected animals (Fig 1); however, this did not reach significance due to high variance in the detected signals.

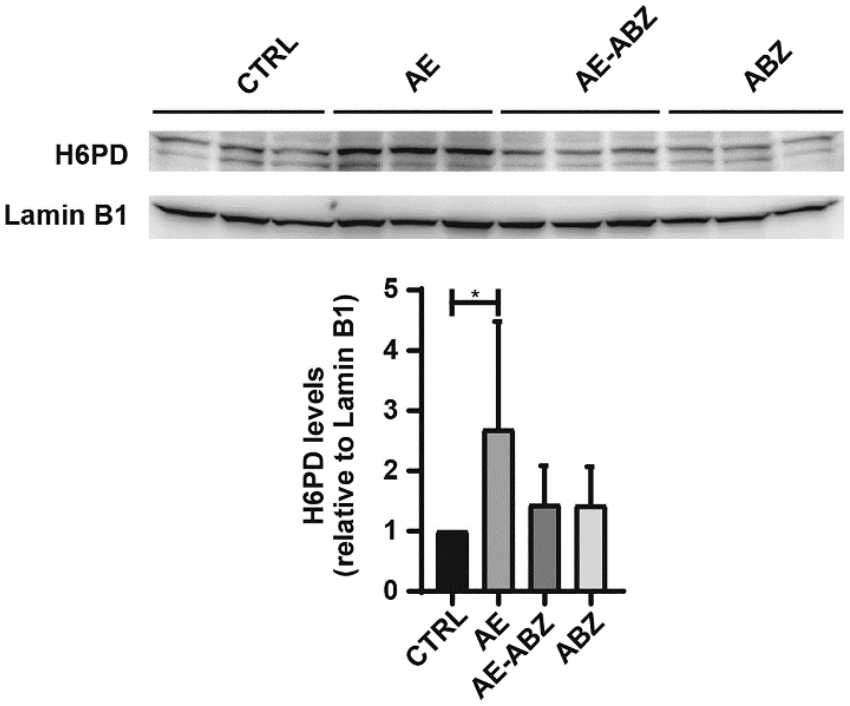

Fig 5. Increased H6PD protein expression upon *E. multilocularis* infection. Western blot and semi-quantitative analysis by densitometry of protein levels of H6PD in mock-infected control mice (CTRL), *E. multilocularis* infected mice (AE), infected mice treated with ABZ (AE-ABZ) or uninfected mice treated with ABZ (ABZ). One representative blot (of two) containing samples from three different mice is shown in the top panel. Densitometry results represent data from the two blots on samples from six mice (mean ± SD), normalized to lamin B1 control and with CTRL set as 1. No outliers were excluded. The non-parametric Kruskal-Wallis test was used to assess significance. *P≤0.05.

Increased miR-146a-5p and miR-1839-5p expression in secondary *E. multilocularis* infection and reversal by ABZ treatment

Boubaker *et al.* [59], using an early stage mouse model of *E. multilocularis* infection, identified several miRs with altered expression in liver tissues from infected mice. In the present study, the levels of the miRs exhibiting a target site in the 3'UTR of genes involved in UPR and ERS pathways were determined. The analysis of the seven mouse miRs miR-148a-3p, miR-15a-5p, miR-22, miR-146a-5p, miR-1839-5p, miR-30a-5p and miR-30a-3p revealed significantly higher levels (2.1-fold and 3.2-fold, respectively) of miR-1839-5p and miR-146a-5p in liver tissue samples of *E. multilocularis* infected mice (AE) compared to control animals (CTRL). The other miRs remained unchanged (S3 Fig). Interestingly, ABZ treatment of AE mice decreased miR-1839-5p (2.8 fold) and miR-146a-5p (5.8 fold) compared to the levels found in CTRL animals or even lower, and ABZ alone tended to decrease miR-1839-5p and miR-146a-5p expression levels (Fig 6).

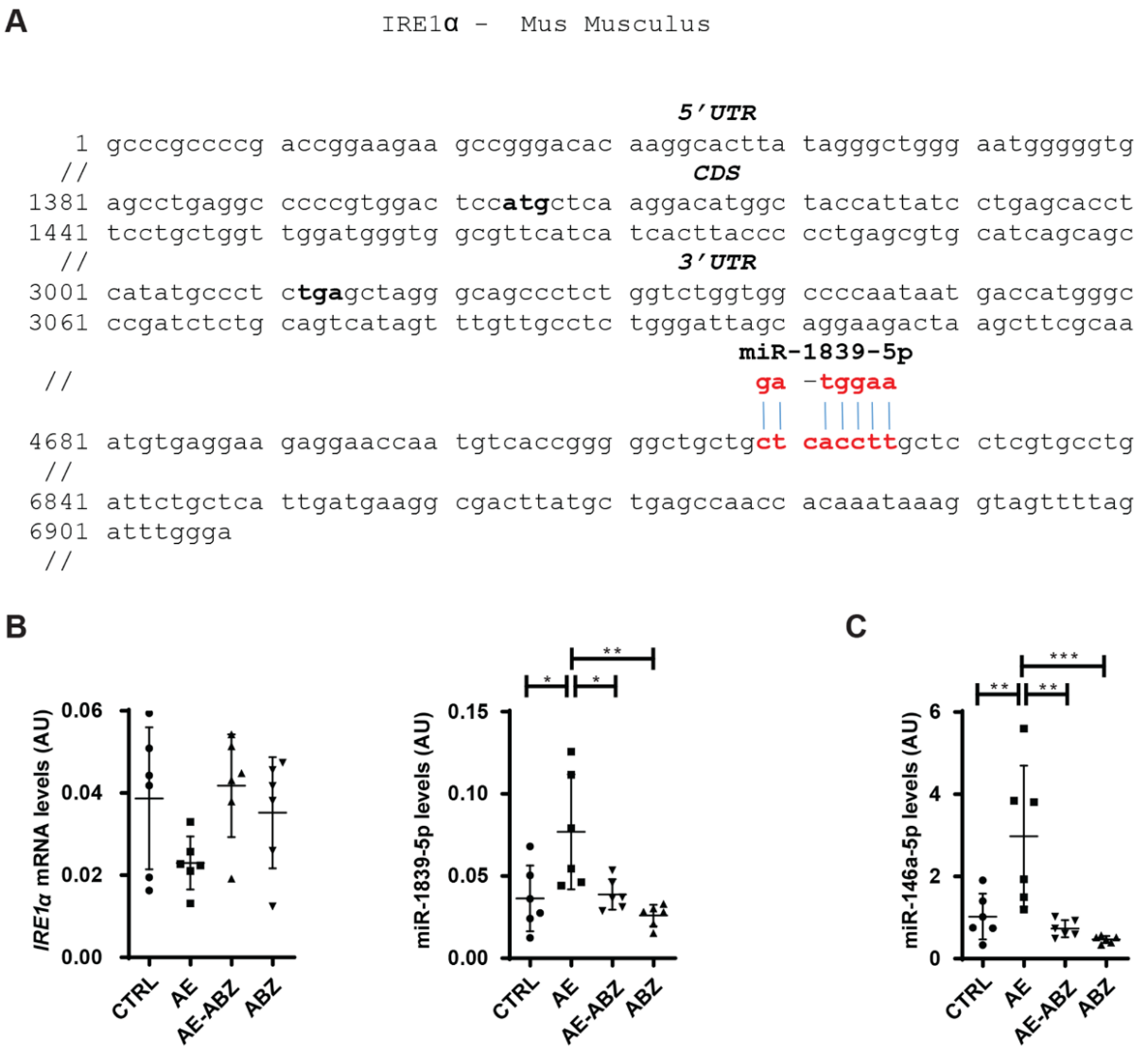

Figure 6. Altered expression of IRE1α related miRs upon *E. multilocularis* infection and reversal by ABZ treatment. A) Nucleotide sequence containing the murine IRE1α mRNA 3'-UTR. The start and stop codon of the IRE1α CDS are indicated in bold and the miR-1839-5p binding site is highlighted by red and bold letters. B) IRE1α mRNA levels normalized to the β-actin housekeeping gene and relative to the levels obtained in control mice, and miR-1839-5p levels normalized to the Sno234 housekeeping gene and relative to uninfected controls. C) miR-146-5p levels normalized to Sno234 and relative to uninfected controls. B, C) mock-infected control mice (CTRL), *E. multilocularis* infected mice (AE), infected mice treated with ABZ (AE-ABZ) or uninfected mice treated with ABZ (ABZ). Results represent mean ± SD. No outliers were excluded. One-way ANOVA test was used to assess significance. *P≤0.05; **p≤0.01; ***p≤ 0.001.

Discussion

Recent studies on viral, bacterial or intracellular parasitic infections emphasize the important roles of the UPR and ERS pathways in pathogen induced diseases [23-25, 64, 65]. Activation of the UPR, a specific form of ERS triggered by an accumulation of unfolded or misfolded

proteins within the ER, can be mediated by three branches, represented by the ER transmembrane stress sensor proteins ATF6, PERK and IRE1α [66-74] (Fig 7). In non-stressed cells, these proteins remain in an inactive state, bound to the luminal chaperone GRP78. Upon activation, GRP78 is released to support luminal protein folding, followed by the activation of ATF6, PERK and IRE1α and their downstream targets such as eIF2α, ATF4, XBP1 and CHOP in order to mediate the stress response [75-77].

The results of the present study revealed a pronounced induction of ATF6 in livers of mice infected with *E. multilocularis*. In contrast, the PERK and IRE1α branches were not activated but rather down regulated. Unfortunately, the levels of phosphorylated PERK, eIF2α and IRE1α could not be assessed due to the failure to identify specific antibodies. The decreased levels of ATF4 in livers of infected animals suggests that the observed upregulation of CHOP is caused by enhanced ATF6 activity. CHOP, well-known as a mediator of apoptosis, was previously found to play an important role in the efficient expansion of the intracellular fungus *Histoplasma capsulatum* [78]. Following infection an increase in CHOP levels led to augmented apoptosis of macrophages, thus suppressing the host's defense and contributing to the virulence of this particular pathogen. Another study, using intestinal epithelial cell lines, showed a direct effect of heat-labile enterotoxins of *Escherichia coli* on the induction upregulation of CHOP, which led to an accelerated apoptosis of the host cells [79]. Thus, the upregulation of CHOP in murine hepatocytes during *E. multilocularis* infection might similarly promote parasitic growth.

In contrast to the pro-apoptotic UPR mediator CHOP, the protein levels of the PERK target ATF4 were significantly decreased in livers of *E. multilocularis* infected compared to mock-infected mice. This is different from a previous study on human cutaneous leishmaniasis where both CHOP and ATF4 were found to be upregulated [80]. Decreased levels of ATF4 were recently described as a mechanism of acquired resistance to cope with a limited availability of amino acids in cancer cells [81]. Unrestricted tumor growth requires a high demand of nutrients and has been associated with a depletion of essential amino acids in the tumor tissue. Similar metabolic perturbations and adaptive responses may occur in patients with hepatic AE. A recent study summarizing analyses of serum samples from *E. multilocularis* infected and healthy adults (group size: n=18) revealed decreased levels of branched-chain amino acids such as leucine, isoleucine and valine along with lowered levels of serine and glutamine in samples from infected patients [82]. In contrast, the aromatic amino acids tyrosine and phenylalanine were increased, together with glutamate. Thus, the observed decrease in ATF4 expression may be a response to adapt the amino acid availability in the situation of parasitic growth.

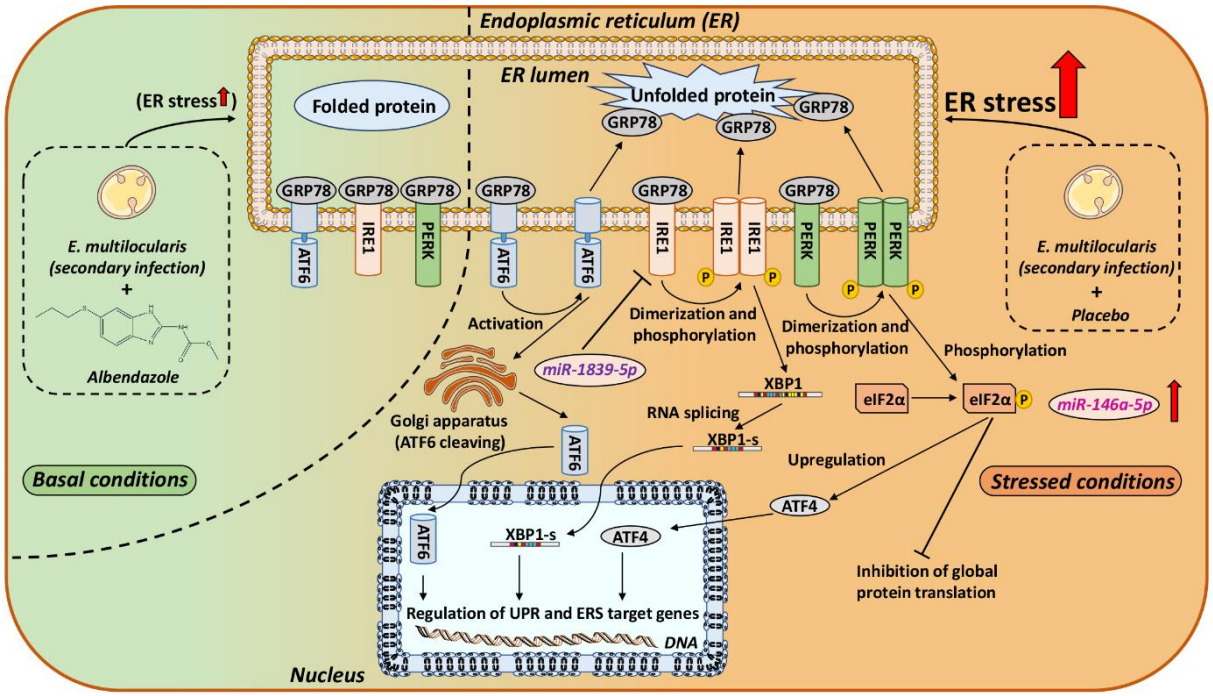

Fig 7. Schematic overview of ERS signaling pathways under basal and *E. multilocularis* infection stressed conditions. The ER chaperone GRP78 binds to unfolded luminal proteins and dissociates from the three major ERS sensors: ATF6, IRE1α and PERK. Loss of GRP78 binding leads to the translocation of ATF6 to the golgi apparatus, where it is cleaved by proteases. The cleaved form of ATF6 translocates into the nucleus to act as a transcription factor for ER chaperons (*e.g.* ERP72) and ERS related genes. ERS promotes IRE1α dimerization and autophosphorylation, which activates the endoribonuclease activity resulting in the splicing and thereby activation of XBP. XBP1-s promotes the expression of ERAD related genes and chaperones (*e.g.* GRP78). Activation of PERK is initiated by dimerization and self-phosphorylation. Activated PERK phosphorylates eIF2α, leading to eIF2α-mediated inhibition of global protein translation in order to decrease the luminal protein load. Besides, phosphorylated eIF2α increases the transcription of ATF4, which in turn upregulates expression of genes related to cell homeostasis restoration. If prolonged ERS occurs and pro-adaptive UPR fails, ATF4 induces genes (including CHOP) leading to apoptosis. During ERS, increased levels of miR-1839-5p are proposed to control IRE1α gene expression and therefore affect the cellular ERS response.

Similar to ARF4 also IRE1α protein expression levels were decreased in liver tissues of AE infected mice. The reason of the decreased IRE1α expression in *E. multilocularis* infected mice and the underlying mechanism remain unclear. IRE1 enzymes are transmembrane proteins exhibiting Ser/Thr protein kinase and endoribonuclease activities and acting as major ERS sensors [83, 84]. There are two IRE1 isoforms in mammals: the ubiquitously expressed IRE1α and IRE1β which is predominantly expressed in the intestine and lung [85]. Further analysis of the liver resident IRE1α showed that the decreased protein expression in *E. multilocularis* infected mouse livers is supported by lower mRNA levels along with an increased expression

of miR-1839-5p that has a target site in the 3'UTR of IRE1α as predicted by the computer-based programs Targetscan (Whitehead Institute, Cambridge, MA, USA, RRID:SCR_010845) [86] and RNA22 (Thomas Jefferson University, Philadelphia, PA, USA, RRID:SCR_016507) [87]. Additionally, miR-146a-5p was found to be enhanced in livers of infected mice. An earlier study in primary dermal fibroblasts provided evidence for a down regulation of miR-146a-5p by IRE1-dependent cleavage in response to UPR activation. A decreased hepatic IRE1α expression and activity upon *E. multilocularis* infection might suppress the activation of pro-inflammatory cytokines such as IL-1β as well as of NF-κB. Whether this promotes the progression of AE remains to be investigated.

An extensive analysis of miRs altered in livers of mice after primary infection with *E. multilocularis* by Boubaker *et al.* identified, besides miR-1839-5p and miR-146a-5p, several other miRs that were dysregulated, *i.e.* miR-148-3p, miR-15a-5p, miR-22, miR-30a-5p and miR-30a-3p [59]. The fact that miR-1839-5p and miR-146a-5p were increased in primary as well as in the secondary form of infection suggests these two miRs as potential biomarkers of AE. In this regard, Luis *et al.* reported an association of several circulating miRs, including miR-146a-5p, with ERS and organ damage in a model of trauma hemorrhagic shock [88]. Further, Wilczynski *et al.* reported increased miR-146a expression levels in tumor tissues of patients with ovarian cancer [89]. The advanced AE resembles a tumorigenic situation with alterations in the microenvironment and immune responses. Thus, follow-on research should address whether miR-146a-5p and miR-1839-5p can serve as serum biomarkers of AE.

Beside the UPR, the ER-associated degradation (ERAD) is an important quality control machinery to cope with ER stressors. ERAD plays a crucial role in the degradation of terminally misfolded proteins by retro-translocating them from the ER to the cytoplasm for deglycosylation and ubiquitination and subsequent proteasomal degradation [90, 91]. Prior to ERAD, misfolded proteins undergo repeated cycles of re-folding by the assistance of several ER-resident chaperones including lectins such as CRT and CNX, protein disulfide isomerase family members like ERP72 and ERP57 as well as members of the heat shock protein 70 family (e.g. GRP78) [92-95]. The elevated expression of CRT together with GRP78 and ERP72 indicates a higher demand for protein folding capacity in the ER in livers from infected mice. This was accompanied by an elevated demand for NADPH redox equivalents in the ER and/or an enhanced need for the products of the ER pentose phosphate pathway as indicated by the elevated H6PD expression. H6PD was found to promote cancer cell proliferation and the modulation of its expression affected GRP78, ATF6 and CHOP, emphasizing its role in ERS regulation [96].

Importantly, treatment with the parasitostatic benzimidazole ABZ, which was shown to decrease the weight of parasitic cysts in the livers of *E. multilocularis* infected mice, reversed the observed effects on UPR and ERS pathways and on associated ERAD and ER redox genes. In the absence of infection, ABZ did not affect any of the investigated ER related targets, underlining its favorable safety profile regarding ERS related adverse effects.

In conclusion, the present study showed that *E. multilocularis* infection leads to a modulation of the UPR, characterized by an activation of the ATF6 branch with an upregulation of CHOP along with decreased ARF4 and IRE1α protein levels and increased miR-1839-5p and miR-146a-5p that could serve as potential biomarkers of *E. multilocularis* infections. ABZ, the most commonly used drug to treat AE ameliorated the effects of *E. multilocularis* infection on ER related genes. Whether drugs targeting UPR and ERS pathways in combination with ABZ may improve the treatment of AE remains to be explored.

Acknowledgements

This study was supported by the Swiss National Science Foundation Grant number 31003A-179400 (to A.O.) and 31003A-179439 (to BLS).

Data Availability

All relevant data are within the manuscript and in its supporting information files.

Author Contributions

Conceptualization	Alex Odermatt, Michael Weingartner, Fadi Jebbawi.
Data curation	Michael Weingartner, Fadi Jebbawi, Simon Stücheli
Formal analysis	Michael Weingartner, Fadi Jebbawi
Funding acquisition	Alex Odermatt, Britta Lundström-Stadelmann
Investigation	Michael Weingartner, Fadi Jebbawi, Junhua Wang
Methodology	Michael Weingartner, Fadi Jebbawi, Junhua Wang, Britta Lundström-Stadelmann
Project administration	Michael Weingartner, Fadi Jebbawi
Resources	Alex Odermatt, Britta Lundström-Stadelmann, Bruno Gottstein, Guido Beldi
Supervision	Alex Odermatt, Britta Lundström-Stadelmann, Bruno Gottstein, Guido Beldi
***Visualization*:**	Michael Weingartner
***Writing – original draft*:**	Michael Weingartner
Writing – review & editing	All authors

Rights and permissions

References

1. Spicher M, Roethlisberger C, Lany C, Stadelmann B, Keiser J, Ortega-Mora LM, et al. In vitro and in vivo treatments of echinococcus protoscoleces and metacestodes with artemisinin and artemisinin derivatives. Antimicrob Agents Chemother. 2008;52(9):3447-50. Epub 2008/07/16. doi: 10.1128/AAC.00553-08. PubMed PMID: 18625777; PubMed Central PMCID: PMCPMC2533465.

2. Conraths FJ, Probst C, Possenti A, Boufana B, Saulle R, Torre GL, et al. Potential risk factors associated with human alveolar echinococcosis: Systematic review and meta-analysis. PLOS Neglected Tropical Diseases. 2017;11(7):e0005801. doi: 10.1371/journal.pntd.0005801.

3. Kowalczyk M, Kurpiewski W, Zieliński E, Zadrożny D, Klepacki Ł, Juśkiewicz W, et al. A rare case of the simultaneous location of Echinococcus multilocularis in the liver and the head of the pancreas: case report analysis and review of literature. BMC Infectious Diseases. 2019;19(1):661. doi: 10.1186/s12879-019-4274-y.

4. Ritler D, Rufener R, Li JV, Kämpfer U, Müller J, Bühr C, et al. In vitro metabolomic footprint of the Echinococcus multilocularis metacestode. Scientific Reports. 2019;9(1):1-13. doi: 10.1038/s41598-019-56073-y.

5. Schweiger A, Ammann RW, Candinas D, Clavien P-A, Eckert J, Gottstein B, et al. Human Alveolar Echinococcosis after Fox Population Increase, Switzerland. Emerging Infectious Diseases. 2007;13(6):878-82. doi: 10.3201/eid1306.061074.

6. Kantarci M, Bayraktutan U, Karabulut N, Aydinli B, Ogul H, Yuce I, et al. Alveolar echinococcosis: spectrum of findings at cross-sectional imaging. Radiographics. 2012;32(7):2053-70. Epub 2012/11/15. doi: 10.1148/rg.327125708. PubMed PMID: 23150858.

7. Kayacan SM, Vatansever S, Temiz S, Uslu B, Kayacan D, Akkaya V, et al. Alveolar echinococcosis localized in the liver, lung and brain. Chin Med J (Engl). 2008;121(1):90-2. Epub 2008/01/23. PubMed PMID: 18208675.

8. Niu F, Chong S, Qin M, Li S, Wei R, Zhao Y. Mechanism of Fibrosis Induced by Echinococcus spp. Diseases. 2019;7(3). doi: 10.3390/diseases7030051.

9. Bulakçı M, Kartal MG, Yılmaz S, Yılmaz E, Yılmaz R, Şahin D, et al. Multimodality imaging in diagnosis and management of alveolar echinococcosis: an update. Diagnostic and Interventional Radiology. 2016;22(3):247-56. doi: 10.5152/dir.2015.15456.

10. Gottstein B, Wang J, Boubaker G, Marinova I, Spiliotis M, Muller N, et al. Susceptibility versus resistance in alveolar echinococcosis (larval infection with Echinococcus multilocularis). Vet Parasitol. 2015;213(3-4):103-9. Epub 2015/08/12. doi: 10.1016/j.vetpar.2015.07.029. PubMed PMID: 26260407.

11. Aasen TD, Nasrollah L, Seetharam A. Acute Liver Failure Secondary to Albendazole: Defining Albendazole's Role in the Management of Echinococcal Infection: 722. American Journal of Gastroenterology. 2015;110:S316.

12. Hemphill A, Stadelmann B, Rufener R, Spiliotis M, Boubaker G, Muller J, et al. Treatment of echinococcosis: albendazole and mebendazole--what else? Parasite. 2014;21:70. Epub 2014/12/20. doi: 10.1051/parasite/2014073. PubMed PMID: 25526545; PubMed Central PMCID: PMCPMC4271654.

13. Choi GY, Yang HW, Cho SH, Kang DW, Go H, Lee WC, et al. Acute drug-induced hepatitis caused by albendazole. J Korean Med Sci. 2008;23(5):903-5. Epub 2008/10/29. doi: 10.3346/jkms.2008.23.5.903. PubMed PMID: 18955802; PubMed Central PMCID: PMCPMC2580005.

14. Marin Zuluaga JI, Marin Castro AE, Perez Cadavid JC, Restrepo Gutierrez JC. Albendazole-induced granulomatous hepatitis: a case report. J Med Case Rep. 2013;7:201. Epub 2013/07/31. doi: 10.1186/1752-1947-7-201. PubMed PMID: 23889970; PubMed Central PMCID: PMCPMC3750323.

15. Ammann RW, Hirsbrunner R, Cotting J, Steiger U, Jacquier P, Eckert J. Recurrence Rate after Discontinuation of Long-Term Mebendazole Therapy in Alveolar Echinococcosis (Preliminary-Results). American Journal of Tropical Medicine and Hygiene. 1990;43(5):506-15. doi: DOI 10.4269/ajtmh.1990.43.506. PubMed PMID: WOS:A1990EL12600009.

16. Buttenschoen K, Gruener B, Carli Buttenschoen D, Reuter S, Henne-Bruns D, Kern P. Palliative operation for the treatment of alveolar echinococcosis. Langenbecks Arch Surg. 2009;394(1):199-204. Epub 2008/06/26. doi: 10.1007/s00423-008-0367-6. PubMed PMID: 18575882.

17. Charbonnet P, Bühler L, Sagnak E, Villiger P, Morel P, Mentha G. Devenir à long terme des malades opérés et traités pour échinococcose alvéolaire. Annales de Chirurgie. 2004;129(6):337-42. doi: 10.1016/j.anchir.2004.01.017.

18. Baumann S, Shi R, Liu W, Bao H, Schmidberger J, Kratzer W, et al. Worldwide literature on epidemiology of human alveolar echinococcosis: a systematic review of research published in the twenty-first century. Infection. 2019;47(5):703-27. Epub 2019/05/31. doi: 10.1007/s15010-019-01325-2. PubMed PMID: 31147846.

19. Kuscher S, Kronberger IE, Loizides A, Plaikner M, Ninkovic M, Brunner A, et al. Exploring the limits of hepatic surgery for alveolar echinococcosis—10-years' experience in an endemic area of Austria. European Surgery. 2019;51(4):189-96. doi: 10.1007/s10353-019-0596-7.

20. Qu B, Guo L, Sheng G, Yu F, Chen G, Wang Y, et al. Management of Advanced Hepatic Alveolar Echinococcosis: Report of 42 Cases. The American Journal of Tropical Medicine and Hygiene. 2017;96(3):680-5. doi: 10.4269/ajtmh.16-0557.

21. Sréter T, Széll Z, Egyed Z, Varga I. Echinococcus multilocularis: An Emerging Pathogen in Hungary and Central Eastern Europe? Emerging Infectious Diseases. 2003;9(3):384-6. doi: 10.3201/eid0903.020320.

22. Vuitton DA, Demonmerot F, Knapp J, Richou C, Grenouillet F, Chauchet A, et al. Clinical epidemiology of human AE in Europe. Veterinary Parasitology. 2015;213(3):110-20. doi: 10.1016/j.vetpar.2015.07.036.

23. Galluzzi L, Diotallevi A, Magnani M. Endoplasmic reticulum stress and unfolded protein response in infection by intracellular parasites. Future Sci OA. 2017;3(3):FSO198. Epub 2017/09/09. doi: 10.4155/fsoa-2017-0020. PubMed PMID: 28883998; PubMed Central PMCID: PMCPMC5583660.

24. Pillich H, Loose M, Zimmer KP, Chakraborty T. Diverse roles of endoplasmic reticulum stress sensors in bacterial infection. Mol Cell Pediatr. 2016;3(1):9. Epub 2016/02/18. doi: 10.1186/s40348-016-0037-7. PubMed PMID: 26883353; PubMed Central PMCID: PMCPMC4755955.

25. Zhang L, Wang A. Virus-induced ER stress and the unfolded protein response. Front Plant Sci. 2012;3:293. Epub 2013/01/08. doi: 10.3389/fpls.2012.00293. PubMed PMID: 23293645; PubMed Central PMCID: PMCPMC3531707.

26. Neerukonda SN, Katneni UK, Bott M, Golovan SP, Parcells MS. Induction of the unfolded protein response (UPR) during Marek's disease virus (MDV) infection. Virology. 2018;522:1-12. Epub 2018/07/07. doi: 10.1016/j.virol.2018.06.016. PubMed PMID: 29979959.

27. Mehrbod P, Ande SR, Alizadeh J, Rahimizadeh S, Shariati A, Malek H, et al. The roles of apoptosis, autophagy and unfolded protein response in arbovirus, influenza virus, and HIV infections. Virulence. 2019;10(SI1):376-413. doi: 10.1080/21505594.2019.1605803.

28. Smith JA. A new paradigm: innate immune sensing of viruses via the unfolded protein response. Frontiers in Microbiology. 2014;5. doi: 10.3389/fmicb.2014.00222.

29. Borsa M, Ferreira PLC, Petry A, Ferreira LGE, Camargo MM, Bou-Habib DC, et al. HIV infection and antiretroviral therapy lead to unfolded protein response activation. Virol J. 2015;12:77. doi: 10.1186/s12985-015-0298-0.

30. Perera N, Miller JL, Zitzmann N. The role of the unfolded protein response in dengue virus pathogenesis. Cell Microbiol. 2017;19(5). doi: 10.1111/cmi.12734.

31. Ambrose RL, Mackenzie JM. West Nile Virus Differentially Modulates the Unfolded Protein Response To Facilitate Replication and Immune Evasion. J Virol. 2011;85(6):2723-32. doi: 10.1128/JVI.02050-10.

32. Isler JA, Skalet AH, Alwine JC. Human cytomegalovirus infection activates and regulates the unfolded protein response. J Virol. 2005;79(11):6890-9. Epub 2005/05/14. doi: 10.1128/JVI.79.11.6890-6899.2005. PubMed PMID: 15890928; PubMed Central PMCID: PMCPMC1112127.

33. Bechill J, Chen Z, Brewer JW, Baker SC. Coronavirus infection modulates the unfolded protein response and mediates sustained translational repression. J Virol. 2008;82(9):4492-501. Epub 2008/02/29. doi: 10.1128/JVI.00017-08. PubMed PMID: 18305036; PubMed Central PMCID: PMCPMC2293058.

34. Burnett HF, Audas TE, Liang G, Lu RR. Herpes simplex virus-1 disarms the unfolded protein response in the early stages of infection. Cell Stress Chaperones. 2012;17(4):473-83. Epub 2012/01/25. doi: 10.1007/s12192-012-0324-8. PubMed PMID: 22270612; PubMed Central PMCID: PMCPMC3368031.

35. Ii Timberlake M, Dwivedi Y. Linking unfolded protein response to inflammation and depression: potential pathologic and therapeutic implications. Mol Psychiatry. 2019;24(7):987-94. Epub 2018/09/15. doi: 10.1038/s41380-018-0241-z. PubMed PMID: 30214045; PubMed Central PMCID: PMCPMC6416085.

36. So JS. Roles of Endoplasmic Reticulum Stress in Immune Responses. Mol Cells. 2018;41(8):705-16. Epub 2018/08/07. doi: 10.14348/molcells.2018.0241. PubMed PMID: 30078231; PubMed Central PMCID: PMCPMC6125421.

37. Treacy-Abarca S, Mukherjee S. Legionella suppresses the host unfolded protein response via multiple mechanisms. Nature Communications. 2015;6. doi: 10.1038/ncomms8887.

38. Lim YJ, Choi JA, Choi HH, Cho SN, Kim HJ, Jo EK, et al. Endoplasmic reticulum stress pathway-mediated apoptosis in macrophages contributes to the survival of Mycobacterium tuberculosis. PLoS One. 2011;6(12):e28531. Epub 2011/12/24. doi: 10.1371/journal.pone.0028531. PubMed PMID: 22194844; PubMed Central PMCID: PMCPMC3237454.

39. Wang T, Zhou J, Gan X, Wang H, Ding X, Chen L, et al. Toxoplasma gondii induce apoptosis of neural stem cells via endoplasmic reticulum stress pathway. Parasitology. 2014;141(7):988-95. doi: 10.1017/S0031182014000183.

40. Inácio P, Zuzarte-Luís V, Ruivo MTG, Falkard B, Nagaraj N, Rooijers K, et al. Parasite-induced ER stress response in hepatocytes facilitates Plasmodium liver stage infection. EMBO reports. 2015;16(8):955-64. doi: 10.15252/embr.201439979.

41. Banerjee A, Czinn SJ, Reiter RJ, Blanchard TG. Crosstalk between endoplasmic reticulum stress and anti-viral activities: A novel therapeutic target for COVID-19. Life Sciences. 2020;255:117842. doi: 10.1016/j.lfs.2020.117842.

42. Crunkhorn S. ER stress modulator reverses diabetes. Nature Reviews Drug Discovery. 2015;14(8):528-. doi: 10.1038/nrd4702.

43. Schögler A, Caliaro O, Brügger M, Oliveira Esteves BI, Nita I, Gazdhar A, et al. Modulation of the unfolded protein response pathway as an antiviral approach in airway epithelial cells. Antiviral Research. 2019;162:44-50. doi: 10.1016/j.antiviral.2018.12.007.

44. Leung AK, Calabrese JM, Sharp PA. Quantitative analysis of Argonaute protein reveals microRNA-dependent localization to stress granules. Proc Natl Acad Sci U S A. 2006;103(48):18125-30. Epub 2006/11/23. doi: 10.1073/pnas.0608845103. PubMed PMID: 17116888; PubMed Central PMCID: PMCPMC1838717.

45. Leung AK, Sharp PA. Function and localization of microRNAs in mammalian cells. Cold Spring Harb Symp Quant Biol. 2006;71:29-38. Epub 2007/03/27. doi: 10.1101/sqb.2006.71.049. PubMed PMID: 17381277.

46. Geslain R, Cubells L, Bori-Sanz T, Alvarez-Medina R, Rossell D, Marti E, et al. Chimeric tRNAs as tools to induce proteome damage and identify components of stress responses. Nucleic Acids Res. 2010;38(5):e30. Epub 2009/12/17. doi: 10.1093/nar/gkp1083. PubMed PMID: 20007146; PubMed Central PMCID: PMCPMC2836549.

47. Maurel M, Chevet E. Endoplasmic reticulum stress signaling: the microRNA connection. Am J Physiol Cell Physiol. 2013;304(12):C1117-26. Epub 2013/03/22. doi: 10.1152/ajpcell.00061.2013. PubMed PMID: 23515532.

48. Zhou X, Li X, Wu M. miRNAs reshape immunity and inflammatory responses in bacterial infection. Signal Transduct Target Ther. 2018;3:14. Epub 2018/05/31. doi: 10.1038/s41392-018-0006-9. PubMed PMID: 29844933; PubMed Central PMCID: PMCPMC5968033.

49. Drury RE, O'Connor D, Pollard AJ. The Clinical Application of MicroRNAs in Infectious Disease. Front Immunol. 2017;8:1182. Epub 2017/10/11. doi: 10.3389/fimmu.2017.01182. PubMed PMID: 28993774; PubMed Central PMCID: PMCPMC5622146.

50. Tribolet L, Kerr E, Cowled C, Bean AGD, Stewart CR, Dearnley M, et al. MicroRNA Biomarkers for Infectious Diseases: From Basic Research to Biosensing. Front Microbiol. 2020;11:1197. Epub 2020/06/26. doi: 10.3389/fmicb.2020.01197. PubMed PMID: 32582115; PubMed Central PMCID: PMCPMC7286131.

51. Gallo A, Tandon M, Alevizos I, Illei GG. The majority of microRNAs detectable in serum and saliva is concentrated in exosomes. PLoS One. 2012;7(3):e30679. Epub 2012/03/20. doi: 10.1371/journal.pone.0030679. PubMed PMID: 22427800; PubMed Central PMCID: PMCPMC3302865.

52. Wu L, Zheng K, Yan C, Pan X, Liu Y, Liu J, et al. Genome-wide study of salivary microRNAs as potential noninvasive biomarkers for detection of nasopharyngeal carcinoma. BMC Cancer. 2019;19(1):843. Epub 2019/08/29. doi: 10.1186/s12885-019-6037-y. PubMed PMID: 31455274; PubMed Central PMCID: PMCPMC6712819.

53. Ishige F, Hoshino I, Iwatate Y, Chiba S, Arimitsu H, Yanagibashi H, et al. MIR1246 in body fluids as a biomarker for pancreatic cancer. Sci Rep. 2020;10(1):8723. Epub 2020/05/28. doi: 10.1038/s41598-020-65695-6. PubMed PMID: 32457495; PubMed Central PMCID: PMCPMC7250935.

54. Sisto R, Capone P, Cerini L, Sanjust F, Paci E, Pigini D, et al. Circulating microRNAs as potential biomarkers of occupational exposure to low dose organic solvents. Toxicol Rep. 2019;6:126-35. Epub 2019/01/24. doi: 10.1016/j.toxrep.2019.01.001. PubMed PMID: 30671348; PubMed Central PMCID: PMCPMC6330509.

55. Byrd AE, Brewer JW. Micro(RNA)managing endoplasmic reticulum stress. IUBMB Life. 2013;65(5):373-81. Epub 2013/04/05. doi: 10.1002/iub.1151. PubMed PMID: 23554021; PubMed Central PMCID: PMCPMC3637854.

56. Bartoszewska S, Kochan K, Madanecki P, Piotrowski A, Ochocka R, Collawn JF, et al. Regulation of the unfolded protein response by microRNAs. Cell Mol Biol Lett.

2013;18(4):555-78. Epub 2013/10/05. doi: 10.2478/s11658-013-0106-z. PubMed PMID: 24092331; PubMed Central PMCID: PMCPMC3877167.

57. Lerner AG, Upton JP, Praveen PV, Ghosh R, Nakagawa Y, Igbaria A, et al. IRE1alpha induces thioredoxin-interacting protein to activate the NLRP3 inflammasome and promote programmed cell death under irremediable ER stress. Cell Metab. 2012;16(2):250-64. Epub 2012/08/14. doi: 10.1016/j.cmet.2012.07.007. PubMed PMID: 22883233; PubMed Central PMCID: PMCPMC4014071.

58. Upton JP, Wang L, Han D, Wang ES, Huskey NE, Lim L, et al. IRE1alpha cleaves select microRNAs during ER stress to derepress translation of proapoptotic Caspase-2. Science. 2012;338(6108):818-22. Epub 2012/10/09. doi: 10.1126/science.1226191. PubMed PMID: 23042294; PubMed Central PMCID: PMCPMC3742121.

59. Boubaker G, Strempel S, Hemphill A, Muller N, Wang J, Gottstein B, et al. Regulation of hepatic microRNAs in response to early stage Echinococcus multilocularis egg infection in C57BL/6 mice. PLoS Negl Trop Dis. 2020;14(5):e0007640. Epub 2020/05/23. doi: 10.1371/journal.pntd.0007640. PubMed PMID: 32442168; PubMed Central PMCID: PMCPMC7244097 following competing interests: Sebastian Strempel is employee of Microsynth AG.

60. F J. Innate and adaptive immune responses following PD-L1 immune checkpoint blockade in treating chronic alveolar echinococcosis. N/A. 2020;N/A.

61. Wang J, Jebbawi F, Bellanger A-P, Beldi G, Millon L, Gottstein B. Immunotherapy of alveolar echinococcosis via PD-1/PD-L1 immune checkpoint blockade in mice. Parasite Immunology. 2018;40(12):e12596. doi: 10.1111/pim.12596.

62. Weingartner M, Stücheli S. The ratio of ursodeoxycholyltaurine to 7-oxolithocholyltaurine serves as a biomarker of decreased 11β-hydroxysteroid dehydrogenase 1 activity in mouse.

63. Schmittgen TD, Livak KJ. Analyzing real-time PCR data by the comparative C(T) method. Nat Protoc. 2008;3(6):1101-8. Epub 2008/06/13. doi: 10.1038/nprot.2008.73. PubMed PMID: 18546601.

64. Celli J, Tsolis RM. Bacteria, the endoplasmic reticulum and the unfolded protein response: friends or foes? Nat Rev Microbiol. 2015;13(2):71-82. Epub 2014/12/24. doi: 10.1038/nrmicro3393. PubMed PMID: 25534809; PubMed Central PMCID: PMCPMC4447104.

65. Pathinayake PS, Hsu ACY, Waters DW, Hansbro PM, Wood LG, Wark PAB. Understanding the Unfolded Protein Response in the Pathogenesis of Asthma. Frontiers in Immunology. 2018;9. doi: 10.3389/fimmu.2018.00175.

66. Abhishek K, Das S, Kumar A, Kumar A, Kumar V, Saini S, et al. Leishmania donovani induced Unfolded Protein Response delays host cell apoptosis in PERK dependent manner. PLoS Neglected Tropical Diseases. 2018;12(7). doi: 10.1371/journal.pntd.0006646.

67. Adams CJ, Kopp MC, Larburu N, Nowak PR, Ali MMU. Structure and Molecular Mechanism of ER Stress Signaling by the Unfolded Protein Response Signal Activator IRE1. Frontiers in Molecular Biosciences. 2019;6. doi: 10.3389/fmolb.2019.00011.

68. Amen OM, Sarker SD, Ghildyal R, Arya A. Endoplasmic Reticulum Stress Activates Unfolded Protein Response Signaling and Mediates Inflammation, Obesity, and Cardiac Dysfunction: Therapeutic and Molecular Approach. Frontiers in Pharmacology. 2019;10. doi: 10.3389/fphar.2019.00977.

69. Bergmann TJ, Molinari M. Three branches to rule them all? UPR signalling in response to chemically versus misfolded proteins-induced ER stress. Biology of the Cell. 2018;110(9):197-204. doi: 10.1111/boc.201800029.

70. Bravo R, Parra V, Gatica D, Rodriguez AE, Torrealba N, Paredes F, et al. Endoplasmic reticulum and the unfolded protein response: dynamics and metabolic integration. Int Rev Cell Mol Biol. 2013;301:215-90. Epub 2013/01/16. doi: 10.1016/B978-0-12-407704-1.00005-1. PubMed PMID: 23317820; PubMed Central PMCID: PMCPMC3666557.

71. Hollien J. Evolution of the unfolded protein response. Biochimica et Biophysica Acta (BBA) - Molecular Cell Research. 2013;1833(11):2458-63. doi: 10.1016/j.bbamcr.2013.01.016.

72. Clark EM, Nonarath HJT, Bostrom JR, Link BA. Establishment and validation of an endoplasmic reticulum stress reporter to monitor zebrafish ATF6 activity in development and disease. Disease Models & Mechanisms. 2020;13(1). doi: 10.1242/dmm.041426.

73. Oslowski CM, Urano F. Measuring ER stress and the unfolded protein response using mammalian tissue culture system. Methods in enzymology. 2011;490:71-92. doi: 10.1016/B978-0-12-385114-7.00004-0.

74. Sundaram A, Appathurai S, Plumb R, Mariappan M. Dynamic changes in complexes of IRE1α, PERK, and ATF6α during endoplasmic reticulum stress. Molecular Biology of the Cell. 2018;29(11):1376-88. doi: 10.1091/mbc.E17-10-0594.

75. Walter P, Ron D. The Unfolded Protein Response: From Stress Pathway to Homeostatic Regulation. Science. 2011;334(6059):1081-6. doi: 10.1126/science.1209038.

76. Shaheen A. Effect of the unfolded protein response on ER protein export: a potential new mechanism to relieve ER stress. Cell Stress & Chaperones. 2018;23(5):797-806. doi: 10.1007/s12192-018-0905-2.

77. Almanza A, Carlesso A, Chintha C, Creedican S, Doultsinos D, Leuzzi B, et al. Endoplasmic reticulum stress signalling – from basic mechanisms to clinical applications. The FEBS Journal. 2019;286(2):241-78. doi: 10.1111/febs.14608.

78. English BC, Van Prooyen N, Ord T, Ord T, Sil A. The transcription factor CHOP, an effector of the integrated stress response, is required for host sensitivity to the fungal intracellular pathogen Histoplasma capsulatum. PLoS Pathog. 2017;13(9):e1006589. Epub 2017/09/28. doi: 10.1371/journal.ppat.1006589. PubMed PMID: 28953979; PubMed Central PMCID: PMCPMC5633207.

79. Lu X, Li C, Li C, Li P, Fu E, Xie Y, et al. Heat-Labile Enterotoxin-Induced PERK-CHOP Pathway Activation Causes Intestinal Epithelial Cell Apoptosis. Front Cell Infect Microbiol. 2017;7:244. Epub 2017/06/24. doi: 10.3389/fcimb.2017.00244. PubMed PMID: 28642847; PubMed Central PMCID: PMCPMC5463185.

80. Dias-Teixeira KL, Calegari-Silva TC, Medina JM, Vivarini AC, Cavalcanti A, Teteo N, et al. Emerging Role for the PERK/eIF2alpha/ATF4 in Human Cutaneous Leishmaniasis. Sci Rep. 2017;7(1):17074. Epub 2017/12/08. doi: 10.1038/s41598-017-17252-x. PubMed PMID: 29213084; PubMed Central PMCID: PMCPMC5719050.

81. Mesclon F, Lambert-Langlais S, Carraro V, Parry L, Hainault I, Jousse C, et al. Decreased ATF4 expression as a mechanism of acquired resistance to long-term amino acid limitation in cancer cells. Oncotarget. 2017;8(16):27440-53. Epub 2017/05/04. doi: 10.18632/oncotarget.15828. PubMed PMID: 28460466; PubMed Central PMCID: PMCPMC5432347.

82. Lin C, Chen Z, Zhang L, Wei Z, Cheng KK, Liu Y, et al. Deciphering the metabolic perturbation in hepatic alveolar echinococcosis: a (1)H NMR-based metabolomics study. Parasit Vectors. 2019;12(1):300. Epub 2019/06/15. doi: 10.1186/s13071-019-3554-0. PubMed PMID: 31196218; PubMed Central PMCID: PMCPMC6567409.

83. Paschen W, Mengesdorf T. Endoplasmic reticulum stress response and neurodegeneration. Cell Calcium. 2005;38(3-4):409-15. Epub 2005/08/10. doi: 10.1016/j.ceca.2005.06.019. PubMed PMID: 16087231.

84. Chen Y, Brandizzi F. IRE1: ER stress sensor and cell fate executor. Trends Cell Biol. 2013;23(11):547-55. Epub 2013/07/25. doi: 10.1016/j.tcb.2013.06.005. PubMed PMID: 23880584; PubMed Central PMCID: PMCPMC3818365.

85. Akhter MS, Uddin MA, Kubra KT, Barabutis N. Autophagy, Unfolded Protein Response and Lung Disease. Curr Res Cell Biol. 2020;1. Epub 2020/11/10. doi: 10.1016/j.crcbio.2020.100003. PubMed PMID: 33163960; PubMed Central PMCID: PMCPMC7643908.

86. Agarwal V, Bell GW, Nam JW, Bartel DP. Predicting effective microRNA target sites in mammalian mRNAs. Elife. 2015;4. Epub 2015/08/13. doi: 10.7554/eLife.05005. PubMed PMID: 26267216; PubMed Central PMCID: PMCPMC4532895.

87. Miranda KC, Huynh T, Tay Y, Ang YS, Tam WL, Thomson AM, et al. A pattern-based method for the identification of MicroRNA binding sites and their corresponding heteroduplexes. Cell. 2006;126(6):1203-17. Epub 2006/09/23. doi: 10.1016/j.cell.2006.07.031. PubMed PMID: 16990141.

88. Luis A, Hackl M, Jafarmadar M, Keibl C, Jilge JM, Grillari J, et al. Circulating miRNAs Associated With ER Stress and Organ Damage in a Preclinical Model of Trauma Hemorrhagic Shock. Front Med (Lausanne). 2020;7:568096. Epub 2020/10/20. doi: 10.3389/fmed.2020.568096. PubMed PMID: 33072784; PubMed Central PMCID: PMCPMC7542230.

89. Wilczynski M, Zytko E, Szymanska B, Dzieniecka M, Nowak M, Danielska J, et al. Expression of miR-146a in patients with ovarian cancer and its clinical significance. Oncol Lett. 2017;14(3):3207-14. Epub 2017/09/21. doi: 10.3892/ol.2017.6477. PubMed PMID: 28927067; PubMed Central PMCID: PMCPMC5588008.

90. Halperin L, Jung J, Michalak M. The many functions of the endoplasmic reticulum chaperones and folding enzymes. IUBMB Life. 2014;66(5):318-26. doi: 10.1002/iub.1272.

91. Ruggiano A, Foresti O, Carvalho P. ER-associated degradation: Protein quality control and beyond. Journal of Cell Biology. 2014;204(6):869-79. doi: 10.1083/jcb.201312042.

92. Danilczyk UG, Cohen-Doyle MF, Williams DB. Functional Relationship between Calreticulin, Calnexin, and the Endoplasmic Reticulum Luminal Domain of Calnexin. Journal of Biological Chemistry. 2000;275(17):13089-97. doi: 10.1074/jbc.275.17.13089.

93. Ni M, Lee AS. ER chaperones in mammalian development and human diseases. FEBS letters. 2007;581(19):3641-51. doi: 10.1016/j.febslet.2007.04.045.

94. Radons J. The human HSP70 family of chaperones: where do we stand? Cell Stress & Chaperones. 2016;21(3):379-404. doi: 10.1007/s12192-016-0676-6.

95. Williams DB. Beyond lectins: the calnexin/calreticulin chaperone system of the endoplasmic reticulum. Journal of Cell Science. 2006;119(4):615-23. doi: 10.1242/jcs.02856.

96. Tsachaki M, Mladenovic N, Stambergova H, Birk J, Odermatt A. Hexose-6-phosphate dehydrogenase controls cancer cell proliferation and migration through pleiotropic effects on the unfolded-protein response, calcium homeostasis, and redox balance. FASEB J. 2018;32(5):2690-705. Epub 2018/01/04. doi: 10.1096/fj.201700870RR. PubMed PMID: 29295867; PubMed Central PMCID: PMCPMC5901385.

Supplementary data

Primary antibodies (ab)				
Target protein	**Species**	**Type**	**Dilutions**	
			Primary ab	**Secondary ab**
H6PD	Rabbit	Polyclonal	1:1000	1:2000
CRT	Rabbit	Polyclonal	1:1000	1:2000
CNX	Rabbit	Polyclonal	1:1000	1:2000
GRP78	Mouse	Monoclonal	1:1000	1:4000
CHOP	Mouse	Monoclonal	1:1000	1:4000
ATF4	Rabbit	Monoclonal	1:1000	1:2000
ATF6	Rabbit	Monoclonal	1:1000	1:2000
ERP72	Mouse	Monoclonal	1:1000	1:4000
IRE1α	Mouse	Monoclonal	1:1000	1:4000
PERK	Mouse	Monoclonal	1:1000	1:4000
eIF2α	Mouse	Monoclonal	1:1000	1:4000
Lamin B1	Rabbit	Monoclonal	1:1000	1:2000

S1 Table. Antibodies and corresponding dilutions.

Primers		
Target gene	**Forward primer (5'-3')**	**Reverse primer (5'-3')**
IRE1α	TGTGGTCAAGATGGACTGGC	5TCGGAGGAGGTCTCACAG
Xbp1-s	GAGTCCGCAGCAGGTG	GTGTCAGAGTC-CATGGGA′
Xbp1	AAGAACACGCTTGGGAATGG	ACTCCCCTTGGCCTCCAC
β-Actin	ACCCTGTGCTGCTCACCGA	CTGGATGGCTACGTACATGGCT

S2 Table. Primers used for RT-qPCR.

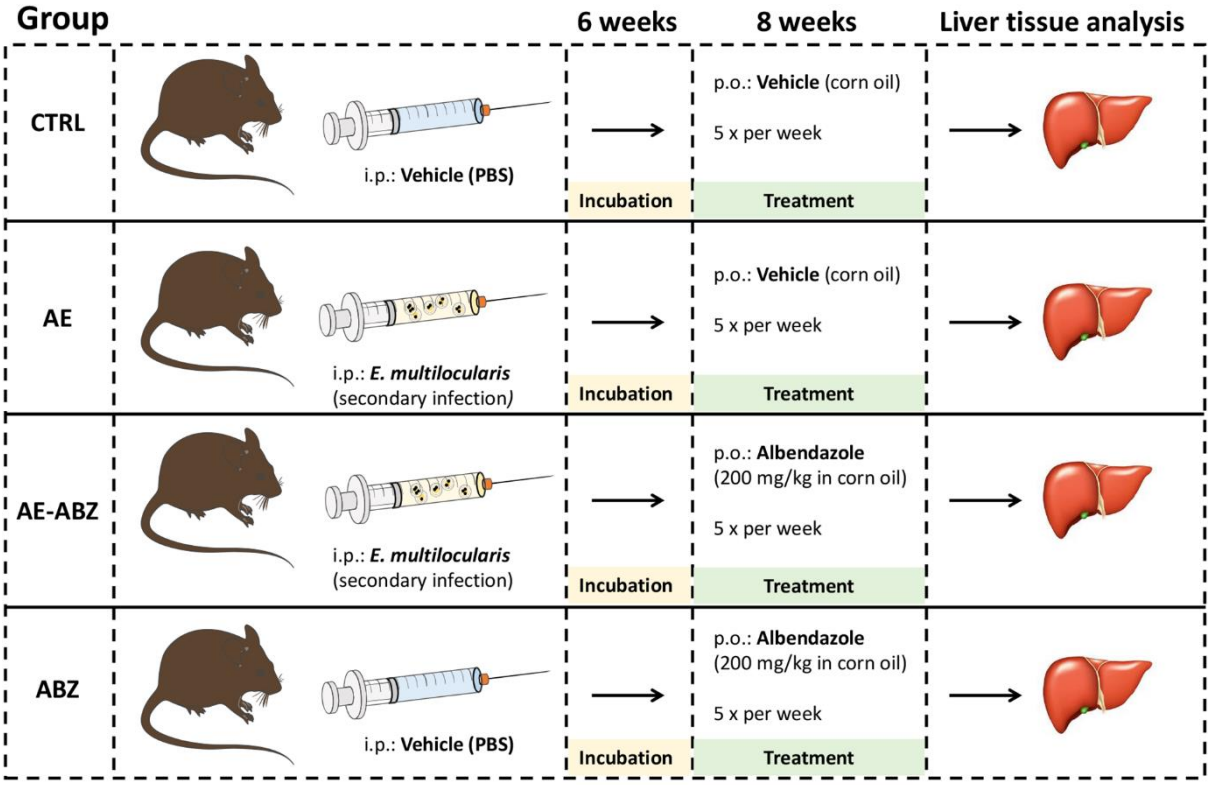

S1 Fig. Schematic overview of experimental setup. Animals were divided into four groups: $CTRL_{(n=6)}$, $AE_{(n=6)}$, $AE\text{-}ABZ_{(n=6)}$, and $ABZ_{(n=6)}$. CTRL and ABZ mice received an intraperitoneal administration of 100 µL PBS. AE and AE-ABZ mice were treated by secondary *E. multilocularis* infection using approximately 100 vesicular cysts resuspended in 100 µL PBS. Treatment started 6 weeks after infection. CTRL and AE mice received 100 µL corn oil orally 5 times per week for 8 weeks. AE-ABZ and ABZ mice received ABZ (200 mg/kg body weight) in 100 µL corn oil orally 5 times per week for 8 weeks. Animals were sacrificed at the end of treatment.

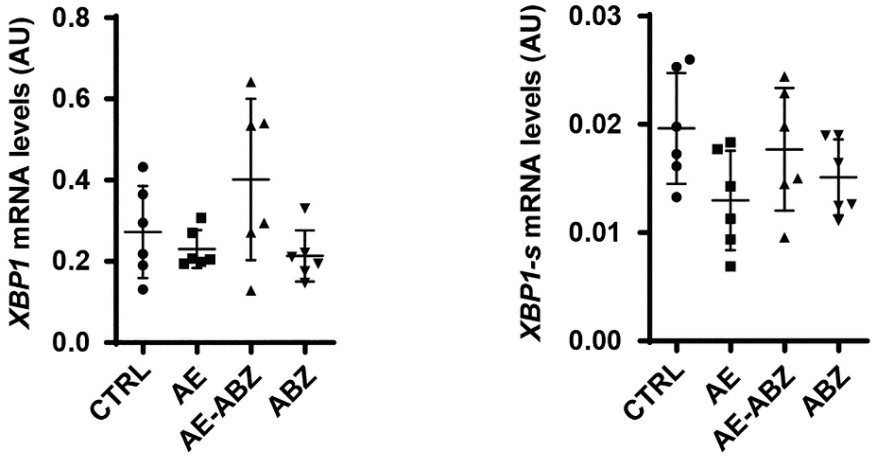

S2 Fig. XBP1 mRNA and XBP1-s mRNA levels are not altered upon *E. multilocularis* infection. XBP1 and XBP1-s mRNA levels in mock-infected control mice ($CTRL_{n=6}$), *E. multilocularis* infected mice ($AE_{n=6}$), infected mice treated with ABZ ($AE\text{-}ABZ_{n=6}$) or uninfected mice treated with ABZ ($ABZ_{n=6}$). Results represent mean ± SD. No outliers were excluded. One-way ANOVA was applied to test significance.

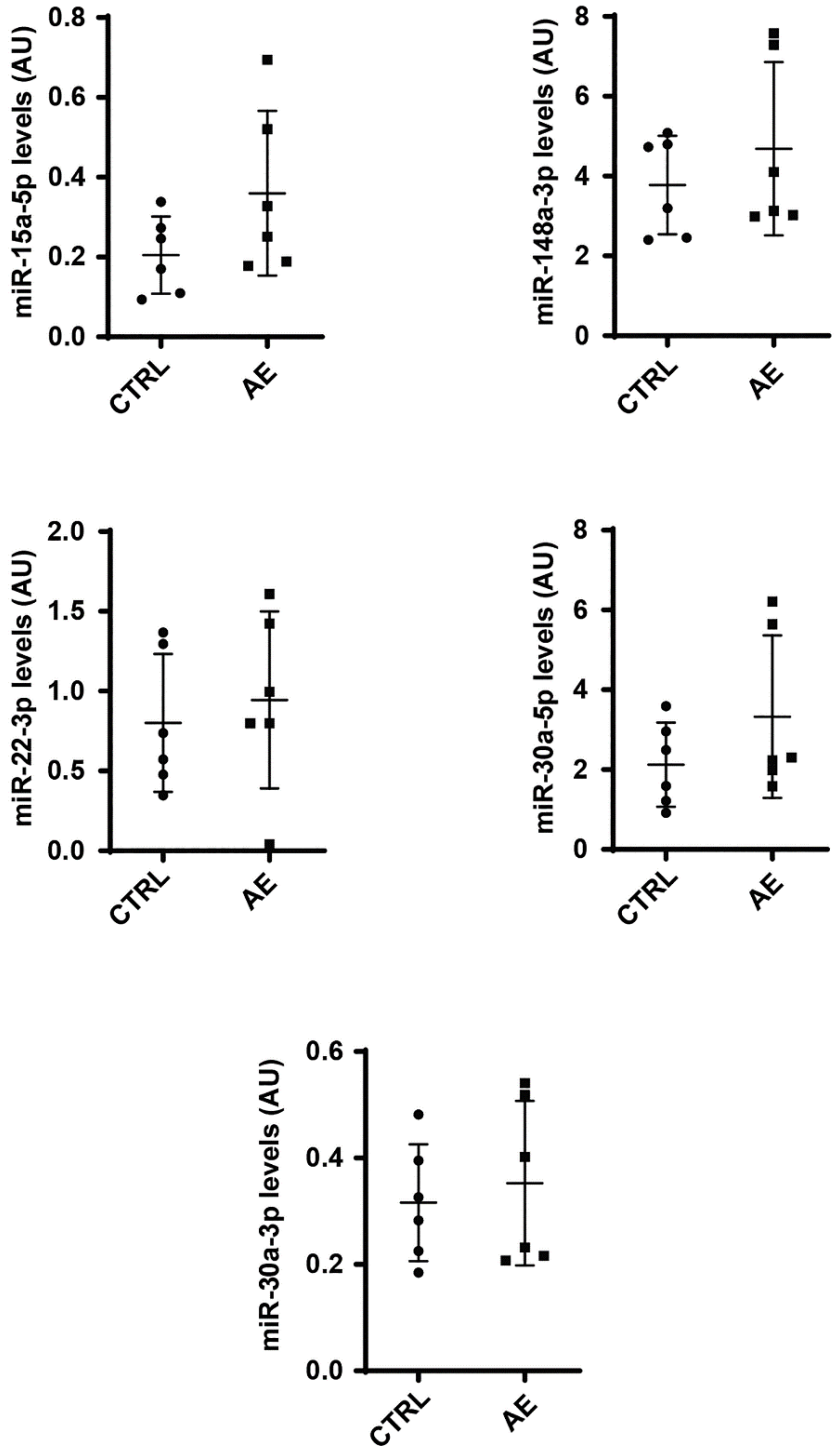

S3 Fig. *E. multilocularis* infection does not affect miR-15a-5p, miR-148a-3p, miR-22-3p, miR-30a-3p and miR-30a-5p expression levels. miR-15a-5p, miR-148a-3p, miR-22-3p, miR-30a-5p and miR-30a-3p levels, in mock-infected, mock-treated mice (CTRL $_{n=6}$) and *E. multilocularis* infected mock-treated mice (AE $_{n=6}$). Results represent mean ± SD. No outliers were excluded. Two-tailed unpaired t-test was applied to test significance.

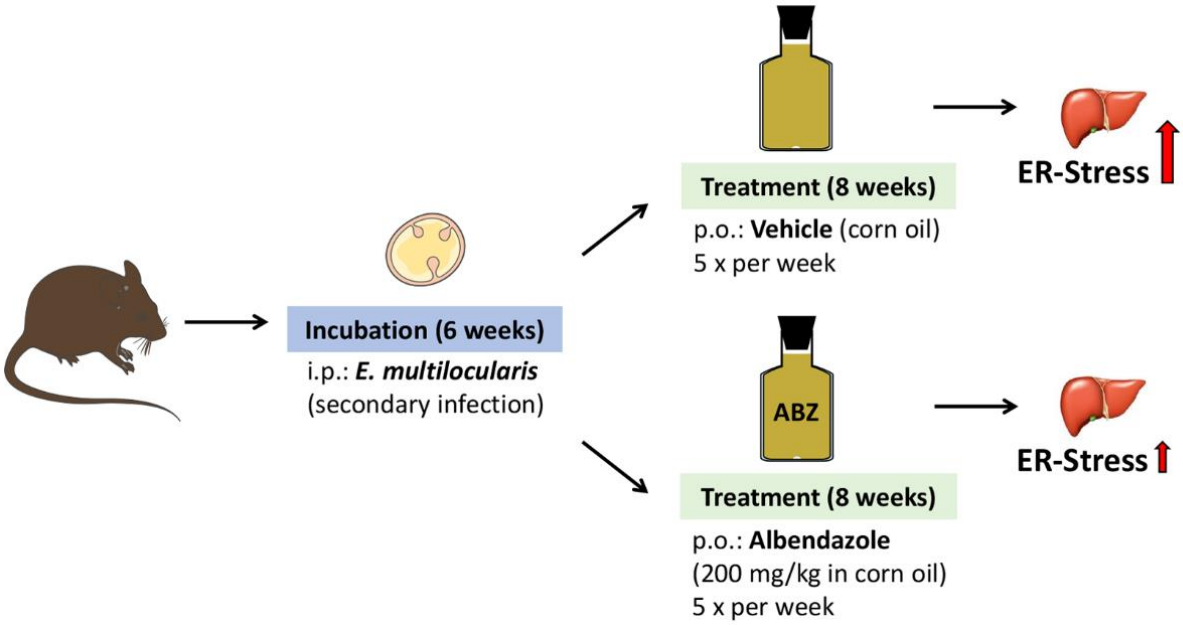

Striking image. Experimental setup and key finding that *E. multilocularis* infection causes ER-stress in mouse liver. Treatment of infected mice using the anthelminthic drug albendazole attenuates the altered expression of selected ER-stress related genes.

6.2 *Echinococcus multilocularis* related disturbances in bile acid profiles

6.2.1 Manuscript in preparation:

Impact on serum bile acid concentrations by alveolar echinococcosis and treatment with albendazole in mice

Cristina Gómez[1,*], Fadi Jebbawi[1,*], Michael Weingartner[1,*], Junhua Wang[2,3], Bruno Stieger[4], Bruno Gottstein[2,3], Guido Beldi[5], Britta Lundström-Stadelmann[2], Alex Odermatt[1,†]

[1] Division of Molecular and Systems Toxicology, Department of Pharmaceutical Sciences, University of Basel, Klingelbergstrasse 50, 4056 Basel, Switzerland.

[2] Institute of Parasitology, Department of Infectious Diseases and Pathobiology, Vetsuisse Faculty, University of Bern, Längassstrasse 122, 3012, Berne, Switzerland.

[3] Institute for Infectious Diseases, Faculty of Medicine, University of Berne, Friedbühlstrasse 51, 3010, Berne, Switzerland.

[4] Department of Clinical Pharmacology and Toxicology, University Hospital Zürich, Zürich, Switzerland.

[5] Department of Visceral Surgery and Medicine, University Hospital of Berne, Freiburgstrasse, 3010 Berne, Switzerland.

[*] The authors contributed equally to the manuscript.

[†] Correspondence: alex.odermatt@unibas.ch

Target journal: Metabolites

Contribution to the project:

- Experimental work
- Analysis and interpretation of the data
- Graphical work (figures)
- Revising the manuscript

Impact on serum bile acid concentrations by alveolar echinococcosis and treatment with albendazole in mice

Cristina Gómez[1,*], Fadi Jebbawi[1,*], Michael Weingartner[1,*], Junhua Wang[2,3], Bruno Stieger[4], Bruno Gottstein[2,3], Guido Beldi[5], Britta Lundström-Stadelmann[2], Alex Odermatt[1,†]

[1] Division of Molecular and Systems Toxicology, Department of Pharmaceutical Sciences, University of Basel, Klingelbergstrasse 50, 4056 Basel, Switzerland.

[2] Institute of Parasitology, Department of Infectious Diseases and Pathobiology, Vetsuisse Faculty, University of Bern, Längassstrasse 122, 3012, Berne, Switzerland.

[3] Institute for Infectious Diseases, Faculty of Medicine, University of Berne, Friedbühlstrasse 51, 3010, Berne, Switzerland.

[4] Department of Clinical Pharmacology and Toxicology, University Hospital Zürich, Zürich, Switzerland.

[5] Department of Visceral Surgery and Medicine, University Hospital of Berne, Freiburgstrasse, 3010 Berne, Switzerland.

[*] The authors contributed equally to the manuscript.

[†] Correspondence: alex.odermatt@unibas.ch

Keywords: Bile acid; BSEP; NTCP; alveolar echinococcosis; Echinococcus multilocularis; albendazole; LC-MS/MS

Abstract

Alveolar echinococcosis (AE) caused by *Echinococcus multilocularis* is a chronic, progressive liver disease widely distributed in the northern hemisphere. The main treatment options include surgical interventions and chemotherapy with benzimidazoles such as albendazole (ABZ). To improve current diagnosis and therapy of AE, further investigations into parasite-host interactions are needed. This study used LC-MS/MS to assess serum bile acid profiles in an AE mouse model and evaluated the effects of the anthelmintic drug ABZ. Additionally, mRNA and protein expression of key enzymes and transporters regulating serum bile acid concentrations were analyzed. AE significantly altered serum bile acid concentrations, with significantly decreased unconjugated bile acids and either unchanged or increased concentrations of taurine-conjugated bile acids, suggesting ratios of free to taurine-conjugated bile acids as useful markers of AE. The expression of the bile acid synthesis enzymes CYP7A1 and AKR1D1 tended to be decreased or were decreased in the AE group, along with decreased expression of the bile acid transporters NTCP and BSEP. Importantly, treatment with ABZ partially or completely reversed the effects by *E. multilocularis* infection, whereby ABZ itself had no effect on the bile acid profile and expression of relevant enzymes and transporters. Further research is needed to uncover the exact mechanism of the AE-induced changes in bile acid homeostasis and to test whether serum bile acids and ratios thereof can serve as biomarkers of AE and for monitoring therapeutic efficacy.

Introduction

Human alveolar echinococcosis (AE) caused by *Echinococcus multilocularis* is a severe disease with a high morbidity and poor prognosis if managed inappropriately [1,2]. *E. multilocularis* is distributed and recognized as an emerging zoonosis in some regions of the northern hemisphere [1–3]. In Europe, adult worm infections of *E. multilocularis* occur mainly in red and arctic foxes, although dogs and cats can also act as definitive hosts [3,4]. The course of infection is characterized by a long-term, primarily intrahepatic growth of metacestode tissue in the intermediate host, including small mammals and mice [5]. Severe *E. multilocularis* infections lead to liver failure and hepatic encephalopathy. The clinical manifestations include epigastric pain and jaundice, which may be followed by fever, anemia and weight loss. Invasion of the bile ducts leads to cholangitis, portal hypertension, and biliary cirrhosis. The disease can progress to the cirrhotic stage after a long latent, asymptomatic period [5,6]. A characteristic feature of AE is its tumor-like growth, which may lead to infiltration of neighboring organs. The liver is the first organ to be affected. Hepatic lesions are localized to the right hepatic lobe

in seven of ten cases. The parasite destroys the liver parenchyma, and complications such as biliary obstruction, portal hypertension, and bleeding esophageal varices have been described in advanced disease stages and are attributed to the invasive growth of the *E. multilocularis* lesion in the liver [5–7].

The only curative treatment of AE is surgical resection of the tumor-like metacestode liver tissue, supported by pre- and post-operative chemotherapy [2]. The treatment in those AE cases that are inoperable consists of a long-term and often life-long treatment with the benzimidazoles albendazole (ABZ) or mebendazole. Long-term treatment with benzimidazoles is required because these drugs are parasitostatic but not parasitocidal, and as a result adverse reactions including severe hepatotoxicity are frequently observed [2,7,8].

Although it is well-known that impaired liver function in situations such as cholestasis and cirrhosis or in drug-induced liver injury can have profound effects on bile acid homeostasis, little is known whether serum bile acids are altered during *E. multilocularis* infection and whether this is influenced by ABZ treatment.

Bile acids, synthesized from cholesterol in the liver, represent the main organic component in bile fluid [9,10]. They play important roles in the elimination of cholesterol from the body, for lipid absorption, and as signaling molecules to regulate metabolic processes. Bile acids are conjugated in the liver with glycine or taurine in a species-dependent manner, followed by secretion into the intestine. Most of the bile acids are absorbed by active transport in the distal ileum and their concentrations are tightly controlled by the enterohepatic cycle [9–11]. In many hepatic and intestinal diseases serum bile acid concentrations are altered due to impaired hepatic synthesis and metabolism and/or intestinal absorption. Thus, serum bile acid concentrations may serve as prognostic and diagnostic markers of liver dysfunctions and diseases [12–16].

Bile acids are transported across the basolateral and canalicular membranes of hepatocytes by numerous transport proteins. Whilst Na^+-taurocholate co-transporting polypeptide (NTCP) and organic anion transporters (OATPs) are important for the uptake of bile acids from blood through the basolateral membrane into the hepatocytes (Figure 1) [17–21], the bile salt export pump (BSEP) represents the rate-limiting step in the elimination of bile acids into the bile fluid. Inherited and acquired forms of liver diseases, which impair the proper function of BSEP, can lead to an accumulation of bile acids and cause hepatocellular damage or even cell death [18,19,21]. Elevated levels of bile acids lead to the activation of the farnesoid X receptor (FXR), which downregulates the expression of the rate-limiting bile acid synthesis enzyme CYP7A1 and the sinusoidal uptake transporter NTCP but upregulates the efflux transporter BSEP to

reduce the concentration of intracellular bile acids [18,19,21]. FXR activation upon hepatic bile acid accumulation also increases sinusoidal bile acid efflux by inducing the expression of multidrug resistance-associated protein (MRP)4 and heterodimeric organic solute transporters (OST)α and OSTβ [11,17,20,22,23].

The present study employed ultra-high performance liquid chromatography-tandem mass spectrometry (LC-MS/MS) to investigate changes in the serum bile acid profile in mice following *E. multilocularis* infection. Furthermore, the effect of the currently most frequently used treatment, i.e. ABZ, was assessed on the bile acid profile. Additionally, the mRNA and protein expression levels of key bile acid transporters and enzymes involved in bile acid synthesis was studied in liver tissues.

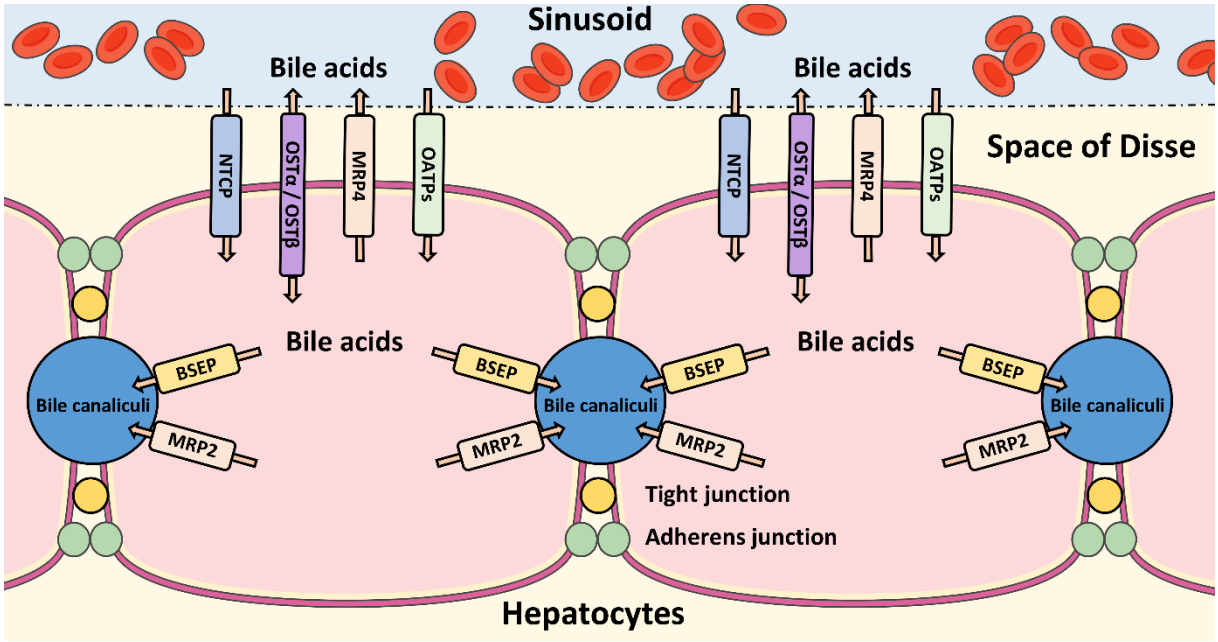

Figure 1. Schematic overview of key transport proteins involved in hepatic bile acid homeostasis.

Results

Serum bile acid profiles

To assess potential effects of *E. multilocularis* infection and its main treatment by ABZ on the serum bile acid profiles in mice, a recently established LC-MS/MS-based method was applied to quantify several taurine-conjugated and unconjugated bile acids [24]. The mean concentrations of each individual bile acid as well as the sums of taurine-conjugated,

unconjugated and all bile acids analyzed for the four treatment groups are listed in Table 1, and data for individual bile acids are shown in Supplemental Figure S1. The concentrations of all unconjugated primary (CA, CDCA, αMCA, βMCA, ωMCA) and secondary (UDCA, DCA, HDCA, 7oxoDCA and 12oxoLCA) bile acids were 4.6-fold lower in the AE group compared with the control group. In contrast, the taurine-conjugated bile acids (TCDCA, TUDCA, TDCA, TαMCA and TωMCA) were either not altered or significantly increased (TCA and TβMCA) in AE compared to CTRL mice, with 1.5-fold higher levels of total taurine-conjugated bile acids in the AE group. The total circulating bile acids were 2.5-fold lower in AE compared to CTRL mice.

Compound	**CTRL (n=6)** (nM mean ± SD)	**AE (n=6)** (nM mean ± SD)	**AE-ABZ (n=5)** (nM mean ± SD)	**CTRL-ABZ (n=6)** (nM mean ± SD)
Unconjugated				
CA	2960 ± 1586	753 ± 761*†	2218 ± 2861	2760 ± 1521
CDCA	305 ± 148	70 ± 34*†	237 ± 200	365 ± 346
ωMCA	3074 ± 1654	489 ± 192*†	1744 ± 1467	2522 ± 741
αMCA	554 ± 385	44 ± 37*†	287 ± 308	463 ± 399
βMCA	4747 ± 3497	1080 ± 899*†	4452 ± 4387	4131 ± 2559
UDCA	590 ± 358	122 ±81*†	784 ± 811	686 ± 549
HDCA	245 ± 95	29 ± 18*†	174 ± 137	263 ± 91
DCA	917 ± 261	374 ± 146*†	1217 ± 939	1176 ± 654
12oxoLCA	15 ± 6	5 ± 1 *‡	17 ± 13	14 ± 7
7oxoDCA	686 ± 441	93 ± 74*†	443 ± 430	609 ± 305
AlloCA	122 ± 45	18 ± 13*†	63 ± 73	119 ± 52
Total unconjugated	**14215 ± 7740**	**3078 ± 2082***	**11636 ± 11085**	**13107 ± 6512**
Taurine-conjugated				
TCA	345 ± 173	920 ± 620†	305 ± 282	232 ± 110
TCDCA	27 ± 29	40 ± 23	19 ± 8	22 ± 19
TωMCA	970 ± 228	642 ± 208	607 ±446	822 ± 236
TαMCA	253 ± 104	325 ± 188	329 ± 372	244 ± 158
TβMCA	606 ± 285	1396 ± 916†	578 ± 596	398 ± 187
TUDCA	110 ± 37	120 ± 33	132 ± 80	125 ± 36
TDCA	81 ± 43	137 ± 69	108 ± 72	80 ± 39
Total taurine-conjugated	**2392 ± 755**	**3578 ±1820**	**2078 ± 1787**	**1924 ± 685**
Total bile acids	**16607 ± 8135**	**6656 ± 3172**	**13714 ± 12722**	**15031 ± 6963**

Table 1. Effects of *E. multilocularis* infection and ABZ treatment on bile acids in serum of mice. Serum was collected from non-infected control (CTRL, n=6), *E. multilocularis* infected (AE, n=6), *E. multilocularis* infected and ABZ treated (AE-ABZ, n=5, one outlier with aberrant concentrations was removed), and non-infected and ABZ treated control mice (CTRL-ABZ, n=6). * $p < 0.05$ CRTL *vs.* AE group, † $p < 0.05$ CTRL-ABZ *vs.* AE group, and ‡ $p < 0.05$ AE *vs.* AE-ABZ. Values are expressed as mean ± SD (nM).

ABZ is the drug of choice to treat AE in human [1,2]. In this mouse model of AE, ABZ treatment was well tolerated and no significant changes in any of the serum bile acids analyzed were detected in the CTRL-ABZ compared to the CTRL group (Table 1, Supplemental Figure S1). Importantly, ABZ treatment of *E. multilocularis* infected mice partially or completely reversed the changes in serum bile acid concentrations observed in AE mice (compare AE-ABZ with AE), and the bile acid concentrations of all analyzed metabolites in the AE-ABZ group were comparable to those of the CTRL and CTRL-ABZ groups. A comparison of the relative abundance of each individual bile acid in percentage shows highly similar profiles for CTRL, CTRL-ABZ and AE-ABZ but a clearly distinct profile for the AE group (Figure 2).

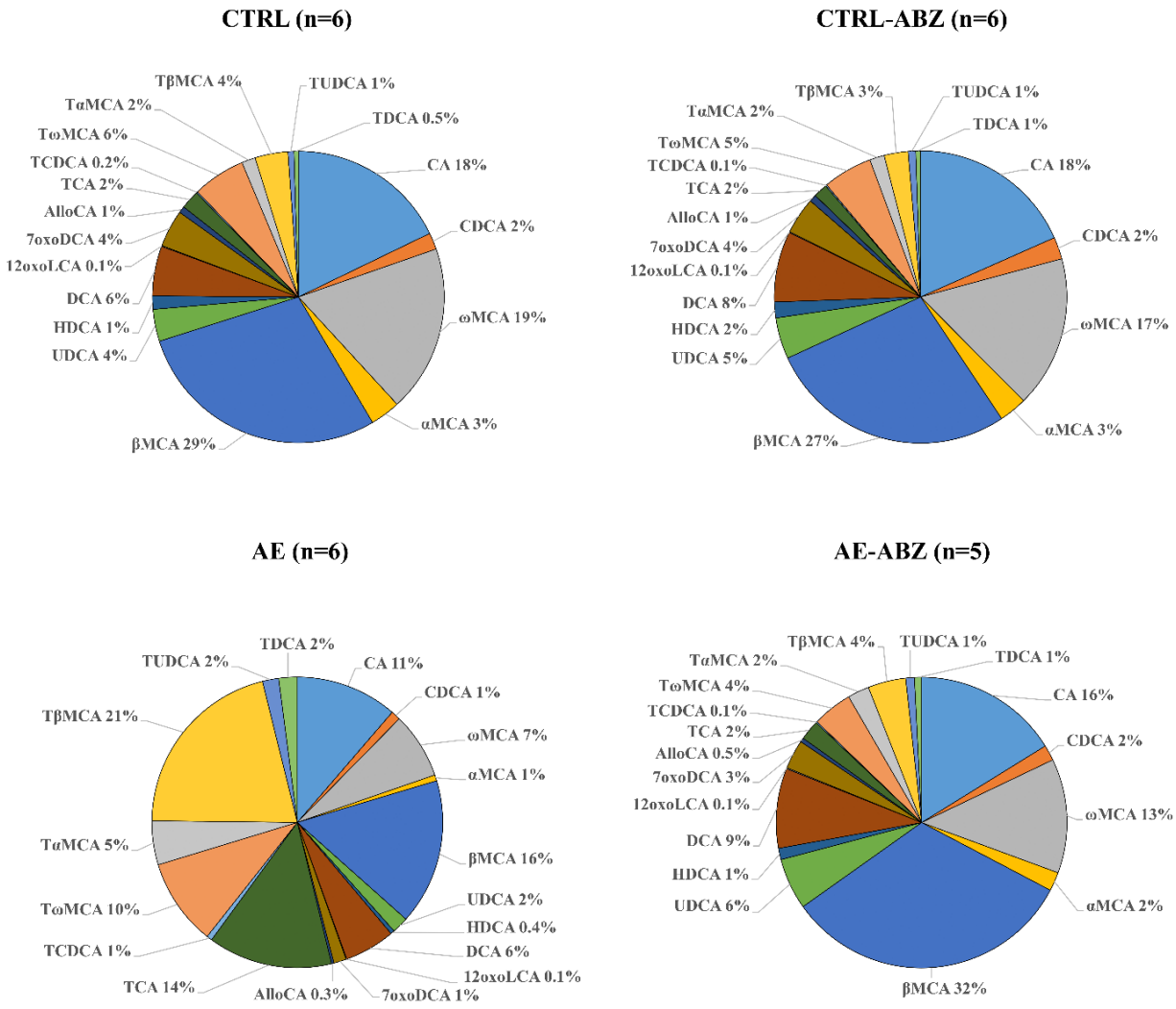

Figure 2. Bile acid profiles in serum of the four different mouse groups. The relative amounts of individual bile acids, indicated by different colors, are shown for the four different groups: non-infected control (CTRL, n=6), *E. multilocularis* infected (AE, n=6), non-infected and ABZ treated control (CTRL-ABZ, n=6), and *E. multilocularis* infected and ABZ treated mice (AE-ABZ, n=5, one outlier with aberrant concentrations was removed). Data represent relative abundances (%) of individual bile acids.

As ratios often show lower inter-individual variations than single analytes, they may represent more sensitive markers to detect changes in bile acid homeostasis. The ratio of total taurine-conjugated to unconjugated bile acids as well as the ratios of TCA/CA, TαMCA/αMCA and TβMCA/βMCA all were approximately 10-fold increased compared to the CTRL group in AE mice, followed by complete reversal upon ABZ treatment (Figure 3, Figure S3 and Table 2).

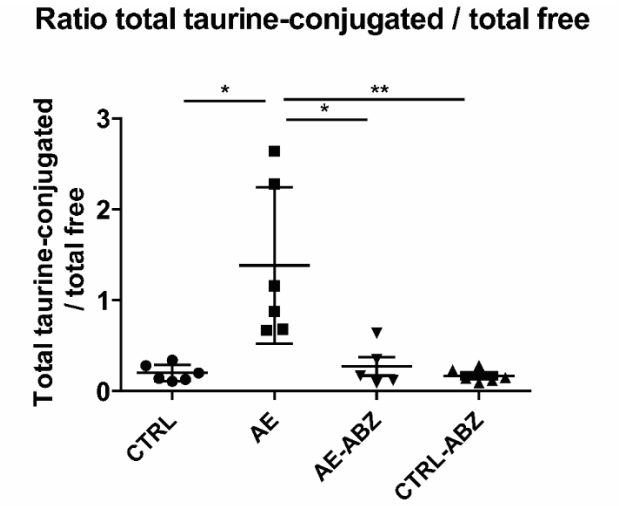

Figure 3: Increased ratio of taurine-conjugated to unconjugated bile acids in AE. The sum of the taurine-conjugated bile acids divided by the sum of free bile acids was determined in the four different treatment groups. Non-infected control (CTRL, n=6), *E. multilocularis* infected (AE, n=6), non-infected and ABZ treated control (CTRL-ABZ, n=6), and *E. multilocularis* infected and ABZ treated mice (AE-ABZ, n=5, one outlier with aberrant concentrations was removed). Values are expressed as mean ± SD. * $p < 0.05$ and ** $p < 0.01$.

Ratio	**CTRL (n=6)** (mean ± SD)	**AE (n=6)** (mean ± SD)	**AE-ABZ (n=5)** (mean ± SD)	**CTRL-ABZ (n=6)** (mean ± SD)
Total taurine-conjugated/total free	0.20 ± 0.09	1.38 ± 0.86*†	0.17 ± 0.07‡	0.27 ± 0.23
TCA/CA	0.15 ± 0.14	1.63 ± 1.33*†	0.25 ± 0.26‡	0.09 ± 0.02
TαMCA/αMCA	0.72 ± 0.63	9.17 ± 5.74*†	1.50 ± 1.04‡	0.58 ± 0.17
TβMCA/βMCA	0.17 ± 0.10	1.63 ± 1.18*†	0.21 ± 0.19‡	0.12 ± 0.09

Table 2. Increased ratio of taurine-conjugated to unconjugated bile acids in AE. The ratio of total taurine-conjugated to total unconjugated bile acids as well as the ratios of TCA/CA, TαMCA/αMCA and TβMCA/βMCA were calculated the four different treatment groups. Non-infected control (CTRL, n=6), *E. multilocularis* infected (AE, n=6), non-infected and ABZ treated control (CTRL-ABZ, n=6), and *E. multilocularis* infected and ABZ treated mice (AE-ABZ, n=5, one outlier with aberrant concentrations was removed). Values are expressed as mean ± SD. * $p < 0.05$ CTRL *vs*. AE group, † $p < 0.05$ CTRL-ABZ *vs*. AE group, and ‡ $p < 0.05$ AE *vs*. AE-ABZ group.

Effect of AE and ABZ treatment on enzymes involved in bile acid synthesis

To assess whether AE and/or the treatment with ABZ affect bile acid synthesis, the mRNA levels of the rate-limiting enzyme Cyp7a1 the sterol 27-hydroxylase Cyp27a1, which initiates the acidic pathway or alternative pathway for bile acid synthesis and of the 5β-reductase Akr1d1 were analyzed by quantitative PCR (qPCR). The expression of Cyp7a1, and to a lesser extent that of Cyp27a1, tended to be decreased in liver tissues of E. multilocularis infected mice (Figure 4). These trends were reversed by treatment with ABZ. Attempts to determine the protein expression of these enzymes in mouse liver tissues failed as no suitable antibodies and conditions could be identified. Regarding the 5β-reductase Akr1d1, significantly lower mRNA levels along with reduced protein levels were observed in liver tissues from AE mice compared to CTRL, and ABZ treatment reversed the decreased mRNA and protein expression.

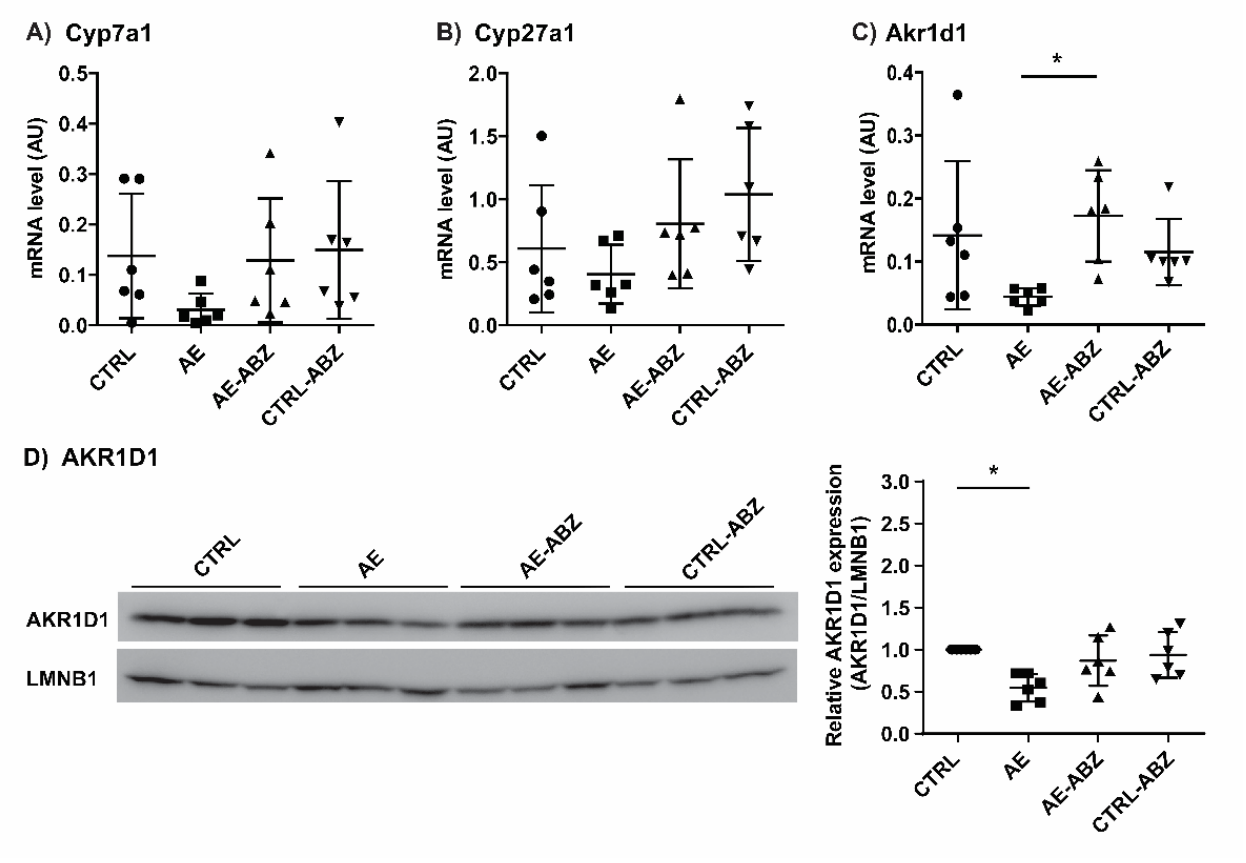

Figure 4. Expression levels of enzymes involved in bile acid synthesis. The mRNA levels of Cyp7a1 (A), Cyp27a1 (B) and Akr1d1 (C) and the protein levels of AKR1D1 (D) were determined in liver tissues of non-infected control (CTRL, n=6), *E. multilocularis* infected (AE, n=6), non-infected and ABZ treated control (CTRL-ABZ, n=6), and *E. multilocularis* infected and ABZ treated mice (AE-ABZ, n=6). One representative blot (of two) containing samples from three different mice is shown in (D) on the left and densitometry results are shown on the right, representing data from the two blots on samples from six mice, normalized to lamin B1 (LMNB1) control and with CTRL set as 1. Values are expressed as mean ± SD. * $p < 0.05$.

Influence of AE and ABZ treatment on the expression of bile acid transporters

Besides enzymes involved in bile acid synthesis and metabolism, several transport proteins regulate the composition and concentrations of bile acids in blood, liver tissue and bile fluid. To investigate a possible involvement of bile acid transporters in the observed alteration of the bile acid profile upon E. multilocularis infection, the mRNA levels of Bsep, Ntcp, Ostα, Ostβ, Mrp2, Mrp4, Oatp1a1 and Oatp4 were quantified by qPCR. Significantly lower levels of Ntcp mRNA and a trend decrease in the levels of Bsep mRNA were observed in liver tissues of E. multilocularis infected mice (Figure 5). Furthermore, a decrease in Ostα and Oatp4 mRNA levels and a trend decrease in Mrp4 mRNA expression was found in the AE group (Supplemental Figure S2). These effects were fully reversed by ABZ treatment and ABZ itself had no direct effect on any of the genes of bile acid transporters measured. The mRNA levels of Oatp1a1, Mrp2 and Ostβ were not different between the treatment groups.

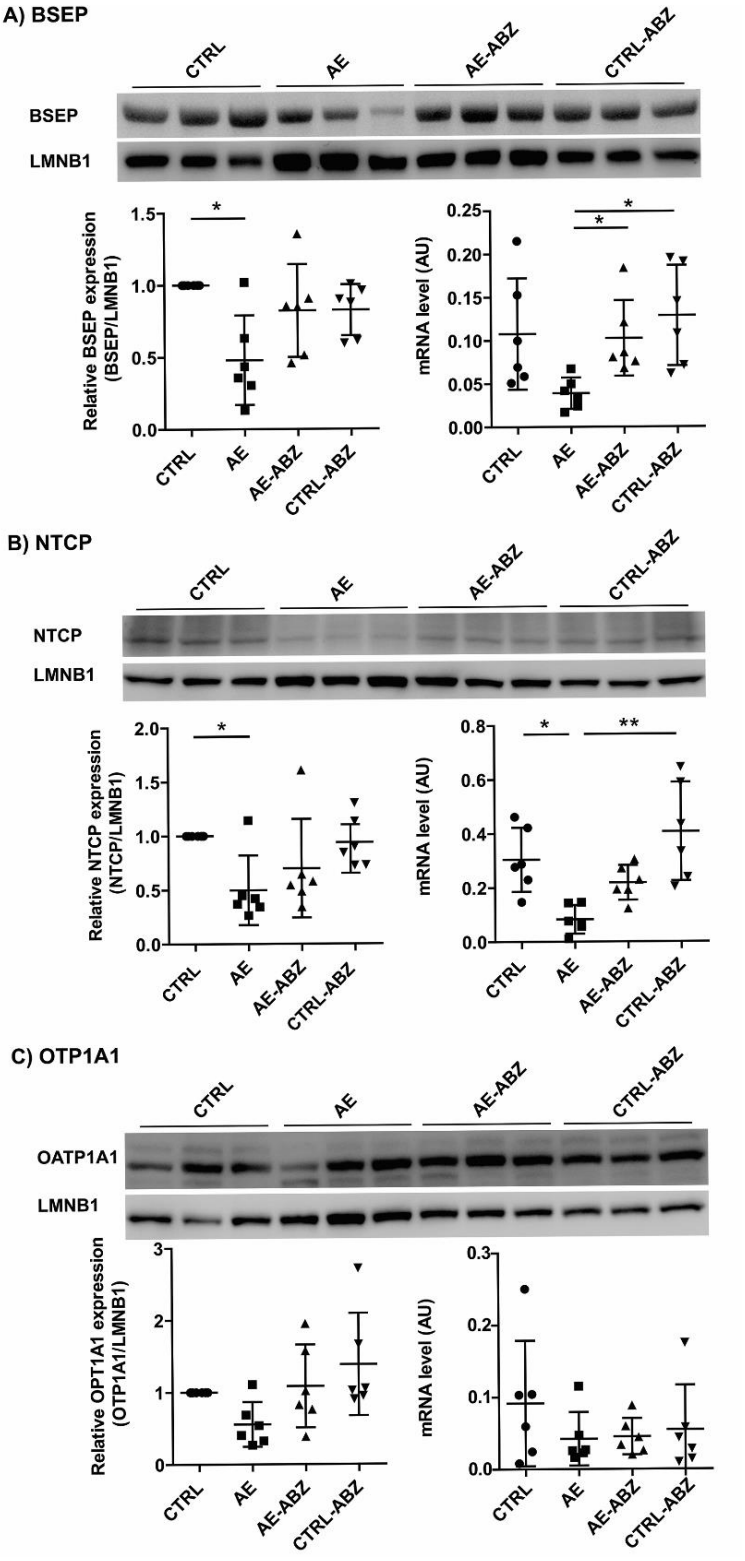

Figure 5. Hepatic mRNA and protein expression levels of BSEP, NTCP and OATP1A1 in the four treatment groups. Western blot and semi-quantitative analysis by densitometry of protein levels of transporters BSEP (A), NTCP (B) and OATP1A1 (C) in liver tissues of non-infected control (CTRL, n=6), *E. multilocularis* infected (AE, n=6), non-infected and ABZ treated control (CTRL-ABZ, n=6), and *E. multilocularis* infected and ABZ treated mice (AE-ABZ, n=6). One representative blot (of two) containing samples from three different mice is shown in the top panel. Densitometry results represent data from the two blots on samples from six mice (mean ± SD), normalized to lamin B1 (LMNB1) control and with CTRL set as 1. * $p < 0.05$ and ** $p < 0.01$.

For the assessment of protein expression using western blot, suitable antibodies could be identified for BSEP, NTCP and OATP1A1. Protein expression was analyzed by densitometry and normalized to the house keeping protein LMNB1. The protein expression levels of the bile acid transporters BSEP and NTCP were both significantly lower in the *E. multilocularis* infected mice (AE group) compared to CTRL mice (Figure 5A, B). In contrast, OATP1A1 expression was not significantly altered in any of the four treatment groups (Figure 5C).

Discussion

AE affects the liver as the primary site and progresses by continuous infiltrative proliferation, thereby destroying liver tissue, invading the adjacent organs and metastasizing to lung and brain [1,6]. Like other worm infections the disease progression of AE is usually slow and often not diagnosed until it is well advanced [6,25]. The evaluation of serum bile acid concentrations, including the determination of bile acid profiles as well as ratios of certain bile acids (e.g. taurine-conjugated/unconjugated, CA/CDCA) have the potential as diagnostic markers to distinguish different liver diseases and monitor disease progression and therapeutic efficacy [12–14,16].

The present study revealed an interesting alteration of the serum bile acid profile upon infection with *E. multilocularis*, characterized by decreased free bile acids but unchanged or slightly elevated taurine-conjugated metabolites. The ratio of total free to total taurine-conjugated bile acids as well as that of TCA/CA and TβMCA/βMCA are suggested as useful markers to detect the effect of AE and monitor the efficacy of treatment with ABZ on serum bile acids. Common symptoms observed in AE patients at a late stage of disease include jaundice, abdominal pain, and weight loss [6,25,26]. Studies in patients with jaundice showed altered bile acid metabolism, with an the increase in circulating levels of conjugated bile acids, and an elevated ratio of taurine-conjugated to free bile acids in patients with the symptoms [16,27]. The utility of the bile acid ratio markers mentioned above should be further studied in animal models and in human.

Gene expression analyses indicated a decreased hepatic bile acid synthesis by lower CYP7A1 and AKR1D1 expression along with decreased canalicular biliary secretion via BSEP, reduced bile acid uptake from the portal circulation by NTCP and OATP4, and reduced efflux to the general circulation by OSTα and MRP4. An inhibition of the above mentioned bile acid transporters may be a result of the inflammation caused by the proliferative growth of the metacestodes, leading to reduced FXR-mediated activation of SHP and PPARα that are

involved in the regulation of the expression of these bile acid transporters [11]. A rapid reduction of bile formation via downregulation of both basolateral bile acids uptake (NTCP) and canalicular efflux system (BSEP) have been observed in response to inflammation [18,22]. A decreased activity of BSEP and OSTα-OSTβ directly relates to decreased bile acid-dependent activation of FXR signaling, which can lead to liver injury [11,20]. In other conditions, such as chronic forms of cholestatic liver, downregulation of NTCP and upregulation of basolateral bile acid export systems was observed (MRP4, OSTα-OSTβ) [17,18]. This contrasts the present study on AE where OSTα and MRP4 were decreased. Moreover, if FXR activity is compromised one would expect an elevated expression of the rate-limiting bile acid synthesis enzyme CYP7A1. Also, both serum TCA, acting as FXR agonist, and TβMCA, an FXR antagonist [28] were elevated, making it difficult to conclude on the consequences of FXR activity. Unfortunately, due to the lack of sufficient sample amount, bile acid profiles in liver tissues and bile fluid, which could provide further mechanistic insight, could not be determined and need to be investigated in a follow-on study. Further studies are needed to uncover the mechanism underlying the altered bile acid homeostasis in AE and to elucidate the consequences for AE progression.

Evidence from earlier studies of worm infections with the liver as the primary affected site indicate an important role of bile acids in the modulation of worm-host interactions. The liver fluke *Opisthorchis viverrini*, for example, resides in the biliary tree in an environment of very high bile acid concentrations, and a study in infected hamsters found elevated levels of the secondary bile acid DCA [29], suggesting disturbed activity of the microbiome and/or altered intestinal reuptake of bile acids. Another example includes *Echinococcus granulosus*, where the development of the larvae into secondary hydatid cysts is promoted by bile acids and high levels of bile acids are needed for the development of adult worms [30]. Interestingly, a serum metabolome analysis in Beagle dogs infected with *Toxocara canis* showed that the bile acid CA was increased 24 h post-infection but decreased 10 days after infection along with a pronounced increase in TCA and TCDCA, thus indicating a shift from free to taurine-conjugated bile acids [31], similar to the observed effect in the present study in AE. Furthermore, a study in mice infected with cysticerci of *Taenia crassiceps* showed altered hepatic metabolism with enhanced production of taurine and glycine [32]. Although that study did not assess serum bile acids, the enhanced production of these amino acids suggests an increased capacity for bile acid conjugation. These observations may provide an explanation for the observed shift from free to taurine-conjugated bile acids in AE in the present study, with a potentially higher rate of taurine-conjugation in infected livers. Besides an altered hepatic bile

acid metabolism and transport, parasite infections can disturb also intestinal activity and bile acid transport. For example, mice infected with *Trichinella spiralis* displayed gut dysfunction with a decreased bile acid reuptake in the ileum, suggesting an enhanced fecal loss of bile acids [33]. Thus, follow-on experiments should investigate the role of microbiota and intestinal bile acid transport in AE models. Furthermore, it will be important to study the role of FXR, as agonists of this receptor were found to exert protective effects on microbial infections [34–36].

Additionally, the present work showed that ABZ treatment ameliorated *E. multilocularis* infection and almost completely reversed the effects on serum bile acids and gene expression. ABZ treatment itself did not affect bile acid homeostasis, suggesting that hepatotoxic effects seen upon long-term treatment [37] are not due to disruption of bile acid homeostasis, although bile acids can be affected following liver damage.

Ultimately, an improved understanding of the pathways involved in the disturbed bile acid homeostasis may help designing novel therapeutic strategies to combat AE in human, either alone or in combination with benzimidazoles such as ABZ.

Materials and Methods

Chemicals and reagents

Ultrapure water was obtained using a Milli-Q® Integral 3 purification system equipped with an EDS-Pak® Endfilter for the removal of endocrine active substances (Merck Millipore, Burlington, MA, USA). Acetonitrile (HPLC-S Grade) was purchased from Biosolve (Dieuze, France), methanol (CHROMASOLV™ LC-MS grade) from Honeywell (Charlotte, NC, USA), isopropanol (EMSURE® for analysis) from Merck Millipore and formic acid (Puriss. p.a. ≥98%) from Sigma-Aldrich (St. Louis, MO, USA). Bile acids and internal standards were purchased from Sigma-Aldrich or Steraloids (Newport, RI, USA) as described recently [24].

Rabbit monoclonal anti-LMNB1 antibody was purchased from Abcam (Cat#ab133741, RRID:AB_2616597, Cambridge, UK) and horseradish peroxidase (HRP)-conjugated goat anti-rabbit secondary antibody from Cell Signaling (Cat#7074, RRID:AB_2099233, Cambridge, UK). Mouse monoclonal anti-AKR1D1 antibody was obtained from Santa Cruz Biotechnology (Cat# sc-365932, RRID:AB_10917896, Dallas, TX, USA). Rabbit polyclonal antibodies raised against BSEP [38], OATP1A1 [39] and NTCP [40] were described previously. Rabbit polyclonal anti-CYP7A1 antibody was obtained from Abcam (Cat#ab65596, RRID:AB_1566114), rabbit polyclonal anti-CYP7A1 antibody from Santa Cruz Biotechnology (Cat#sc-25536, RRID:AB_2088578) and mouse monoclonal anti-CYP7A1 antibody from

Merck (Cat#MABD42, RRID:AB_2756360, Billerica, MA, USA). Polyvinylidene difluoride (PVDF) membranes (Cat#IPVH00010) and Immobilon Western Chemiluminescence horseradish-peroxidase substrate kit (Cat#WBKLS0050) were obtained from Merck (Darmstadt, Hessen, Germany). HRP-conjugated goat anti-mouse secondary antibody (Cat# A0168, RRID:AB_257867) and all other reagents were purchased from Sigma-Aldrich (St. Louis, MO, USA).

Mice

Female C57BL/6 mice (8 weeks old, n=24) were housed under standard conditions in a conventional daylight/night cycle room. Mice were fed a standard pellet chow and water *ad libitum*. All the experiments were performed in accordance with of the Federation of European Laboratory Animal Science Association (FELASA) guidelines. The experiments performed in this animal study were reviewed and accepted by the cantonal veterinary authority of the Canton of Bern, Switzerland, and were performed in agreement with the guidelines for care and use of laboratory animals (license BE-112/17).

Mice were randomly divided into four groups: (1) non-infected control (CTRL, n=6), (2) *E. multilocularis* infected (AE, n=6), *E. multilocularis* infected treated with albendazole (AE-ABZ, n=6), and (4) non-infected treated with ABZ (CTRL-ABZ, n=6). Animals were examined daily for their health status and changes in weight during the experimental period. All animal experiments were conducted within a laminar flow safety hood. At the end of the experimental part the mice were euthanized using CO_2. Blood was collected and serum was separated by centrifugation at 3000 × g for 15 min. Serum samples were kept at -80°C for later analysis. Liver tissue was immediately collected, frozen in liquid nitrogen, and stored at -80°C for later analysis.

Infection with *E. multilocularis* metacestodes was performed by intraperitoneal injection [41]. Briefly, *E. multilocularis* (isolate H95) was extracted and maintained by serial passages in C57BL/6 mice. Aseptic removal of infectious material from the abdominal cavity of previously infected animals was used for propagation of AE in mice. Collected tissue was grinded through a sterile 50 μm filter, roughly 100 vesicular cysts were suspended in 100 μL sterile PBS and administrated via intraperitoneal injection to groups 2 (AE) and 3 (AE-ABZ). Mice of control groups 1 (CTRL) and 4 (CTRL-ABZ) received 100 μL of sterile PBS.

ABZ treatment started after six weeks of initial infection. Mice of groups 1 (CTRL) and 2 (AE) were administered 100 μL corn oil and groups 3 (AE-ABZ) and 4 (CTRL-ABZ) received 100

µL ABZ in corn oil (200 mg/kg mouse/injection) orally five times per week. The treatment was terminated after 8 weeks by killing the examined animals.

Quantification of bile acids in serum

Bile acids were quantified as described recently [24]. Briefly, 10 µL of serum were diluted 1:4 with water, followed by adding 900 µL of 2-propanol for protein precipitation and a mixture of deuterated internal standards. Extraction was performed by continuous shaking for 30 min at 4°C and centrifugation at 16000 × g for 10 min. Supernatants were transferred to new tubes, evaporated to dryness and reconstituted with 100 µL of methanol to water (1:1, v/v). Samples were analyzed by LC-MS/MS consisting of an Agilent 1290 UPLC coupled to an Agilent 6490 triple quadrupole mass spectrometer equipped with an electrospray ionization (ESI) source (Agilent Technologies, Basel, Switzerland). Chromatographic separation of bile acids was achieved using reversed-phase column (ACQUITY UPLC BEH C18, 1.7 mm, 2.1 µm, 150 mm, Waters, Wexford, Ireland).

Total RNA extraction and qPCR

Total RNA was isolated from liver tissues using the Qiagen RNeasy MiniKit and QIAcub instrument according to the manufacturer's protocol (SABioscience, Frederick, MD, USA). The quality and concentration of RNA was determined using a Nanodrop™ one C (Cat#13-400-519, Thermo Fisher Scientific, Waltham, MA, USA). Only samples with a 260 nm to 280 nm ratio between 1.9 and 2.1 and a 260 nm to 230 nm ratio between 1.5 and 2.0 were further processed. cDNA was synthesized using GoScript Reverse Transcriptase (Cat#A5003, Promega, Madison, WI, USA). The KAPA SYBR Fast Kit (Cat# SFUKB, Merck, Darmstadt, Germany) was used for qPCR analysis, and the reactions were performed on a Rotor Gene Real-Time Cycler (Corbett Research, Sydney, New South Wales, Australia). Data were normalized to the expression levels of the endogenous control gene β-actin. The primers are listed in Supplemental Table 1.

Protein expression / western blot

Approximately 7 mg of frozen liver tissues were homogenized (6500 rpm, 30 s, 4°C, Precellys 24 tissue homogenizer) in 450 µL RIPA buffer (50 mM Tris-HCl, pH 8.0, with 150 mM sodium chloride, 1.0% NP-40, 0.5% sodium deoxycholate, and 0.1% sodium dodecyl sulfate) containing protease inhibitor cocktail (Cat#11836153001, Merck, Darmstadt, Germany) and centrifuged (4 min, 4°C, 16,000 × g). Protein concentration in supernatants was measured using standard bicinchoninic acid assay (Pierce BCA Protein Assay Kit, Thermo Fisher Scientific).

Samples were heated (5 min at 95°C) in Laemmli solubilization buffer (LSB; 60 mM Tris-HCl, 10% glycerol, 0.01% bromophenol blue, 2% sodium dodecyl sulfate, pH 6.8, 5% β-mercaptoethanol) and 20 µg of total protein were separated by 8-14% SDS-PAGE and transferred to PVDF membranes (Immobilon-P Membran, PVDF, pore size: 0.45 µm). The membranes were blocked (1 h, 25°C) in TBST containing 5% nonfat dry milk (5% nonfat dry milk powder in 20 mM Tris-HCl with 0.1% Tween-20) or 1% bovine serum albumin (in 20 mM Tris-HCl with 0.1% Tween-20). AKR1D1 protein expression was determined using mouse monoclonal anti-AKR1D1 antibody (1:1000, 4°C, over-night). The washed membranes were incubated with HRP-conjugated secondary goat anti-mouse antibody (1:4000, 25°C, 1 h). BSEP protein expression was analyzed using a rabbit polyclonal anti-BSEP antibody [38] (1:4000, 4°C, over-night). The membrane was washed and incubated with HRP-conjugated secondary goat anti-rabbit antibody (1:4000, 25°C, 1 h). OATP1A1 protein expression was determined using a rabbit polyclonal anti-OATP1A1 antibody [39] (1:1000, 4°C, over-night) and HRP-conjugated secondary goat anti-rabbit antibody (1:4000, 25°C, 1 h). Protein levels of NTCP were measured using rabbit polyclonal anti-NTCP antibody [40] (1:1000, 4°C over-night) and HRP-conjugated secondary goat anti-rabbit antibody (1:4000). LMNB1 served as loading control and was detected using rabbit monoclonal anti-LMNB1 antibody (1:1000, 4°C, over-night) followed by HRP-conjugated secondary goat anti-rabbit antibody (1:2000, 25°C, 1 h). Protein bands were visualized by Immobilon Western Chemiluminescence HRP substrate and semi-quantitatively analyzed by densitometry, normalized to LMNB1 protein levels, using Image J software (RRID:SCR_003070, version 1.53n).

Data analysis and statistics

For LC-MS/MS data, MassHunter Acquisition Software (Agilent Technologies, Inc.) and MassHunter Quantitative Analysis vB.07.01 (Agilent Technologies, Inc.) was used for quantification. The Kruskal–Wallis test and Dunn's multiple comparison were used to analyze significance of differences between groups. Statistical significance was established at $p<0.05$. Statistical analysis and graphs were performed using GraphPad Prism v5.02 (GraphPad Software).

Conclusions

This work applied LC-MS/MS to quantify bile acids in serum samples of mice infected with E. multilocularis in the absence or presence of the parasitostatic drug ABZ. The results revealed decreased free and unchanged or increased taurine-conjugated bile acids, suggesting the use of ratios of free to taurine-conjugated bile acids as markers for AE and to monitor therapeutic efficacy. Gene expression analyses showed decreases in bile acid synthesis enzymes and in key transport proteins. ABZ, which did not affect bile acid homeostasis itself, reversed the observed effects on serum bile acids and on gene expression. Follow-on studies need to uncover the exact mechanism underlying the observed effects and to evaluate the bile acid ratio markers in AE and its treatment.

Acknowledgments

This study was supported by the Swiss National Science Foundation Grant number 31003A-179400 (to A.O.) and 31003A-179439 (to BLS).

Conflict of Interests

The authors do not have any conflict of interests to report.

Author Contributions

Conceptualization and Methodology, M.W., F. J., and C.G.; Data Acquisition and Analysis, M.W., F. J., S.S., and C.G; Writing-Original Draft Preparation, C.G.; Writing-Review and Editing, M.W., F. J., C.G., S.S., and A.O.; Supervision, A.O.; Project Administration, A.O.; Funding Acquisition, A.O. and B.L.S. All authors have read and agreed to the published version of the manuscript.

Supplementary Materials

The following data are available online, Table S1: Oligonucleotide primers for mRNA quantification by qPCR; Figure S1: Concentrations of individual bile acids quantified in serum of mice from the four treatment groups; Figure S2: Effect of AE on mRNA expression levels of additional bile acid transporters. Figure S3: Increased ratios of taurine-conjugated to unconjugated bile acids in AE.

References

1. Craig, P. Echinococcus multilocularis. *Curr. Opin. Infect. Dis.* **2003**, *16*, 437–444, doi:10.1097/00001432-200310000-00010.

2. Hemphill, A.; Stadelmann, B.; Rufener, R.; Spiliotis, M.; Boubaker, G.; Müller, J.; Müller, N.; Gorgas, D.; Gottstein, B. Treatment of echinococcosis: Albendazole and mebendazole-what else? *Parasite* **2014**, *21*, doi:10.1051/parasite/2014073.

3. Deplazes, P.; Rinaldi, L.; Alvarez Rojas, C.A.; Torgerson, P.R.; Harandi, M.F.; Romig, T.; Antolova, D.; Schurer, J.M.; Lahmar, S.; Cringoli, G.; et al. *Global Distribution of Alveolar and Cystic Echinococcosis*; Elsevier Ltd, 2017; Vol. 95;.

4. Kato, N.; Nonaka, N.; Oku, Y.; Kamiya, M. Modified cellular immune responses in dogs infected with Echinococcus multilocularis. *Parasitol. Res.* **2005**, *95*, 339–345, doi:10.1007/s00436-005-1303-0.

5. Gottstein, B.; Hemphill, A. Echinococcus multilocularis: The parasite-host interplay. *Exp. Parasitol.* 2008, *119*, 447–452.

6. Graeter, T.; Ehing, F.; Oeztuerk, S.; Mason, R.A.; Haenle, M.M.; Kratzer, W.; Seufferlein, T.; Gruener, B. Hepatobiliary complications of alveolar echinococcosis: A long-term follow-up study. *World J. Gastroenterol.* **2015**, *21*, 4925–4932, doi:10.3748/wjg.v21.i16.4925.

7. Lundström-Stadelmann, B.; Rufener, R.; Ritler, D.; Zurbriggen, R.; Hemphill, A. The importance of being parasiticidal… an update on drug development for the treatment of alveolar echinococcosis. *Food Waterborne Parasitol.* **2019**, *15*, doi:10.1016/j.fawpar.2019.e00040.

8. Wen, H.; Vuitton, L.; Tuxun, T.; Li, J.; Vuitton, D.A.; Zhang, W.; McManus, D.P. Echinococcosis: Advances in the 21st century. *Clin. Microbiol. Rev.* **2019**, *32*, 1–39, doi:10.1128/CMR.00075-18.

9. Chiang, J.Y.L.L. Bile acids: regulation of synthesis. *J. Lipid Res.* **2009**, *50*, 1955–1966, doi:10.1194/jlr.R900010-JLR200.

10. Russell, D.W.; Setchell, K.D.R. Bile Acid Biosynthesis. *Biochemistry* **1992**, *31*, 4737–4749.

11. Jia, W.; Xie, G.; Jia, W. Bile acid–microbiota crosstalk in gastrointestinal inflammation and carcinogenesis. *Nat. Rev. Gastroenterol. Hepatol.* **2018**, *15*, 111–128, doi:10.1038/nrgastro.2017.119.

12. Sugita, T.; Amano, K.; Nakano, M.; Masubuchi, N.; Sugihara, M.; Matsuura, T. Analysis of the serum bile acid composition for differential diagnosis in patients with liver disease. *Gastroenterol. Res. Pract.* **2015**, *2015*, 1–10, doi:10.1155/2015/717431.

13. Luo, L.; Aubrecht, J.; Li, D.; Warner, R.L.; Johnson, K.J.; Kenny, J.; Colangelo, J.L. Assessment of serum bile acid profiles as biomarkers of liver injury and liver disease in humans. *PLoS One* **2018**, *13*, e0193824, doi:10.1371/journal.pone.0193824.

14. Manzotti, C.; Casazza, G.; Stimac, T.; Nikolova, D.; Gluud, C. Total serum bile acids or serum bile acid profile, or both, for the diagnosis of intrahepatic cholestasis of pregnancy. *Cochrane Database Syst. Rev.* **2019**, *2019*, doi:10.1002/14651858.CD012546.pub2.

15. Cepa, S.; Potter, D.; Wong, L.; Schutt, L.; Tarrant, J.; Pang, J.; Zhang, X.; Andaya, R.; Salphati, L.; Ran, Y.; et al. Individual serum bile acid profiling in rats aids in human risk assessment of drug-induced liver injury due to BSEP inhibition. *Toxicol. Appl. Pharmacol.* **2018**, *338*, 204–213, doi:10.1016/j.taap.2017.11.007.

16. Makino, I.; Nakagawa, S.; Mashimo, K. Conjugated and Unconjugated Serum Bile Acid Levels in Patients with Hepatobiliary Diseases. *Gastroenterology* **1969**, *56*, 1033–1039, doi:10.1016/S0016-5085(69)80004-1.

17. Dawson, P.A.; Lan, T.; Rao, A. Bile acid transporters. *J. Lipid Res.* **2009**, *50*, 2340–2357, doi:10.1194/jlr.R900012-JLR200.

18. Stieger, B. *The role of the sodium-taurocholate cotransporting polypeptide (NTCP) and of the bile salt export pump (BSEP) in physiology and pathophysiology of bile Formation*; 2011; Vol. 201; ISBN 9783642145407.

19. Cheng, X.; Buckley, D.; Klaassen, C.D. Regulation of hepatic bile acid transporters Ntcp and Bsep expression. *Biochem. Pharmacol.* **2007**, *74*, 1665–1676, doi:10.1016/j.bcp.2007.08.014.

20. Alrefai, W.A.; Gill, R.K. Bile Acid Transporters: Structure, Function, Regulation and Pathophysiological Implications. *Pharm. Res.* **2007**, *24*, 1803–1823, doi:10.1007/s11095-007-9289-1.

21. Slijepcevic, D.; Van De Graaf, S.F.J. Bile Acid Uptake Transporters as Targets for Therapy. *Dig. Dis.* **2017**, *35*, 251–258, doi:10.1159/000450983.

22. Halilbasic, E.; Claudel, T.; Trauner, M. Bile acid transporters and regulatory nuclear receptors in the liver and beyond. *J. Hepatol.* **2013**, *58*, 155–168, doi:10.1016/j.jhep.2012.08.002.

23. Mennone, A.; Soroka, C.J.; Cai, S.-Y.; Harry, K.; Adachi, M.; Hagey, L.; Schuetz, J.D.; Boyer, J.L. Mrp4−/− mice have an impaired cytoprotective response in obstructive cholestasis. *Hepatology* **2006**, *43*, 1013–1021, doi:10.1002/hep.21158.

24. Gómez, C.; Stücheli, S.; Kratschmar, D. V.; Bouitbir, J.; Odermatt, A. Development and Validation of a Highly Sensitive LC-MS/MS Method for the Analysis of Bile Acids in Serum, Plasma, and Liver Tissue Samples. *Metabolites* **2020**, *10*, 282, doi:10.3390/metabo10070282.

25. Liu, Y.H.; Wang, X.G.; Chen, Y.T. Computerized tomography of liver in alveolar echinococcosis treated with albendazole. *Zhonghua Nei Ke Za Zhi* **1993**, *32*, 733–735.

26. Rosenfeld, G.; Nimmo, M.; Hague, C.; Buczkowski, A.; Yoshida, E.M. *Echinococcus presenting as painless jaundice*; 2012; Vol. 26;.

27. Jenniskens, M.; Langouche, L.; Vanwijngaerden, Y.M.; Mesotten, D.; Van den Berghe, G. Cholestatic liver (dys)function during sepsis and other critical illnesses. *Intensive Care Med.* **2016**, *42*, 16–27, doi:10.1007/s00134-015-4054-0.

28. Sayin, S.I.; Wahlström, A.; Felin, J.; Jäntti, S.; Marschall, H.U.; Bamberg, K.; Angelin, B.; Hyötyläinen, T.; Orešič, M.; Bäckhed, F. Gut microbiota regulates bile acid metabolism by reducing the levels of tauro-beta-muricholic acid, a naturally occurring FXR antagonist. *Cell Metab.* **2013**, *17*, 225–235, doi:10.1016/j.cmet.2013.01.003.

29. Vale, N.; Gouveia, M.J.; Botelho, M.; Sripa, B.; Suttiprapa, S.; Rinaldi, G.; Gomes, P.; Brindley, P.J.; Correia da Costa, J.M. Carcinogenic liver fluke Opisthorchis viverrini oxysterols detected by LC-MS/MS survey of soluble fraction parasite extract. *Parasitol. Int.* **2013**, *62*, 535–542, doi:10.1016/j.parint.2013.08.001.

30. Zheng, H.; Zhang, W.; Zhang, L.; Zhang, Z.; Li, J.; Lu, G.; Zhu, Y.; Wang, Y.; Huang, Y.; Liu, J.; et al. The genome of the hydatid tapeworm Echinococcus granulosus. *Nat. Genet.* **2013**, *45*, 1168–1175, doi:10.1038/ng.2757.

31. Zheng, W. Bin; Zou, Y.; Elsheikha, H.M.; Liu, G.H.; Hu, M.H.; Wang, S.L.; Zhu, X.Q. Serum metabolomic alterations in Beagle dogs experimentally infected with Toxocara canis. *Parasites and Vectors* **2019**, *12*, 1–10, doi:10.1186/s13071-019-3703-5.

32. Corbin, I.; Blackburn, B.J.; Wolowiec, T.; Novak, M. Metabolic profile of the liver of mice infected with cysticerci of Taenia crassiceps. *Parasitol. Int.* **1996**, *82*, 273–275, doi:10.1007/s004360050111.

33. Kalia, N.; Hardcastle, J.; Keating, C.; Pelegrin, P.; Grundy, D.; Grasa, L.; Bardhan, K.D. Intestinal secretory and absorptive function in Trichinella spiralis mouse model of postinfective gut dysfunction: Role of bile acids. *Gut* **2008**, *57*, 41–48, doi:10.1136/gut.2006.118356.

34. Zhang, C.; Gan, Y.; Lv, J.W.; Qin, M.Q.; Hu, W.R.; Liu, Z.B.; Ma, L.; Song, B.D.; Li, J.; Jiang, W.Y.; et al. The protective effect of obeticholic acid on lipopolysaccharide-induced disorder of maternal bile acid metabolism in pregnant mice. *Int. Immunopharmacol.* **2020**, *83*, doi:10.1016/j.intimp.2020.106442.

35. Wu, Z.Y.; Li, H.; Li, J.R.; Lv, X.Q.; Jiang, J.D.; Peng, Z.G. Farnesoid X receptor agonist GW4064 indirectly inhibits HCV entry into cells via down-regulating scavenger receptor class B type I. *Eur. J. Pharmacol.* **2019**, *853*, 111–120, doi:10.1016/j.ejphar.2019.03.033.

36. Mouzannar, K.; Fusil, F.; Lacombe, B.; Ollivier, A.; Ménard, C.; Lotteau, V.; Cosset, F.L.; Ramière, C.; André, P. Farnesoid X receptor-α is a proviral host factor for hepatitis B virus that is inhibited by ligands in vitro and in vivo. *FASEB J.* **2019**, *33*, 2472–2483, doi:10.1096/fj.201801181R.

37. Stadelmann, B.; Rufener, R.; Aeschbacher, D.; Spiliotis, M.; Gottstein, B.; Hemphill, A. Screening of the Open Source Malaria Box Reveals an Early Lead Compound for the Treatment of Alveolar Echinococcosis. *PLoS Negl. Trop. Dis.* **2016**, *10*, 1–19, doi:10.1371/journal.pntd.0004535.

38. Gerloff, T.; Stieger, B.; Hagenbuch, B.; Madon, J.; Landmann, L.; Roth, J.; Hofmann, A.F.; Meier, P.J. The sister of P-glycoprotein represents the canalicular bile salt export pump of mammalian liver. *J. Biol. Chem.* **1998**, *273*, 10046–10050, doi:10.1074/jbc.273.16.10046.

39. Eckhardt, U.; Schroeder, A.; Stieger, B.; Höchli, M.; Landmann, L.; Tynes, R.; Meier, P.J.; Hagenbuch, B. Polyspecific substrate uptake by the hepatic organic anion transporter Oatp1 in stably transfected CHO cells. *Am. J. Physiol. - Gastrointest. Liver Physiol.* **1999**, *276*, 1037–1042, doi:10.1152/ajpgi.1999.276.4.g1037.

40. Stieger, B.; Hagenbuch, B.; Landmann, L.; Höchli, M.; Schroeder, A.; Meier, P.J. In situ localization of the hepatocytic na+/taurocholate cotransporting polypeptide in rat liver. *Gastroenterology* **1994**, *107*, 1781–1787, doi:10.1016/0016-5085(94)90821-4.

41. Jebbawi, F. Innate and adaptive immune responses following PD-L1 immune checkpoint blockade in treating chronic alveolar echinococcosis. *N/A* **2020**, N/A.

Supplemental material

Gene	Forward	Reverse
Bsep	TGGTAGAGAAGAGGCGACAAT	TGAGGTAGCCATGTCCAGAA
Ntcp	GCCACACTATGTACCCTACGTC	TTTAGTCGGAAGAGAGCAGAGA
Mrp4	CATCAAGTCCAGGGAAAAGGTTG	GAGGGCCGAGATGAGGGA G
Mrp2	GCTTAGTTCAAGTCTATGGAGT	TCCGGCCGATACCGCACTTGATA
Cyp7a1	CTTGAGGATGGTTCCTATAAC	TTAAAAGTCAAAGGGTCTGG
Cyp27a1	AAAGCTGTGATTAAGGAGAC	CAAACTGTGTATTCTTGGGG
Oatp4	CAACCTGACTGGTTTTCTATG	AAGTGAAGGATCCAATGAAG
Ostα	CTTGACCCCAGGTACACAGC	ATGGGGCAAAGGGTGTTCTT
Ostβ	AGATGCGGCTCCTTGGAATTA	TGGCAGAAAGACAAGTGATG
Oatp1a1	TAGCTTGCCTCCAGTATGCCTT	ACAGGCCAAATGCTATGTATGC
Akr1d1	GAAAAGATAGCAGAAGGGAAGGT	GGGACATGCTCTGTATTCCATAA
β actin	ACCCTGTGCTGCTCACCGA	CTGGATGGCTACGTACATGGCT

Table S1: Oligonucleotide primers for mRNA quantification by qPCR.

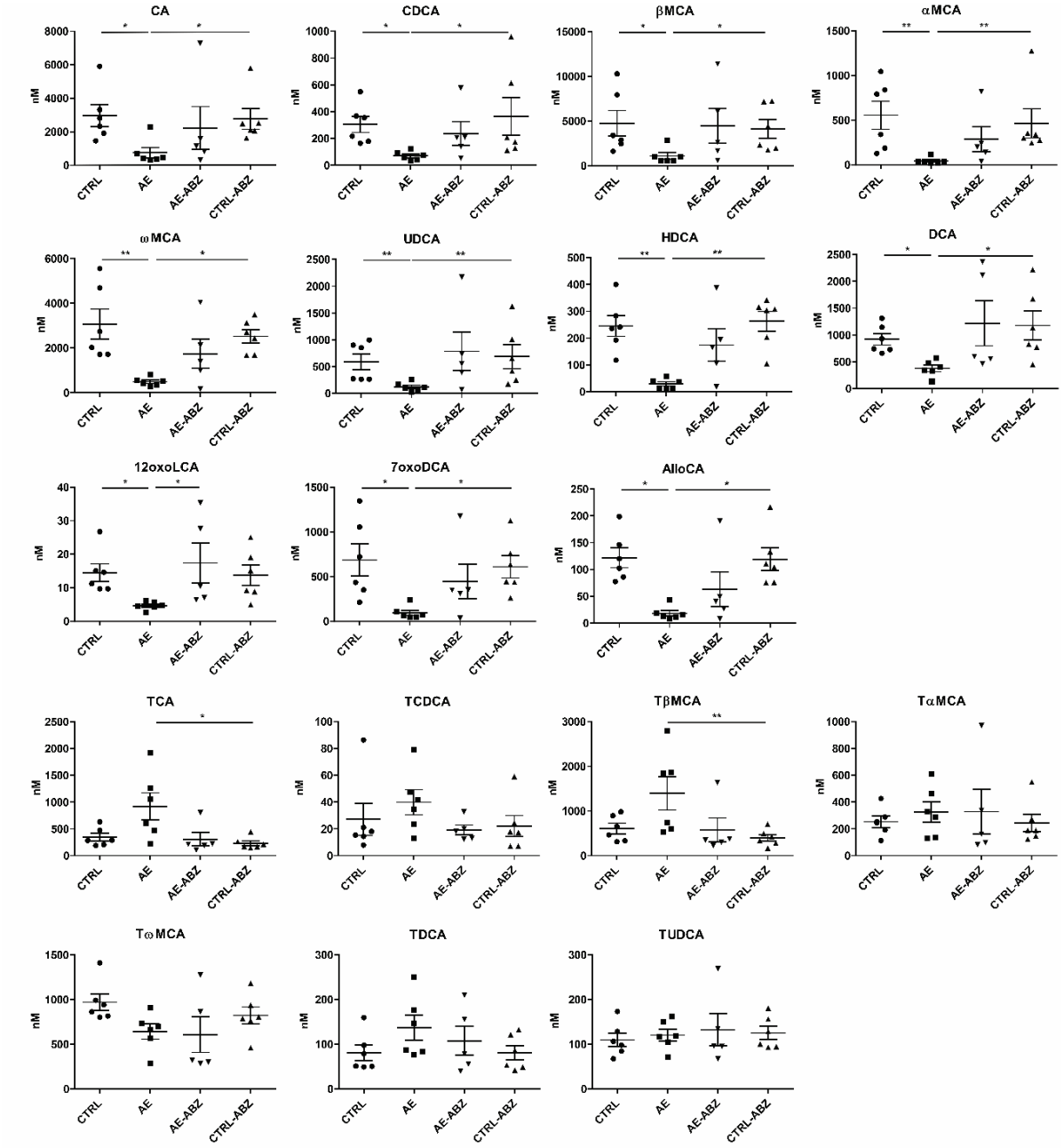

Figure S1. Concentrations of individual bile acids quantified in serum of mice from the four treatment groups. Non-infected control (CTRL, n=6), *E. multilocularis* infected (AE, n=6), non-infected and ABZ treated control (CTRL-ABZ, n=6), and *E. multilocularis* infected and ABZ treated mice (AE-ABZ, n=5, one outlier with aberrant concentrations was removed). Values are expressed as mean ± SD (nM). * $p < 0.05$ and ** $p < 0.01$.

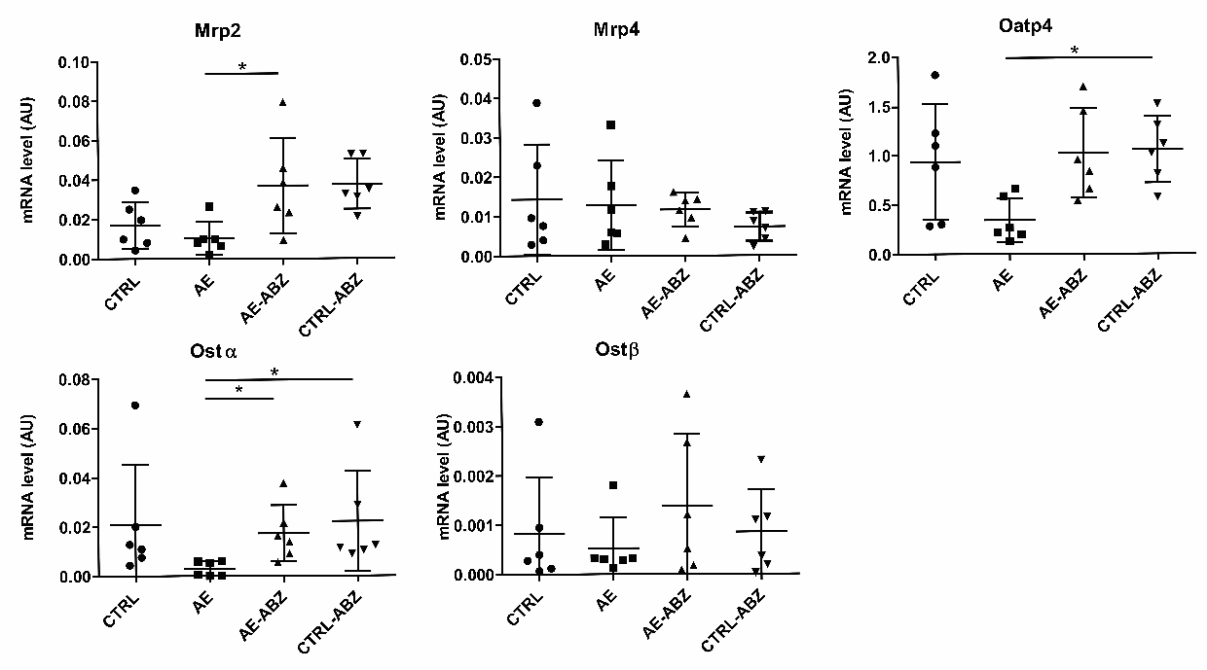

Figure S2. Effect of AE on mRNA expression levels of additional bile acid transporters. The mRNA levels of Mrp2, Mrp4, Ostα, Ostβ, and Oatp4 were determined in liver tissues of non-infected control (CTRL, n=6), *E. multilocularis* infected (AE, n=6) non-infected and ABZ treated control (CTRL-ABZ, n=6), and *E. multilocularis* infected and ABZ treated mice (AE-ABZ, n=6). Values are expressed as mean ± SD. * $p < 0.05$.

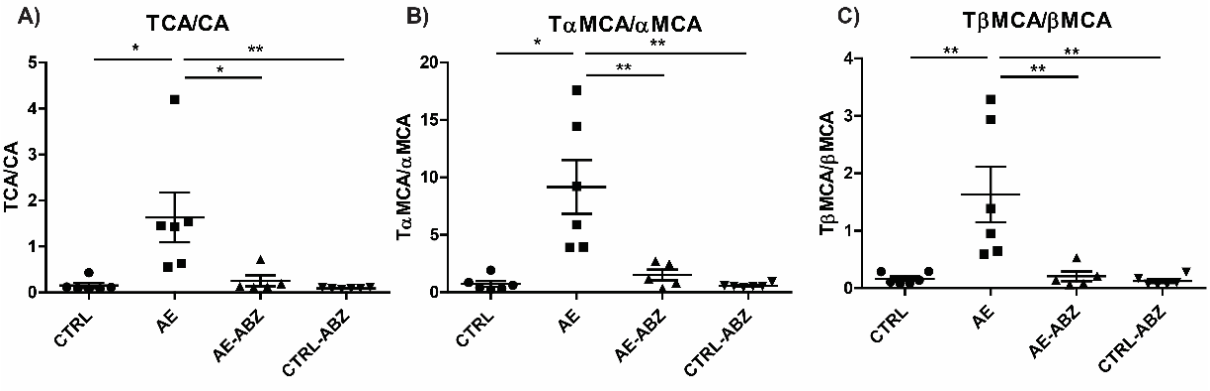

Figure S3: Increased ratios of taurine-conjugated to unconjugated bile acids in AE. The ratios of the concentrations of the taurine-conjugated cholic acid (A), α-muricholic acid (B) and β-muricholic acid (C) to the respective unconjugated bile acid were determined in the four different treatment groups. Non-infected control (CTRL, n=6), *E. multilocularis* infected (AE, n=6), non-infected and ABZ treated control (CTRL-ABZ, n=6), and *E. multilocularis* infected and ABZ treated mice (AE-ABZ, n=5, one outlier with aberrant concentrations was removed). Values are expressed as mean ± SD. * $p < 0.05$ and ** $p < 0.01$.

7 Impact of 11β-HSD1 and H6PD on bile acid profile

7.1 Involvement of 11β-HSD1 and H6PD on the murine bile acid profile

7.1.1 Published article:

The ratio of ursodeoxycholyltaurine to 7-oxolithocholyltaurine serves as a biomarker of decreased 11β-hydroxysteroid dehydrogenase 1 activity in mouse

Michael Weingartner[1†], Simon Stücheli[1†], Denise V. Kratschmar[1], Julia Birk[1], Petra Klusonova[1], Karen E. Chapman[2], Gareth G. Lavery[3], Alex Odermatt[1*]

[1] Division of Molecular and Systems Toxicology, Department of Pharmaceutical Sciences, University of Basel, Basel, Switzerland.

[2] University/BHF Centre for Cardiovascular Science, University of Edinburgh, Queen's Medical Research Institute, Edinburgh, UK.

[3] Institute of Metabolism and Systems Research, University of Birmingham, Birmingham, UK.

[†]These authors contributed equally to the present study.

Contribution to the project:

- Experimental work
- Analysis and interpretation of data
- Graphical work (including figures)
- Revising the manuscript

Received: 29 April 2020 | Revised: 6 December 2020 | Accepted: 27 December 2020

DOI: 10.1111/bph.15367

RESEARCH PAPER - THEMED ISSUE

The ratio of ursodeoxycholyltaurine to 7-oxolithocholyltaurine serves as a biomarker of decreased 11β-hydroxysteroid dehydrogenase 1 activity in mouse

Michael Weingartner[1] | Simon Stücheli[1] | Denise V. Kratschmar[1] | Julia Birk[1] | Petra Klusonova[1] | Karen E. Chapman[2] | Gareth G. Lavery[3] | Alex Odermatt[1]

[1]Division of Molecular and Systems Toxicology, Department of Pharmaceutical Sciences, University of Basel, Basel, Switzerland

[2]Queen's Medical Research Institute, University/BHF Centre for Cardiovascular Science, University of Edinburgh, Edinburgh, UK

[3]Institute of Metabolism and Systems Research, University of Birmingham, Birmingham, UK

Correspondence
Alex Odermatt, Division of Molecular and Systems Toxicology, Department of Pharmaceutical Sciences, University of Basel, Klingelbergstrasse 50, 4056 Basel, Switzerland.
Email: alex.odermatt@unibas.ch

Funding information
Biological Sciences Research Council David Phillips Fellowship, Grant/Award Number: BB/G023468/1 (to G.G.L); Schweizerischer Nationalfonds zur Förderung der Wissenschaftlichen Forschung, Grant/Award Number: 31003A-179400 (to A.O.)

Background and Purpose: 11β-Hydroxysteroid dehydrogenase 1 (11β-HSD1) regulates tissue-specific glucocorticoid metabolism and its impaired expression and activity are associated with major diseases. Pharmacological inhibition of 11β-HSD1 is considered a promising therapeutic strategy. This study investigated whether alternative 7-oxo bile acid substrates of 11β-HSD1 or the ratios to their 7-hydroxy products can serve as biomarkers for decreased enzymatic activity.

Experimental Approach: Bile acid profiles were measured by ultra-HPLC tandem-MS in plasma and liver tissue samples of four different mouse models with decreased 11β-HSD1 activity: global (11KO) and liver-specific 11β-HSD1 knockout mice (11LKO), mice lacking hexose-6-phosphate dehydrogenase (*H6pd*KO) that provides cofactor NADPH for 11β-HSD1 and mice treated with the pharmacological inhibitor carbenoxolone. Additionally, 11β-HSD1 expression and activity were assessed in *H6pd*KO- and carbenoxolone-treated mice.

Key Results: The enzyme product to substrate ratios were more reliable markers of 11β-HSD1 activity than absolute levels due to large inter-individual variations in bile acid concentrations. The ratio of the 7β-hydroxylated ursodeoxycholyltaurine (UDC-Tau) to 7-oxolithocholyltaurine (7oxoLC-Tau) was diminished in plasma and liver tissue of all four mouse models and decreased in *H6pd*KO- and carbenoxolone-treated mice with moderately reduced 11β-HSD1 activity. The persistence of 11β-HSD1 oxoreduction activity in the face of H6PD loss indicates the existence of an alternative NADPH source in the endoplasmic reticulum.

Conclusions and Implications: The plasma UDC-Tau/7oxo-LC-Tau ratio detects decreased 11β-HSD1 oxoreduction activity in different mouse models. This ratio

Abbreviations: 11β-HSD, 11β-hydroxysteroid dehydrogenase; 11KO, global 11β-HSD1 knockout; 11LKO, liver-specific 11β-HSD1 knockout; 7oxoDCA, 7-oxodeoxycholic acid; 7oxoLCA, 7-oxolithocholic acid; 7oxoLC-Tau, 7-oxolithocholyltaurine; CA, cholic acid; CDCA, chenodeoxycholic acid; CDC-Gly, chenodeoxycholylglycine; CDC-Tau, chenodeoxycholyltaurine; CHAPS, 3-[(3-cholamidopropyl)dimethylammonio]-1-propanesulfonate; C-Gly, cholylglycine; C-Tau, cholyltaurine; CTRL, control; DCA, deoxycholic acid; DC-Tau, deoxycholyltaurine; ER, endoplasmic reticulum; H6PD, hexose-6-phosphate dehydrogenase; *H6pd*KO, global *H6pd* knockout; HDCA, hyodeoxycholic acid; LCA, lithocholic acid; LC-Tau, lithocholyltaurine; LLOD, lower limit of detection; MCA, muricholic acid; MOPS, 3-(*N*-morpholino)propanesulfonic acid; MC-Tau, muricholyltaurine; UDCA, ursodeoxycholic acid; UDC-Gly, ursodeoxycholylglycine; UDC-Tau, ursodeoxycholyltaurine; UHPLC–MS/MS, ultra-HPLC tandem-MS.

Michael Weingartner and Simon Stücheli contributed equally to the present study.

may be a useful biomarker of decreased 11β-HSD1 activity in pathophysiological situations or upon pharmacological inhibition.

KEYWORDS
11β-hydroxysteroid dehydrogenase, bile acid, biomarker, disease, glucocorticoid, inhibitor

1 | INTRODUCTION

A dysregulation of glucocorticoid production or a hyposensitivity or hypersensitivity to these hormones has been associated with major diseases such as osteoporosis, cognitive and mood disturbances, cardio-metabolic disorders, cancer and immune diseases (Quax et al., 2013). Besides a tightly regulated synthesis, the tissue-specific metabolism has a key role in mediating glucocorticoid-regulated functions. **11β-Hydroxysteroid dehydrogenase type 1 (11β-HSD1)** and **type 2 (11β-HSD2)** catalyse the conversion of inactive 11-oxoglucocorticoids (cortisone, 11-dehydrocorticosterone) to potent 11β-hydroxyglucocorticoids (cortisol, corticosterone) and the reverse reaction, respectively, and both enzymes are cell specifically expressed (Odermatt & Kratschmar, 2012). 11β-HSD1, although catalysing both oxidation and oxoreduction *in vitro*, predominantly acts as an oxoreductase *in vivo* due to co-expression with hexose-6-phosphate dehydrogenase (H6PD) that provides NADPH co-substrate in the endoplasmic reticulum (ER) (Atanasov et al., 2004; Banhegyi et al., 2004; Lavery et al., 2006) (Figure 1). 11β-HSD1 is essential for the therapeutic effects of pharmacologically administered cortisone and **prednisone** (Hult et al., 1998).

Rodent studies and clinical investigations demonstrated an association between excessive 11β-HSD1 activity and adverse health effects including insulin resistance and type II diabetes mellitus, osteoporosis, impaired wound healing, skin aging, cognitive impairment and glaucoma (Gathercole et al., 2013; Terao & Katayama, 2016; Wyrwoll et al., 2011). Therefore, 11β-HSD1 attracted high attention for potential therapeutic applications and a variety of small molecule inhibitors have been developed in order to assess their effects in preclinical and clinical studies (Feig et al., 2011; Freude et al., 2016; Hardy et al., 2020; Markey et al., 2017; Rosenstock et al., 2010; Schwab et al., 2017; Scott et al., 2014; Tiganescu et al., 2018; Webster et al., 2017; Ye et al., 2017).

Biomarkers of *in vivo* 11β-HSD1 activity can facilitate preclinical and clinical investigations into states of 11β-HSD1 deficiency and the efficacy of pharmacological inhibitors. Currently, decreased ratios of urinary (tetrahydrocorticosterone + allo-tetrahydrocorticosterone)/tetrahydro-11-dehydrocorticosterone and (tetrahydrocortisol + allo-tetrahydrocortisol)/tetrahydrocortisone are used as biomarkers for decreased 11β-HSD1 activity in rodents and human, respectively (Abrahams et al., 2012; Courtney et al., 2008; Freude et al., 2016; Jamieson et al., 1999; Lavery et al., 2013; Webster et al., 2017). However, these ratios require analysis of urine samples (usually 24-h sampling) and small sample volumes remain a challenge when analysing mouse urine. Moreover, the tetrahydro-glucocorticoid ratios are strongly influenced by 11β-HSD2 activity, as are plasma or serum cortisol/cortisone and corticosterone/11-dehydrocorticosterone ratios (Quinkler & Stewart, 2003; Ulick et al., 1979, 1990). These glucocorticoid metabolite ratios are therefore not useful to monitor disease states with altered 11β-HSD1 activity or to assess 11β-HSD1 inhibitors in preclinical and clinical studies.

Besides cortisone and 11-dehydrocorticosterone, 11β-HSD1 can catalyse the carbonyl reduction of a broad range of substrates, including 11-oxygenated glucocorticoids, progestins and androgens, 7-oxygenated androgens, oxysterols and bile acids and several xenobiotics (Odermatt & Klusonova, 2015).

Experiments using human liver microsomes and HEK-293 cells expressing human 11β-HSD1 and H6PD revealed that human 11β-HSD1 can convert the gut microbiota-derived 7-oxolithocholic acid (7oxoLCA) and its taurine- and glycine-conjugated forms to chenodeoxycholic acid (CDCA) and to a lesser extent to the 7β-stereoisomer ursodeoxycholic acid (UDCA) and their taurine- and glycine-conjugated forms (Odermatt et al., 2011). Unlike human 11β-HSD1, the mouse and rat enzymes are not stereo specific and

What is already known

- 11β-HSD1 catalyses the oxoreduction of 11-oxo-glucocorticoids and 7-oxo bile acids.
- Pharmacological inhibition of 11β-HSD1 is considered a promising strategy to treat glucocorticoid-dependent diseases.

What this study adds

- Ratio UDC-Tau/7oxoLC-Tau detects decreased 11β-HSD1 activity in genetically modified mouse models and upon pharmacological inhibition.
- These ratios are better markers of decreased 11β-HSD1 activity than concentrations of individual bile acids.

What is the clinical significance

- UDC-Tau/7oxoLC-Tau ratio provides a biomarker of the efficacy of pharmacological 11β-HSD1 inhibition in preclinical models.

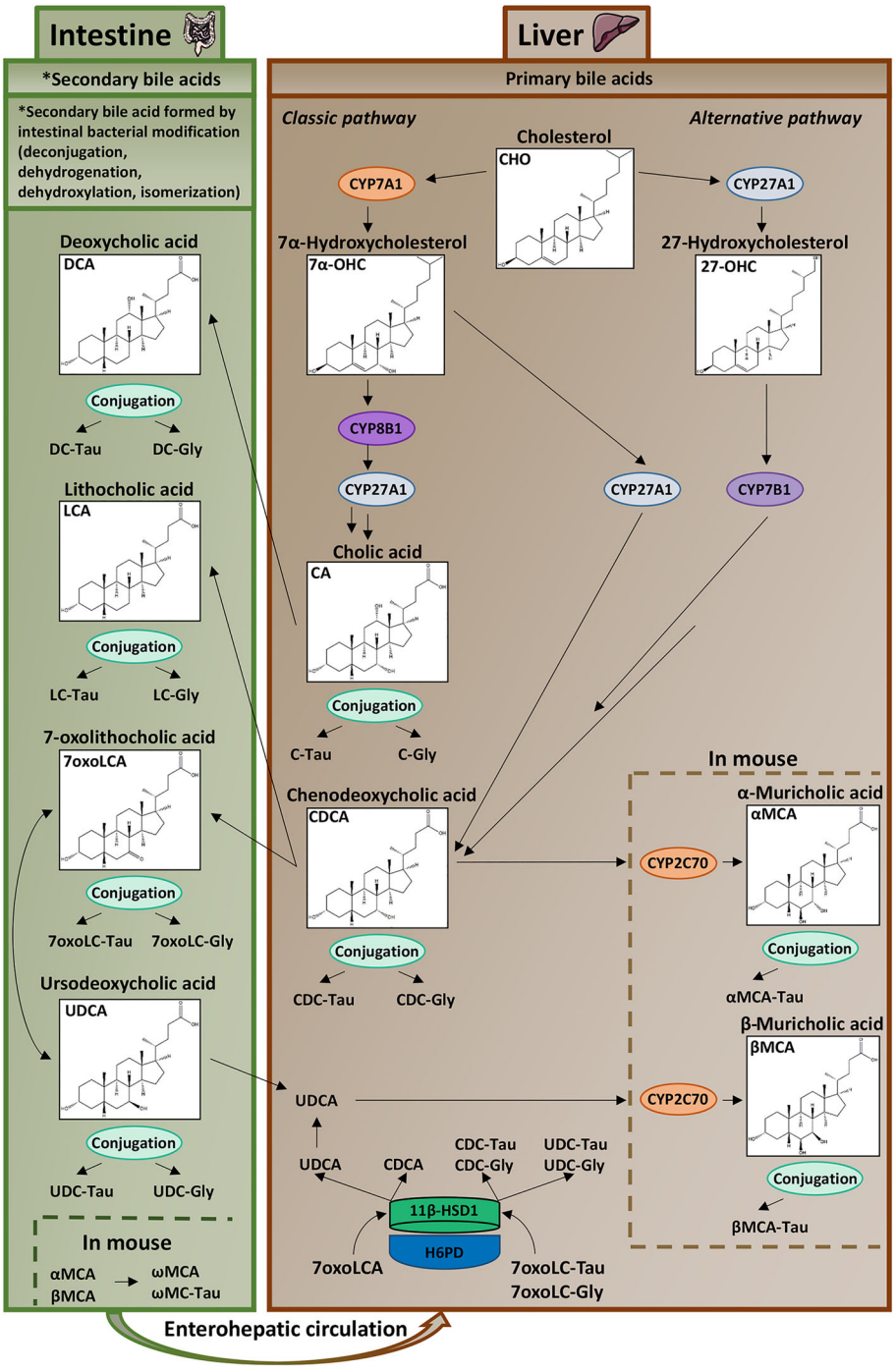

FIGURE 1 Schematic overview of bile acid homeostasis and a role for 11β-HSD1. 11β-HSD1 catalyses the carbonyl reduction of the substrates cortisone and 7oxoLCA to the corresponding products cortisol, and UDCA and CDCA, respectively. 11β-HSD1 activity requires regeneration of cofactor NADPH from $NADP^+$ by H6PD-dependent conversion of glucose-6-phosphate (G6P) to 6-phosphogluconate (6PG). The formation of muricholic acid metabolites by murine Cyp2c70 is indicated

were found to equally produce CDCA and UDCA (Arampatzis et al., 2005). A comparison of liver-specific 11β-HSD1 knockout (11LKO) and control (CTRL) mice showed completely abolished 7oxoLCA oxoreduction in liver microsomes from 11LKO, indicating that 11β-HSD1 is the major if not only enzyme catalysing this reaction in the liver. Plasma and intrahepatic levels of 7oxoLCA and its taurine-conjugated form 7-oxolithocholyltaurine (7oxoLC-Tau) were found to be increased in 11LKO and in global 11β-HSD1 knockout (11KO) mice (Penno et al., 2013). Furthermore, 11KO mice exhibited increased plasma and intrahepatic levels of most bile acids, resembling a mild cholestasis phenotype.

Because we previously observed marked inter-animal variation in circulating bile acid levels, we hypothesized that the ratios of 7β-hydroxy- to 7-oxo-bile acids might serve as biomarkers for decreased 11β-HSD1 activity and that such ratios may be superior markers than individual metabolite levels. We analysed plasma and liver tissue bile acids in 11KO and 11LKO mice in order to calculate the ratios of UDCA/7oxoLCA, CDCA/7oxoLCA, ursodeoxycholyltaurine (UDC-Tau)/7oxoLC-Tau and chenodeoxycholyltaurine (CDC-Tau)/7oxoLC-Tau (Penno et al., 2014; Penno, Morgan, et al., 2013). Furthermore, we analysed bile acid composition in plasma and liver tissue samples from global *H6pd* knockout (*H6pd*KO) mice as a model of decreased

11β-HSD1 oxoreduction activity and from C57BL/6JRj mice treated with the pharmacological inhibitor carbenoxolone.

2 | METHODS

2.1 | Materials

Cholic acid (CA), CDCA, deoxycholic acid (DCA), lithocholic acid (LCA), UDCA, deoxycholylglycine, chenodeoxycholylglycine (CDC-Gly), CDC-Tau, cortisone, cortisol, corticosterone, 11-dehydrocorticosterone, carbenoxolone, [2,2,4,4-$^{2}H_4$]-CA (>98% isotopic purity), [2,2,4,4-$^{2}H_4$]-CDCA (>98% isotopic purity) and [2,2,4,4-$^{2}H_4$]-LCA (>98% isotopic purity) were obtained from Sigma-Aldrich (St. Louis, MO, USA). 7-Oxodeoxycholic acid (7oxoDCA), 7oxoLCA, hyodeoxycholic acid (HDCA), α-muricholic acid (αMCA), βMCA, ωMCA, ursodeoxycholylglycine (UDC-Gly), lithocholyltaurine (LC-Tau), α-muricholyltaurine (αMC-Tau), βMC-Tau, ωMC-Tau and [2,2,4,4-$^{2}H_4$]-DCA (>98% isotopic purity) were purchased from Steraloids (Newport, RI, USA). Cholylglycine (C-Gly), cholyltaurine (C-Tau), deoxycholyltaurine (DC-Tau) and UDC-Tau were obtained from Calbiochem (Läufelfingen, Switzerland). [2,2,4,4-$^{2}H_4$]-UDCA (>98% isotopic purity), [2,2,4,4-$^{2}H_4$]-C-Gly (>98% isotopic purity), [2,2,4,4-$^{2}H_4$]-CDC-Gly (>98% isotopic purity), [2,2,4,4-$^{2}H_4$]-UDC-Gly (>98% isotopic purity) and [2,2,4,6,6,17α,21,21-$^{2}H_8$]-corticosterone were purchased from CDN isotopes (Pointe-Claire, Quebec, Canada). 7oxoLC-Tau and 7-oxolithocholylglycine were a kind gift from Dr. Alan F. Hofmann (University of California, San Diego, CA, USA). [1,2,6,7-^{3}H]-Cortisol was purchased from PerkinElmer (Schwerzenbach, Switzerland), [1,2-^{3}H]-cortisone from Anawa (Kloten, Switzerland) and scintillation cocktail (IrgaSafe Plus) from Zinsser Analytic GmbH (Frankfurt am Main, Germany). Ultra-HPLC tandem-MS (UHPLC–MS/MS)-grade purity methanol, acetonitrile and formic acid were obtained from Biosolve (Dieuze, France). RIPA buffer, β-mercaptoethanol, HRP-conjugated goat anti-mouse secondary antibody (Cat#A0168, LOT#079M4881V, RRID:AB_257867), rabbit polyclonal anti-H6PD antibody (Cat#HPA004824, LOT#A06407 RRID:AB_1079037), dNTPs, KAPA SYBR® FAST qPCR Kit, polyvinylidene difluoride membranes (Cat# IPVH00010, pore size: 0.45 μm), Immobilon Western Chemiluminescence HRP substrate kit and protease inhibitor cocktail were purchased from Merck (Darmstadt, Germany). Rabbit polyclonal anti-11β-HSD1 antibody (Cat#10004303, LOT#126826-12, RRID:AB_10077698) was purchased from Cayman chemicals (Ann Arbor, MI, USA), HRP-conjugated goat anti-rabbit secondary antibody (Cat# 7074, LOT#22, RRID:AB_2099233) from Cell Signaling (Cambridge, UK) and mouse monoclonal anti-β-actin (ACTB) antibody (Cat#sc-47778, LOT#D0618, Clone#C4, RRID:AB_2714189) from Santa Cruz Biotechnology (Dallas, TX, USA). Pierce® bicinchoninic acid protein assay kit and RapidOut DNA Removal kit were purchased from Thermo Fisher Scientific (Waltham, MA, USA), RNeasy Mini Kit from Qiagen (Venlo, Netherlands), GoScript Reverse Transcriptase, Oligo-dT primers and RNasin® Ribonuclease Inhibitor from Promega (Madison, WI, USA) and primers for RT-qPCR from Microsynth AG (Balgach, Switzerland). HEK-293 cells (RRID:CVCL_0045) were purchased from the American Type Culture Collection (Manassas, VA, USA). FBS was obtained from Connectorate (Dietikon, Switzerland). Penicillin/streptomycin and non-essential amino acids were purchased from BioConcept (Allschwil, Switzerland). All other reagents were purchased from Sigma-Aldrich.

2.2 | Animal experimentation

Animal studies are reported in compliance with the ARRIVE guidelines (Percie du Sert et al., 2020) and with the recommendations made by the *British Journal of Pharmacology* (Lilley et al., 2020). 11KO mice were described earlier (Semjonous et al., 2011); a targeted deletion of exon 5 in *Hsd11b1* was obtained using the Cre-loxP system. E14TG2a embryonic stem cells bearing a triloxed allele were injected into C57BL/6J (RRID:IMSR_JAX:000664) blastocysts and chimeric mice were mated with C57BL/6J females. Mice heterozygous for a triloxed allele were crossed with ZP3-Cre to create the null allele and bread to homozygosity to generate 11KO. 11KO were intercrossed to maintain the C57BL/6J/129SvJ background. To obtain 11LKO, the floxed homozygous 11KO mice on the mixed C57BL/6J/129SvJ background were crossed with Albumin-Cre transgenic mice on a C57BL/6J background to target Cre expression to hepatocytes (Lavery et al., 2012). Mice were group housed at the University of Birmingham (Birmingham, UK), in a climate-controlled facility under standard conditions on a 12-h light/dark cycle and fed ad libitum with standard chow (Cat#D12328, Research Diets, Inc., New Brunswick, USA) and free access to drinking water. 11KO, 11LKO and their respective control littermates, 15-week-old male mice, were fasted overnight and anaesthetized with isoflurane prior to collection of blood samples by intra-cardiac puncture and isolation of livers. Samples were collected between 7:00 and 10:00. Studies with 11KO and 11LKO were conducted under Home Office license PPL 70/8516, following approval by the Joint Ethics and Research Governance Committee of the University of Birmingham in accordance with the United Kingdom Animals (Scientific Procedures) Act, 1986 and the EU Directive 2010/63/EU for animal experiments.

For *H6pd*KO mice, a deletion of exons 2 and 3 in *H6pd* was generated by homologous recombination in 129SvJ embryonic stem cells, followed by injection into C57BL/6J blastocysts and resulting chimeric mice were mated with C57BL/6J female mice. Mice were intercrossed to maintain the C57BL/6J/129SvJ background. From these, heterozygous mice were intercrossed to obtain *H6pd*KO mice and control littermates (*H6pd*^{tm1Pmst}, RRID:MGI:3624665, Lavery et al., 2006). *H6pd*KO mice were transferred from the University of Birmingham to the PharmaCenter animal facility (University of Basel, Switzerland), where they were bred and housed. The C57BL/6JRj (RRID:MGI:2670020) mice used for carbenoxolone treatment were purchased from Janvier Laboratories (Saint Berthevin, France). These animals were acclimatized to the new environment (Basel, Switzerland) for 1 week prior to the experiment. Experiments with *H6pd*KO and

C57BL/6JRj mice were performed on 10- to 12-week-old males. The Cantonal Veterinary Office in Basel, Switzerland, approved all procedures (cantonal licenses 2758_26280 and 2758_29462). Mice were group housed in acclimate-controlled facility under standard conditions and a 12-h light/12-h dark cycle with free access to standard chow (Cat#3432, KLIBA NAFAG, Kaiseraugst, Switzerland) and drinking water in ventilated cages. All experiments were performed between 7:00 and 10:00. Mice (not fasted) were killed by exposure to CO_2 until respiratory arrest was observed, absence of pain reaction was verified and cardiac puncture was performed immediately to collect blood. Plasma samples were prepared by centrifugation at 2,000× *g*, 10 min, 4°C and stored at −80°C. Liver tissue samples were either immediately used for 11β-HSD1 activity assay or snap frozen in liquid nitrogen and stored at −80°C until further analysis. In experiments including carbenoxolone treatment, C57BL/6JRj mice received carbenoxolone (100 $mg \cdot kg^{-1} \cdot day^{-1}$) for 4 days via i.p. injection (50 $mg \cdot kg^{-1}$ in PBS at 7:00 and 17:00). The dose was established in preliminary experiments. Animals for the carbenoxolone treatment were distributed, treated and killed in randomized block design (study performed at the beginning of 2017). Only the person handling the animals was aware of the group allocation. Animals which displayed obvious signs of health issues like excessive loss of weight (more than 20%) were excluded from the study. These criteria were defined prior to the study. *H6pd*KO and corresponding control littermates were randomly assigned to groups. Resulting sample material from plasma and liver tissue (experimental unit) was extracted, measured and analysed in a blinded and simple randomized design. Final sample batches from UHPLC–MS/MS analysis were transferred to Excel and unblinded for statistical evaluations.

2.3 | Quantification of bile acids and steroids

Stock solutions of analytes, internal standards (10 $mmol \cdot L^{-1}$) and mixtures of analytes (Penno et al., 2013) were prepared in methanol. Calibrators for plasma analysis of bile acids (25 µl) or steroids (50 µl) were prepared by serial dilution of charcoal-treated mouse plasma spiked with analytes. Calibration curves for liver samples were prepared by serial dilution of analytes in PBS (200 µl, pH 7.2). Calibration curves for cell culture supernatant were prepared by serial dilution in serum-free culture medium. All calibrators were subsequently treated as samples. An internal standard mixture was prepared of $^2H_4$-CA, $^2H_4$-CDCA, $^2H_4$-DCA, $^2H_4$-UDCA, $^2H_4$-C-Gly, $^2H_4$-CDC-Gly, $^2H_4$-UDC-Gly and $^2H_4$-LCA for quantification of bile acids in plasma and liver, of $^2H_4$-CDCA, $^2H_4$-UDCA and $^2H_4$-LCA for bile acid quantification in cell culture supernatant, and of $^2H_8$-corticosterone and $^2H_4$-cortisone for steroid quantification.

Plasma samples (25 µl) for bile acids were diluted with water (75 µl), spiked with internal standard (100 $nmol \cdot L^{-1}$) and subjected to protein precipitation by isopropanol (900 µl). Samples were incubated (30 min, 4°C, 1,400 rpm) and centrifuged (10 min, 4°C, 16,000× *g*), and supernatants were transferred into a fresh tube. Liver samples (approximately 30 mg) were homogenized using a Precellys 24 tissue homogenizer (Bertin Instruments, Montigny-le-Bretonneux, France) (4°C, 3×, 30 s at 6,500 rpm, cycle break 30 s) in water–chloroform–methanol (1 ml, 20/20/60; v/v/v) containing internal standard (100 $nmol \cdot L^{-1}$). Samples were incubated (15 min, 850 rpm, 37°C) and centrifuged (10 min, 25°C, 16,000× *g*), and supernatants (800 µl) were transferred to a fresh tube. All plasma and liver samples were re-extracted and supernatants combined. Cell culture supernatant (450 µl) was spiked with internal standard (100 $nmol \cdot L^{-1}$), subjected to protein precipitation by isopropanol (1 ml), incubated (30 min, 4°C, 1,300 rpm) and centrifuged (10 min, 4°C, 16,000× *g*), and the resulting supernatant was transferred to a fresh tube. Supernatants of plasma (2 ml), liver (1.6 ml), and cell culture (1.45 ml) were evaporated to dryness using a Genevac EZ-2 evaporator (35°C). Plasma samples (50 µl) for steroids were spiked with internal standard (3.3 $nmol \cdot L^{-1}$) and extracted by solid phase extraction (3 cc, Oasis HLB cartridges) as described (Strajhar et al., 2016). Extracts (1 ml) were evaporated to dryness (35°C). Sample residues for bile acid detection were reconstituted (10 min, 25°C, 1,300 rpm) in methanol–water (50/50 v/v; 50 µl for plasma, 200 µl for liver, 50 µl for cell culture supernatant). Sample residues for steroid measurement were reconstituted (10 min, 4°C, 1,300 rpm) in methanol (25 µl). All reconstituted samples were sonicated (10 min, 25°C) and centrifuged (10 min, 25°C, 16,000× *g*), and supernatants were transferred to glass vials.

The injection volume for bile acid detection was 2 µl (plasma and cell culture supernatant) or 3 µl (liver) and for plasma steroids 5 µl. Samples were stored at −20°C until analysis by UHPLC–MS/MS as described earlier (Penno, Arsenijevic, et al., 2013) with minor modifications. Briefly, analytes were detected by multiple reaction monitoring using an Agilent Triple Quadrupole 6490 instrument with electrospray ionization and polarity switching. Analytes were separated with a reverse-phase column (Acquity UPLC BEH C18, 1.7 µm, 2.1 × 150 mm, Waters, Milford, MA, USA) at 65°C within 17.5 min for bile acids or 10 min for steroids. The mobile phase consisted of water–acetonitrile–formic acid (A) (95/5/0.1, v/v/v) and (B) (5/95/0.1, v/v/v). Gradient elution (% mobile phase B) was performed at constant flow (0.63 $ml \cdot min^{-1}$): bile acids, 0–8 min (25%); 8–17.5 min (35–68.25%); 17.5–18 min (68.25–25%); followed by a washout 18–20 min (25–100%) and 20–22 min (100%); and steroids, 0–10 min (25–70%); followed by a washout 10–12 min (100%). The column was post run reconstituted to initial %B within 2 min prior to further injections. Data acquisition and quantification were performed using MassHunter (Acquisition software version B.09.00, build 9.0.9037.0 and quantitative software version B.07.01, build 7.1.524.0).

2.4 | Expression of mouse 11β-HSD1 in HEK-293 cells and oxoreduction of 7oxoLCA

HEK-293 cells, cultured in DMEM supplemented with 10% FBS, 10 $mmol \cdot L^{-1}$ HEPES, 100 $units \cdot ml^{-1}$ penicillin, 0.1 $mg \cdot ml^{-1}$

streptomycin and non-essential amino acids in a 5% CO_2 atmosphere at 37°C, were transfected with plasmid expressing mouse 11β-HSD1 bearing a C-terminal FLAG epitope (Arampatzis et al., 2005) using the calcium phosphate transfection method. The medium was changed 8 h after transfection and after 48 h, cells were cultured in medium containing G-418 as selection antibiotic (800 $\mu g \cdot ml^{-1}$). HEK-293 cells stably expressing mouse 11β-HSD1 are referred to as MO1F cells. Cells (100,000 per well) were seeded on poly-L-lysine coated 24-well plates. After 24 h, cells were washed twice with serum-free culture medium and incubated with 400 $nmol \cdot L^{-1}$ 7oxoLCA, either with or without 5 $\mu mol \cdot L^{-1}$ carbenoxolone, for 0, 4 and 24 h. Of the supernatant, 450 µl was then transferred to a 2-ml tube and stored at −20°C until bile acid quantification.

2.5 | *In vivo* 11β-HSD1 activity assessment

Mice were injected i.p. with 5 $mg \cdot kg^{-1}$ of cortisone (in DMSO). After 10 min, mice were killed by CO_2 asphyxiation and cardiac puncture was performed immediately to collect blood. Plasma was prepared and stored as described above. Plasma was extracted, and cortisone and cortisol levels were measured by UHPLC–MS/MS as described above.

2.6 | *Ex vivo* activity assay

Freshly isolated liver tissue samples (50–100 mg) were placed in tubes, followed by injection of radiolabelled substrate mixture (10 µl containing either 950 $nmol \cdot L^{-1}$ cortisone + 50 $nmol \cdot L^{-1}$ ^{3}H-cortisone [60 $Ci \cdot mmol^{-1}$] or 950 $nmol \cdot L^{-1}$ cortisol + 50 $nmol \cdot L^{-1}$ of ^{3}H-cortisol [70 $Ci \cdot mmol^{-1}$]). Samples were incubated at 16°C for 10 min. Freshly isolated epididymal white adipose tissue samples (50–100 mg) were similarly treated but incubated for 10 min at 37°C. Reactions were terminated by snap freezing and stored at −80°C. For the extraction of cortisone and cortisol, samples were sonicated for 30 s in 200-µl water; 750-µl ethyl acetate was added, followed by incubation (15 min, 4°C, 1,300 rpm) then centrifugation (10 min, 4°C, 16,100× *g*). The supernatant (600 µl) was transferred to a fresh tube and the extraction repeated. Combined supernatants (1.2 ml) were evaporated to dryness in a Genevac EZ-2 (35°C). Residues were reconstituted in 1.2-ml methanol by sonication (10 min, 25°C), followed by evaporation to dryness and storage at −80°C. To the white adipose tissue samples, 1-ml methanol was added, samples were vortexed for 10 s and centrifuged (10 min, 25°C, 21,000× *g*), and supernatant (950 µl) was transferred to a new tube. Samples were evaporated to dryness and stored at −80°C. Residues of the liver and white adipose tissue samples were then reconstituted in 40-µl methanol containing 0.5 $mmol \cdot L^{-1}$ of cortisone and cortisol, by sonication (10 min, 25°C). Samples (10 µl) were then separated on SIL G-25 UV TLC plates (Macherey-Nagel, Düren, Germany) in chloroform/methanol (90/10, v/v) and analysed by scintillation counting.

2.7 | Quantification of mRNA expression by RT-qPCR

Liver samples (approximately 14 mg) were homogenized (6,500 rpm, 4°C, 30 s; Precellys 24 tissue homogenizer in 400-µl RLT buffer [RNeasy Mini, Qiagen]) and centrifuged (3 min, 25°C, 16,000× *g*). Total RNA was isolated from the supernatant (QIAcube, standard protocol for animal tissues and cells, Qiagen) and genomic DNA was removed by DNAse digestion. RNA was quantified and transcribed (500 ng) into cDNA and then qPCR was performed (4-ng cDNA per reaction in triplicate, 40 cycles) using KAPA SYBR® FAST. Oligonucleotide primers: *Hsd11b1* forward 5′-TGG TGC TCT TCC TGG CCT-3′, reverse 5′- CCC AGT GAC AAT CAC TTT CTT T-3′; *H6pd* forward 5′- CTT GAA GGA GAC CAT AGA TGC G-3′, reverse 5′- TGA TGT TGA GAG GCA GTT CC-3′; peptidylpropyl isomerase A (Ppia) forward 5′- CAA ATG CTG GAC CAA ACA CAA ACG-3′, reverse 5′- GTT CAT GCC TTC TTT CAC CTT CCC-3′. Comparison of gene expression was performed using the 2-ΔCT method with *Ppia* as the internal control (Schmittgen & Livak, 2008).

2.8 | Protein expression analysis by Western blot

Liver samples (approximately 6 mg) were homogenized (6,500 rpm, 30 s, 4°C, Precellys 24 tissue homogenizer) in RIPA buffer (450 µl) containing protease inhibitor cocktail and centrifuged (4 min, 4°C, 16,000× *g*). Protein concentration was quantified by using a bicinchoninic acid protein assay and samples were prepared (5 min at 95°C) in Laemmli solubilization buffer (60 $mmol \cdot L^{-1}$ Tris–HCl, 10% glycerol, 0.01% bromophenol blue, 2% sodium dodecyl sulfate, pH 6.8, 5% β-mercaptoethanol). The protein extract (20 µg) was separated by 14% SDS-PAGE and transferred to polyvinylidene difluoride membranes. The membranes were blocked (1 h, 25°C) in TBS-T (5% defatted milk, 20 $mmol \cdot L^{-1}$ Tris buffered saline with 0.1% Tween-20). All antibody dilutions and incubations were performed in TBS-T. 11β-HSD1 protein expression was measured with rabbit polyclonal anti-11β-HSD1 antibody (1:1,000, 4°C, overnight). The membrane was washed and incubated with HRP-conjugated goat anti-rabbit secondary antibody (1:2,000, 25°C, 1 h). H6PD protein expression was determined using rabbit polyclonal anti-H6PD antibody (1:1,000, 4°C, overnight) and HRP-conjugated goat anti-rabbit secondary antibody (1:2,000, 25°C, 1 h). ACTB was detected using mouse monoclonal anti-ACTB antibody (1:1,000, 4°C, overnight) followed by HRP-conjugated goat anti-mouse secondary antibody (1:4,000, 25°C, 1 h). Protein content was visualized by Immobilon Western Chemiluminescence HRP substrate kit. 11β-HSD1 and H6PD were quantified by densitometry normalized to ACTB protein levels using ImageJ software (version 1.53n, RRID:SCR_003070). The Immuno-related procedures used comply with the recommendations made by the *British Journal of Pharmacology* (Alexander et al., 2018).

2.9 | Estimation of NADPH levels in the ER

A method by Rogoff et al. (2010) to estimate NADPH content in liver microsomes was modified. Approximately 100 mg of frozen mouse liver tissue was thawed and homogenized in nine volumes of buffer containing 50 mmol·L^{-1} KCl, 2 mmol·L^{-1} $MgCl_2$, 0.25 mol·L^{-1} sucrose, 20 mmol·L^{-1} Tris, pH 7.5 and protease inhibitor cocktail. The homogenate was centrifuged at 12,000× *g* at 4°C for 20 min and the supernatant was centrifuged again at 105,000× *g* at 4°C for 60 min. The resulting pellet was resuspended in 600 µl homogenization buffer and centrifuged again at 105,000× *g* at 4°C for 60 min. The pellet was then resuspended in 50-µl buffer containing 100 mmol·L^{-1} KCl, 20 mmol·L^{-1} NaCl, 1 mmol·L^{-1} $MgCl_2$, 20 mmol·L^{-1} 3-(*N*-morpholino) propanesulfonic acid (MOPS), pH 7.2 and protease inhibitor cocktail. Protein concentration was determined by using a bicinchoninic acid assay. Resuspended microsomes (protein concentration: 0.5 mg·ml^{-1}) were permeabilized with alamethicin (0.1 mg·mg^{-1} protein) and 3-[(3-cholamidopropyl)dimethylammonio]-1-propanesulfonate (CHAPS) 0.25% (w/v) and EDTA (final concentration of 160 nmol·L^{-1}) were added. Permeabilized microsomes were incubated for 30 min at 4°C with mixing every 5 min. Next, 100 µl of microsomal preparation per well were incubated in a 96-well plate at 25°C for 5 min. The absorbance of total reduced pyridine nucleotides ([NADPH] + [NADH]) was measured at wavelength 335–345 nm. NADPH levels were then determined by incubating 100 µl of permeabilized microsomes with 1.4 IU GSH reductase and 0.75 mmol·L^{-1} of oxidized GSH for 20 min at 25°C whilst shaking at 350 rpm. The resulting decrease in absorbance is a measure of the NADPH content. Absorbance of total reduced pyridine nucleotides was measured against buffer in the absence of microsomes. To determine NADPH content, the absorbance of buffer containing 1.4 IU and 0.75 mmol·L^{-1} GSSG was subtracted from the absorbance obtained from the microsomal preparation. All samples were tested at least in duplicate.

2.10 | Statistical analysis

Sample size ranged from seven to 20 animals. The different sample sizes for the different parameters measured were chosen according to experiments from previous studies where statistically significant effects have been observed. Data were tested for normal distribution by a D'Agostino and Pearson omnibus normality test followed by a non-parametric (two-tailed) Mann–Whitney *U* test for analysis of significance. Data represent mean ± SEM. All statistical analyses were performed using GraphPad Prism 5.0 software (RRID:SCR_002798), and $P < 0.05$ was considered significant. Effect sizes were determined for bile acid concentrations measured by UHPLC–MS/MS in plasma and liver samples from transgene or treated mice versus their respective controls (Table S1). Data represent the effect size calculated based on Cohen's *d* effect size (ES *d*) with correction of unequal sample sizes for the analysis of data from non-parametric analysis (Mann–Whitney *U* test) calculated as Hedges' *g* with corresponding confidence intervals of the effect size. The data and statistical analysis comply with the recommendations of the *British Journal of Pharmacology* on experimental design and analysis in pharmacology (Curtis et al., 2018).

2.11 | Nomenclature of targets and ligands

Key protein targets and ligands in this article are hyperlinked to corresponding entries in the IUPHAR/BPS Guide to PHARMACOLOGY http://www.guidetopharmacology.org and are permanently archived in the Concise Guide to PHARMACOLOGY 2019/20 (Alexander et al., 2019).

3 | RESULTS

3.1 | Increased circulating bile acids in 11KO mice

A previous study indicated that 11β-HSD1 is the only enzyme catalysing the conversion of 7oxoLCA to CDCA and UDCA, reporting an accumulation of 7oxoLCA and 7oxoLC-Tau in plasma and liver tissue from 11KO mice, although with large inter-individual variations (Penno, Morgan, et al., 2013). Here, we have performed a reanalysis of the bile acid profiles from the previous study which shows increased levels of almost all bile acids (primary and secondary, free and conjugated) in plasma samples from 11KO mice, compared to control littermates, resembling a mild cholestasis phenotype (Table 1). However, due to the high inter-individual variations, only some values reached significance. The levels of taurine-conjugated bile acids were almost an order of magnitude higher than those of their free forms. Because glycine-conjugated bile acids are considered to be of minor importance or absent in mice, consistent with previous findings (Alnouti et al., 2008; Garcia-Canaveras et al., 2012; Penno et al., 2014), they were not included in the analysis here. In liver tissue of 11KO, free bile acids were elevated or tended to be elevated, with the exception of the 7β-hydroxylated bile acid βMCA that was fourfold lower. The taurine-conjugated bile acids showed a weak trend to be increased in livers of 11KO. However, 7oxoLC-Tau was more than 10-fold higher in livers of 11KO mice compared to control littermates (CTRL) and UDC-Tau was about 30-fold lower.

3.2 | The UDC-Tau/7oxoLC-Tau ratio in plasma and liver tissue detects the lack of 11β-HSD1 activity in 11KO mice

The concentrations of the 11β-HSD1 substrates 7oxoLCA and 7oxoLC-Tau increased about 20-fold and 40-fold, respectively, in plasma of 11KO compared to CTRL (Table 1, Figure S1), with large inter-individual variations, as reported earlier (Penno, Morgan, et al., 2013). It needs to be noted that no outliers were excluded from the analysis. The respective products of 11β-HSD1, that is, CDCA, UDCA and their taurine-conjugated forms, also were higher in 11KO

TABLE 1 Bile acid profiles in plasma and liver of 11KO mice

	Plasma (nmol·L^{-1})		Liver (fmol·mg^{-1})	
	CTRL	11KO	CTRL	11KO
Analyte	(*n* = 18)	(*n* = 17)	(*n* = 9)	(*n* = 9)
CA	703 ± 323	18,836 ± 10,398	1,673 ± 558	6,911 ± 4,710
CDCA	13.9 ± 3.8	192 ± 108	38 ± 10	49 ± 16
DCA	289 ± 71	1,603 ± 687	239 ± 53	318 ± 88
7oxoDCA	908 ± 439	29,886 ± 14,966*	1,396 ± 455	13,196 ± 9,162
HDCA	17.7 ± 4.0	236 ± 70*	74 ± 15	343 ± 124*
αMCA	101 ± 48	4,578 ± 2,091*	340 ± 90	4,018 ± 2,136*
βMCA	572 ± 165	826 ± 355	3,457 ± 968	897 ± 387*
ωMCA	604 ± 190	2,351 ± 1,182	1,461 ± 450	1,506 ± 644
UDCA	69 ± 18	486 ± 223	168 ± 38	291 ± 184
7oxoLCA	10.2 ± 3.1	201 ± 100*	18.2 ± 4.4	67 ± 24
αMCA/βMCA	0.22 ± 0.05	9.1 ± 5.0*	0.12 ± 0.21	3.65 ± 0.60*
UDCA/7oxoLCA	41 ± 18	16.9 ± 13.8*	13.7 ± 4.2	4.5 ± 1.2
CDCA/7oxoLCA	4.6 ± 2.4	1.93 ± 0.98	2.3 ± 0.5	1.03 ± 0.14*
C-Tau	3,578 ± 2,331	110,304 ± 94,731	32,352 ± 7,659	51,276 ± 15,249
CDC-Tau	266 ± 175	3,961 ± 3,339	991 ± 185	1,980 ± 765
DC-Tau	1,412 ± 863	12,212 ± 9,988	5,760 ± 1,324	7,711 ± 2,315
LC-Tau	6.3 ± 4.5	89 ± 69	59 ± 11	85 ± 21
αMCA-Tau + βMCA-Tau	4,203 ± 2,384	29,184 ± 23,757	19,635 ± 4,314	20,556 ± 7,700
ωMCA-Tau	5,132 ± 2,836	17,184 ± 13,056	24,404 ± 4,625	14,609 ± 4,313
UDC-Tau	331 ± 185	2,947 ± 2,920	1,673 ± 350	53 ± 27*
7oxoLC-Tau	143 ± 77	5,931 ± 3,962	174 ± 34	2,718 ± 1,135*
UDC-Tau/7oxoLC-Tau	2.2 ± 0.3	0.30 ± 0.11*	9.5 ± 1.6	0.020 ± 0.004*
CDC-Tau/7oxoLC-Tau	1.05 ± 0.23	0.63 ± 0.09	6.9 ± 1.1	0.83 ± 0.06*
Sum primary BA	1,458 ± 493.0	23,782 ± 12,339	5,675 ± 1,570	12,167 ± 7,413
Sum primary BA-Tau	8,379 ± 4,391	137,957 ± 117,634	54,651 ± 12,386	73,866 ± 23,548

Note: The results represent mean ± SEM (nmol·L^{-1} and fmol·mg^{-1} for plasma and liver, respectively). Analyte concentrations with a S/N ≤ 3 represent the LLOD of the UHPLC–MS/MS method. Samples yielding a concentration below LLOD were included as LLOD/2 (nmol·L^{-1} and fmol·mg^{-1}, respectively) in the calculations of a specific analyte. Blue- and yellow-coloured boxes indicate statistically significant increases and decreases, respectively. Unequal group sizes reflect exclusion of one plasma sample due to insufficient collection of blood sample volume and the availability of only nine livers due to the use of nine randomly assigned livers for gene expression analyses in a previous study.

Abbreviations: 11KO, global *Hsd11b1* knockout; CTRL, control littermates.

*$P < 0.05$ significantly different as indicated; non-parametric, Mann–Whitney *U* test (two-tailed).

plasma compared to CTRL, although clearly less pronounced than the 7-oxo metabolites. In liver tissue, 7oxoLCA was 3.7-fold and 7oxoLC-Tau 15-fold higher in 11KO compared to CTRL (Table 1, Figure S2). The respective products CDCA, UDCA and CDC-Tau tended to increase, whereas UDC-Tau decreased 30-fold. Importantly, the 11β-HSD1 product to substrate ratios (the ratio of CDCA and UDCA and their taurine-conjugated forms to the respective 7oxo metabolites) showed less variation than the individual metabolite concentrations (Figures S1 and S2). UDC-Tau/7oxoLC-Tau was the most distinguishing marker for the lack of 11β-HSD1 activity when considering both plasma and liver tissue samples (Table 1, Figure 2).

Interestingly, in plasma and liver tissue of 11KO mice, the levels of the 7α-hydroxylated bile acid αMCA were 45-fold and 12-fold higher than in CTRL, whereas its 7β-hydroxylated form βMCA was not different in CTRL plasma but 3.8-fold lower in liver tissue (Table 1). The respective αMCA/βMCA ratios were 40-fold and 30-fold higher in 11KO compared to CTRL, suggesting a possible effect of 11β-HSD1 on isomerization. Due to a limitation of the applied analytical method, αMC-Tau and βMC-Tau could not be separated and therefore, the corresponding ratio not determined.

3.3 | 11LKO mice exhibit decreased plasma and liver tissue UDC-Tau/7oxoLC-Tau ratios

The liver shows the highest 11β-HSD1 expression; nevertheless, an earlier study reported 25–30% residual *in vivo* (whole body) 11β-HSD1 oxoreduction activity in 11LKO mice lacking 11β-HSD1

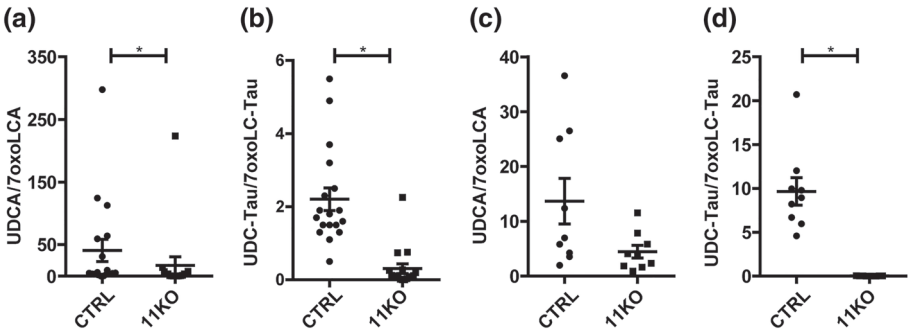

FIGURE 2 Plasma and liver tissue UDCA/7oxoLCA and UDC-Tau/7oxoLC-Tau ratios in 11KO mice. (a) UDCA/7oxoLCA ratios and (b) UDC-Tau/7oxoLC-Tau ratios in plasma of 11KO mice (CTRL n = 18; 11KO n = 17); (c) UDCA/7oxoLCA ratios and d) UDC-Tau/7oxoLC-Tau ratios in liver tissue of 11KO mice (CTRL n = 9; 11KO n = 9). Analyte concentrations defined by a S/N ≤ 3 represent the LLOD of the UHPLC–MS/MS method. Samples yielding a concentration below LLOD were included as LLOD/2 (nmol·L^{-1} and fmol·mg^{-1} for plasma and liver, respectively) in the calculations of a specific analyte. The results represent mean ± SEM. *P < 0.05 significantly different as indicated; non-parametric, Mann–Whitney U test (two-tailed). Unequal group sizes reflect exclusion of one plasma sample due to insufficient collection of blood sample volume and the availability of only nine livers due to the use of nine randomly assigned livers for gene expression analysis in a previous study

specifically in hepatocytes (Lavery et al., 2006). Thus, 11LKO mice represent a model of reduced 11β-HSD1 activity but with complete loss of activity in hepatocytes.

The free bile acids in plasma and liver tissue of 11LKO tended to be higher compared to CTRL (Table 2), an effect considerably more pronounced in 11KO (Table 1). 7oxoLCA was 11-fold higher in plasma and twofold in liver tissue (Table 2). The plasma UDCA/7oxoLCA and CDCA/7oxoLCA ratios were sevenfold and twofold lower in 11LKO compared to CTRL, whilst remaining unchanged in liver tissue. Plasma 7oxoLC-Tau was slightly more abundant than its free form and it was 20-fold higher in 11LKO than in CTRL, whilst CDC-Tau was not different, and UDC-Tau was sixfold lower in 11LKO, resulting in significantly decreased product to substrate ratios (Table 2, Figure 3; see also Figure S3 for individual data points). In liver tissue, 7oxoLC-Tau was 5.5-fold increased, CDC-Tau not different and UDC-Tau threefold lower in 11LKO compared to CTRL (Table 2; see also Figure S4). In agreement with 11KO, the CDC-Tau/7oxoLC-Tau and UDC-Tau/7oxoLC-Tau ratios were lower in 11LKO liver tissue compared to CTRL (fivefold and 16-fold, respectively). The αMCA/βMCA ratio was 3.3-fold higher in plasma and 7.3-fold in liver tissue of 11LKO (Table 2).

3.4 | *H6pd*KO mice exhibit moderately decreased 11β-HSD1 oxoreduction activity

Previous characterization of *H6pd*KO mice suggested, based on experiments using microsomal preparations, a complete loss of 11β-HSD1 oxoreduction activity (Lavery et al., 2006). To assess the conversion of 11-oxo- to 11β-hydroxyglucocorticoids *in vivo*, *H6pd*KO mice and control littermates received cortisone i.p. and were killed 10 min later, followed by measuring formed cortisol. 11β-HSD1 oxoreduction activity was reduced to approximately 60% of the level in control mice (Figure 4a), despite comparable hepatic 11β-HSD1 mRNA and protein expression (Figure 4b,c). As expected, H6PD mRNA and protein expression were abolished in *H6pd*KO. Similarly, *ex vivo* oxoreduction was reduced in liver of *H6pd*KO mice to half the activity of controls (Figure 4d). There was a corresponding increase in dehydrogenase activity to approximately fivefold the level in control liver (Figure 4e). The ratio of oxoreduction to dehydrogenase activity was estimated to be about five in CTRL and 0.5 in *H6pd*KO liver tissue. Similar experiments in white adipose tissue showed approximately 40% residual oxoreduction activity in *H6pd*KO compared to CTRL, whilst dehydrogenase activity increased 30-fold to 40-fold (Figure S5). Thus, in contrast to the expectation of a complete loss of 11β-HSD1 oxoreduction activity, these results revealed a moderately decreased oxoreduction in *H6pd*KO mice despite an increase in dehydrogenase activity.

An estimation of the impact of the lack of H6PD on NADPH levels in the ER using liver microsomes indicated that the content of total reduced pyridine nucleotides (NADPH + NADH) did not differ between control and *H6pd*KO (Figure 4f), but NADPH content of *H6pd*KO mouse liver microsomes was moderately lower by approximately 30% compared to control (Figure 4g).

3.5 | The UDC-Tau/7oxoLC-Tau ratio detects decreased 11β-HSD1 oxoreductase activity in *H6pd*KO mice

Next, plasma and liver tissue bile acid profiles between *H6pd*KO and control mice were compared. Unlike in 11KO, primary and taurine-conjugated bile acids were not generally elevated in plasma of *H6pd*KO mice (Table 3). 7oxoLCA was 1.8-fold higher in *H6pd*KO plasma, whilst UDCA was threefold lower and CDCA not different between the two genotypes. The ratio of CDCA/7oxoLCA only tended lower, whereas UDCA/7oxoLCA was 3.7-fold lower in *H6pd*KO plasma (Figure 4h). 7oxoLC-Tau was about ninefold higher in *H6pd*KO plasma than in CTRL, whereas UDC-Tau was not different and CDC-Tau tended to increase. Both ratios CDC-Tau/7oxoLC-Tau and UDC-Tau/7oxoLC-Tau (Figure 4h; see also Figure S6) were

TABLE 2 Bile acid profiles in plasma and liver of 11LKO mice

	Plasma (nmol·L^{-1})		Liver (fmol·mg^{-1})	
	CTRL	11LKO	CTRL	11LKO
Analyte	(*n* = 17)	(*n* = 16)	(*n* = 17)	(*n* = 16)
CA	528 ± 87	3,141 ± 1,837	2,004 ± 606	5,589 ± 1,271*
CDCA	15.2 ± 3.3	42 ± 14	17.4 ± 3.1	26 ± 6
DCA	148 ± 33	184 ± 87	66 ± 22	94 ± 32
7oxoDCA	188 ± 55	2,306 ± 1,488	985 ± 455	6,477 ± 1,679*
HDCA	25 ± 5	33 ± 12	33 ± 8	82 ± 23
αMCA	67 ± 17	425 ± 285	356 ± 91	2,685 ± 749*
βMCA	904 ± 145	276 ± 104*	2,693 ± 619	2,423 ± 511
ωMCA	888 ± 149	937 ± 479	1,268 ± 356	3,178 ± 763
UDCA	75 ± 10	77 ± 37	103 ± 26	249 ± 52*
7oxoLCA	6.8 ± 1.3	76 ± 38	28 ± 5	63 ± 17
αMCA/βMCA	0.18 ± 0.10	0.60 ± 0.09*	0.13 ± 0.02	0.96 ± 0.13*
UDCA/7oxoLCA	32 ± 12	4.5 ± 2.4*	5.0 ± 1.1	6.0 ± 1.0
CDCA/7oxoLCA	3.9 ± 1.6	1.86 ± 0.97*	0.91 ± 0.12	0.74 ± 0.12
C-Tau	2,993 ± 1,687	2,091 ± 1,778	59,664 ± 15,995	66,470 ± 11,753
CDC-Tau	76 ± 48	78 ± 53	2,355 ± 515	2,667 ± 536
DC-Tau	200 ± 106	289 ± 149	3,843 ± 1,822	2,367 ± 735
LC-Tau	16.0 ± 0.7	1.81 ± 0.70	50 ± 13	40 ± 9
αMCA-Tau + βMCA-Tau	1,854 ± 851	2,878 ± 1,923	30,702 ± 6,384	29,952 ± 6,056
ωMCA-Tau	2,133 ± 1,324	1,286 ± 1,088	32,951 ± 6,074	28,000 ± 4,968
UDC-Tau	103 ± 60	16.1 ± 9.8*	2,754 ± 531	886 ± 489*
7oxoLC-Tau	9.1 ± 3.3	187 ± 110	560 ± 123	3,101 ± 935*
UDC-Tau/7oxoLC-Tau	158 ± 149	0.72 ± 0.22*	6.5 ± 1.1	0.40 ± 0.22*
CDC-Tau/7oxoLC-Tau	122 ± 120	0.78 ± 0.12*	5.6 ± 1.3	1.09 ± 0.11*
Sum primary BA	1,588 ± 179	3,962 ± 2,156	5,174 ± 1,266	10,971 ± 2,449
Sum primary BA-Tau	5,026 ± 2,272	5,063 ± 3,625	95,475 ± 19,081	99,975 ± 17,536

Note: The results represent mean ± SEM (nmol·L^{-1} and fmol·mg^{-1} for plasma and liver, respectively). Analyte concentrations defined by a S/N ≤ 3 represent the LLOD of the UHPLC–MS/MS method. Samples yielding a concentration below LLOD were included as LLOD/2 (nmol·L^{-1} and fmol·mg^{-1}, respectively) in the calculations of a specific analyte. Blue- and yellow-coloured boxes indicate statistically significant increases and decreases, respectively. Unequal group sizes reflect exclusion of one 11LKO animal due to unexpected health issues prior to reaching the age for the experiment.
Abbreviations: 11LKO, liver-specific *Hsd11b1* knockout; CTRL, control littermates.
*$P < 0.05$, significantly different as indicated; non-parametric, Mann–Whitney *U* test (two-tailed).

significantly lower in *H6pd*KO plasma. In agreement with 11KO and 11LKO, these observations were supported by a similar bile acid profile in liver tissue with almost threefold increased 7oxoLCA and twofold decreased UDCA in *H6pd*KO but no difference in CDCA (Table 3, Figure S7). The CDCA/7oxoLCA and UDCA/7oxoLCA ratios were twofold and fivefold lower, respectively, in *H6pd*KO liver tissue (Table 3, Figure 4i). The levels of the taurine-conjugated bile acids were about an order of magnitude higher than those of their free forms. 7oxoLC-Tau was fourfold higher in *H6pd*KO compared to control, but due to inter-individual variation, the value did not reach significance. CDC-Tau was not different between the two genotypes, whilst UDC-Tau decreased twofold. The ratios CDC-Tau/7oxoLC-Tau and UDC-Tau/7oxoLC-Tau (Figure 4i; see also Figure S7) were threefold and fivefold lower, respectively, in *H6pd*KO liver tissue.

As seen in 11KO and 11LKO, the ratio of αMCA/βMCA was significantly higher in *H6pd*KO plasma (fourfold) and liver tissue (fivefold). In *H6pd*KO mice, this was due to significantly lower βMCA. αMCA was not different between the genotypes (Table 3).

3.6 | The UDC-Tau/7oxoLC-Tau ratio detects pharmacologically diminished 11β-HSD1 activity

The UDC-Tau/7oxoLC-Tau ratio detected the reduced 11β-HSD1 activity due to genetic alteration of its expression (11KO, 11LKO) or reaction direction (*H6pd*KO). To see if enzyme inhibition without genetic manipulation also can be detected, the known 11β-HSD1 inhibitor carbenoxolone was used. Inhibition by carbenoxolone of

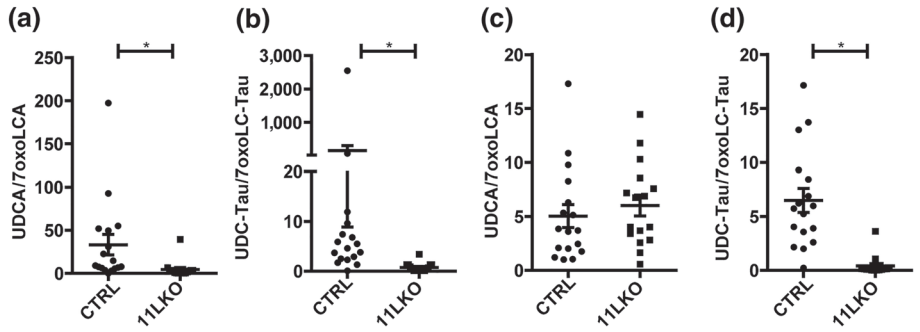

FIGURE 3 Plasma and liver tissue UDCA/7oxoLCA and UDC-Tau/7oxoLC-Tau ratios in 11LKO mice. (a) UDCA/7oxoLCA ratios and (b) UDC-Tau/7oxoLC-Tau ratios in plasma of 11LKO mice (CTRL n = 17; 11LKO n = 16); (c) UDCA/7oxoLCA ratios and (d) UDC-Tau/7oxoLC-Tau ratios in liver tissue of 11LKO mice (CTRL n = 17; 11LKO n = 16). Analyte concentrations defined by a S/N ≤ 3 represent the LLOD of the UHPLC–MS/MS method. Samples yielding a concentration below LLOD were included as LLOD/2 (nmol·L^{-1} and fmol·mg^{-1} for plasma and liver, respectively) in the calculations of a specific analyte. The results represent mean ± SEM. *P < 0.05 significantly different as indicated; non-parametric, Mann–Whitney U test (two-tailed). Unequal group sizes reflect exclusion of one 11LKO animal due to unexpected health issues prior to reaching the age for the experiment

11β-HSD1-dependent metabolism of 7oxoLCA was first assessed *in vitro*. HEK-293 cells stably expressing murine 11β-HSD1 (MO1F cells) showed a time-dependent conversion of 7oxoLCA to comparable amounts of UDCA and CDCA, with almost complete metabolism of 7oxoLCA after 24 h (Figure S8). Incubation with carbenoxolone almost fully blocked the formation of UDCA and CDCA, supporting the use of product/substrate ratios as markers of 11β-HSD1 activity.

Next, mice were treated i.p. with 100 mg·kg^{-1}·day^{-1} of carbenoxolone for 4 days. carbenoxolone treatment decreased cortisone to cortisol conversion by approximately 30%, revealing moderate 11β-HSD1 inhibition (Figure 5a). Interestingly, analysis of mRNA showed a reduction in *Hsd11b1* mRNA expression and a trend for increased *H6pd* mRNA (Figure 5b). This was corroborated by similar effects on H6PD (30% increase) and 11β-HSD1 (50–60% decrease) protein expression (Figure 5c), suggesting that besides pharmacological inhibition, a reduced expression contributed to the lower 11β-HSD1 activity in this model.

Analysis of bile acid profiles revealed that the sum of free primary bile acids tended to be lower (2.5-fold) in plasma upon carbenoxolone treatment, whereas taurine-conjugated primary bile acids seemed to be not affected (Table 4). 7oxoLCA concentrations were below the lower limit of detection (LLOD) in plasma and liver tissue samples in this mouse cohort, so the respective product/substrate ratios with UDCA and CDCA could not be calculated. In plasma of carbenoxolone-treated mice, 7oxoLC-Tau tended to increase, whilst UDC-Tau and CDC-Tau were not affected by carbenoxolone (Figure S9). Nevertheless, CDC-Tau/7oxoLC-Tau and UDC-Tau/7oxoLC-Tau (Figure 5d; see also Figure S9) were 1.6-fold and twofold lower in plasma of carbenoxolone-treated mice. In liver tissue, only UDC-Tau/7oxoLC-Tau was predictive for decreased 11β-HSD1 activity (2.6-fold decreased; Table 4, Figures 5e and S10).

In contrast to the other three mouse models, the αMCA/βMCA ratio was unchanged in plasma and even threefold lower in liver tissue; thus, this ratio is not indicative of altered 11β-HSD1 activity.

4 | DISCUSSION

This proof-of-concept study proposes that the UDC-Tau/7oxoLC-Tau ratio can serve as a biomarker for decreased 11β-HSD1 activity *in vivo*. The UDC-Tau/7oxoLC-Tau ratio in plasma and liver tissue successfully detected complete loss of 11β-HSD1 activity in 11KO mice, loss of hepatic 11β-HSD1 activity in 11LKO mice and moderately decreased oxoreduction activity in *H6pd*KO- and carbenoxolone-treated mice. Of note, the four models differed with respect to their genetic background (11KO, 11LKO and *H6pd*KO on a mixed C57BL/6J/129SvJ background, carbenoxolone group were C57BL/6JRj) that can affect lipid and bile acid homeostasis (Jolley et al., 1999), feeding regimen (11KO and 11LKO fasted overnight, the other two models *ad libitum* feeding; some differences in the composition of the chow) and environment (different animal facilities) that can impact the microbiome and thereby influence bile acid homeostasis (Rausch et al., 2016). A biomarker reporting decreased 11β-HSD1 oxoreduction activity in plasma opens the possibility for non-invasive applications in preclinical studies of pharmacological inhibitors for potential therapeutic applications; whether it can also be used to explore the pathophysiological role of 11β-HSD1 in situations of elevated activity remains to be investigated (Gathercole et al., 2013). Determination of this ratio in liver tissue at the end of the study can provide additional information.

The plasma UDCA/7oxoLCA ratio was also a marker for decreased 11β-HSD1 activity. However, because the levels of free bile acids are lower than those of their taurine-conjugated forms and were below the LLOD in some mice, this is likely to be less useful practically than the ratio of the taurine-conjugated metabolites. Whilst in mice and rats taurine-conjugated bile acids are predominant and the UDC-Tau/7oxoLC-Tau ratio is easier to assess, the ratio of the free UDCA/7oxoLCA has the advantage to be species independent, as glycine-conjugated bile acids are predominant in human and other higher mammals (Alnouti et al., 2008; Garcia-Canaveras et al., 2012; Penno et al., 2014). Improvements of the analytical

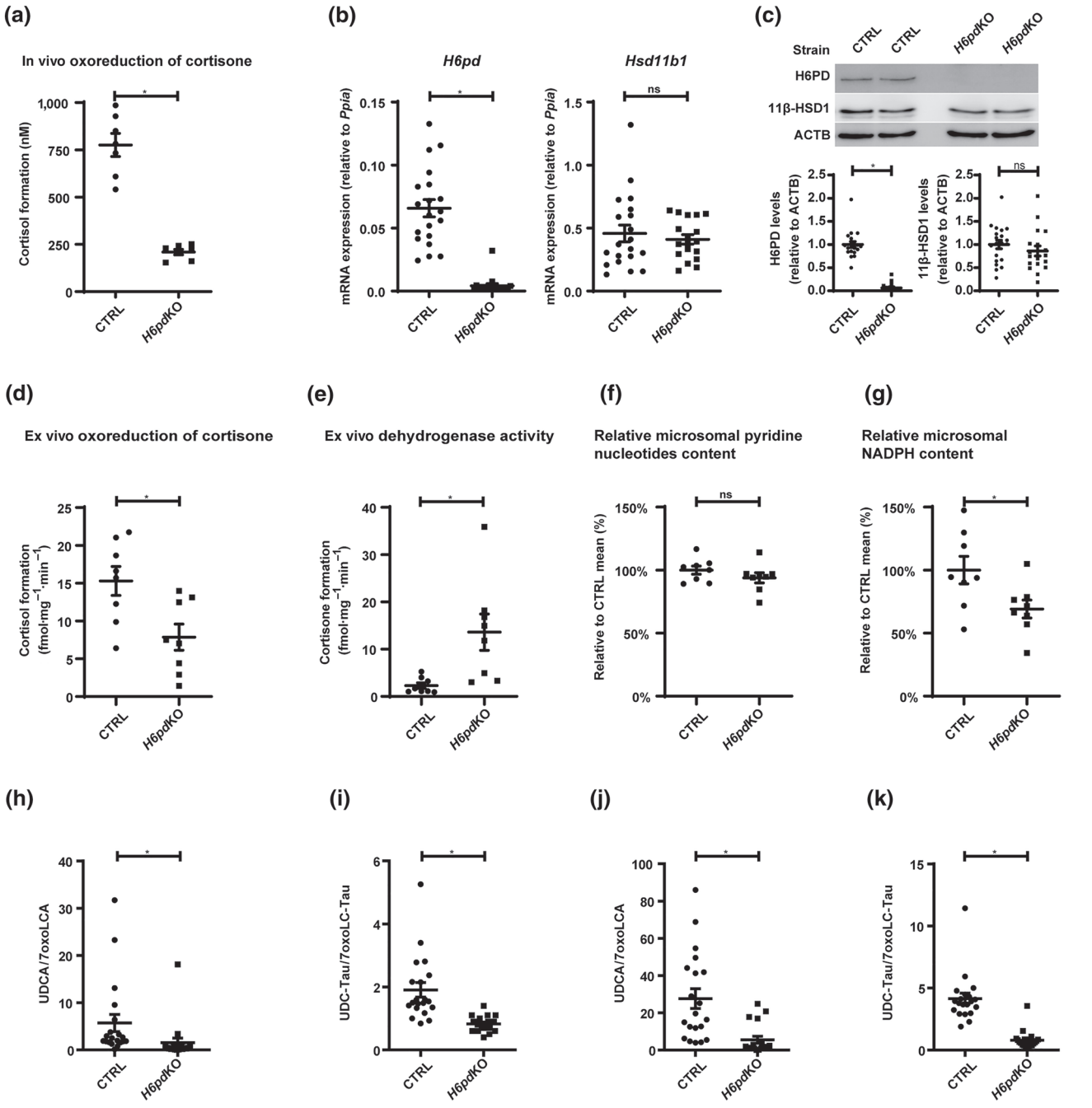

FIGURE 4 Characterization of 11β-HSD1 expression and activity and plasma and liver tissue UDCA/7oxoLCA and UDC-Tau/7oxoLC-Tau ratios in *H6pd*KO mice. (a) Estimation of the cortisone to cortisol conversion *in vivo*, determined as plasma concentration (nmol·L^{-1}) of cortisol 10 min after i.p. administration of 5 mg·kg^{-1} of cortisone (in DMSO) (CTRL n = 7; *H6pd*KO n = 7). (b) mRNA and (c) Western blot and semi-quantitative analysis of protein levels of H6PD and 11β-HSD1 in CTRL and *H6pd*KO animals (CTRL n = 20; *H6pd*KO n = 18). (d) Conversion of cortisone to cortisol and (e) of cortisol to cortisone determined ex vivo in mouse liver tissue (CTRL n = 8; *H6pd*KO n = 8). (f) Reduced pyridine nucleotides content and (g) NADPH content in mouse liver microsomes (relative to the mean of the CTRL; CTRL n = 8; *H6pd*KO n = 8). (h) UDCA/7oxoLCA ratios and (i) UDC-Tau/7oxoLC-Tau ratios in plasma of *H6pd*KO mice (CTRL n = 20; *H6pd*KO n = 18); (j) UDCA/7oxoLCA ratios and (k) UDC-Tau/7oxoLC-Tau ratios in liver tissue of *H6pd*KO mice (CTRL n = 20; *H6pd*KO n = 18). Analyte concentrations defined by a S/N ≤ 3 represent the LLOD of the UHPLC–MS/MS method. Samples yielding a concentration below LLOD were included as LLOD/2 (nmol·L^{-1} and fmol·mg^{-1} for plasma and liver, respectively) in the calculations of a specific analyte. Results represent mean ± SEM. *P < 0.05 significantly different as indicated; non-parametric, Mann–Whitney U test (two-tailed). Unequal group sizes reflect exclusion of two *H6pd*KO animals from further analysis due to the occurrence of liver cysts

TABLE 3 Bile acid profiles in plasma and liver of *H6pd*KO mice

	Plasma (nmol·L^{-1})		Liver (fmol·mg^{-1})	
	CTRL *H6pd*KO	*H6pd*KO	CTRL	*H6pd*KO
Analyte	(*n* = 20)	(*n* = 18)	(*n* = 20)	(*n* = 18)
CA	385 ± 245	214 ± 100	6,174 ± 1,321	4,324 ± 1,460
CDCA	8.8 ± 4.0	8.6 ± 1.5	304 ± 54	280 ± 55
DCA	187 ± 39	113 ± 13*	244 ± 31	166 ± 23
7oxoDCA	142 ± 97	167 ± 88	4,332 ± 1,175	4,555 ± 1,647
HDCA	18.4 ± 5.7	17.5 ± 2.5	350 ± 67	277 ± 39
αMCA	32 ± 16	37 ± 18	2,921 ± 688	2,544 ± 596
βMCA	259 ± 138	54 ± 19*	9,297 ± 1,932	2,652 ± 512*
ωMCA	71 ± 26	43 ± 9	2,154 ± 367	1,087 ± 183
UDCA	45 ± 24	15.4 ± 5.7*	365 ± 57	174 ± 48*
7oxoLCA	12.0 ± 2.4	20 ± 2*	37 ± 13	103 ± 28
αMCA/βMCA	0.12 ± 0.01	0.51 ± 0.06*	0.23 ± 0.02	0.98 ± 0.15*
UDCA/7oxoLCA	5.7 ± 1.8	1.53 ± 0.99*	28 ± 5	5.5 ± 1.9*
CDCA/7oxoLCA	1.38 ± 0.53	0.77 ± 0.39	20 ± 3	10.5 ± 3.5*
C-Tau	5,602 ± 3,712	9,620 ± 8,041	565,130 ± 129,003	394,188 ± 108,185
CDC-Tau	234 ± 133	429 ± 317	28,597 ± 7,271	30,359 ± 7,770
DC-Tau	381 ± 238	565 ± 404	25,629 ± 5,137	19,979 ± 5,696
LC-Tau	4.7 ± 3.9	12.2 ± 10.7	947 ± 67	997 ± 114
αMCA-Tau + βMCA-Tau	1,247 ± 877	854 ± 733	354,892 ± 80,362	193,231 ± 45,864
ωMCA-Tau	2,436 ± 1,627	2,974 ± 2,355	151,216 ± 38,734	80,001 ± 14,690
UDC-Tau	228 ± 161	293 ± 244	22,609 ± 5,964	9,885 ± 2,777*
7oxoLC-Tau	72 ± 46	651 ± 569	5,541 ± 1,045	22,711 ± 6,325
UDC-Tau/7oxoLC-Tau	1.91 ± 0.23	0.83 ± 0.06*	4.1 ± 0.4	0.80 ± 0.18*
CDC-Tau/7oxoLC-Tau	3.03 ± 0.32	1.70 ± 0.10*	5.0 ± 0.5	1.75 ± 0.24*
Sum primary BA	730 ± 426	333 ± 142	19,060 ± 3,852	9,975 ± 2,444
Sum primary BA-Tau	14,127 ± 9,474	22,922 ± 19,167	971,227 ± 220,934	627,664 ± 162,026

Note: The results represent mean ± SEM (nmol·L^{-1} and fmol·mg^{-1} for plasma and liver, respectively). Analyte concentrations defined by a S/N ≤ 3 represent the LLOD of the UHPLC–MS/MS method. Samples yielding a concentration below LLOD were included as LLOD/2 (nmol·L^{-1} and fmol·mg^{-1}, respectively) in the calculations of a specific analyte. Blue- and yellow-coloured boxes indicate statistically significant increases and decreases, respectively. Unequal group sizes reflect exclusion of two *H6pd*KO animals from further analysis due to the occurrence of liver cysts.

Abbreviations: CTRL, control littermates; *H6pd*KO, global *H6pd* knockout.

*$P < 0.05$, significantly different as indicated; non-parametric, Mann–Whitney *U* test (two-tailed).

sensitivity may be achieved by measuring just UDCA and 7oxoLCA, using larger sample volumes, and optimizing extraction specifically for these two bile acids, which should permit this ratio to be a good and reliable species-independent marker.

Although murine 11β-HSD1 converts 7oxoLC-Tau to UDC-Tau and CDC-Tau (Odermatt et al., 2011), the UDC-Tau/7oxoLC-Tau ratio was superior to the CDC-Tau/7oxoLC-Tau for detecting decreased 11β-HSD1 activity. A possible explanation may be the significant contribution of de novo CDCA synthesis to the circulating and liver tissue levels of CDC-Tau, whereas UDC-Tau and 7oxoLC-Tau are primarily formed from gut microbiota-derived UDCA and 7oxoLCA.

Interestingly, an increase in the ratio of αMCA/βMCA, formed by cytochrome P450 2C70 from CDCA and UDCA, respectively (Takahashi et al., 2016), nicely detected the decreased 11β-HSD1 activity in the three genetically modified mouse models. However, in carbenoxolone-treated mice, this ratio was not changed in plasma and showed an opposite change in liver. Plausibly, carbenoxolone inhibits cytochrome P450 2C70 or decreases its expression. Carbenoxolone might also affect gut microbiota as it was earlier shown to alter colonic mucus (Finnie et al., 1996). This merits future investigation.

Pharmacological treatment using carbenoxolone led to approximately 30% decreased 11β-HSD1 activity. It needs to be noted that the level of 11β-HSD1 inhibition is an estimation and it was determined at one given time point (i.e., at about 8 am) and the formation of cortisol upon injection of cortisone was determined after 10 min. Nevertheless, inhibition of 11β-HSD1 could be demonstrated and the bile acid biomarker detected the decreased activity. The results suggested that besides direct inhibition, a reduced enzyme expression

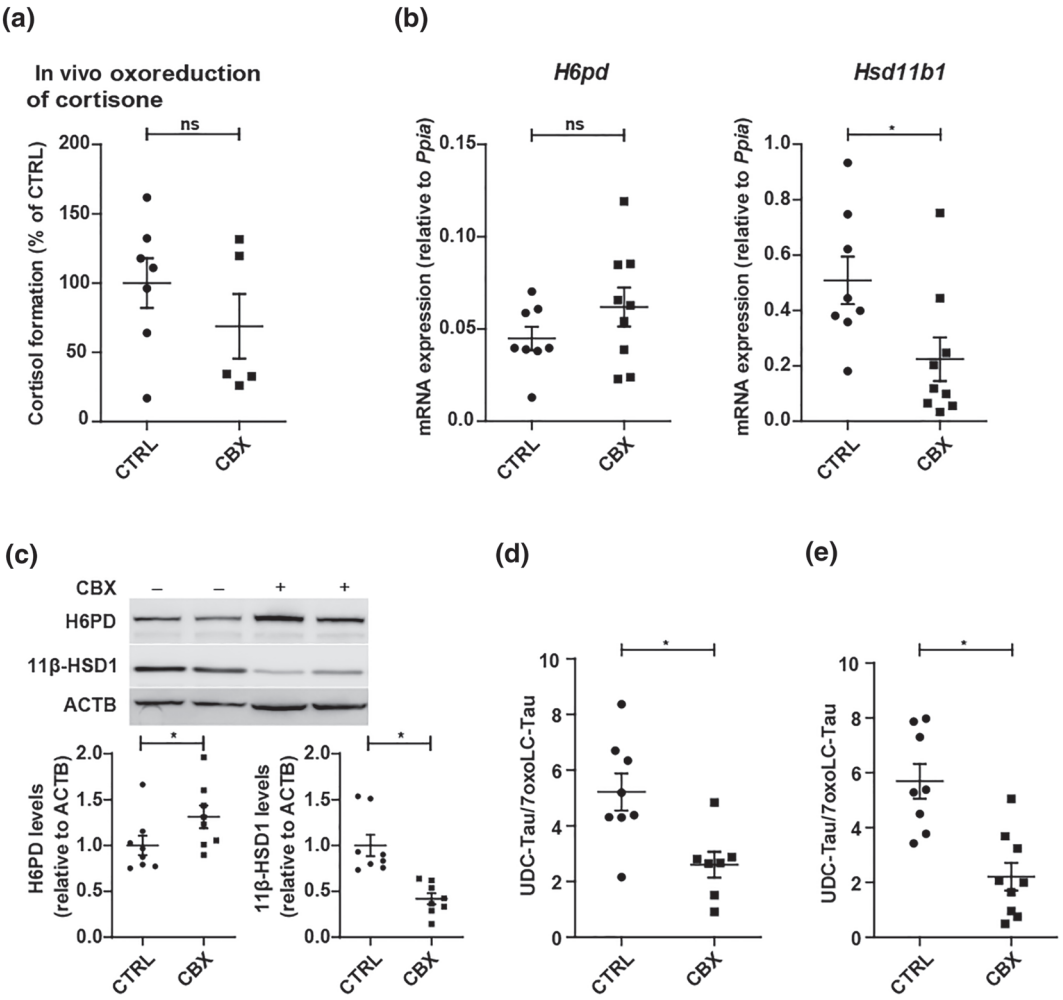

FIGURE 5 Characterization of 11β-HSD1 expression and activity and plasma and liver tissue UDC-Tau/7oxoLC-Tau ratios in carbenoxolone-treated mice. Control mice were treated with the pharmacologic 11β-HSD1 inhibitor carbenoxolone (CBX, 100 mg·kg^{-1}·day^{-1}, i.p.) or PBS (CTRL). (a) Conversion of cortisone to cortisol *in vivo*, measured after i.p. administration of 5 mg·kg^{-1} of cortisone (in DMSO) (CTRL n = 7; CBX n = 5). (b) mRNA expression of *H6pd* and *Hsd11b1* in CTRL- and CBX-treated animals (CTRL n = 8; CBX n = 9). (c) Western blot and semi-quantitative analysis of protein levels of H6PD and 11β-HSD1 in CTRL- and CBX-treated mice (CTRL n = 8; CBX n = 8). (d) UDC-Tau/7oxoLC-Tau ratios in CTRL mice treated with PBS (CTRL) or the pharmacologic 11β-HSD1 inhibitor carbenoxolone (CBX 100 mg·kg^{-1}·day^{-1}, i.p.) (CTRL n = 8; CBX n = 9) in plasma and (e) in liver tissue. Analyte concentrations defined by a S/N ≤ 3 represent the LLOD of the UHPLC–MS/MS method. Samples yielding a concentration below LLOD were included as LLOD/2 (nmol·L^{-1} and fmol·mg^{-1} for plasma and liver, respectively) in the calculations of a specific analyte. Results represent mean ± SEM. No outliers were excluded. *P < 0.05 significantly different as indicated; non-parametric, Mann–Whitney U test (two-tailed). Unequal group sizes reflect exclusion of one animal of the CTRL group due to unexpected health issues prior to the experiment and exclusion of two plasma samples of the CBX group due to insufficient collection of blood sample volume

contributed to the decreased activity. carbenoxolone also inhibits 11β-HSD2 (Stewart et al., 1990). However, our preliminary observations suggest that this enzyme does not accept CDCA and UDCA as substrates, therefore unlikely affecting the bile acid ratios of interest.

*H6pd*KO mice retained approximately 50% of 11β-HSD1 oxoreduction activity measured in control animals. This is consistent with observations made in isolated macrophage from *H6pd*KO mice, which also retained about 50–60% 11β-HSD1 oxoreduction activity (Marbet et al., 2018). Based on earlier experiments using liver microsomes (Lavery et al., 2006), it was anticipated that in the absence of H6PD, 11β-HSD1 would function exclusively as dehydrogenase and the effect on the respective bile acid ratios would be comparable with that in 11KO mice, yet the accumulation of 7oxo metabolites and the ratios derived from them clearly were less pronounced. These findings indicate the existence of a yet unknown mechanism generating NADPH in the ER capable of driving 11β-HSD1 reaction direction towards oxoreduction activity. This is supported by the continued presence of NADPH in the *H6pd*KO liver, albeit at reduced levels, seen previously (Rogoff et al., 2010) and also found here. A possible candidate for generating NADPH within the ER includes luminal 6-phosphogluconate dehydrogenase (Bublitz et al., 1987). However, the gene encoding this enzyme still remains to be identified.

The mild cholestasis phenotype of 11KO mice with 10-fold to 20-fold increased plasma bile acids (Table 1, Penno et al., 2014) raises

TABLE 4 Bile acid profiles in plasma and liver in mice with decreased 11β-HSD1 oxoreduction activity by pharmacologic inhibition using carbenoxolone

	Plasma (nmol·L^{-1})		Liver (fmol·mg^{-1})	
	CTRL	CBX	CTRL	CBX
Analyte	(*n* = 8)	(*n* = 7)	(*n* = 8)	(*n* = 9)
CA	1,000 ± 795	408 ± 275	513 ± 84	329 ± 71
CDCA	145 ± 120	11.0 ± 2.3	242 ± 17	114 ± 45
DCA	592 ± 245	169 ± 62*	186 ± 15	61 ± 21*
7oxoDCA	237 ± 178	281 ± 212	46 ± 17	88 ± 50
HDCA	146 ± 90	26 ± 12	224 ± 17	113 ± 34*
αMCA	162 ± 110	42 ± 17	288 ± 33	129 ± 42*
βMCA	659 ± 481	318 ± 179	1,608 ± 136	4,409 ± 1,557
ωMCA	238 ± 134	47 ± 25	306 ± 25	580 ± 183
UDCA	226 ± 126	39 ± 18*	99 ± 14	17.8 ± 6.2*
7oxoLCA	NA	NA	NA	NA
αMCA/βMCA	0.24 ± 0.05	0.28 ± 0.15	0.18 ± 0.02	0.06 ± 0.02*
UDCA/7oxoLCA	NA	NA	NA	NA
CDCA/7oxoLCA	NA	NA	NA	NA
C-Tau	7,002 ± 4,900	9,530 ± 6,466	63,049 ± 11,354	48,334 ± 9,673
CDC-Tau	339 ± 223	265 ± 175	5,274 ± 533	3,975 ± 857
DC-Tau	348 ± 275	222 ± 124	6,723 ± 719	2,114 ± 766*
LC-Tau	8.8 ± 5.6	2.01 ± 1.22	1,271 ± 127	541 ± 81*
αMCA-Tau + βMCA-Tau	1,876 ± 1,853	1,383 ± 943	55,442 ± 6,370	63,438 ± 12,465
ωMCA-Tau	3,124 ± 1,998	12,920 ± 11,548	25,304 ± 3,379	32,334 ± 8,484
UDC-Tau	296 ± 221	332 ± 251	4,071 ± 501	1,125 ± 174*
7oxoLC-Tau	84 ± 56	125 ± 94	836 ± 178	760 ± 209
UDC-Tau/7oxoLC-Tau	5.2 ± 0.7	2.6 ± 0.5*	5.7 ± 0.6	2.2 ± 0.5*
CDC-Tau/7oxoLC-Tau	2.6 ± 0.4	1.60 ± 0.38*	7.7 ± 1.0	6.2 ± 1.0
Sum primary BA	2,192 ± 1,630	818 ± 483	2,463 ± 192	4,869 ± 1,611
Sum primary BA-Tau	9,513 ± 7,033	11,511 ± 7,034	127,836 ± 17,002	116,873 ± 15,450

Note: The results represent mean ± SEM (nmol·L^{-1} and fmol·mg^{-1} for plasma and liver, respectively). Analyte concentrations defined by a S/N ≤ 3 represent the LLOD of the UHPLC–MS/MS method. Samples yielding a concentration below LLOD were included as LLOD/2 (nmol·L^{-1} and fmol·mg^{-1}, respectively) in the calculations of a specific analyte. Yellow-coloured boxes indicate statistically significant decreases. Unequal group sizes reflect exclusion of one animal of the CTRL group due to unexpected health issues prior to the experiment and exclusion of two plasma samples of the carbenoxolone (CBX group due to insufficient collection of blood sample volume.

Abbreviations: CBX, mice treated with the pharmacologic 11β-HSD1 inhibitor carbenoxolone (100 mg·kg^{-1}·day^{-1}, i.p.); CTRL, control mice treated with PBS; NA, not analysed, if most values were below LLOD.

*$P < 0.05$, significantly different as indicated; non-parametric, Mann–Whitney *U* test (two-tailed).

some concerns that pharmacological 11β-HSD1 inhibition might induce cholestasis. In paediatric patients with adrenal insufficiency and cholestasis, glucocorticoid treatment reversed the hepatic phenotype (Al-Hussaini et al., 2012; Cheung et al., 2003), indicating a direct role of glucocorticoids in maintaining bile acid homeostasis. However, no evidence for cholestasis was seen in the present study when 11β-HSD1 was inhibited by carbenoxolone and there was only a trend increase of total free but not conjugated bile acids in 11LKO mice and no change of total bile acids in *H6pd*KO mice. These observations do not support concerns of a general risk of cholestasis upon inhibition of 11β-HSD1. The more pronounced effect on plasma and liver tissue bile acid profiles in 11KO mice may be explained by the fact that they lack 11β-HSD1 during all stages of life and throughout the enterohepatic circuit and also by altered hypothalamus–pituitary–adrenal axis, whereas 11LKO only lack hepatic 11β-HSD1, and *H6pd*KO- and carbenoxolone-treated mice retain partial 11β-HSD1 activity.

A suitable biomarker reporting the *in vivo* 11β-HSD1 activity in health and disease situations or upon pharmacological interventions could greatly facilitate such studies. The currently used urinary (tetrahydrocorticosterone + allo-tetrahydrocorticosterone)/tetrahydro-11-dehydrocorticosterone ratio has limited value as it can lead to erroneous conclusions because of interference through altered

11β-HSD2 and 5α-reductase activities and feedback modulation. Furthermore, it needs 24-h urine sampling that due to small collection volume and contamination by food and faeces and the stress of metabolic cage housing may lead to erroneous results.

Although our data support the UDC-Tau/7oxoLC-Tau ratio as a useful *in vivo* marker of 11β-HSD1 activity, our study has several limitations:- (1) the present study included only male mice at 10–15 weeks of age and it will be important to study also mice at both young and very old age that may exhibit metabolic differences as well as female mice, being mindful of the effect of the oestrous cycle on bile acid homeostasis (Papacleovoulou et al., 2011); (2) the impact of feeding and diet should be studied; (3) samples were taken in the morning between 7 and 10 am and the influence of circadian rhythm and/or stress should be assessed; (4) in case of pharmacological inhibition, a possible interference of the compound with hepatic enzymes and transporters that also are involved in bile acid homeostasis needs to be kept in mind; (5) the impact of the microbiome on the production of UDCA and 7oxoLCA needs to be investigated; it has been shown that 11β-HSD1 deficiency alters the microbiome in a diet-specific manner (Johnson et al., 2017); (6) disease models with altered 11β-HSD1 activity should be studied and (7) the sensitivity of the LC–MS/MS-based quantification method can be increased by measuring specifically the bile acid metabolites needed for the ratio and by increasing sample volume and optimizing extraction. In follow-on research, the predictivity of the UDC-Tau/7oxoLC-Tau ratio for detecting altered 11β-HSD1 activity should be investigated in mouse models addressing the abovementioned factors. Finally, experiments in humans are required to establish whether such a bile acid ratio is a useful biomarker to detect altered 11β-HSD1 activity upon pharmacological treatment or in disease situations.

ACKNOWLEDGEMENTS

We thank Dr. Antonio Checa, Karolinska Institutet, Sweden, for his statistical support and advice.

AUTHOR CONTRIBUTIONS

M.W., S.S., D.V.K., J.B. and P.K. designed and conducted the experiments, analysed data, and reviewed the paper; K.E.C. consulted for the study and reviewed the paper; G.G.L. consulted for the study and reviewed the paper; and A.O. designed the experiments, supervised the study and wrote the paper.

CONFLICT OF INTEREST

The authors have nothing to disclose.

DECLARATION OF TRANSPARENCY AND SCIENTIFIC RIGOUR

This Declaration acknowledges that this paper adheres to the principles for transparent reporting and scientific rigour of preclinical research as stated in the *BJP* guidelines for Design & Analysis, Immunoblotting and Immunochemistry and Animal Experimentation, and as recommended by funding agencies, publishers, and other organizations engaged with supporting research.

DATA AVAILABILITY STATEMENT

The data that support the findings of this study are available from the corresponding author upon reasonable request. All related study data will be provided according to the related data management plan as open access at https://zenodo.org/.

REFERENCES

Abrahams, L., Semjonous, N. M., Guest, P., Zielinska, A., Hughes, B., Lavery, G. G., & Stewart, P. M. (2012). Biomarkers of hypothalamic-pituitary-adrenal axis activity in mice lacking 11β-Hsd1 and H6pdh. *Journal of Endocrinology*, *214*, 367–372. https://doi.org/10.1530/JOE-12-0178

Alexander, S. P. H., Roberts, R. E., Broughton, B. R. S., Sobey, C. G., George, C. H., Stanford, S. C., … Ahluwalia, A. (2018). Goals and practicalities of immunoblotting and immunohistochemistry: A guide for submission to the *British Journal of Pharmacology*. *British Journal of Pharmacology*, *175*, 407–411. https://doi.org/10.1111/bph.14112

Alexander, S. P. H., Fabbro, D., Kelly, E., Mathie, A., Peters, J. A., Veale, E. L., … …GTP collaborators. (2019). The Concise Guide to PHARMACOLOGY 2019/20: Enzymes. *British Journal of Pharmacology*, *176*, S297–S396. https://doi.org/10.1111/bph.14752

Al-Hussaini, A., Almutairi, A., Mursi, A., Alghofely, M., & Asery, A. (2012). Isolated cortisol deficiency: A rare cause of neonatal cholestasis. *Saudi Journal of Gastroenterology*, *18*, 339–341. https://doi.org/10.4103/1319-3767.101137

Alnouti, Y., Csanaky, I. L., & Klaassen, C. D. (2008). Quantitative-profiling of bile acids and their conjugates in mouse liver, bile, plasma, and urine using LC–MS/MS. *Journal of Chromatography. B, Analytical Technologies in the Biomedical and Life Sciences*, *873*, 209–217. https://doi.org/10.1016/j.jchromb.2008.08.018

Arampatzis, S., Kadereit, B., Schuster, D., Balazs, Z., Schweizer, R. A., Frey, F. J., … Odermatt, A. (2005). Comparative enzymology of 11β-hydroxysteroid dehydrogenase type 1 from six species. *Journal of Molecular Endocrinology*, *35*, 89–101. https://doi.org/10.1677/jme.1.01736

Atanasov, A. G., Nashev, L. G., Schweizer, R. A., Frick, C., & Odermatt, A. (2004). Hexose-6-phosphate dehydrogenase determines the reaction direction of 11β-hydroxysteroid dehydrogenase type 1 as an oxoreductase. *FEBS Letters*, *571*, 129–133. https://doi.org/10.1016/j.febslet.2004.06.065

Banhegyi, G., Benedetti, A., Fulceri, R., & Senesi, S. (2004). Cooperativity between 11β-hydroxysteroid dehydrogenase type 1 and hexose-6-phosphate dehydrogenase in the lumen of the endoplasmic reticulum. *Journal of Biological Chemistry*, *279*, 27017–27021. https://doi.org/10.1074/jbc.M404159200

Bublitz, C., Lawler, C. A., & Steavenson, S. (1987). The topology of phosphogluconate dehydrogenases in rat liver microsomes. *Archives of Biochemistry and Biophysics*, *259*, 22–28. https://doi.org/10.1016/0003-9861(87)90465-6

Cheung, M., Bansal, S., Aw, M. M., Buchanan, C. R., Mieli-Vergani, G., & Dhawan, A. (2003). Liver failure in a neonate with congenital adrenal hyporesponsiveness. *European Journal of Pediatrics*, *162*, 558. https://doi.org/10.1007/s00431-003-1249-0

Courtney, R., Stewart, P. M., Toh, M., Ndongo, M. N., Calle, R. A., & Hirshberg, B. (2008). Modulation of 11β-hydroxysteroid dehydrogenase (11βHSD) activity biomarkers and pharmacokinetics of Pf-00915275, a selective 11βHSD1 inhibitor. *The Journal of Clinical Endocrinology and Metabolism*, *93*, 550–556. http://www.ncbi.nlm.nih.gov/entrez/query.fcgi?cmd=Retrieve&db=PubMed&dopt=Citation&list_uids=17986636, https://doi.org/10.1210/jc.2007-1912

Curtis, M. J., Alexander, S., Cirino, G., Docherty, J. R., George, G. H., Giembycz, M. A., … Ahluwali, A. (2018). Experimental design and analysis and their reporting II: updated and simplified guidance for authors

and peer reviewers. *British Journal of Pharmacology*, *175*, 987–993. https://doi.org/10.1111/bph.14153

Feig, P. U., Shah, S., Hermanowski-Vosatka, A., Plotkin, D., Springer, M. S., Donahue, S., … Kaufman, K. D. (2011). Effects of an 11β-hydroxysteroid dehydrogenase type 1 inhibitor, MK-0916, in patients with type 2 diabetes mellitus and metabolic syndrome. *Diabetes, Obesity & Metabolism*, *13*, 498–504. https://doi.org/10.1111/j.1463-1326.2011.01375.x

Finnie, I. A., Campbell, B. J., Taylor, B. A., Milton, J. D., Sadek, S. K., Yu, L. G., & Rhodes, J. M. (1996). Stimulation of colonic mucin synthesis by corticosteroids and nicotine. *Clinical Science (London, England: 1979)*, *91*, 359–364. https://doi.org/10.1042/cs0910359

Freude, S., Heise, T., Woerle, H. J., Jungnik, A., Rauch, T., Hamilton, B., … Graefe-Mody, U. (2016). Safety, pharmacokinetics and pharmacodynamics of BI 135585, a selective 11β-hydroxysteroid dehydrogenase-1 (HSD1) inhibitor in humans: Liver and adipose tissue 11β-HSD1 inhibition after acute and multiple administrations over 2 weeks. *Diabetes, Obesity & Metabolism*, *18*, 483–490. https://doi.org/10.1111/dom.12635

Garcia-Canaveras, J. C., Donato, M. T., Castell, J. V., & Lahoz, A. (2012). Targeted profiling of circulating and hepatic bile acids in human, mouse, and rat using a UPLC-MRM-MS-validated method. *Journal of Lipid Research*, *53*, 2231–2241. https://doi.org/10.1194/jlr.D028803

Gathercole, L. L., Lavery, G. G., Morgan, S. A., Cooper, M. S., Sinclair, A. J., Tomlinson, J. W., & Stewart, P. M. (2013). 11β-Hydroxysteroid dehydrogenase 1: Translational and therapeutic aspects. *Endocrine Reviews*, *34*, 525–555. https://doi.org/10.1210/er.2012-1050

Hardy, R. S., Botfield, H., Markey, K., Mitchell, J. L., Alimajstorovic, Z., Westgate, C. S. J., … Sinclair, A. J. (2020). 11βHSD1 inhibition with AZD4017 improves lipid profiles and lean muscle mass in idiopathic intracranial hypertension. *Journal of Clinical Endocrinology and Metabolism*, *106*, 174–187. https://doi.org/10.1210/clinem/dgaa766

Hult, M., Jornvall, H., & Oppermann, U. C. (1998). Selective inhibition of human type 1 11β-Hydroxysteroid dehydrogenase by synthetic steroids and Xenobiotics. *FEBS Letters*, *441*, 25–28. https://doi.org/10.1016/s0014-5793(98)01515-4

Jamieson, A., Wallace, A. M., Andrew, R., Nunez, B. S., Walker, B. R., Fraser, R., … Connell, J. M. (1999). Apparent cortisone reductase deficiency: A functional defect in 11β-hydroxysteroid dehydrogenase type 1. *Journal of Clinical Endocrinology and Metabolism*, *84*, 3570–3574. https://doi.org/10.1210/jcem.84.10.6031

Johnson, J. S., Opiyo, M. N., Thomson, M., Gharbi, K., Seckl, J. R., Heger, A., & Chapman, K. E. (2017). 11β-Hydroxysteroid dehydrogenase-1 deficiency alters the gut microbiome response to Western diet. *Journal of Endocrinology*, *232*, 273–283. https://doi.org/10.1530/JOE-16-0578

Jolley, C. D., Dietschy, J. M., & Turley, S. D. (1999). Genetic differences in cholesterol absorption in 129/Sv and C57BL/6 mice: Effect on cholesterol responsiveness. *American Journal of Physiology*, *276*, G1117–G1124. https://doi.org/10.1152/ajpgi.1999.276.5.G1117

Lavery, G. G., Idkowiak, J., Sherlock, M., Bujalska, I., Ride, J. P., Saqib, K., … Stewart, P. M. (2013). Novel H6PDH mutations in two girls with premature adrenarche: 'Apparent' and 'true' CRD can be differentiated by urinary steroid profiling. *European Journal of Endocrinology of the European Federation of Endocrine Societies*, *168*, K19–K26. https://doi.org/10.1530/EJE-12-0628

Lavery, G. G., Walker, E. A., Draper, N., Jeyasuria, P., Marcos, J., Shackleton, C. H., … Stewart, P. M. (2006). Hexose-6-phosphate dehydrogenase knock-out mice lack 11 β-hydroxysteroid dehydrogenase type 1-mediated glucocorticoid generation. *Journal of Biological Chemistry*, *281*, 6546–6551. https://doi.org/10.1074/jbc.M512635200

Lavery, G. G., Zielinska, A. E., Gathercole, L. L., Hughes, B., Semjonous, N., Guest, P., … Stewart, P. M. (2012). Lack of significant metabolic abnormalities in mice with liver-specific disruption of 11β-hydroxysteroid dehydrogenase type 1. *Endocrinology*, *153*, 3236–3248. https://doi.org/10.1210/en.2012-1019

Lilley, E., Stanford, S. C., Kendall, D. E., Alexander, S. P., Cirino, G., Docherty, J. R., … Ahluwalia, A. (2020). ARRIVE 2.0 and the *British Journal of Pharmacology*: Updated guidance for 2020. *British Journal of Pharmacology*, *177*(16), 3611–3616. https://bpspubs.onlinelibrary.wiley.com/doi/full/10.1111/bph.15178

Marbet, P., Klusonova, P., Birk, J., Kratschmar, D. V., & Odermatt, A. (2018). Absence of hexose-6-phosphate dehydrogenase results in reduced overall glucose consumption but does not prevent 11β-hydroxysteroid dehydrogenase-1-dependent glucocorticoid activation. *The FEBS Journal*, *285*, 3993–4004. https://doi.org/10.1111/febs.14642

Markey, K. A., Ottridge, R., Mitchell, J. L., Rick, C., Woolley, R., Ives, N., … Sinclair, A. J. (2017). Assessing the efficacy and safety of an 11β-hydroxysteroid dehydrogenase type 1 inhibitor (AZD4017) in the idiopathic intracranial hypertension drug trial, IIH: DT: Clinical methods and design for a phase II randomized controlled trial. *JMIR Research Protocol*, *6*, e181. https://doi.org/10.2196/resprot.7806

Odermatt, A., Da Cunha, T., Penno, C. A., Chandsawangbhuwana, C., Reichert, C., Wolf, A., … Baker, M. E. (2011). Hepatic reduction of the secondary bile acid 7-oxolithocholic acid is mediated by 11β-hydroxysteroid dehydrogenase 1. *The Biochemical Journal*, *436*, 621–629. https://doi.org/10.1042/BJ20110022

Odermatt, A., & Klusonova, P. (2015). 11β-Hydroxysteroid dehydrogenase 1: Regeneration of active glucocorticoids is only part of the story. *Journal of Steroid Biochemistry and Molecular Biology*, *151*, 85–92. https://doi.org/10.1016/j.jsbmb.2014.08.011

Odermatt, A., & Kratschmar, D. V. (2012). Tissue-specific modulation of mineralocorticoid receptor function by 11β-hydroxysteroid dehydrogenases: An overview. *Molecular and Cellular Endocrinology*, *350*, 168–186. https://doi.org/10.1016/j.mce.2011.07.020

Papacleovoulou, G., Abu-Hayyeh, S., & Williamson, C. (2011). Nuclear receptor-driven alterations in bile acid and lipid metabolic pathways during gestation. *Biochimica et Biophysica Acta*, *1812*, 879–887. https://doi.org/10.1016/j.bbadis.2010.11.001

Penno, C. A., Arsenijevic, D., Da Cunha, T., Kullak-Ublick, G. A., Montani, J.-P., & Odermatt, A. (2013). Quantification of multiple bile acids in uninephrectomized rats using ultra-performance liquid chromatography-tandem mass spectrometry. *Analytical Methods*, *5*, 1155–1164. https://doi.org/10.1039/c3ay26520j

Penno, C. A., Morgan, S. A., Rose, A. J., Herzig, S., Lavery, G. G., & Odermatt, A. (2014). 11β-Hydroxysteroid dehydrogenase-1 is involved in bile acid homeostasis by modulating fatty acid transport protein-5 in the liver of mice. *Molecular Metabolism*, *3*, 554–564. https://doi.org/10.1016/j.molmet.2014.04.008

Penno, C. A., Morgan, S. A., Vuorinen, A., Schuster, D., Lavery, G. G., & Odermatt, A. (2013). Impaired oxidoreduction by 11β-hydroxysteroid dehydrogenase 1 results in the accumulation of 7-oxolithocholic acid. *Journal of Lipid Research*, *54*, 2874–2883. https://doi.org/10.1194/jlr.M042499

Percie du Sert, N., Hurst, V., Ahluwalia, A., Alam, S., Avey, M. T., Baker, M., … Würbel, H. (2020). The ARRIVE guidelines 2.0: Updated guidelines for reporting animal research. *PLoS Biology*, *18*(7), e3000410. https://doi.org/10.1371/journal.pbio.3000410

Quax, R. A., Manenschijn, L., Koper, J. W., Hazes, J. M., Lamberts, S. W., van Rossum, E. F., & Feelders, R. A. (2013). Glucocorticoid sensitivity in health and disease. *Nature Reviews. Endocrinology*, *9*, 670–686. https://doi.org/10.1038/nrendo.2013.183

Quinkler, M., & Stewart, P. M. (2003). Hypertension and the cortisol-cortisone shuttle. *Journal of Clinical Endocrinology and Metabolism*, *88*, 2384–2392. https://doi.org/10.1210/jc.2003-030138

Rausch, P., Basic, M., Batra, A., Bischoff, S. C., Blaut, M., Clavel, T., … Baines, J. F. (2016). Analysis of factors contributing to variation in the

C57BL/6J fecal microbiota across German animal facilities. *International Journal of Medical Microbiology*, *306*, 343–355. https://doi.org/10.1016/j.ijmm.2016.03.004

Rogoff, D., Black, K., McMillan, D. R., & White, P. C. (2010). Contribution of hexose-6-phosphate dehydrogenase to NADPH content and redox environment in the endoplasmic reticulum. *Redox Report*, *15*, 64–70. https://doi.org/10.1179/174329210X12650506623249

Rosenstock, J., Banarer, S., Fonseca, V. A., Inzucchi, S. E., Sun, W., Yao, W., … Huber, R. (2010). The 11-β-hydroxysteroid dehydrogenase type 1 inhibitor INCB13739 improves hyperglycemia in patients with type 2 diabetes inadequately controlled by metformin monotherapy. *Diabetes Care*, *33*, 1516–1522. https://doi.org/10.2337/dc09-2315

Schmittgen, T. D., & Livak, K. J. (2008). Analyzing real-time PCR data by the comparative C_T method. *Nature Protocols*, *3*, 1101–1108. https://www.ncbi.nlm.nih.gov/pubmed/18546601, https://doi.org/10.1038/nprot.2008.73

Schwab, D., Sturm, C., Portron, A., Fuerst-Recktenwald, S., Hainzl, D., Jordan, P., … DuBiner, H. (2017). Oral administration of the 11β-hydroxysteroid-dehydrogenase type 1 inhibitor RO5093151 to patients with glaucoma: An adaptive, randomised, placebo-controlled clinical study. *BMJ Open Ophthalmol*, *1*, e000063. https://doi.org/10.1136/bmjophth-2016-000063

Scott, J. S., Goldberg, F. W., & Turnbull, A. V. (2014). Medicinal chemistry of inhibitors of 11β-hydroxysteroid dehydrogenase type 1 (11β-HSD1). *Journal of Medicinal Chemistry*, *57*, 4466–4486. https://doi.org/10.1021/jm4014746

Semjonous, N. M., Sherlock, M., Jeyasuria, P., Parker, K. L., Walker, E. A., Stewart, P. M., & Lavery, G. G. (2011). Hexose-6-phosphate dehydrogenase contributes to skeletal muscle homeostasis independent of 11β-hydroxysteroid dehydrogenase type 1. *Endocrinology*, *152*, 93–102. https://doi.org/10.1210/en.2010-0957

Stewart, P. M., Wallace, A. M., Atherden, S. M., Shearing, C. H., & Edwards, C. R. (1990). Mineralocorticoid activity of carbenoxolone: Contrasting effects of carbenoxolone and liquorice on 11β-hydroxysteroid dehydrogenase activity in man. *Clinical Science (London, England : 1979)*, *78*, 49–54. https://doi.org/10.1042/cs0780049

Strajhar, P., Schmid, Y., Liakoni, E., Dolder, P. C., Rentsch, K. M., Kratschmar, D. V., … Liechti, M. E. (2016). Acute effects of lysergic acid diethylamide on circulating steroid levels in healthy subjects. *Journal of Neuroendocrinology*, *28*(3), 12374–12386. https://doi.org/10.1111/jne.12374

Takahashi, S., Fukami, T., Masuo, Y., Brocker, C. N., Xie, C., Krausz, K. W., … Gonzalez, F. J. (2016). Cyp2c70 is responsible for the species difference in bile acid metabolism between mice and humans. *Journal of Lipid Research*, *57*, 2130–2137. https://doi.org/10.1194/jlr.M071183

Terao, M., & Katayama, I. (2016). Local cortisol/corticosterone activation in skin physiology and pathology. *Journal of Dermatological Science*, *84*, 11–16. https://doi.org/10.1016/j.jdermsci.2016.06.014

Tiganescu, A., Hupe, M., Uchida, Y., Mauro, T., Elias, P. M., & Holleran, W. M. (2018). Topical 11β-hydroxysteroid dehydrogenase type 1 inhibition corrects cutaneous features of systemic glucocorticoid excess in female mice. *Endocrinology*, *159*, 547–556. https://doi.org/10.1210/en.2017-00607

Ulick, S., Levine, L. S., Gunczler, P., Zanconato, G., Ramirez, L. C., Rauh, W., … New, M. I. (1979). A syndrome of apparent mineralocorticoid excess associated with defects in the peripheral metabolism of cortisol. *Journal of Clinical Endocrinology and Metabolism*, *49*, 757–764. https://doi.org/10.1210/jcem-49-5-757

Ulick, S., Tedde, R., & Mantero, F. (1990). Pathogenesis of the type 2 variant of the syndrome of apparent mineralocorticoid excess. *Journal of Clinical Endocrinology and Metabolism*, *70*, 200–206. https://doi.org/10.1210/jcem-70-1-200

Webster, S. P., McBride, A., Binnie, M., Sooy, K., Seckl, J. R., Andrew, R., … Walker, B. R. (2017). Selection and early clinical evaluation of the brain-penetrant 11β-hydroxysteroid dehydrogenase type 1 (11β-HSD1) inhibitor UE2343 (Xanamem). *British Journal of Pharmacology*, *174*, 396–408. https://doi.org/10.1111/bph.13699

Wyrwoll, C. S., Holmes, M. C., & Seckl, J. R. (2011). 11β-Hydroxysteroid dehydrogenases and the brain: From zero to hero, a decade of progress. *Frontiers in Neuroendocrinology*, *32*, 265–286. https://doi.org/10.1016/j.yfrne.2010.12.001

Ye, X. Y., Chen, S. Y., Wu, S., Yoon, D. S., Wang, H., Hong, Z., … Robl, J. A. (2017). Discovery of clinical candidate 2-((2*S*,6*S*)-2-phenyl-6-hydroxyadamantan-2-yl)-1-(3′-hydroxyazetidin-1-yl)ethanone [BMS-816336], an orally active novel selective 11β-hydroxysteroid dehydrogenase type 1 inhibitor. *Journal of Medicinal Chemistry*, *60*, 4932–4948. https://doi.org/10.1021/acs.jmedchem.7b00211

SUPPORTING INFORMATION

Additional supporting information may be found online in the Supporting Information section at the end of this article.

How to cite this article: Weingartner M, Stücheli S, Kratschmar DV, et al. The ratio of ursodeoxycholyltaurine to 7-oxolithocholyltaurine serves as a biomarker of decreased 11β-hydroxysteroid dehydrogenase 1 activity in mouse. *Br J Pharmacol*. 2021;1–18. https://doi.org/10.1111/bph.15367

Supplementary data

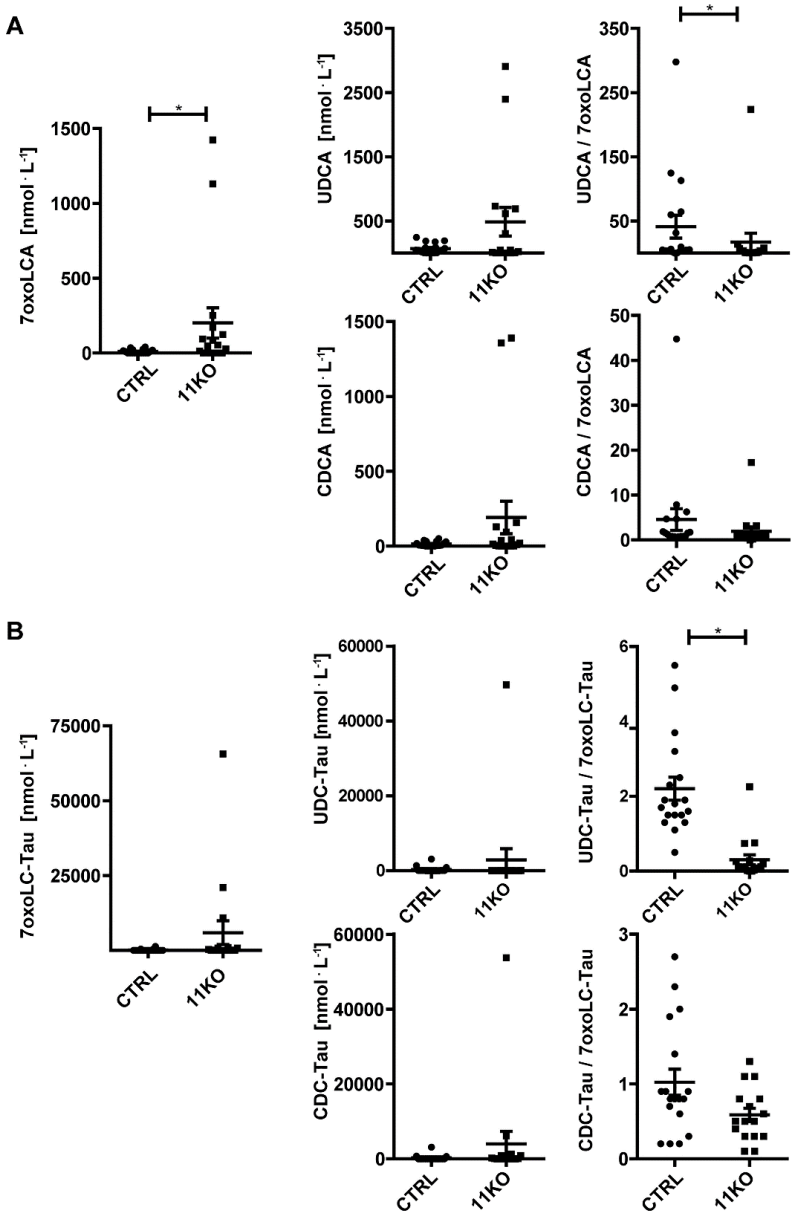

Supplementary Figure 1. Decreased 11β-HSD1 bile acid product to substrate ratios in plasma of 11KO mice. 11β-HSD1 bile acid substrates (7oxoLCA, 7oxoLC-Tau) and products (UDCA, CDCA and their taurine conjugated forms) were measured in plasma of 11KO mice (nmol·L^{-1}). Calculation of the product to substrate ratios attenuated the large animal-to-animal variations and detected the lack of 11β-HSD1 oxoreduction activity. a) Plasma concentrations of CTRL (n = 18) and 11KO mice (n = 17) for 7oxoLCA, CDCA, UDCA and the corresponding ratios; and b) for 7oxoLC-Tau, CDC-Tau, UDC-Tau and the corresponding ratios. The results represent mean ± SEM. No outliers were excluded. Analyte concentrations defined by a S/N ≤ 3 represent the LLOD of the UHPLC-MS/MS method. Samples yielding a concentration below LLOD were included as LLOD/2 in the calculations of a specific analyte. *P<0.05 significantly different as indicated; non-parametric, Mann-Whitney U-test (two-tailed). Unequal group sizes reflect exclusion of one plasma sample due to insufficient collection of blood sample volume.

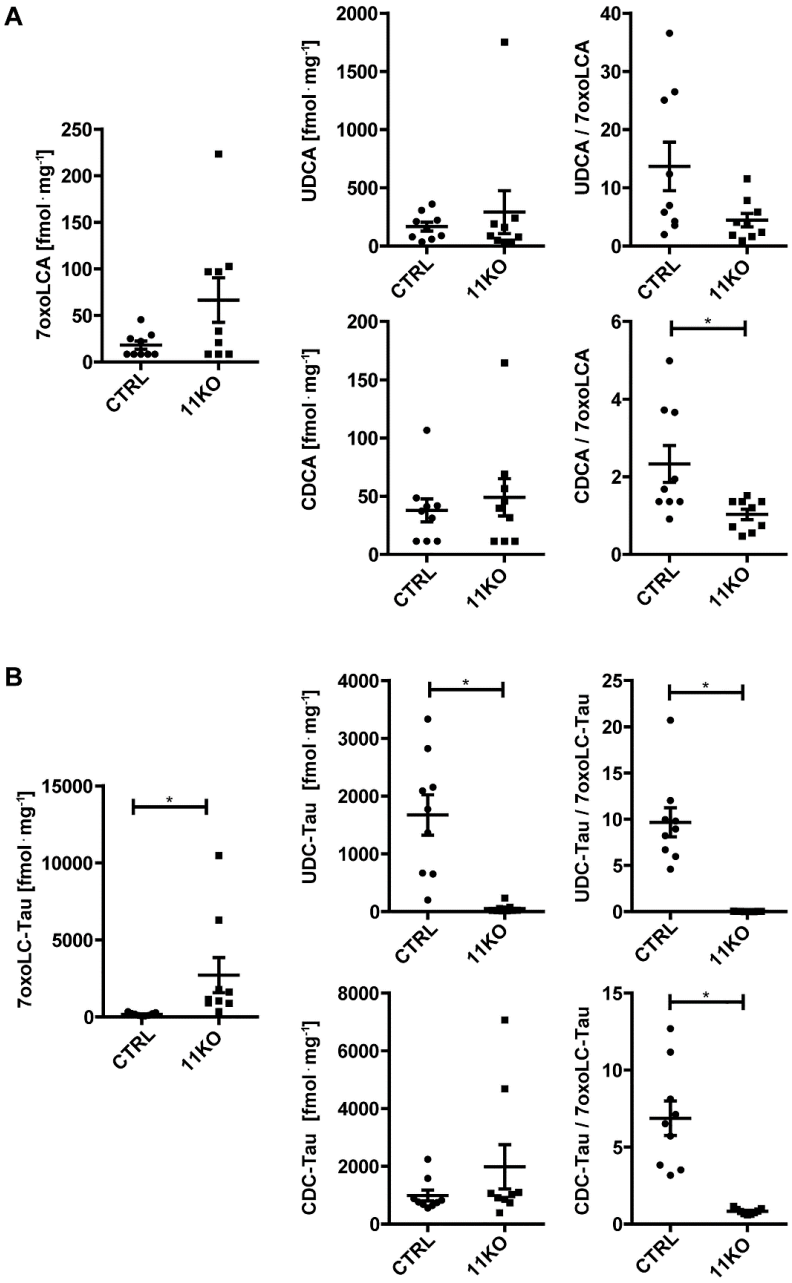

Supplementary Figure 2. **Decreased 11β-HSD1 bile acid product to substrate ratios in liver tissue of 11KO mice**. 11β-HSD1 bile acid substrates (7oxoLCA, 7oxoLC-Tau) and products (UDCA, CDCA and their taurine conjugated forms) were measured in liver tissue of 11KO mice (fmol·mg^{-1}). Calculation of the product to substrate ratios attenuated the large animal-to-animal variations and detected the lack of 11β-HSD1 oxoreduction activity. a) Liver tissue concentrations of CTRL (n = 9) and 11KO mice (n = 9) for 7oxoLCA, CDCA, UDCA and the corresponding ratios; and b) for 7oxoLC-Tau, CDC-Tau, UDC-Tau and the corresponding ratios. The results represent mean ± SEM. No outliers were excluded. Analyte concentrations defined by a S/N ≤ 3 represent the LLOD of the UHPLC-MS/MS method. Samples yielding a concentration below LLOD were included as LLOD/2 in the calculations of a specific analyte. *P<0.05 significantly different as indicated; non-parametric, Mann-Whitney U-test (two-tailed). Unequal group sizes reflect the availability of only nine livers due to the use of nine randomly assigned livers for gene expression analyses in a previous study.

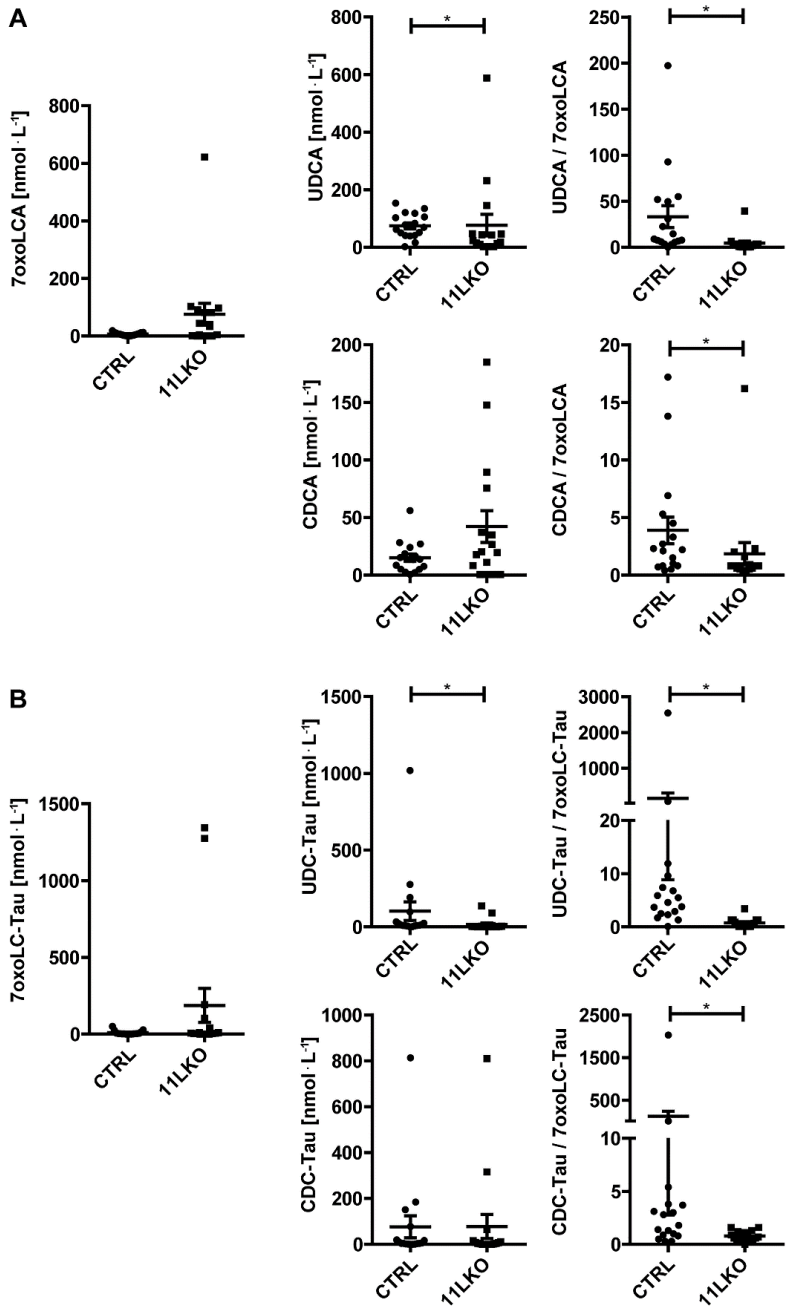

Supplementary Figure 3. Decreased 11β-HSD1 bile acid product to substrate ratios in plasma of 11LKO mice. 11β-HSD1 bile acid substrates (7oxoLCA, 7oxoLC-Tau) and products (UDCA, CDCA and their taurine conjugated forms) were measured in plasma of 11LKO mice (nmol·L^{-1}). Calculation of the product to substrate ratios attenuated the large animal-to-animal variations and detected the decreased 11β-HSD1 oxoreduction activity. a) Plasma concentrations for 7oxoLCA, CDCA, UDCA and the corresponding ratios, and b) for 7oxoLC-Tau, CDC-Tau, UDC-Tau and the corresponding ratios of CTRL (n = 17) and 11LKO mice (n = 16). The results represent mean ± SEM. No outliers were excluded. Analyte concentrations defined by a S/N ≤ 3 represent the LLOD of the UHPLC-MS/MS method. Samples yielding a concentration below LLOD were included as LLOD/2 in the calculations of a specific analyte. *P<0.05 significantly different as indicated; non-parametric, Mann-Whitney U-test (two-tailed). Unequal group sizes reflect exclusion of one 11LKO animal due to unexpected health issues prior to reaching the age for the experiment.

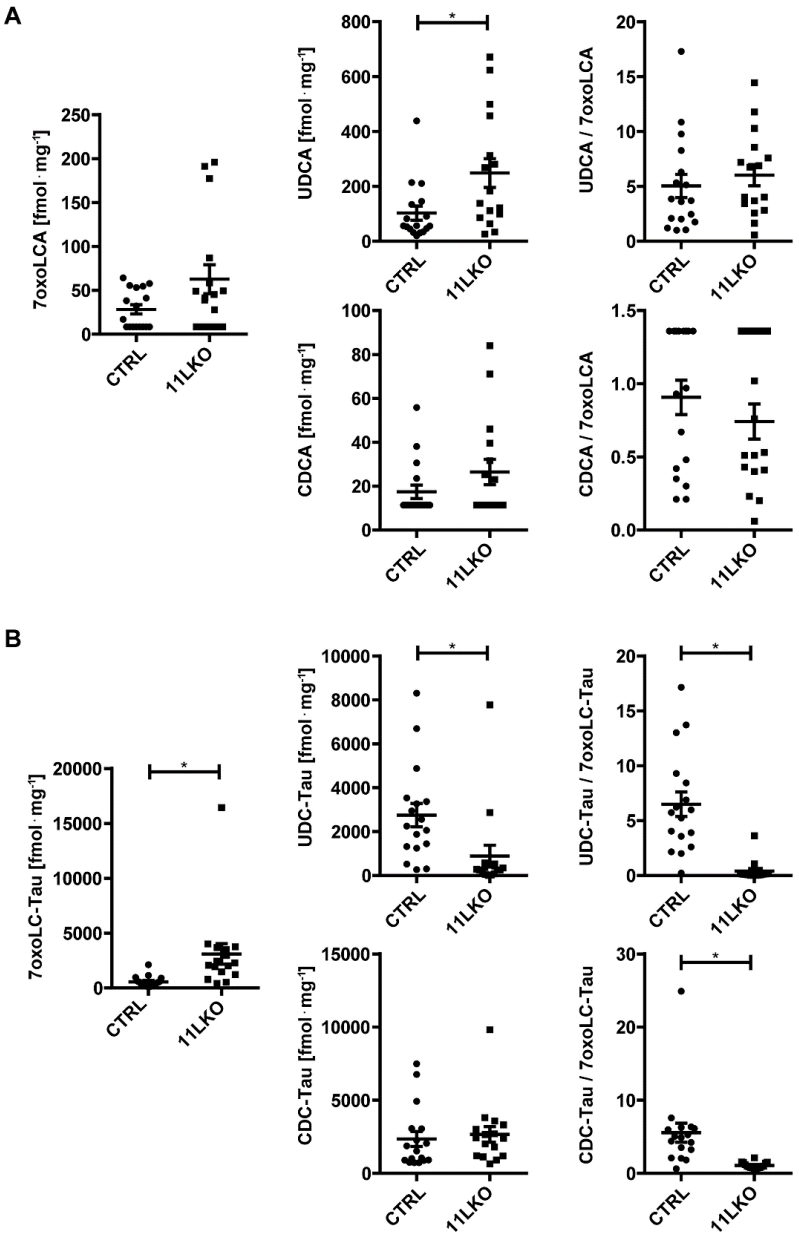

Supplementary Figure 4. Decreased 11β-HSD1 bile acid product to substrate ratios in liver tissue of 11LKO mice. 11β-HSD1 bile acid substrates (7oxoLCA, 7oxoLC-Tau) and products (UDCA, CDCA and their taurine conjugated forms) were measured in liver tissue of 11LKO mice (fmol·mg^{-1}). Calculation of the product to substrate ratios attenuated the large animal-to-animal variations and detected the decreased 11β-HSD1 oxoreduction activity. a) Liver tissue concentrations for 7oxoLCA, CDCA, UDCA and the corresponding ratios, and b) for 7oxoLC-Tau, CDC-Tau, UDC-Tau and the corresponding ratios of CTRL (n = 17) and 11LKO mice (n = 16). The results represent mean ± SEM. No outliers were excluded. Analyte concentrations defined by a S/N ≤ 3 represent the LLOD of the UHPLC-MS/MS method. Samples yielding a concentration below LLOD were included as LLOD/2 in the calculations of a specific analyte. *P<0.05 significantly different as indicated; non-parametric, Mann-Whitney U-test (two-tailed). Unequal group sizes reflect exclusion of one 11LKO animal due to unexpected health issues prior to reaching the age for the experiment.

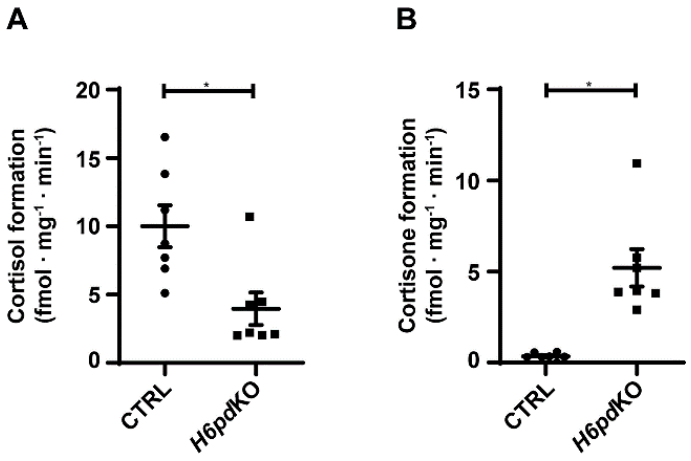

Supplementary Figure 5. Decreased 11β-HSD1 oxoreduction activity in white adipose tissue of *H6pd*KO mice. a) Estimation of the conversion of cortisone to cortisol, and b) of cortisol to cortisone measured *ex vivo* in mouse white adipose tissue (CTRL n = 7; *H6pd*KO n = 7). Results represent mean ± SEM, *P<0.05 significantly different as indicated; non-parametric, Mann-Whitney U-test (two-tailed).

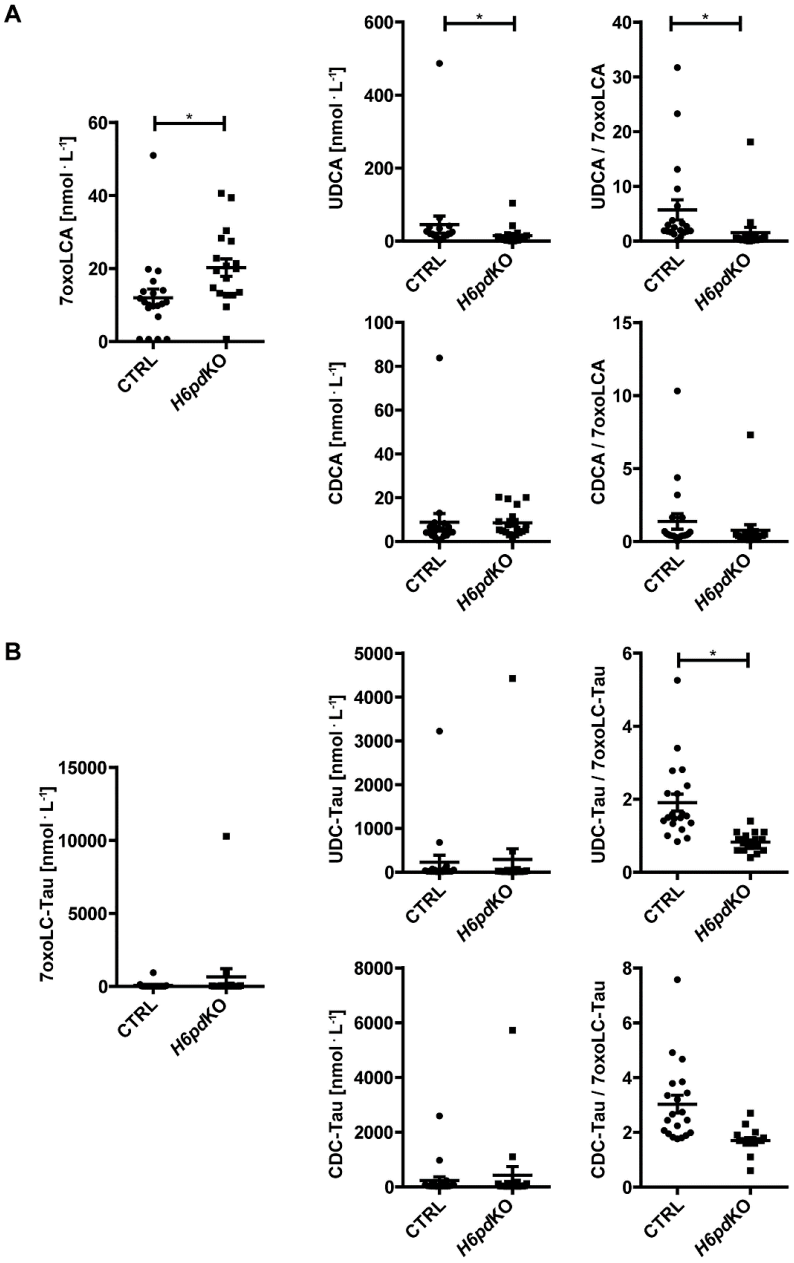

Supplementary Figure 6. Decreased 11β-HSD1 bile acid product to substrate ratios in plasma of *H6pd*KO mice. 11β-HSD1 bile acid substrates (7oxoLCA, 7oxoLC-Tau) and products (UDCA, CDCA and their taurine conjugated forms) were measured in plasma of *H6pd*KO mice. Calculation of the product to substrate ratios attenuated the large animal-to-animal variations and detected the decreased 11β-HSD1 oxoreduction activity. a) Plasma concentrations (nmol·L^{-1}) for 7oxoLCA, CDCA, UDCA and the corresponding ratios, and b) for 7oxoLC-Tau, CDC-Tau, UDC-Tau and the corresponding ratios of CTRL (n = 20) and *H6pd*KO mice (n = 18). The results represent mean ± SEM. No outliers were excluded. Analyte concentrations defined by a S/N ≤ 3 represent the LLOD of the UHPLC-MS/MS method. Samples yielding a concentration below LLOD were included as LLOD/2 in the calculations of a specific analyte. *P<0.05 significantly different as indicated; non-parametric, Mann-Whitney U-test (two-tailed). Unequal group sizes reflect exclusion of two *H6pd*KO animals from further analysis due to the occurrence of liver cysts.

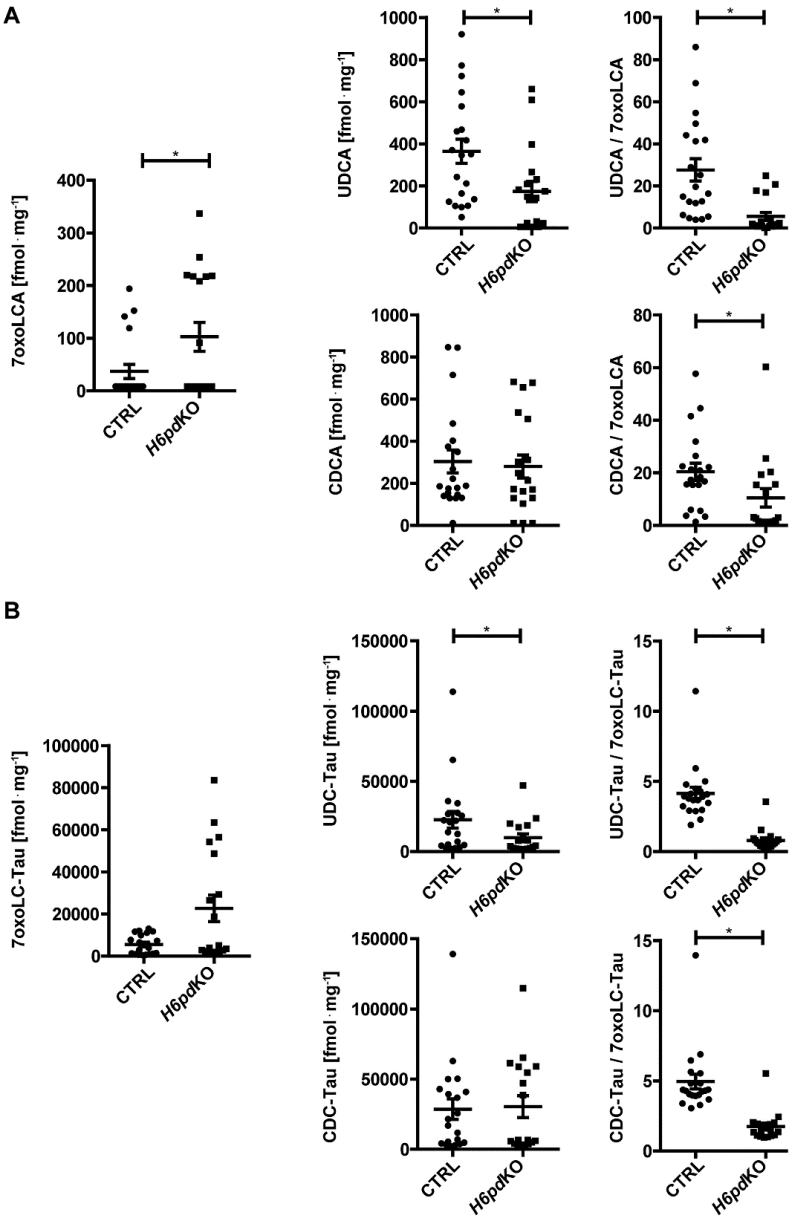

Supplementary Figure 7. Decreased 11β-HSD1 bile acid product to substrate ratios in liver tissue of *H6pd*KO mice. 11β-HSD1 bile acid substrates (7oxoLCA, 7oxoLC-Tau) and products (UDCA, CDCA and their taurine conjugated forms) were measured in liver tissue of *H6pd*KO mice. Calculation of the product to substrate ratios attenuated the large animal-to-animal variations and detected the decreased 11β-HSD1 oxoreduction activity. a) Liver tissue concentrations (fmol·mg^{-1}) for 7oxoLCA, CDCA, UDCA and the corresponding ratios, and b) for 7oxoLC-Tau, CDC-Tau, UDC-Tau and the corresponding ratios of CTRL (n = 20) and *H6pd*KO mice (n = 18). The results represent mean ± SEM. No outliers were excluded. Analyte concentrations defined by a S/N ≤ 3 represent the LLOD of the UHPLC-MS/MS method. Samples yielding a concentration below LLOD were included as LLOD/2 in the calculations of a specific analyte. *P<0.05 significantly different as indicated; non-parametric, Mann-Whitney U-test (two-tailed). Unequal group sizes reflect exclusion of two *H6pd*KO animals from further analysis due to the occurrence of liver cysts.

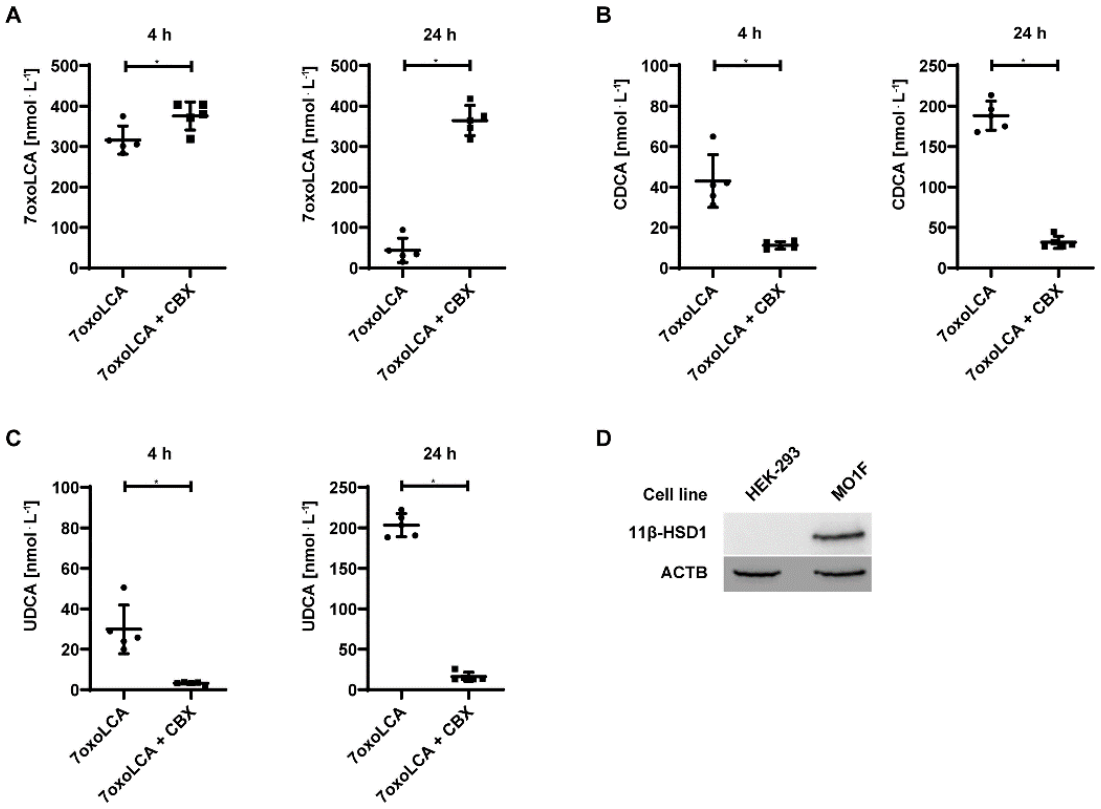

Supplementary Figure 8. Metabolism of 7oxoLCA to UDCA and CDCA by murine 11β-HSD1 and inhibition by CBX. HEK-293 cells expressing murine 11β-HSD1 (MO1F) were incubated with 400 nmol L^{-1} 7oxoLCA in the absence and presence of 5 µmol L^{-1} of CBX, followed by quantification of substrate and products. a) 7oxoLCA concentration [nmol L^{-1}] after 4 h and 24 h of incubation. b) CDCA formation represented as concentration [nmol L^{-1}] after 4 h and 24h of incubation. c) UDCA formation represented as concentration [nmol L^{-1}] after 4 h and 24 h of incubation. d) Representative western blot analysis of protein levels of 11β-HSD1 in untransfected HEK-293 cells and in MO1F cells. ACTB served as loading control. The results represent mean ± SD, n=5. *P<0.05 significantly different as indicated; non-parametric, Mann-Whitney U-test (two-tailed).

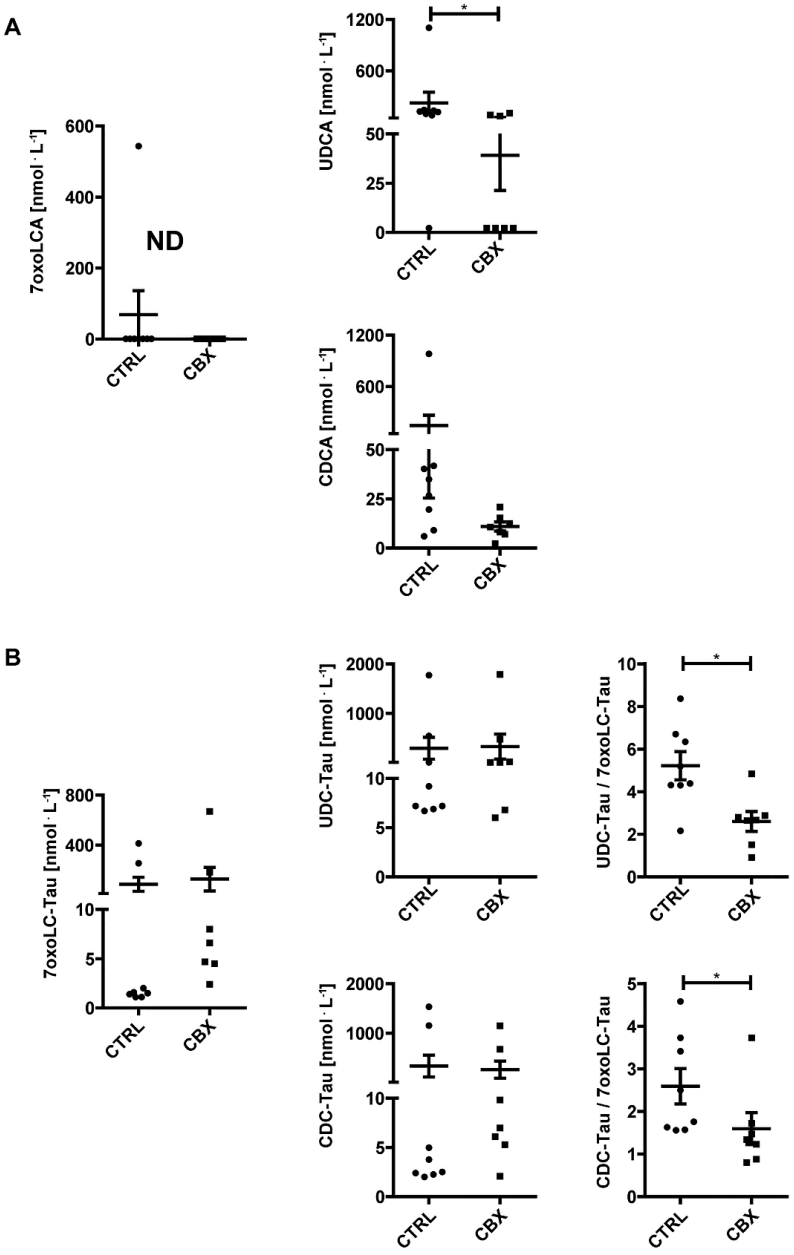

Supplementary Figure 9. Decreased 11β-HSD1 bile acid product to substrate ratios in plasma of mice treated with the inhibitor carbenoxolone (CBX). 11β-HSD1 bile acid substrates (7oxoLCA, 7oxoLC-Tau) and products (UDCA, CDCA and their taurine conjugated forms) were measured in plasma of control mice either treated with the pharmacologic 11β-HSD1 inhibitor CBX (100 mg kg^{-1} d^{-1}, *i.p.*) or PBS (CTRL) (CTRL n = 8; CBX n = 7). Calculation of the product/substrate ratios attenuated the large animal-to-animal variations and detected the diminished 11β-HSD1 oxoreduction activity. a) Plasma concentrations ($nmol \cdot L^{-1}$) of 7oxoLCA, CDCA, UDCA and the corresponding ratios. Some values were below LLOD. b) Plasma concentrations ($nmol \cdot L^{-1}$) of 7oxoLC-Tau, CDC-Tau, UDC-Tau and the corresponding ratios. The results represent mean ± SEM. No outliers were excluded. Analyte concentrations defined by a S/N of ≤ 3 represent the LLOD of the UHPLC-MS/MS method. Samples yielding a concentration below LLOD were included as LLOD/2 in the calculations of a specific analyte. *P<0.05 significantly different as indicated; non-parametric, Mann-Whitney U-test (two-tailed). Unequal group sizes reflect exclusion of one animal of the CTRL group due to unexpected health issues prior to the experiment and exclusion of two plasma samples of the CBX group due to insufficient collection of blood sample volume.

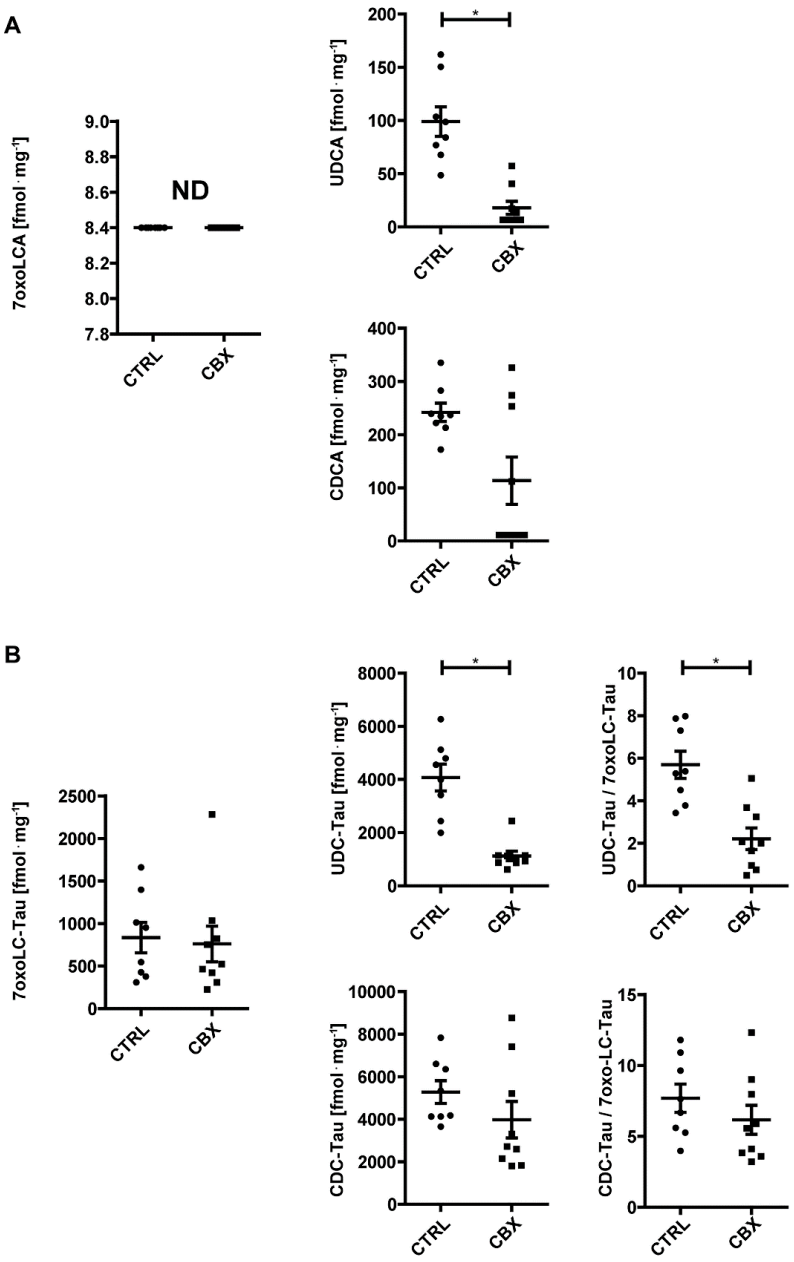

Supplementary Figure 10. **Decreased 11β-HSD1 bile acid product to substrate ratios in liver tissue of mice treated with the inhibitor carbenoxolone (CBX).** 11β-HSD1 bile acid substrates (7oxoLCA, 7oxoLC-Tau) and products (UDCA, CDCA and their taurine conjugated forms) were measured in liver tissue of control mice either treated with the pharmacologic 11β-HSD1 CBX (100 mg kg^{-1} d^{-1}, *i.p.*) or PBS (CTRL) (CTRL n = 8; WT CBX n = 9). Calculation of the product/substrate ratios attenuated the large animal-to-animal variations and detected the diminished 11β-HSD1 oxoreduction activity. a) Liver tissue concentrations (fmol·mg^{-1}) of 7oxoLCA, CDCA, UDCA and the corresponding ratios. Some values were below LLOD. b) Liver tissue concentrations (fmol·mg^{-1}) of 7oxoLC-Tau, CDC-Tau, UDC-Tau and the corresponding ratios. The results represent mean ± SEM. No outliers were excluded. Analyte concentrations defined by a S/N ≤ 3 represent the LLOD of the UHPLC-MS/MS method. Samples yielding a concentration below LLOD were included as LLOD/2 in the calculations of a specific analyte. *P<0.05 significantly different as indicated; non-parametric, Mann-Whitney U-test (two-tailed). Unequal group sizes reflect exclusion of one animal of the CTRL group due to unexpected health issues prior to the experiment.

Analyte	11 KO Plasma [nmol L^{-1}]			11KO Liver [fmol mg^{-1}]			11LKO Plasma [nmol L^{-1}]			11LKO Liver [fmol mg^{-1}]			11H6pdKO Plasma [nmol L^{-1}]			H6pdKO Liver [fmol mg^{-1}]			CBX Plasma [nmol L^{-1}]			CBX Liver [fmol mg^{-1}]		
	ES (g)	CI		ES (g)	CI		ES (g)	CI		ES (g)	CI		ES (g)	CI		ES (g)	CI		ES (g)	CI		ES (g)	CI	
		+	-		+	-		+	-		+	-		+	-		+	-		+	-		+	-
CA	2.4	3.3	1.6	1.5	2.6	0.5	2.0	2.8	1.2	3.6	4.7	2.5	-0.9	-0.2	-1.5	-1.3	-0.6	-2.0	-0.9	0.1	-2.0	-2.3	-1.0	-3.6
CDCA	2.3	3.2	1.5	0.8	1.8	-0.2	2.6	3.5	1.7	1.8	2.6	1.0	-0.1	0.6	-0.7	-0.4	0.2	-1.1	-1.5	-0.3	-2.6	-3.8	-2.1	-5.5
DCA	2.7	3.6	1.8	1.1	2.0	0.1	0.5	1.2	-0.2	1.0	1.7	0.3	-2.4	-1.6	-3.3	-2.8	-1.9	-3.7	-2.2	-0.9	-3.5	-6.8	-4.1	-9.4
7oxoDCA	2.7	3.6	1.8	1.8	2.9	0.7	2.0	2.8	1.2	4.4	5.7	3.2	0.3	0.9	-0.4	0.2	0.8	-0.5	0.2	1.2	-0.8	1.1	2.2	0.0
HDCA	4.4	5.6	3.1	3.0	4.3	1.6	0.9	1.6	0.1	2.8	3.8	1.9	-0.2	0.4	-0.8	-1.3	-0.6	-2.0	-1.8	-0.6	-3.0	-4.1	-2.3	-5.9
αMCA	3.0	4.0	2.0	2.4	3.6	1.2	1.8	2.6	1.0	4.3	5.6	3.1	0.3	0.9	-0.4	-0.6	0.1	-1.2	-1.4	-0.3	-2.6	-4.2	-2.4	-6.0
βMCA	0.9	1.6	0.2	-3.4	-2.0	-4.8	-4.8	-3.5	-6.2	-0.5	0.2	-1.2	-2.0	-1.2	-2.8	-4.5	-3.3	-5.7	-0.9	0.2	-2.0	2.6	3.9	1.2
ωMCA	2.0	2.9	1.2	0.1	1.0	-0.8	0.1	0.8	-0.5	3.2	4.2	2.1	-1.4	-0.7	-2.1	-3.5	-2.5	-4.6	-1.9	-0.7	-3.1	2.1	3.4	0.9
UDCA	2.6	3.5	1.7	0.9	1.9	-0.1	0.1	0.8	-0.6	3.5	4.6	2.4	-1.6	-0.9	-2.4	-3.5	-2.5	-4.5	-2.0	-0.7	-3.2	-7.1	-4.4	-9.9
7oxoLCA	2.7	3.6	1.8	2.8	4.1	1.5	2.6	3.5	1.6	2.8	3.7	1.8	3.5	4.5	2.5	3.0	3.9	2.1	NA			NA		
αMCA/βMCA	14.3	17.7	10.9	30.7	40.8	20.6	24.0	29.8	18.2	49.3	61.2	37.4	54.6	66.9	42.3	42.2	51.8	32.7	1.3	2.4	0.2	-21.1	-13.5	-28.8
UDCA/7oxoLCA	-8.4	-6.3	-10.5	-11.6	-7.7	-15.6	-17.0	-12.9	-21.2	5.2	6.6	3.7	-16.6	-12.8	-20.4	-34.2	-26.5	-41.9	NA			NA		
CDCA/7oxoLCA	-8.1	-6.1	-10.1	-13.5	-9.0	-18.0	-8.3	-6.2	-10.4	-7.7	-5.7	-9.7	-7.6	-5.8	-9.5	-17.2	-13.2	-21.1	NA			NA		
C-Tau	9.1	11.3	6.9	6.1	8.3	3.9	-2.8	-1.9	-3.8	2.6	3.6	1.7	3.8	4.9	2.8	-8.4	-6.4	-10.4	1.6	2.7	0.4	-4.9	-2.9	-6.9
CDC-Tau	8.9	11.1	6.7	6.9	9.4	4.5	0.2	0.9	-0.5	3.2	4.3	2.2	4.8	6.0	3.5	1.4	2.1	0.7	-1.3	-0.2	-2.4	-6.5	-4.0	-9.1
DC-Tau	8.7	10.8	6.5	4.0	5.7	2.4	3.8	4.9	2.6	-5.7	-4.2	-7.3	3.3	4.3	2.3	-6.1	-4.6	-7.6	-2.0	-0.8	-3.3	-21.9	-14.0	-29.8
LC-Tau	9.6	12.0	7.3	6.1	8.2	3.9	-110.3	-83.7	-136.9	-4.8	-3.5	-6.2	5.6	7.0	4.2	3.2	4.1	2.2	-5.7	-3.4	-8.0	-23.8	-15.2	-32.3
αMCA-Tau + βMCA-Tau	8.4	10.5	6.3	0.6	1.5	-0.4	3.8	4.9	2.6	-0.7	0.0	-1.4	-2.8	-1.9	-3.7	-14.3	-11.0	-17.6	-1.2	-0.1	-2.3	2.9	4.4	1.5
ωMCA-Tau	33.2	41.0	25.4	-8.6	-5.6	-11.5	-3.8	-2.6	-4.9	-4.8	-3.5	-6.2	1.6	2.3	0.8	-14.0	-10.8	-17.2	4.3	6.2	2.5	3.9	5.7	2.2
UDC-Tau	7.2	9.0	5.4	-25.5	-17.1	-33.9	-10.8	-8.1	-13.5	-19.9	-15.0	-24.7	1.9	2.6	1.1	-15.8	-12.2	-19.4	0.5	1.6	-0.5	-26.9	-17.2	-36.5
7oxoLC-Tau	11.8	14.6	8.9	12.4	16.5	8.2	12.6	15.8	9.5	21.1	26.2	15.9	8.6	10.7	6.6	22.8	28.0	17.6	1.9	3.1	0.7	-1.4	-0.3	-2.5
UDC-Tau/7oxoLC-Tau	-46.7	-35.7	-57.6	-32.7	-22.0	-43.5	-8.0	-5.9	-10.0	-41.2	-31.3	-51.2	-36.8	-28.5	-45.1	-61.3	-47.5	-75.0	-14.9	-9.5	-20.3	-22.2	-14.2	-30.2
CDC-Tau/7oxoLC-Tau	-13.4	-10.2	-16.5	-30.5	-20.5	-40.4	-7.6	-5.7	-9.6	-26.2	-19.8	-32.5	-32.2	-24.9	-39.4	-47.8	-37.0	-58.5	-9.0	-5.6	-12.4	-5.3	-3.1	-7.4
Sum primary BA	14.6	18.0	11.1	4.7	6.5	2.9	8.6	10.8	6.4	16.3	20.3	12.3	-7.2	-5.4	-8.9	-16.3	-12.6	-20.0	-3.9	-2.2	-5.6	7.7	10.6	4.8
Sum primary BA-Tau	8.9	11.1	6.7	4.0	5.6	2.4	0.1	0.7	-0.6	1.3	2.1	0.6	3.5	4.5	2.5	-10.3	-7.9	-12.7	1.0	2.1	-0.1	-2.4	-1.0	-3.7

Supplementary Table 1. Effect sizes of bile acid profiles measured by UHPLC-MS/MS in plasma and liver samples were determined for mice with global *Hsd11b1* knockout (11KO), liver-specific *Hsd11b1* knockout (11LKO), global *H6pd* knockout (*H6pd*KO) compared to the respective control littermates. Additionally, mice treated with the pharmacological inhibitor carbenoxolone (CBX) were compared to untreated control mice. Results represent the effect size calculated based on Cohen's d effect size (ES d) with correction of unequal sample sizes for the analysis of data from non-parametric analysis (Mann-Whitney U-test) calculated as Hedges g (ES g) and corresponding confidence intervals of the effect size (± CI). NA, not analysed.

8 General discussion and outlook

The ER plays an important role in various cellular processes. During the last decades, research has identified ER specific activities which are linked to the development of numerous pathologies. Prolonged ERS and activation of the UPR were linked to the pathogenesis of many diseases including type 2 diabetes mellitus (Cnop *et al.*, 2012), atherosclerosis (Hotamisligil, 2010), Parkinson's disease (Ryu *et al.*, 2002), Alzheimer's disease (Gerakis and Hetz, 2018) as well as different infectious diseases (Li *et al.*, 2015; Pillich *et al.*, 2016) and multiple types of cancer (Chen and Cubillos-Ruiz, 2021). Among other factors, depletion of luminal NADPH levels or a decreased ratio of NADPH/$NADP^+$ were reported to cause ER stress and, to some extent cell death (Kapuy and Banhegyi, 2013). To date, H6PD represents the only known source of luminal NADPH. While other potential NADPH-generating enzymes such as isocitrate dehydrogenase (Margittai and Banhegyi, 2008), malic enzyme (Wang *et al.*, 2011) and 6-phosphogluconolactone dehydrogenase (Hino and Minakami, 1982a) were suggested to contribute to the luminal NADPH-production, their identity within the ER has yet to be confirmed and H6PD remains the sole undisputed characterized protein capable to generate NADPH in the ER. In this context, it is important to mention the challenges when measuring activities of luminal enzymes. Isolation and purification of microsomal fractions in the course of experimental work can lead to decreased/loss of enzyme activity. On the other hand, contamination of microsomal preparations with other cellular organelles such as mitochondria can result in misleading conclusions. This incontrovertible framework complicates studies related to the luminal NADPH homeostasis.

In the first part of this thesis, we intended to take these limitations into account when exploring the interacctome of H6PD. We applied proximity biotinylation (BioID) to identify vicinal proteins of H6PD and therefore potential interactors. BioID takes advantage of a mutant form of *Escherichia coli* biotin ligase (BirA*) which is able to promiscuously biotinylate vicinal and interacting proteins (Liu *et al.*, 2018). BirA*, fused to the bait (here H6PD), labels proteins covalently within a radius of approximately 10 nm (Kim *et al.*, 2014). Harsh lysis of cells is followed by purification of biotinylated proteins via immunoprecipitation using streptavidin-labeled beads. Isolated proteins are afterwards identified by MS analysis. Among the potential interactors, we expected to identify hits harboring the RMF-motif and therefore to be qualified as potential NAD(P)(H)-binding proteins. Over 82 distinct SDRs exist in human. However, their enzymatic functions and subcellular locations have yet to be fully elucidated (Kallberg *et*

al., 2010). Regarding this circumstance, we hypothesized that other luminal NADP(H)-dependent SDR exist that interact with H6PD either directly or within a multi-protein complex. However, the dataset originating from our BioID-based approach (the whole lists of proteins can be found in chapters 10.1 and 10.2, respectively) did not include any enzyme associated with NADP(H)-consumption. A critical evaluation of the presented results is therefore important to ensure further projects in the study of the luminal NADPH homeostasis are using optimal models. The MDA-MB 231 cell line used in our study endogenously expresses H6PD and the lumen-facing NADPH-dependent 17β-HSD12, but lacks 11β-HSD1 expression (Tsachaki *et al.*, 2015; Cossu *et al.*, 2020; Tsachaki *et al.*, 2020). Whilst an interaction between H6PD and 17β-HSD12 in H6PD-BirA*-HA expressing cells was not observed, we were confident that the BioID-based approach was functional because we detected the well-studied interaction between H6PD and 11β-HSD1 (Atanasov *et al.*, 2008; Zhang *et al.*, 2009) in cells expressing H6PD-BirA*-HA and 11β-HSD1-FLAG. Among the potential interactors identified, AGR2 was selected for detailed analysis. Our Co-IP experiments suggest that AGR2 directly interacts with H6PD in MCF7 cells. Moreover our results indicate that H6PD protein expression and H6PD activity are dependent on the expression of its interacting partner AGR2. HEK-293 cells transfected with plasmid DNA coding for H6PD in combination with plasmid coding for AGR2 showed increased H6PD activity compared to cells solely transfected with plasmid DNA coding for H6PD. The next logical step in this project is to test H6PD enzyme activity in MCF7 cells following targeted AGR2 depletion using siRNA. This experiment would support our hypothesis that AGR2 directly affects H6PD activity. Moreover, a second independent BioID-based screen for potential H6PD interactors in MCF7 cells might be useful to confirm our observations.

At this point, it is further important to critically evaluate the utility of BioID. Like every method, BioID has its advantages and disadvantages. First, proximity biotinylation is considered non-toxic and therefore extended biotinylation periods do not represent a major concern in this regard (Cho *et al.*, 2020). Further, the strong interaction between streptavidin and biotin allows stringent purification procedures using streptavidin-coupled beads and, as a result, reduction of non-specific binding (Larochelle *et al.*, 2019). Many of the disadvantages of BioID are based on the enzymatic features of the used biotin ligase. BirA* has a molecular mass of 35 kDa (Varnaite and MacNeill, 2016). The increased molecular weight of the resulting fusion protein (here H6PD-BirA*-HA) may affect localization and functionality of the protein of interest. Moreover, biotinylation by BioID takes its time. Unspecific biotinylation is therefore a time-dependent issue when preforming this method. Addressing these concerns and problems,

Branon and colleagues engineered TurboID (35 kDa) and miniTurbo (28 kDa), two more efficient versions of BioID (Branon *et al.*, 2018). Whereas the biotinylation process in BioID-based approached takes between 12 h up to 168 h (Uezu *et al.*, 2016), applications of TurboID and miniTurbo were shown to sufficiently biotinylate neighboring proteins within 10 min (Zhang *et al.*, 2019). Further, in 2020, Kido et al. presented AirID, a novel version of BirA*, developed with the motive to minimize the application problems of TurboID (Kido *et al.*, 2020). Summarizing the first project of this thesis we can state that BioID represents an attractive method to screen for PPI. It is necessary, however, to consider the limitations of this method and, to carefully select the cell type/model for experimental work.

The second part of this work was devoted to better understand the roles of ERS and the UPR in parasitic infection. An increasing number of studies have highlighted the utility of targeting modulation of ERS and the UPR in a number of diseases (Rivas *et al.*, 2015; Rahmati *et al.*, 2018). Currently, several compounds have been investigated for their UPR modulating features. For example Salubrinal, a selective inhibitor of eIF2α dephosphorylation, was shown to protect mammalian cells from ERS and inhibit viral replication in cells infected with *Herpes simplex virus* (Boyce *et al.*, 2005). Other compounds such as the IRE1α-RNase inhibitor STF-083010, a drug candidate for the treatment of multiple myeloma or GSK2656157, a PERK kinase inhibitor developed for the treatment of pancreatic cancer and multiple myeloma are, among others, in the preclinical development stage (Papandreou *et al.*, 2011; Atkins *et al.*, 2013; Axten *et al.*, 2013). In the second project we investigated whether an infection with *E. multilocularis* causes ERS in mice. Animals were subjected to either *E. multilocularis* or mock-infection and, six weeks after infection, treatment with the anthelmintic drug ABZ or placebo for a duration of eight weeks. Analysis of liver tissue revealed increased protein levels of ATF6, CHOP, CRT, ERP72, GRP78 in mock-treated mice upon *E. multilocularis* infection, whereas PERK and its target eIF2α were found unaltered. IRE1α and ATF4 protein levels were found to be decreased. These findings indicate a direct impact of *E. multilocularis* infection on the cellular stress response. Treatment of infected animals with ABZ (partially) reversed the observed alterations in protein expression, emphasizing the effectiveness of the drug in the treatment of *E. multilocularis* infection in mice.

Interestingly, H6PD protein levels were found to be increased in the liver tissue of mock-treated infected animals. In a previous publication, Tsachaki et al. reported decreased ATF4, ATF6, CHOP, GRP78 and XBP1-s protein levels after knock-down of H6PD in the triple negative breast cancer cell line SUM 159. Moreover, ERP72 and CRT protein levels were found to be

increased after knock-down of H6PD. Protein expression of PERK and eIF2α were unaltered (Tsachaki *et al.*, 2018).

Our study revealed that mock-treated mice infected with *E. multilocularis* were exposed to ER stress over an extended period. Prolonged ER stress can initiate apoptosis mediated via CHOP. Regulation of CHOP-induced apoptosis by microbes is considered a useful strategy for the microorganism (Hu *et al.*, 2018). However, we cannot state whether this also applies to *E. multilocularis* infection. Further, observed increased CRT, ERP72 and GRP78 protein levels might be associated with a demand for increased luminal protein folding capacity. During ER stress PDI family member ERP72, CRT and GRP78 act as luminal chaperones (Wu and Kaufman, 2006). In our study we used mouse liver tissue to determine protein expression levels. Hepatocytes constitute approximately 80% of the total liver volume and mass (Tanaka and Miyajima, 2016). Besides their other functions, they are found to play an important role in immune response by secreting various innate immunity protein such as hepcidin, hemopexin or fibrinogen (Zhou *et al.*, 2016). In a previous study, mice infected with *E. multilocularis* showed overexpressed gene levels of a number of acute phase proteins including hemopexin (Lin *et al.*, 2011). This finding would supports the hypothesis that luminal protein folding capacity in the analyzed hepatic liver tissue was increased.

Finally, it is known that disturbances of the luminal pyridine nucleotide redox state result in ER stress (Szaraz *et al.*, 2010). The observed increase of H6PD protein expression in animals infected with *E. multilocularis* may be a consequence of an increased demand for reduced pyridine nucleotides in the ER lumen. However, the exact use of NADPH in this context remains unclear and additional work is required to unravel the specific role of H6PD in the UPR and ERS. Further, although one cannot postulate a direct correlation between the results presented by Tsachaki et al. and the results in our study, it might be of importance for further investigations to pay attention to the fact, that similar proteins of the UPR are altered upon either silencing of H6PD or its upregulation.

In term of the clinical relevance of our results we also need to address *E. multilocularis* infection in human. Alveolar echinococcosis (AE), caused by the larval stage of *E. multilocularis*, represents a dangerous zoonosis, listed among the neglected tropical diseases (Casulli, 2020). AE is characterized by an asymptomatic course and high mortality (approximately 90% within 10 years and up to 100% within 15 years) in untreated cases, highlighting the risk of this disease (Maddah *et al.*, 2016). Treatment of AE is limited to surgical interventions (including liver transplantation) and (life-long) therapy using anthelmintic drugs such as ABZ (Siles-Lucas *et al.*, 2018). A study by Torgerson *et al.* approximated over 18’000 (CIs 11’900-

28’200) new cases of AE every year, corresponding to approximately 666’000 (CIs 331’000 – 1’300’000) disease-adjusted life years (Torgerson *et al.*, 2010). While approximately 91% of all new AE cases are reported in China (Wang *et al.*, 2020), increasing numbers of cases were recently described in southern Germany (Mueller *et al.*, 2020). Thus, considering the geographically spread of *E. multilocularis* and the increasing numbers of AE, the need for better understanding of both parasite and clinical manifestation as well as additional treatment options become evident (Chauchet *et al.*, 2014; Mueller *et al.*, 2020). In conclusion, our results enable the opportunity to consider the UPR and UPR-related processes as druggable targets in *E. multilocularis* infection. However, given the stage of development of such drug candidates, it will still take some time before results can be expected in this regard (Cubillos-Ruiz *et al.*, 2017).

In the second project of this part, we analyzed the BA profiles of serum from *E. multilocularis* infected mice. For decades, the measurement of BA profiles has been considered as a biomarker of liver function (Mills *et al.*, 1998; Lucangioli *et al.*, 2009; Luo *et al.*, 2018). Perturbation of BA (ratios) was shown to indicate drug induced liver injuries (Yamazaki *et al.*, 2013). The utility of BA as biomarkers has been described in the context of several maladies such as viral hepatitis (Simko and Michael, 1998) or nonalcoholic fatty liver disease (Dasarathy *et al.*, 2011). In our study, we observed significantly increased levels of TCA and TβMCA, which represent the most abundant bile acids in mice (Li and Dawson, 2019), whereas other tauine-conjugated bile acids were not altered. All unconjugated primary and secondary BA levels were found to be decreased in mock-treated infected animals compared to non-infected mice. Interestingly, the (total) BA profile was restored after treating infected animals with ABZ (chapter 6.2, Fig. 2), thereby demonstrating the effectiveness of the drug. Protein or gene expression levels of relevant hepatic BA transporters were found either decreased (BSEP, NTCP, Oatp4, Ostα) or unaltered (OATP1A1, Mrp2, Mrp4, Ostβ). Likewise, enzymes involved in BA synthesis tended to decrease (AKR1D1) or were not altered (CYP7A1, CYP27A1) regarding their protein (AKR1D1) and gene expression (AKR1D1, CYP7A1, CYP27A1) levels. This suggests that the observed alterations in the BA profiles in our study might be at least partly mediated by decreased activity of farnesoid X receptor (FXR) activation (Fiorucci *et al.*, 2021). As a result of inflammation, however, the trend decrease in CYP7A1 is opposite to what would be expected upon lower FXR activity. We suggest that the observed shift from free to taurine-conjugated BA in the serum is a direct result of *E. multilocularis* infection. It would therefore be important to quantify BA in liver tissue collected in the context of this study to verify this hypothesis.

Either way, our BA profile findings could be useful in the effort to develop new strategies to diagnose *E. multilocularis* infection. Further, biomarker(s) to detect *E. multilocularis* infection would be helpful to track disease progression and therapeutic efficacy. However, the alterations in BA levels need to be confirmed and validated in human, in order to show whether BA profiles are a suitable biomarker for AE. Moreover, TβMCA, one of the BA found to be increased in *E. multilocularis* infected mice, is synthesized by CYP2C70 mediated conversion of UDCA (Chapter 3, Fig. 3) and therefore this BA is found in mice and rats but not in human (Yao *et al.*, 2018). Regarding the limitations of our approach in this context, it is also important to mention the difference between the mouse model used in this study and the pathogenesis of AE in human. In our work, we examined liver tissue of mice subjected to *E. multilocularis* by secondary infection, whereas AE in human is caused by accidental ingestion of infective eggs (Kern *et al.*, 2004). Thus, parasitic growth in human may differ from our model, which in turn may result in alternative effects on BA profiles.

In the last part of this thesis, we addressed the problem of measuring 11β-HSD1 activity *in vivo*. Suitable biomarkers would be helpful in the development of pharmacological 11β-HSD1 inhibitors. Modulation and in particular inhibition of 11β-HSD1 activity represent promising strategies in the treatment of diseases associated with an imbalance of tissue specific glucocorticoid activation. Terao *et al.* postulated the application of 11β-HSD1 inhibitors to promote skin repair and wound healing (Terao *et al.*, 2011). Moreover, selective inhibition of 11β-HSD1 is expected to have a beneficial impact on the metabolic syndrome (Koike *et al.*, 2019) and DM type 2 (Hollis and Huber, 2011). Furthermore, in the context of a multicenter phase II clinical trial, Hardy *et al.* examined the effectiveness of the novel 11β-HSD1 inhibitor AZD4017. Their findings demonstrated improved lipid profiles, markers of hepatic function and increased lean muscle mass in obese women diagnosed with idiopathic intracranial hypertension (IIH) after treatment with AZD4017 compared to the placebo-treated control group (Hardy *et al.*, 2021).

The biomarker we present in this work to detect decreased 11β-HSD1 enzyme activity was found to be robust in a number of independent mouse models. However, following the principle of 3Rs (reduce, refine, replace) our study included only male mice at the age of 10-15 weeks. The time point of sacrifice is in contrast to the mean lifespan of male C57BL/6J mice, which is approximately 900 days (Brust *et al.*, 2015). The question whether age or sex influence the BA profile has been addressed in several studies. In previous work Xie *et al.* analyzed BA concentrations in the serum of 502 healthy individuals which demonstrated that BA profiles

were influenced by age, sex and body-mass-index (Xie *et al.*, 2015). Supporting these findings, Frommherz *et al.* reported overall higher median plasma levels of BA in men compared with women. Also, age related differences in BA profiles were described (Frommherz *et al.*, 2016). Finally, many of the potential applications of 11β-HSD1 activity biomarkers are in the context of identifying and monitoring pathophysiological conditions. This is important, since (Poly-)medication in the treatment of (metabolic) diseases is common in the western hemisphere and thereby modulation of BA profiles might affect the utility of presented biomarker (Li *et al.*, 2019). In conclusion, we can state that further investigations in human are needed to confirm the utility of the presented BA biomarker to monitor 11β-HSD1 activity *in vivo* in different disease situations and upon pharmacological treatment.

9 Acknowledgement

I would like to thank Prof. Dr. Alex Odermatt, for giving me the opportunity to learn and work as a PhD student in his research group. His advices, expertise and the encouraging way he supervised the presented projects were indispensable.

Further, I thank Prof. Dr. Jörg Huwyler for his role as my second supervisor. I would also express my gratitude to Prof. Dr. David Hoogewijs for being the external expert of this thesis committee, and Prof. Dr. Daniel Ricklin for his commitment to chair the doctoral exam.

Additionally I would like to thank Dr. Maria Tsachaki for the time and effort she spent for supervising the first months of my time in this group and all the help with the BioID-project.

Many thanks are directed to Dr. Thomas Bock for his assistance with LC-MS measurements and proteomic analysis.

In this regard, I also thank Mr. Pascal Fluder for proofreading the BioID-project manuscript.

I would also thank Dr. Cristina Gómez Castellà, Dr. Fadi Jebbawi and Mr. Simon Stücheli for the opportunity to collaborate on the projects presented in this thesis and of course their help and inputs.

Further, I wish to express warm thanks to Dr. Adam Lister and my former master's thesis supervisor Dr. Daniel Preisig for proofreading the thesis and for their constructive criticism.

This thesis is also an achievement of the whole Molecular and Systems Toxicology group. I highly appreciated the spirit of helping and encouraging each other, the discussions and of course all the good laughs we had together. In this way, I would like to express my gratitude to all present and former group members of the Molecular and Systems Toxicology group.

Finally, I would like to extend my warmest thanks to my parents, my family and all my friends for their support and help during the past years.

10 Appendix

10.1 List of proteins identified by BioID-based proximity labeling in MDA-MB 231 cells stably expressing H6PD-BirA*-HA compared to control (MDA-MB 231 cells)

Log_2-ratio ≥ 1, qValue ≤ 0.05, compared to control (MDA-MB 231)

MOGS	Mannosyl-oligosaccharide glucosidase
CRELD2	Cysteine-rich with EGF-like domain protein 2
TMTC3	Transmembrane and TPR repeat-containing protein 3
TMED2	Transmembrane emp24 domain-containing protein 2
IKBIP	Inhibitor of nuclear factor kappa-B kinase-interacting protein
AGR2	Anterior gradient protein 2 homolog
COL4A2	Collagen alpha-2(IV) chain
SELENOF	15 kDa selenoprotein
HYOU1	Hypoxia up-regulated protein 1
RCN1	Reticulocalbin-1
SDF2L1	Stromal cell-derived factor 2-like protein 1
PDIA4	Protein disulfide-isomerase A4
MCFD2	Multiple coagulation factor deficiency protein
DNAJB12	DnaJ (Hsp40) homolog, subfamily B, member 12, isoform CRA_c
H6PD	FUSION Cterm-BirA C-H6PD linker sequence BirA HA tag
	GDH/6PGL endoplasmic bifunctional protein
MYDGF	Myeloid-derived growth factor
TMED9	Transmembrane emp24 domain-containing protein 9
LMAN1	Protein ERGIC-53
PRKCSH	Glucosidase 2 subunit beta
TXNDC5	Thioredoxin domain-containing protein 5
CALU	Calumenin
SDF4	45 kDa calcium-binding protein (Fragment)
P4HB	Protein disulfide-isomerase
PDIA3	Protein disulfide-isomerase A3
DNAJB11	DnaJ homolog subfamily B member 11

DNAJC3	DnaJ homolog subfamily C member 3
HSPA5	78 kDa glucose-regulated protein
ITGB1	Integrin beta-1
PCYOX1	Prenylcysteine oxidase 1
NUP210	Nuclear pore membrane glycoprotein 210
UGGT1	UDP-glucose:glycoprotein glucosyltransferase 1
ERO1A	ERO1-like protein alpha
CNPY3	Protein canopy homolog 3
SUMF2	Sulfatase-modifying factor 2
LMAN2L	VIP36-like protein
PLOD3	Procollagen-lysine,2-oxoglutarate 5-dioxygenase 3
ERP29	Endoplasmic reticulum resident protein 29
TMX1	Thioredoxin-related transmembrane protein 1
MANF	Mesencephalic astrocyte-derived neurotrophic factor
SEL1L	Protein sel-1 homolog 1
FKBP2	Peptidyl-prolyl cis-trans isomerase FKBP2
NENF	Neudesin
CALR	Calreticulin
P3H1	Prolyl 3-hydroxylase 1
MLEC	Malectin
PDIA6	Protein disulfide-isomerase A6
MESDC2	LDLR chaperone MESD
CANX	Calnexin
PRDX4	Peroxiredoxin-4
TMEM43	Transmembrane protein
NA	Uncharacterized protein (Fragment)
HSP90B1	Endoplasmin
CHID1	Chitinase domain-containing protein 1
RCN2	Reticulocalbin-2
DDOST	Dolichyl-diphosphooligosaccharide--protein glycosyltransferase 48 kDa subunit
SLC39A7	Zinc transporter SLC39A7
NOMO1	Nodal modulator 1
RPN1	Dolichyl-diphosphooligosaccharide--protein glycosyltransferase subunit 1
PLOD2	Procollagen-lysine,2-oxoglutarate 5-dioxygenase 2

DNAJC10	DnaJ homolog subfamily C member 10
ERP44	Endoplasmic reticulum resident protein 44
MIA3	Melanoma inhibitory activity protein 3
TMED10	Transmembrane emp24 domain-containing protein 10
POFUT2	GDP-fucose protein O-fucosyltransferase 2
RPN2	Dolichyl-diphosphooligosaccharide--protein glycosyltransferase subunit 2
ERGIC3	Endoplasmic reticulum-Golgi intermediate compartment protein 3 (Fragment)
LRPAP1	Alpha-2-macroglobulin receptor-associated protein
STIM1	Stromal interaction molecule 1
EMC1	ER membrane protein complex subunit 1
COLGALT1	Procollagen galactosyltransferase 1
TMEM109	Transmembrane protein 109
PDIA5	Protein disulfide-isomerase A5
SERPINH1	Serpin H1
PBXIP1	Pre-B-cell leukemia transcription factor-interacting protein 1
NA	Uncharacterized protein
GANAB	Neutral alpha-glucosidase AB
TAPBP	Tapasin
CKAP4	Cytoskeleton-associated protein 4
P4HA1	Prolyl 4-hydroxylase subunit alpha-1
TXNDC12	Thioredoxin domain-containing protein 12
LAMC1	Laminin subunit gamma-1
PLOD1	Procollagen-lysine,2-oxoglutarate 5-dioxygenase 1
TOR1AIP1	Torsin-1A-interacting protein 1
MAGT1	Magnesium transporter protein 1
POFUT1	GDP-fucose protein O-fucosyltransferase 1
SDF2	Stromal cell-derived factor 2
CCT8	T-complex protein 1 subunit theta
ERAP1	Endoplasmic reticulum aminopeptidase 1
YBX3	Y-box-binding protein 3
PGRMC2	Membrane-associated progesterone receptor component 2
APMAP	Adipocyte plasma membrane-associated protein
RUVBL1	RuvB-like 1
IPO5	Importin-5 (Fragment)

SQSTM1	Sequestosome-1
ASPH	Aspartyl/asparaginyl beta-hydroxylase
MYO1E	Unconventional myosin-Ie
NOP2	Probable 28S rRNA (cytosine(4447)-C(5))-methyltransferase
PPIB	Peptidyl-prolyl cis-trans isomerase B
SEC63	Translocation protein SEC63 homolog
CDA	Cytidine deaminase
EPS8L2	Epidermal growth factor receptor kinase substrate 8-like protein 2
LAMB3	Laminin subunit beta-3
MGST1	Microsomal glutathione S-transferase 1
CORO1B	Coronin-1B

10.2 List of proteins identified by BioID-based proximity labeling in MDA-MB 231 cells stably expressing H6PD-BirA*-HA and 11β-HSD1 compared to control (MDA-MB 231 cells stably expressing 11β-HSD1)

Log_2-ratio ≥ 1; qValue ≤ 0.05, compared to control (MDA-MB 231 cells stably expressing 11β-HSD1)

BRI3BP	BRI3-binding protein
H6PD	FUSION Cterm-BirA C-H6PD linker sequence BirA HA tag
	GDH/6PGL endoplasmic bifunctional protein
SELENOF	15 kDa selenoprotein F
TOR1B	Torsin-1B
PDIA3	Protein disulfide-isomerase A3
PDIA3	Protein disulfide-isomerase A3 (Fragment)
CALU	Calumenin
B3GAT3	Beta-1,3-glucuronyltransferase 3 (Glucuronosyltransferase I), isoform CRA_a
SEL1L	Protein sel-1 homolog 1
PDIA4	Protein disulfide-isomerase A4
HYOU1	Hypoxia up-regulated protein 1 (Fragment)
EDEM3	ER degradation-enhancing alpha-mannosidase-like protein 3
KDELC2	KDEL motif-containing protein 2
LMAN1	Protein ERGIC-53
MYDGF	Myeloid-derived growth factor (Fragment)
P4HB	Protein disulfide-isomerase
CLCC1	Chloride channel CLIC-like protein 1
MESDC2	LDLR chaperone MESD
TXNDC5	Thioredoxin domain-containing protein 5
HSPA5	78 kDa glucose-regulated protein
MAN2A1	Alpha-mannosidase 2
ASPH	Aspartyl/asparaginyl beta-hydroxylase
DNAJB11	DnaJ homolog subfamily B member 11
POFUT1	GDP-fucose protein O-fucosyltransferase 1
IKBIP	Inhibitor of nuclear factor kappa-B kinase-interacting protein

ATF6	Cyclic AMP-dependent transcription factor ATF-6 alpha
HYOU1	Hypoxia up-regulated protein 1
PRKCSH	Glucosidase 2 subunit beta
TMX3	Protein disulfide-isomerase TMX3
EOGT	EGF domain-specific O-linked N-acetylglucosamine transferase
NUCB2	Nucleobindin 2, isoform CRA_b
UGGT2	UDP-glucose:glycoprotein glucosyltransferase 2
SDF4	45 kDa calcium-binding protein
NA	Uncharacterized protein (Fragment)
RCN1	Reticulocalbin-1
FKBP2	Peptidyl-prolyl cis-trans isomerase FKBP2
LRPAP1	Alpha-2-macroglobulin receptor-associated protein
MOGS	Mannosyl-oligosaccharide glucosidase
GLG1	Golgi apparatus protein 1
SLC38A10	Putative sodium-coupled neutral amino acid transporter 10
ERO1A	ERO1-like protein alpha
DNAJC3	DnaJ homolog subfamily C member 3
STIM1	Stromal interaction molecule 1
FAM213A	Redox-regulatory protein FAM213A
POGLUT1	Protein O-glucosyltransferase 1
HSP90B1	Endoplasmin
MANF	Mesencephalic astrocyte-derived neurotrophic factor
PLOD2	Procollagen-lysine,2-oxoglutarate 5-dioxygenase 2
TGFB1	Transforming growth factor beta-1
NENF	Neudesin
TMX1	Thioredoxin-related transmembrane protein 1
PDIA6	Protein disulfide-isomerase A6
ERP29	Endoplasmic reticulum resident protein 29
DNAJB12	DnaJ homolog subfamily B member 12
NOMO1	Nodal modulator 1
PDIA5	Protein disulfide-isomerase A5
TMED4	Transmembrane emp24 domain-containing protein 4
LMAN2L	VIP36-like protein
SUMF2	Sulfatase-modifying factor 2

ERLIN2	Erlin-2
TXNDC12	Thioredoxin domain-containing protein 12
P4HA2	Prolyl 4-hydroxylase subunit alpha-2
ITGB1	Integrin beta-1
CALR	Calreticulin
ACTN1	Alpha-actinin-1
PLOD1	Procollagen-lysine,2-oxoglutarate 5-dioxygenase 1
UGGT1	UDP-glucose:glycoprotein glucosyltransferase 1
PCYOX1	Prenylcysteine oxidase 1
PRDX4	Peroxiredoxin-4
TMED7-TICAM2	Protein TMED7-TICAM2
COL4A1	Collagen alpha-1(IV) chain
ERLEC1	Endoplasmic reticulum lectin 1
SDF2	Stromal cell-derived factor 2
DNAJC10	DnaJ homolog subfamily C member 10
RCN2	Reticulocalbin-2
TGFB2	Transforming growth factor beta-2
CANX	Calnexin
GANAB	Neutral alpha-glucosidase AB
TMEM43	Transmembrane protein 43
SPANXB1	Sperm protein associated with the nucleus on the X chromosome B1
SERPINH1	Serpin H1
POFUT2	GDP-fucose protein O-fucosyltransferase 2
CNPY3	Protein canopy homolog 3
CCDC134	Coiled-coil domain-containing protein 134
RRAD	GTP-binding protein RAD
DDOST	Dolichyl-diphosphooligosaccharide--protein glycosyltransferase 48 kDa subunit
MIA3	Melanoma inhibitory activity protein 3
ERP44	Endoplasmic reticulum resident protein 44
SDF2L1	Stromal cell-derived factor 2-like protein 1
ERGIC3	Endoplasmic reticulum-Golgi intermediate compartment protein 3 (Fragment)
CRELD2	Cysteine-rich with EGF-like domain protein 2
P3H2	Prolyl 3-hydroxylase 2

HSD11B1	Corticosteroid 11-beta-dehydrogenase isozyme 1
NUP210	Nuclear pore membrane glycoprotein 210
RPN2	Dolichyl-diphosphooligosaccharide--protein glycosyltransferase subunit 2
FUT8	Alpha-(1,6)-fucosyltransferase
P4HA1	Prolyl 4-hydroxylase subunit alpha-1
CHID1	Chitinase domain-containing protein 1
TOR1AIP1	Torsin-1A-interacting protein 1
EMC1	ER membrane protein complex subunit 1
MYO1E	Unconventional myosin-Ie
PTGES	Prostaglandin E synthase
RPN1	Dolichyl-diphosphooligosaccharide--protein glycosyltransferase subunit 1
MLEC	Malectin
MAGT1	Magnesium transporter protein 1
SIL1	Nucleotide exchange factor SIL1
PLOD3	Procollagen-lysine,2-oxoglutarate 5-dioxygenase 3
RPLP1	60S acidic ribosomal protein P1
TMTC3	Transmembrane and TPR repeat-containing protein 3
CFL2	Cofilin-2
TMED9	Transmembrane emp24 domain-containing protein 9
P3H1	Prolyl 3-hydroxylase 1
SEC63	Translocation protein SEC63 homolog
TMED10	Transmembrane emp24 domain-containing protein 10
TMEM109	Transmembrane protein 109
LAMC2	Laminin subunit gamma-2
ERAP1	Endoplasmic reticulum aminopeptidase 1
ACTA2	Actin, aortic smooth muscle
BCCIP	BRCA2 and CDKN1A-interacting protein
LAMB3	Laminin subunit beta-3
GPX8	Glutathione peroxidase
COLGALT1	Procollagen galactosyltransferase 1
ERLIN1	Erlin-1
LEMD2	LEM domain-containing protein 2
BCAP31	B-cell receptor-associated protein 31
ADAM9	Disintegrin and metalloproteinase domain-containing protein 9

PNPLA6	Neuropathy target esterase
SLC39A7	Zinc transporter SLC39A7
TAPBP	Tapasin
PDLIM5	PDZ and LIM domain protein 5
IGFBP7	Insulin-like growth factor-binding protein 7
CPS1	Carbamoyl-phosphate synthase [ammonia], mitochondrial
ITGB4	Integrin beta-4
KTN1	Kinectin
HSPH1	Heat shock protein 105 kDa
LAMB1	Laminin subunit beta-1
FKBP7	Peptidyl-prolyl cis-trans isomerase FKBP7
RUVBL1	RuvB-like 1
CKAP4	Cytoskeleton-associated protein 4
NCEH1	Arylacetamide deacetylase-like 1
VTN	Vitronectin
PRDX3	Thioredoxin-dependent peroxide reductase, mitochondrial
CCT8	T-complex protein 1 subunit theta
FLNA	Filamin-A
CDA	Cytidine deaminase
CISD2	CDGSH iron-sulfur domain-containing protein 2
CCPG1	Cell cycle progression protein 1
LAMC1	Laminin subunit gamma-1
MACF1	Microtubule-actin cross-linking factor 1, isoforms 1/2/3/5
XPO1	Exportin-1
HPRT1	Hypoxanthine-guanine phosphoribosyltransferase
SUCO	SUN domain-containing ossification factor
STT3B	Dolichyl-diphosphooligosaccharide--protein glycosyltransferase subunit STT3B
MFSD10	Major facilitator superfamily domain-containing protein 10
CTSA	Carboxypeptidase
FSCN1	Fascin
MGST1	Microsomal glutathione S-transferase 1 (Fragment)
STMN1	Stathmin

11 References

Andrews, T.M., Tata, J.R., 1971. Protein synthesis by membrane-bound and free ribosomes of secretory and non-secretory tissues. Biochem J **121**, 683-694.

Atanasov, A.G., Nashev, L.G., Gelman, L., Legeza, B., Sack, R., Portmann, R., Odermatt, A., 2008. Direct protein-protein interaction of 11beta-hydroxysteroid dehydrogenase type 1 and hexose-6-phosphate dehydrogenase in the endoplasmic reticulum lumen. Biochim Biophys Acta **1783**, 1536-1543.

Atanasov, A.G., Nashev, L.G., Schweizer, R.A., Frick, C., Odermatt, A., 2004. Hexose-6-phosphate dehydrogenase determines the reaction direction of 11beta-hydroxysteroid dehydrogenase type 1 as an oxoreductase. FEBS Lett **571**, 129-133.

Atkins, C., Liu, Q., Minthorn, E., Zhang, S.Y., Figueroa, D.J., Moss, K., Stanley, T.B., Sanders, B., Goetz, A., Gaul, N., Choudhry, A.E., Alsaid, H., Jucker, B.M., Axten, J.M., Kumar, R., 2013. Characterization of a novel PERK kinase inhibitor with antitumor and antiangiogenic activity. Cancer Res **73**, 1993-2002.

Au, S.W., Gover, S., Lam, V.M., Adams, M.J., 2000. Human glucose-6-phosphate dehydrogenase: the crystal structure reveals a structural NADP(+) molecule and provides insights into enzyme deficiency. Structure **8**, 293-303.

Axten, J.M., Romeril, S.P., Shu, A., Ralph, J., Medina, J.R., Feng, Y., Li, W.H., Grant, S.W., Heerding, D.A., Minthorn, E., Mencken, T., Gaul, N., Goetz, A., Stanley, T., Hassell, A.M., Gampe, R.T., Atkins, C., Kumar, R., 2013. Discovery of GSK2656157: An Optimized PERK Inhibitor Selected for Preclinical Development. ACS Med Chem Lett **4**, 964-968.

Bagur, R., Hajnoczky, G., 2017. Intracellular Ca(2+) Sensing: Its Role in Calcium Homeostasis and Signaling. Mol Cell **66**, 780-788.

Banhegyi, G., Benedetti, A., Fulceri, R., Senesi, S., 2004. Cooperativity between 11beta-hydroxysteroid dehydrogenase type 1 and hexose-6-phosphate dehydrogenase in the lumen of the endoplasmic reticulum. J Biol Chem **279**, 27017-27021.

Beck, K.R., Inderbinen, S.G., Kanagaratnam, S., Kratschmar, D.V., Jetten, A.M., Yamaguchi, H., Odermatt, A., 2019a. 11beta-Hydroxysteroid dehydrogenases control access of 7beta,27-dihydroxycholesterol to retinoid-related orphan receptor gamma. J Lipid Res **60**, 1535-1546.

Beck, K.R., Kanagaratnam, S., Kratschmar, D.V., Birk, J., Yamaguchi, H., Sailer, A.W., Seuwen, K., Odermatt, A., 2019b. Enzymatic interconversion of the oxysterols 7beta,25-dihydroxycholesterol and 7-keto,25-hydroxycholesterol by 11beta-hydroxysteroid dehydrogenase type 1 and 2. J Steroid Biochem Mol Biol **190**, 19-28.

Benham, A.M., 2012. Protein secretion and the endoplasmic reticulum. Cold Spring Harb Perspect Biol **4**, a012872.

Bernal-Conde, L.D., Ramos-Acevedo, R., Reyes-Hernandez, M.A., Balbuena-Olvera, A.J., Morales-Moreno, I.D., Arguero-Sanchez, R., Schule, B., Guerra-Crespo, M., 2019. Alpha-Synuclein Physiology and Pathology: A Perspective on Cellular Structures and Organelles. Front Neurosci **13**, 1399.

Bertolotti, A., Zhang, Y., Hendershot, L.M., Harding, H.P., Ron, D., 2000. Dynamic interaction of BiP and ER stress transducers in the unfolded-protein response. Nat Cell Biol **2**, 326-332.

Black, V.H., Sanjay, A., van Leyen, K., Moeller, I., Lauring, B., Kreibich, G., 2002. Cholesterol and steroid synthesizing smooth endoplasmic reticulum of adrenocortical cells contains high levels of translocation apparatus proteins. Endocr Res **28**, 425-430.

Boyce, M., Bryant, K.F., Jousse, C., Long, K., Harding, H.P., Scheuner, D., Kaufman, R.J., Ma, D., Coen, D.M., Ron, D., Yuan, J., 2005. A selective inhibitor of eIF2alpha dephosphorylation protects cells from ER stress. Science **307**, 935-939.

Branon, T.C., Bosch, J.A., Sanchez, A.D., Udeshi, N.D., Svinkina, T., Carr, S.A., Feldman, J.L., Perrimon, N., Ting, A.Y., 2018. Efficient proximity labeling in living cells and organisms with TurboID. Nat Biotechnol **36**, 880-887.

Brini, M., Carafoli, E., 2011. The plasma membrane Ca(2)+ ATPase and the plasma membrane sodium calcium exchanger cooperate in the regulation of cell calcium. Cold Spring Harb Perspect Biol **3**.

Brodsky, J.L., Scott, C.M., 2007. Tipping the delicate balance: defining how proteasome maturation affects the degradation of a substrate for autophagy and endoplasmic reticulum associated degradation (ERAD). Autophagy **3**, 623-625.

Brust, V., Schindler, P.M., Lewejohann, L., 2015. Lifetime development of behavioural phenotype in the house mouse (Mus musculus). Front Zool **12 Suppl 1**, S17.

Casulli, A., 2020. Recognising the substantial burden of neglected pandemics cystic and alveolar echinococcosis. Lancet Glob Health **8**, e470-e471.

Chan, C.P., Siu, K.L., Chin, K.T., Yuen, K.Y., Zheng, B., Jin, D.Y., 2006. Modulation of the unfolded protein response by the severe acute respiratory syndrome coronavirus spike protein. J Virol **80**, 9279-9287.

Chapman, K., Holmes, M., Seckl, J., 2013. 11beta-hydroxysteroid dehydrogenases: intracellular gate-keepers of tissue glucocorticoid action. Physiol Rev **93**, 1139-1206.

Chatuphonprasert, W., Jarukamjorn, K., Ellinger, I., 2018. Physiology and Pathophysiology of Steroid Biosynthesis, Transport and Metabolism in the Human Placenta. Front Pharmacol **9**, 1027.

Chauchet, A., Grenouillet, F., Knapp, J., Richou, C., Delabrousse, E., Dentan, C., Millon, L., Di Martino, V., Contreras, R., Deconinck, E., Blagosklonov, O., Vuitton, D.A., Bresson-Hadni, S., FrancEchino, N., 2014. Increased incidence and characteristics of alveolar echinococcosis in patients with immunosuppression-associated conditions. Clin Infect Dis **59**, 1095-1104.

Chaudhuri, T.K., Paul, S., 2006. Protein-misfolding diseases and chaperone-based therapeutic approaches. FEBS J **273**, 1331-1349.

Chen, X., Cubillos-Ruiz, J.R., 2021. Endoplasmic reticulum stress signals in the tumour and its microenvironment. Nat Rev Cancer **21**, 71-88.

Cho, K.F., Branon, T.C., Udeshi, N.D., Myers, S.A., Carr, S.A., Ting, A.Y., 2020. Proximity labeling in mammalian cells with TurboID and split-TurboID. Nat Protoc **15**, 3971-3999.

Chow, C.Y., Wolfner, M.F., Clark, A.G., 2013. Using natural variation in Drosophila to discover previously unknown endoplasmic reticulum stress genes. Proc Natl Acad Sci U S A **110**, 9013-9018.

Clarke, J.L., Mason, P.J., 2003. Murine hexose-6-phosphate dehydrogenase: a bifunctional enzyme with broad substrate specificity and 6-phosphogluconolactonase activity. Arch Biochem Biophys **415**, 229-234.

Cnop, M., Foufelle, F., Velloso, L.A., 2012. Endoplasmic reticulum stress, obesity and diabetes. Trends Mol Med **18**, 59-68.

Cnop, M., Ladriere, L., Hekerman, P., Ortis, F., Cardozo, A.K., Dogusan, Z., Flamez, D., Boyce, M., Yuan, J., Eizirik, D.L., 2007. Selective inhibition of eukaryotic translation initiation factor 2 alpha dephosphorylation potentiates fatty acid-induced endoplasmic reticulum stress and causes pancreatic beta-cell dysfunction and apoptosis. J Biol Chem **282**, 3989-3997.

Corazzari, M., Gagliardi, M., Fimia, G.M., Piacentini, M., 2017. Endoplasmic Reticulum Stress, Unfolded Protein Response, and Cancer Cell Fate. Front Oncol **7**, 78.

Cossu, V., Bonanomi, M., Bauckneht, M., Ravera, S., Righi, N., Miceli, A., Morbelli, S., Orengo, A.M., Piccioli, P., Bruno, S., Gaglio, D., Sambuceti, G., Marini, C., 2020. Two high-rate pentose-phosphate pathways in cancer cells. Sci Rep **10**, 22111.

Cubillos-Ruiz, J.R., Bettigole, S.E., Glimcher, L.H., 2017. Tumorigenic and Immunosuppressive Effects of Endoplasmic Reticulum Stress in Cancer. Cell **168**, 692-706.

Cuevas-Ramos, D., Fleseriu, M., 2014. Treatment of Cushing's disease: a mechanistic update. J Endocrinol **223**, R19-39.

Dasarathy, S., Yang, Y., McCullough, A.J., Marczewski, S., Bennett, C., Kalhan, S.C., 2011. Elevated hepatic fatty acid oxidation, high plasma fibroblast growth factor 21, and fasting bile acids in nonalcoholic steatohepatitis. Eur J Gastroenterol Hepatol **23**, 382-388.

Eizirik, D.L., Cardozo, A.K., Cnop, M., 2008. The role for endoplasmic reticulum stress in diabetes mellitus. Endocr Rev **29**, 42-61.

Ferrari, P., 2010. The role of 11beta-hydroxysteroid dehydrogenase type 2 in human hypertension. Biochim Biophys Acta **1802**, 1178-1187.

Field, F.J., Born, E., Murthy, S., Mathur, S.N., 1998. Transport of cholesterol from the endoplasmic reticulum to the plasma membrane is constitutive in CaCo-2 cells and differs from the transport of plasma membrane cholesterol to the endoplasmic reticulum. J Lipid Res **39**, 333-343.

Filling, C., Wu, X., Shafqat, N., Hult, M., Martensson, E., Shafqat, J., Oppermann, U.C., 2001. Subcellular targeting analysis of SDR-type hydroxysteroid dehydrogenases. Mol Cell Endocrinol **171**, 99-101.

Fiorucci, S., Distrutti, E., Biagioli, M., 2021. Special FX: Harnessing the Farnesoid-X-Receptor to Control Bile Acid Synthesis. Dig Dis Sci.

Frommherz, L., Bub, A., Hummel, E., Rist, M.J., Roth, A., Watzl, B., Kulling, S.E., 2016. Age-Related Changes of Plasma Bile Acid Concentrations in Healthy Adults--Results from the Cross-Sectional KarMeN Study. PLoS One **11**, e0153959.

Gathercole, L.L., Lavery, G.G., Morgan, S.A., Cooper, M.S., Sinclair, A.J., Tomlinson, J.W., Stewart, P.M., 2013. 11beta-Hydroxysteroid dehydrogenase 1: translational and therapeutic aspects. Endocr Rev **34**, 525-555.

Gerakis, Y., Hetz, C., 2018. Emerging roles of ER stress in the etiology and pathogenesis of Alzheimer's disease. FEBS J **285**, 995-1011.

Glorioso, N., Filigheddu, F., Parpaglia, P.P., Soro, A., Troffa, C., Argiolas, G., Mulatero, P., 2005. 11beta-Hydroxysteroid dehydrogenase type 2 activity is associated with left ventricular mass in essential hypertension. Eur Heart J **26**, 498-504.

Gregory, S., Hill, D., Grey, B., Ketelbey, W., Miller, T., Muniz-Terrera, G., Ritchie, C.W., 2020. 11beta-hydroxysteroid dehydrogenase type 1 inhibitor use in human disease-a systematic review and narrative synthesis. Metabolism **108**, 154246.

Haeri, M., Knox, B.E., 2012. Endoplasmic Reticulum Stress and Unfolded Protein Response Pathways: Potential for Treating Age-related Retinal Degeneration. J Ophthalmic Vis Res **7**, 45-59.

Halperin, L., Jung, J., Michalak, M., 2014. The many functions of the endoplasmic reticulum chaperones and folding enzymes. IUBMB Life **66**, 318-326.

Hardy, R.S., Botfield, H., Markey, K., Mitchell, J.L., Alimajstorovic, Z., Westgate, C.S.J., Sagmeister, M., Fairclough, R.J., Ottridge, R.S., Yiangou, A., Storbeck, K.H., Taylor, A.E., Gilligan, L.C., Arlt, W., Stewart, P.M., Tomlinson, J.W., Mollan, S.P., Lavery, G.G., Sinclair, A.J., 2021. 11betaHSD1 Inhibition with AZD4017 Improves Lipid Profiles and Lean Muscle Mass in Idiopathic Intracranial Hypertension. J Clin Endocrinol Metab **106**, 174-187.

Hebert, D.N., Molinari, M., 2007. In and out of the ER: protein folding, quality control, degradation, and related human diseases. Physiol Rev **87**, 1377-1408.

Hino, Y., Minakami, S., 1982a. Hexose-6-phosphate and 6-phosphogluconate dehydrogenases of rat liver microsomes. Involvement in NADPH and carbon dioxide generation in the luminal space of microsomal vesicles. J Biochem **92**, 547-557.

Hino, Y., Minakami, S., 1982b. Hexose-6-phosphate dehydrogenase of rat liver microsomes. Isolation by affinity chromatography and properties. J Biol Chem **257**, 2563-2568.

Hollis, G., Huber, R., 2011. 11beta-Hydroxysteroid dehydrogenase type 1 inhibition in type 2 diabetes mellitus. Diabetes Obes Metab **13**, 1-6.

Hotamisligil, G.S., 2010. Endoplasmic reticulum stress and atherosclerosis. Nat Med **16**, 396-399.

Hribkova, H., Grabiec, M., Klemova, D., Slaninova, I., Sun, Y.M., 2018. Calcium signaling mediates five types of cell morphological changes to form neural rosettes. J Cell Sci **131**.

Hu, H., Tian, M., Ding, C., Yu, S., 2018. The C/EBP Homologous Protein (CHOP) Transcription Factor Functions in Endoplasmic Reticulum Stress-Induced Apoptosis and Microbial Infection. Front Immunol **9**, 3083.

Iyanagi, T., 2007. Molecular mechanism of phase I and phase II drug-metabolizing enzymes: implications for detoxification. Int Rev Cytol **260**, 35-112.

Julier, C., Nicolino, M., 2010. Wolcott-Rallison syndrome. Orphanet J Rare Dis **5**, 29.

Kallberg, Y., Oppermann, U., Persson, B., 2010. Classification of the short-chain dehydrogenase/reductase superfamily using hidden Markov models. FEBS J **277**, 2375-2386.

Kapuy, O., Banhegyi, G., 2013. Depletion of luminal pyridine nucleotides in the endoplasmic reticulum activates autophagy with the involvement of mTOR pathway. Biomed Res Int **2013**, 942431.

Karaskov, E., Scott, C., Zhang, L., Teodoro, T., Ravazzola, M., Volchuk, A., 2006. Chronic palmitate but not oleate exposure induces endoplasmic reticulum stress, which may contribute to INS-1 pancreatic beta-cell apoptosis. Endocrinology **147**, 3398-3407.

Kaushansky, A., Kappe, S.H., 2015. Host ER stress during malaria parasite infection. EMBO Rep **16**, 883-884.

Kern, P., Ammon, A., Kron, M., Sinn, G., Sander, S., Petersen, L.R., Gaus, W., Kern, P., 2004. Risk factors for alveolar echinococcosis in humans. Emerg Infect Dis **10**, 2088-2093.

Kido, K., Yamanaka, S., Nakano, S., Motani, K., Shinohara, S., Nozawa, A., Kosako, H., Ito, S., Sawasaki, T., 2020. AirID, a novel proximity biotinylation enzyme, for analysis of protein-protein interactions. Elife **9**.

Kim, D.I., Birendra, K.C., Zhu, W., Motamedchaboki, K., Doye, V., Roux, K.J., 2014. Probing nuclear pore complex architecture with proximity-dependent biotinylation. Proc Natl Acad Sci U S A **111**, E2453-2461.

King, C., Sengupta, P., Seo, A.Y., Lippincott-Schwartz, J., 2020. ER membranes exhibit phase behavior at sites of organelle contact. Proc Natl Acad Sci U S A **117**, 7225-7235.

Koike, T., Shiraki, R., Sasuga, D., Hosaka, M., Kawano, T., Fukudome, H., Kurosawa, K., Moritomo, A., Mimasu, S., Ishii, H., Yoshimura, S., 2019. Discovery and Biological Evaluation of Potent and Orally Active Human 11beta-Hydroxysteroid Dehydrogenase Type 1 Inhibitors for the Treatment of Type 2 Diabetes Mellitus. Chem Pharm Bull (Tokyo) **67**, 824-838.

Larochelle, M., Bergeron, D., Arcand, B., Bachand, F., 2019. Proximity-dependent biotinylation mediated by TurboID to identify protein-protein interaction networks in yeast. Journal of Cell Science **132**.

Lavery, G.G., Walker, E.A., Draper, N., Jeyasuria, P., Marcos, J., Shackleton, C.H., Parker, K.L., White, P.C., Stewart, P.M., 2006. Hexose-6-phosphate dehydrogenase knock-out mice lack 11 beta-hydroxysteroid dehydrogenase type 1-mediated glucocorticoid generation. J Biol Chem **281**, 6546-6551.

Lavery, G.G., Walker, E.A., Tiganescu, A., Ride, J.P., Shackleton, C.H., Tomlinson, J.W., Connell, J.M., Ray, D.W., Biason-Lauber, A., Malunowicz, E.M., Arlt, W., Stewart, P.M., 2008a. Steroid biomarkers and genetic studies reveal inactivating mutations in hexose-6-phosphate dehydrogenase in patients with cortisone reductase deficiency. J Clin Endocrinol Metab **93**, 3827-3832.

Lavery, G.G., Walker, E.A., Turan, N., Rogoff, D., Ryder, J.W., Shelton, J.M., Richardson, J.A., Falciani, F., White, P.C., Stewart, P.M., Parker, K.L., McMillan, D.R., 2008b. Deletion of hexose-6-phosphate dehydrogenase activates the unfolded protein response pathway and induces skeletal myopathy. J Biol Chem **283**, 8453-8461.

Laybutt, D.R., Preston, A.M., Akerfeldt, M.C., Kench, J.G., Busch, A.K., Biankin, A.V., Biden, T.J., 2007. Endoplasmic reticulum stress contributes to beta cell apoptosis in type 2 diabetes. Diabetologia **50**, 752-763.

Lee, S., Min, K.T., 2018. The Interface Between ER and Mitochondria: Molecular Compositions and Functions. Mol Cells **41**, 1000-1007.

Legeza, B., Balazs, Z., Nashev, L.G., Odermatt, A., 2013. The microsomal enzyme 17beta-hydroxysteroid dehydrogenase 3 faces the cytoplasm and uses NADPH generated by glucose-6-phosphate dehydrogenase. Endocrinology **154**, 205-213.

Li, J., Dawson, P.A., 2019. Animal models to study bile acid metabolism. Biochim Biophys Acta Mol Basis Dis **1865**, 895-911.

Li, S., Kong, L., Yu, X., 2015. The expanding roles of endoplasmic reticulum stress in virus replication and pathogenesis. Crit Rev Microbiol **41**, 150-164.

Li, W., Liu, R., Li, X., Tao, B., Zhai, N., Wang, X., Li, Q., Zhang, Y., Gu, W., Wang, W., Ning, G., 2019. Saxagliptin alters bile acid profiles and yields metabolic benefits in drug-naive overweight or obese type 2 diabetes patient. J Diabetes **11**, 982-992.

Lin, R., Lu, G., Wang, J., Zhang, C., Xie, W., Lu, X., Mantion, G., Martin, H., Richert, L., Vuitton, D.A., Wen, H., 2011. Time course of gene expression profiling in the liver of experimental mice infected with Echinococcus multilocularis. PLoS One **6**, e14557.

Lin, W., Stone, S., 2020. Unfolded protein response in myelin disorders. Neural Regen Res **15**, 636-645.

Liu, X., Salokas, K., Tamene, F., Jiu, Y., Weldatsadik, R.G., Ohman, T., Varjosalo, M., 2018. An AP-MS- and BioID-compatible MAC-tag enables comprehensive mapping of protein interactions and subcellular localizations. Nat Commun **9**, 1188.

Liu, Y., Nakagawa, Y., Wang, Y., Sakurai, R., Tripathi, P.V., Lutfy, K., Friedman, T.C., 2005. Increased glucocorticoid receptor and 11{beta}-hydroxysteroid dehydrogenase type 1 expression in hepatocytes may contribute to the phenotype of type 2 diabetes in db/db mice. Diabetes **54**, 32-40.

Lucangioli, S.E., Castano, G., Contin, M.D., Tripodi, V.P., 2009. Lithocholic acid as a biomarker of intrahepatic cholestasis of pregnancy during ursodeoxycholic acid treatment. Ann Clin Biochem **46**, 44-49.

Luo, L., Aubrecht, J., Li, D., Warner, R.L., Johnson, K.J., Kenny, J., Colangelo, J.L., 2018. Assessment of serum bile acid profiles as biomarkers of liver injury and liver disease in humans. PLoS One **13**, e0193824.

Maddah, G., Abdollahi, A., Sharifi-Nooghabi, R., Tavassoli, A., Rajabi-Mashadi, M.T., Jabbari-Nooghabi, A., Jabbari-Nooghabi, M., 2016. Difficulties in the diagnosis and management of alveolar hydatid disease: A case series. Caspian J Intern Med **7**, 52-56.

Maly, D.J., Papa, F.R., 2014. Druggable sensors of the unfolded protein response. Nat Chem Biol **10**, 892-901.

Manikandan, P., Nagini, S., 2018. Cytochrome P450 Structure, Function and Clinical Significance: A Review. Curr Drug Targets **19**, 38-54.

Marbet, P., Klusonova, P., Birk, J., Kratschmar, D.V., Odermatt, A., 2018. Absence of hexose-6-phosphate dehydrogenase results in reduced overall glucose consumption but does not prevent 11beta-hydroxysteroid dehydrogenase-1-dependent glucocorticoid activation. FEBS J **285**, 3993-4004.

Marchi, S., Patergnani, S., Pinton, P., 2014. The endoplasmic reticulum-mitochondria connection: one touch, multiple functions. Biochim Biophys Acta **1837**, 461-469.

Margittai, E., Banhegyi, G., 2008. Isocitrate dehydrogenase: A NADPH-generating enzyme in the lumen of the endoplasmic reticulum. Arch Biochem Biophys **471**, 184-190.

Marin de Mas, I., Aguilar, E., Zodda, E., Balcells, C., Marin, S., Dallmann, G., Thomson, T.M., Papp, B., Cascante, M., 2018. Model-driven discovery of long-chain fatty acid metabolic reprogramming in heterogeneous prostate cancer cells. PLoS Comput Biol **14**, e1005914.

Mattson, M.P., LaFerla, F.M., Chan, S.L., Leissring, M.A., Shepel, P.N., Geiger, J.D., 2000. Calcium signaling in the ER: its role in neuronal plasticity and neurodegenerative disorders. Trends Neurosci **23**, 222-229.

Medvedev, K.E., Kinch, L.N., Schaeffer, R.D., Grishin, N.V., 2019. Functional analysis of Rossmann-like domains reveals convergent evolution of topology and reaction pathways. PLoS Comput Biol **15**, e1007569.

Milhavet, O., Martindale, J.L., Camandola, S., Chan, S.L., Gary, D.S., Cheng, A., Holbrook, N.J., Mattson, M.P., 2002. Involvement of Gadd153 in the pathogenic action of presenilin-1 mutations. J Neurochem **83**, 673-681.

Mills, K.A., Mushtaq, I., Johnson, A.W., Whitfield, P.D., Clayton, P.T., 1998. A method for the quantitation of conjugated bile acids in dried blood spots using electrospray ionization-mass spectrometry. Pediatr Res **43**, 361-368.

Mindnich, R.D., Penning, T.M., 2009. Aldo-keto reductase (AKR) superfamily: genomics and annotation. Hum Genomics **3**, 362-370.

Morinaga, N., Yahiro, K., Matsuura, G., Moss, J., Noda, M., 2008. Subtilase cytotoxin, produced by Shiga-toxigenic Escherichia coli, transiently inhibits protein synthesis of Vero cells via degradation of BiP and induces cell cycle arrest at G1 by downregulation of cyclin D1. Cell Microbiol **10**, 921-929.

Mueller, M.C., Marx, M., Peyerl-Hoffmann, G., Kern, W.V., 2020. Spatial distribution and incidence trend of human alveolar echinococcosis in southwest Germany: increased incidence and urbanization of the disease? Infection **48**, 923-927.

Nakamura, M., Bhatnagar, A., Sadoshima, J., 2012. Overview of pyridine nucleotides review series. Circ Res **111**, 604-610.

O'Byrne, C., Utratna, M., 2010. Listeria monocytogenes: at the coalface of host-pathogen research. Bioeng Bugs **1**, 371-377.

Odermatt, A., Arnold, P., Stauffer, A., Frey, B.M., Frey, F.J., 1999. The N-terminal anchor sequences of 11beta-hydroxysteroid dehydrogenases determine their orientation in the endoplasmic reticulum membrane. J Biol Chem **274**, 28762-28770.

Odermatt, A., Da Cunha, T., Penno, C.A., Chandsawangbhuwana, C., Reichert, C., Wolf, A., Dong, M., Baker, M.E., 2011. Hepatic reduction of the secondary bile acid 7-oxolithocholic acid is mediated by 11beta-hydroxysteroid dehydrogenase 1. Biochem J **436**, 621-629.

Odermatt, A., Kratschmar, D.V., 2012. Tissue-specific modulation of mineralocorticoid receptor function by 11beta-hydroxysteroid dehydrogenases: an overview. Mol Cell Endocrinol **350**, 168-186.

Okumura, M., Kadokura, H., Inaba, K., 2015. Structures and functions of protein disulfide isomerase family members involved in proteostasis in the endoplasmic reticulum. Free Radic Biol Med **83**, 314-322.

Omura, T., Kaneko, M., Okuma, Y., Matsubara, K., Nomura, Y., 2013. Endoplasmic reticulum stress and Parkinson's disease: the role of HRD1 in averting apoptosis in neurodegenerative disease. Oxid Med Cell Longev **2013**, 239854.

Papandreou, I., Denko, N.C., Olson, M., Van Melckebeke, H., Lust, S., Tam, A., Solow-Cordero, D.E., Bouley, D.M., Offner, F., Niwa, M., Koong, A.C., 2011. Identification of an Ire1alpha endonuclease specific inhibitor with cytotoxic activity against human multiple myeloma. Blood **117**, 1311-1314.

Park, K., Lee, S.E., Shin, K.O., Uchida, Y., 2019. Insights into the role of endoplasmic reticulum stress in skin function and associated diseases. FEBS J **286**, 413-425.

Paudel, S., Sindelar, R., Saha, M., 2018. Calcium Signaling in Vertebrate Development and Its Role in Disease. Int J Mol Sci **19**.

Paulsen, S.K., Pedersen, S.B., Fisker, S., Richelsen, B., 2007. 11Beta-HSD type 1 expression in human adipose tissue: impact of gender, obesity, and fat localization. Obesity (Silver Spring) **15**, 1954-1960.

Peng, K., Pan, Y., Li, J., Khan, Z., Fan, M., Yin, H., Tong, C., Zhao, Y., Liang, G., Zheng, C., 2016. 11beta-Hydroxysteroid Dehydrogenase Type 1(11beta-HSD1) mediates insulin resistance through JNK activation in adipocytes. Sci Rep **6**, 37160.

Penno, C.A., Morgan, S.A., Rose, A.J., Herzig, S., Lavery, G.G., Odermatt, A., 2014. 11beta-Hydroxysteroid dehydrogenase-1 is involved in bile acid homeostasis by modulating fatty acid transport protein-5 in the liver of mice. Mol Metab **3**, 554-564.

Penno, C.A., Morgan, S.A., Vuorinen, A., Schuster, D., Lavery, G.G., Odermatt, A., 2013. Impaired oxidoreduction by 11beta-hydroxysteroid dehydrogenase 1 results in the accumulation of 7-oxolithocholic acid. J Lipid Res **54**, 2874-2883.

Phillips, M.J., Voeltz, G.K., 2016. Structure and function of ER membrane contact sites with other organelles. Nat Rev Mol Cell Biol **17**, 69-82.

Piccirella, S., Czegle, I., Lizak, B., Margittai, E., Senesi, S., Papp, E., Csala, M., Fulceri, R., Csermely, P., Mandl, J., Benedetti, A., Banhegyi, G., 2006. Uncoupled redox systems in the lumen of the endoplasmic reticulum. Pyridine nucleotides stay reduced in an oxidative environment. J Biol Chem **281**, 4671-4677.

Pillich, H., Loose, M., Zimmer, K.P., Chakraborty, T., 2012. Activation of the unfolded protein response by Listeria monocytogenes. Cell Microbiol **14**, 949-964.

Pillich, H., Loose, M., Zimmer, K.P., Chakraborty, T., 2016. Diverse roles of endoplasmic reticulum stress sensors in bacterial infection. Mol Cell Pediatr **3**, 9.

Prasanthi, J.R., Larson, T., Schommer, J., Ghribi, O., 2011. Silencing GADD153/CHOP gene expression protects against Alzheimer's disease-like pathology induced by 27-hydroxycholesterol in rabbit hippocampus. PLoS One **6**, e26420.

Puhka, M., Vihinen, H., Joensuu, M., Jokitalo, E., 2007. Endoplasmic reticulum remains continuous and undergoes sheet-to-tubule transformation during cell division in mammalian cells. J Cell Biol **179**, 895-909.

Raffaello, A., Mammucari, C., Gherardi, G., Rizzuto, R., 2016. Calcium at the Center of Cell Signaling: Interplay between Endoplasmic Reticulum, Mitochondria, and Lysosomes. Trends Biochem Sci **41**, 1035-1049.

Rahmati, M., Moosavi, M.A., McDermott, M.F., 2018. ER Stress: A Therapeutic Target in Rheumatoid Arthritis? Trends Pharmacol Sci **39**, 610-623.

Rao, R.V., Bredesen, D.E., 2004. Misfolded proteins, endoplasmic reticulum stress and neurodegeneration. Curr Opin Cell Biol **16**, 653-662.

Rivas, A., Vidal, R.L., Hetz, C., 2015. Targeting the unfolded protein response for disease intervention. Expert Opin Ther Tar **19**, 1203-1218.

Rogoff, D., Black, K., McMillan, D.R., White, P.C., 2010. Contribution of hexose-6-phosphate dehydrogenase to NADPH content and redox environment in the endoplasmic reticulum. Redox Rep **15**, 64-70.

Rossi Sebastiano, M., Konstantinidou, G., 2019. Targeting Long Chain Acyl-CoA Synthetases for Cancer Therapy. Int J Mol Sci **20**.

Ryu, E.J., Harding, H.P., Angelastro, J.M., Vitolo, O.V., Ron, D., Greene, L.A., 2002. Endoplasmic reticulum stress and the unfolded protein response in cellular models of Parkinson's disease. J Neurosci **22**, 10690-10698.

Samtleben, S., Jaepel, J., Fecher, C., Andreska, T., Rehberg, M., Blum, R., 2013. Direct imaging of ER calcium with targeted-esterase induced dye loading (TED). J Vis Exp, e50317.

Sandoval, I.V., Bakke, O., 1994. Targeting of membrane proteins to endosomes and lysosomes. Trends Cell Biol **4**, 292-297.

Sanvictores, T., Davis, D.D., 2020. Histology, Rough Endoplasmic Reticulum, StatPearls, Treasure Island (FL), pp.

Schonthal, A.H., 2012. Endoplasmic reticulum stress: its role in disease and novel prospects for therapy. Scientifica (Cairo) **2012**, 857516.

Schwarz, D.S., Blower, M.D., 2016. The endoplasmic reticulum: structure, function and response to cellular signaling. Cell Mol Life Sci **73**, 79-94.

Schweizer, R.A., Zurcher, M., Balazs, Z., Dick, B., Odermatt, A., 2004. Rapid hepatic metabolism of 7-ketocholesterol by 11beta-hydroxysteroid dehydrogenase type 1: species-specific differences between the rat, human, and hamster enzyme. J Biol Chem **279**, 18415-18424.

Scott, J.S., Bowker, S.S., Deschoolmeester, J., Gerhardt, S., Hargreaves, D., Kilgour, E., Lloyd, A., Mayers, R.M., McCoull, W., Newcombe, N.J., Ogg, D., Packer, M.J., Rees, A., Revill, J., Schofield, P., Selmi, N., Swales, J.G., Whittamore, P.R., 2012. Discovery of a potent, selective, and orally bioavailable acidic 11beta-hydroxysteroid dehydrogenase type 1 (11beta-HSD1) inhibitor: discovery of 2-[(3S)-1-[5-(cyclohexylcarbamoyl)-6-propylsulfanylpyridin-2-yl]-3-piperidyl]acet ic acid (AZD4017). J Med Chem **55**, 5951-5964.

Segal, M., Korkotian, E., 2014. Endoplasmic reticulum calcium stores in dendritic spines. Front Neuroanat **8**, 64.

Senesi, S., Legeza, B., Balazs, Z., Csala, M., Marcolongo, P., Kereszturi, E., Szelenyi, P., Egger, C., Fulceri, R., Mandl, J., Giunti, R., Odermatt, A., Banhegyi, G., Benedetti, A., 2010. Contribution of fructose-6-phosphate to glucocorticoid activation in the endoplasmic reticulum: possible implication in the metabolic syndrome. Endocrinology **151**, 4830-4839.

Setz, C., Friedrich, M., Hahn, S., Dorrie, J., Schaft, N., Schuler, G., Schubert, U., 2013. Just one position-independent lysine residue can direct MelanA into proteasomal degradation following N-terminal fusion of ubiquitin. PLoS One **8**, e55567.

Siles-Lucas, M., Casulli, A., Cirilli, R., Carmena, D., 2018. Progress in the pharmacological treatment of human cystic and alveolar echinococcosis: Compounds and therapeutic targets. PLoS Negl Trop Dis **12**, e0006422.

Simko, V., Michael, S., 1998. Urinary bile acids in population screening for inapparent liver disease. Hepatogastroenterology **45**, 1706-1714.

Szaraz, P., Banhegyi, G., Benedetti, A., 2010. Altered redox state of luminal pyridine nucleotides facilitates the sensitivity towards oxidative injury and leads to endoplasmic reticulum stress dependent autophagy in HepG2 cells. Int J Biochem Cell Biol **42**, 157-166.

Talbot, J., Maves, L., 2016. Skeletal muscle fiber type: using insights from muscle developmental biology to dissect targets for susceptibility and resistance to muscle disease. Wiley Interdiscip Rev Dev Biol **5**, 518-534.

Tanaka, M., Miyajima, A., 2016. Liver regeneration and fibrosis after inflammation. Inflamm Regen **36**, 19.

Tardif, K.D., Mori, K., Kaufman, R.J., Siddiqui, A., 2004. Hepatitis C virus suppresses the IRE1-XBP1 pathway of the unfolded protein response. J Biol Chem **279**, 17158-17164.

Terao, M., Murota, H., Kimura, A., Kato, A., Ishikawa, A., Igawa, K., Miyoshi, E., Katayama, I., 2011. 11beta-Hydroxysteroid dehydrogenase-1 is a novel regulator of skin homeostasis and a candidate target for promoting tissue repair. PLoS One **6**, e25039.

Tomlinson, J.W., Stewart, P.M., 2001. Cortisol metabolism and the role of 11beta-hydroxysteroid dehydrogenase. Best Pract Res Clin Endocrinol Metab **15**, 61-78.

Torgerson, P.R., Keller, K., Magnotta, M., Ragland, N., 2010. The global burden of alveolar echinococcosis. PLoS Negl Trop Dis **4**, e722.

Tsachaki, M., Birk, J., Egert, A., Odermatt, A., 2015. Determination of the topology of endoplasmic reticulum membrane proteins using redox-sensitive green-fluorescence protein fusions. Biochim Biophys Acta **1853**, 1672-1682.

Tsachaki, M., Mladenovic, N., Stambergova, H., Birk, J., Odermatt, A., 2018. Hexose-6-phosphate dehydrogenase controls cancer cell proliferation and migration through pleiotropic effects on the unfolded-protein response, calcium homeostasis, and redox balance. FASEB J **32**, 2690-2705.

Tsachaki, M., Strauss, P., Dunkel, A., Navratilova, H., Mladenovic, N., Odermatt, A., 2020. Impact of 17beta-HSD12, the 3-ketoacyl-CoA reductase of long-chain fatty acid synthesis, on breast cancer cell proliferation and migration. Cell Mol Life Sci **77**, 1153-1175.

Uezu, A., Kanak, D.J., Bradshaw, T.W., Soderblom, E.J., Catavero, C.M., Burette, A.C., Weinberg, R.J., Soderling, S.H., 2016. Identification of an elaborate complex mediating postsynaptic inhibition. Science **353**, 1123-1129.

Varnaite, R., MacNeill, S.A., 2016. Meet the neighbors: Mapping local protein interactomes by proximity-dependent labeling with BioID. Proteomics **16**, 2503-2518.

Versteeg, G.A., van de Nes, P.S., Bredenbeek, P.J., Spaan, W.J., 2007. The coronavirus spike protein induces endoplasmic reticulum stress and upregulation of intracellular chemokine mRNA concentrations. J Virol **81**, 10981-10990.

Voeltz, G.K., Rolls, M.M., Rapoport, T.A., 2002. Structural organization of the endoplasmic reticulum. EMBO Rep **3**, 944-950.

von Campenhausen, S., Bornschein, B., Wick, R., Botzel, K., Sampaio, C., Poewe, W., Oertel, W., Siebert, U., Berger, K., Dodel, R., 2005. Prevalence and incidence of Parkinson's disease in Europe. Eur Neuropsychopharmacol **15**, 473-490.

Wang, M., 2005. The role of glucocorticoid action in the pathophysiology of the Metabolic Syndrome. Nutr Metab (Lond) **2**, 3.

Wang, X., Dai, G., Li, M., Jia, W., Guo, Z., Lu, J., 2020. Prevalence of human alveolar echinococcosis in China: a systematic review and meta-analysis. BMC Public Health **20**, 1105.

Wang, X., Mick, G., McCormick, K., 2019. Pyridine nucleotide regulation of hepatic endoplasmic reticulum calcium uptake. Physiol Rep **7**, e14151.

Wang, X., Mick, G.J., Maser, E., McCormick, K., 2011. Manifold effects of palmitoylcarnitine on endoplasmic reticulum metabolism: 11beta-hydroxysteroid dehydrogenase 1, flux through hexose-6-phosphate dehydrogenase and NADPH concentration. Biochem J **437**, 109-115.

Weingartner, M., Stucheli, S., Kratschmar, D.V., Birk, J., Klusonova, P., Chapman, K.E., Lavery, G.G., Odermatt, A., 2021. The ratio of ursodeoxycholyltaurine to 7-oxolithocholyltaurine serves as a biomarker of decreased 11beta-hydroxysteroid dehydrogenase 1 activity in mouse. Br J Pharmacol.

White, P.C., 2018. Alterations of Cortisol Metabolism in Human Disorders. Horm Res Paediatr **89**, 320-330.

White, P.C., Rogoff, D., McMillan, D.R., Lavery, G.G., 2007. Hexose 6-phosphate dehydrogenase (H6PD) and corticosteroid metabolism. Mol Cell Endocrinol **265-266**, 89-92.

Whitworth, J.A., Williamson, P.M., Mangos, G., Kelly, J.J., 2005. Cardiovascular consequences of cortisol excess. Vasc Health Risk Manag **1**, 291-299.

Wu, B., Basu, S., Meng, S., Wang, X., Hu, M., 2011. Regioselective sulfation and glucuronidation of phenolics: insights into the structural basis. Curr Drug Metab **12**, 900-916.

Wu, J., Kaufman, R.J., 2006. From acute ER stress to physiological roles of the Unfolded Protein Response. Cell Death Differ **13**, 374-384.

Xie, G., Wang, Y., Wang, X., Zhao, A., Chen, T., Ni, Y., Wong, L., Zhang, H., Zhang, J., Liu, C., Liu, P., Jia, W., 2015. Profiling of serum bile acids in a healthy Chinese population using UPLC-MS/MS. J Proteome Res **14**, 850-859.

Xu, C., Ng, D.T., 2015. Glycosylation-directed quality control of protein folding. Nat Rev Mol Cell Biol **16**, 742-752.

Yamazaki, M., Miyake, M., Sato, H., Masutomi, N., Tsutsui, N., Adam, K.P., Alexander, D.C., Lawton, K.A., Milburn, M.V., Ryals, J.A., Wulff, J.E., Guo, L., 2013. Perturbation of bile acid homeostasis is an early pathogenesis event of drug induced liver injury in rats. Toxicol Appl Pharmacol **268**, 79-89.

Yao, L., Seaton, S.C., Ndousse-Fetter, S., Adhikari, A.A., DiBenedetto, N., Mina, A.I., Banks, A.S., Bry, L., Devlin, A.S., 2018. A selective gut bacterial bile salt hydrolase alters host metabolism. Elife **7**.

Yoo, Y.S., Han, H.G., Jeon, Y.J., 2017. Unfolded Protein Response of the Endoplasmic Reticulum in Tumor Progression and Immunogenicity. Oxid Med Cell Longev **2017**, 2969271.

Zhang, Y., Song, G., Lal, N.K., Nagalakshmi, U., Li, Y., Zheng, W., Huang, P.J., Branon, T.C., Ting, A.Y., Walley, J.W., Dinesh-Kumar, S.P., 2019. TurboID-based proximity labeling reveals that UBR7 is a regulator of N NLR immune receptor-mediated immunity. Nat Commun **10**, 3252.

Zhang, Y.L., Zhong, X., Gjoka, Z., Li, Y., Stochaj, W., Stahl, M., Kriz, R., Tobin, J.F., Erbe, D., Suri, V., 2009. H6PDH interacts directly with 11beta-HSD1: implications for determining the directionality of glucocorticoid catalysis. Arch Biochem Biophys **483**, 45-54.

Zhou, Z., Xu, M.J., Gao, B., 2016. Hepatocytes: a key cell type for innate immunity. Cell Mol Immunol **13**, 301-315.

12 Curriculum Vitae

Personal Information

Name: Michael Weingartner

E-Mail: michael.weingartner@unibas.ch / michaelweingartner@gmx.ch

Date of birth: October 08, 1990

Place of birth: Lucerne

Address: Stollbergstrasse 29

City: Lucerne

Education

2017-2021: PhD student in the group of Molecular and Systems Toxicology under the supervision of Prof. Dr. Alex Odermatt, Department of Pharmaceutical Sciences, University of Basel

2015: Federal Diploma as pharmacist

2013-2015: M Sc in Pharmacy, University of Basel

2010-2013: B Sc in Pharmaceutical Sciences, University of Basel

2003-2009: Kantonsschule Reussbhühl, Lucerne

1997-2003: Primary school Fluhmühle, Lucerne

Work experience

2017-2021: PhD student

- PhD student in the group of Molecular and Systems Toxicology under the supervision of Prof. Dr. Alex Odermatt, Department of Pharmaceutical Sciences, University of Basel

2016-2017: Pharmacist at Medicus Apotheke AG, Kriens, Lucerne

- Head of in-house production
  manufacturing of small scale pharmaceuticals in accordance with GMP guidelines
- Supervisor of production and quality control
- Contact person for contract manufacturing
- Responsible for development of new pharmaceutical products
- Acquisition of contractual partners
- Deputy pharmacist

2015: Civil service at Betagtenzentrum und Altersheim Staffelnhof, Reussbühl, Lucerne

- Co-worker in cafeteria

2011-2014: Securitas AG (Part-time security employee)

- security guard at major (sport) events, assistance for railway police, guarding and personal protection services
- Swiss Professional Academy for Security and Safety Diploma (2013)

2010: Internship at TopPharm Dr. Schimd's See Apotheke AG, Lucerne

2009: Mandatory Military service

- NBC instructor (corporal) at Spiez laboratory, Spiez, Berne and in Riazzino, Ticino

Publications

(updated: 01.03.2021)

Weingartner M, Stücheli S, Kratschmar DV, Birk J, Klusonova P, Chapman KE, Lavery GG, Odermatt A. The ratio of ursodeoxycholyltaurine to 7-oxolithocholyltaurine serves as a biomarker of decreased 11β-hydroxysteroid dehydrogenase 1 activity in mouse. Br J Pharmacol. 2021 Jan 15. doi: 10.1111/bph.15367. Epub ahead of print. PMID: 33450045.

Preisig D, **Weingartner M**, Varum FJ, Bravo R, Alles R, Huwyler J, Puchkov M. Marker-ion analysis for quantification of mucoadhesivity of microparticles in particle-retention assays. Int J Pharm. 2015 Jun 20;487(1-2):157-66. doi: 10.1016/j.ijpharm.2015.04.020. Epub 2015 Apr 13. PMID: 25882011.